

THE UNIVERSITY OF TULSA

THE GRADUATE SCHOOL

EXPERIMENTS, CFD SIMULATION AND MODELING

OF SAND WEAR AND PERFORMANCE

DEGRADATION IN ESPS

By
Haiwen Zhu

A dissertation submitted in partial fulfillment of
the requirements for the degree of Doctor of Philosophy
in the Discipline of Petroleum Engineering

The Graduate School
The University of Tulsa

2019

ProQuest Number:27672014

All rights reserved

INFORMATION TO ALL USERS

The quality of this reproduction is dependent on the quality of the copy submitted.

In the unlikely event that the author did not send a complete manuscript and there are missing pages, these will be noted. Also, if material had to be removed, a note will indicate the deletion.



ProQuest 27672014

Published by ProQuest LLC (2020). Copyright of the Dissertation is held by the Author.

All Rights Reserved.

This work is protected against unauthorized copying under Title 17, United States Code
Microform Edition © ProQuest LLC.

ProQuest LLC
789 East Eisenhower Parkway
P.O. Box 1346
Ann Arbor, MI 48106 - 1346

THE UNIVERSITY OF TULSA
THE GRADUATE SCHOOL

EXPERIMENTS, CFD SIMULATION AND MODELING
OF SAND WEAR AND PERFORMANCE
DEGRADATION IN ESPs

by
Haiwen Zhu

A DISSERTATION

APPROVED FOR THE DISCIPLINE OF
PETROLEUM ENGINEERING

By Dissertation Committee

Hong-Quan Zhang, Chair
Siamack Shirazi
Mauricio Prado
Zheng Ye
Jianjun Zhu

COPYRIGHT STATEMENT

Copyright © 2019 by Haiwen Zhu

All rights reserved. No part of this publication may be reproduced, stored in a retrieval system, or transmitted, in any form or by any means (electronic, mechanical, photocopying, recording, or otherwise) without the prior written permission of the author.

ABSTRACT

Haiwen Zhu (Doctor of Philosophy in Petroleum Engineering)

Experiments, CFD Simulation and Modeling of Sand Wear and Performance Degradation in ESPs

Directed by Dr. Hong-Quan (Holden) Zhang

137 pp, Chapter 5: Conclusions and Recommendations

(322 words)

A closed-loop experimental facility was designed and constructed to study the sand erosion process in a mixed type ESP, which is referred as MTESP in this dissertation. Four sets of experiments were conducted under different rotation speeds and gas volumetric fraction to investigate erosion effect on ESPs performance, including boosting pressure, efficiency, and vibration. Geometries, including impeller hub outside diameter (OD), impeller hub inside diameter (ID), impeller skirt ring OD, impeller balance ring OD, impeller outside shroud OD, sleeves OD, diffuser skirt slot depth, diffuser outside shroud ID, diffuser skirt slot ID, diffuser balance slot ID and diffuser bore ID were measured after each time-period test to indicate abrasion in ESPs. Stages were painted to obtain erosion patterns, and weight loss was recorded to compare with the predicted erosion rates.

Three ESPs, including two mixed type pumps (DN1750 and MTESP) and one radial type pump (TE2700), were numerically modeled to study the pump type effect on ESP erosion. For each pump, the flow domain of two stages was selected and high-quality structured meshes, comprising 1.2 to 1.8 million hexahedral grids per stage, were generated

by ICEM or Turbogrid. Six erosion models were evaluated to obtain the most accurate model in ESP erosion prediction.

Based on the seal failure analysis and wear mechanism, an improved mechanistic model for prediction of ESP performance in terms of boosting pressure has been developed. The erosion model was chosen based on the comparison among the calculated erosion rate and test results by CFD methods. The method of abrasion prediction is based on Archard (1953) equation. Leakage loss in ESP is calculated with the eroded hub, sleeves, and seals. The discrepancy in model predictions can be improved by adding closure relationships, including seal forces and leakage coefficient correlations.

ACKNOWLEDGEMENTS

First, I want to thank my advisor, Dr. Hong-Quan Zhang, who gave me guidance, encouragement, and support throughout this study. I am also grateful for his professionalism during the formation of this dissertation.

I appreciate the help and sponsor from TUALP members. The advice given by Risa Rutter, Michael Forsberg, Zheng Ye, Shawn Gunter, and Ignacio Martinez has been a great help in my facility setup and test matrix design.

I am grateful for the support and help from the TUALP team. I wish to acknowledge Dr. Jianjun Zhu's help with my CFD, programming and technical writing skills. I would also like to thank Mr. Bryan Sam for his assistance with facility construction and maintenance, as well as Ms. Donna Trankley for her efficient administrative work and grammar check of my publications. Drs. Zhiyuan Wang, Chuan Wang, Zhihua Wang, and Junqi Wang provided me with valuable testing and modeling advice. I would also like to thank Yi Shi, Zulin Zhou, Qingqi Zhao, Jianlin Peng, Jiecheng Zhang and Hattan Banjar for their assistance on my experiments.

I wish to acknowledge the comments and encouragement regarding my dissertation from Dr. Siamack Shirazi and Dr. Mauricio Prado who serve on my doctoral committee.

At last, I thank my parents, Tanyu Zhu and Hong Yu for their support and love during my Ph.D. program and throughout my entire life.

TABLE OF CONTENTS

COPYRIGHT STATEMENT.....	iii
ABSTRACT.....	iv
ACKNOWLEDGEMENTS.....	vi
TABLE OF CONTENTS.....	vii
LIST OF FIGURES	x
LIST OF TABLES.....	xx
INTRODUCTION	1
CHAPTER 1: LITERATURE REVIEW	3
1.1 Erosion Wear.....	6
<i>1.1.1 Erosion mechanism.....</i>	<i>7</i>
<i>1.1.2 Erosion prediction model.....</i>	<i>9</i>
<i>1.1.3 Erosion prediction procedure.....</i>	<i>14</i>
1.2 Abrasion Wear	15
<i>1.2.1 Abrasion mechanism.....</i>	<i>15</i>
<i>1.2.2 The empirical abrasion prediction model.....</i>	<i>18</i>
1.3 Wear in ESPs.....	20
<i>1.3.1 Erosion in ESPs</i>	<i>21</i>
<i>1.3.2 Abrasion on ESPs</i>	<i>26</i>
1.4 Gas-Liquid-Solid CFD Simulation	29
<i>1.4.1 Rotating turbomachinery methodology.....</i>	<i>30</i>
<i>1.4.2 Turbulence model.....</i>	<i>31</i>
<i>1.4.3 Near wall treatment</i>	<i>32</i>
<i>1.4.4 Particle rebound model.....</i>	<i>35</i>
<i>1.4.5 Particle tracking method.....</i>	<i>37</i>
<i>1.4.6 Gas-liquid multiphase simulation.....</i>	<i>39</i>
1.5 Mechanistic Modeling.....	40
CHAPTER 2: EXPERIMENTAL SETUP AND RESULTS.....	44
2.1 Experimental Facility.....	45
<i>2.1.1 Water-air and water-air-sand flow loops</i>	<i>45</i>
<i>2.1.2 ESP test bench.....</i>	<i>47</i>
<i>2.1.3 Stage geometry and seals clearance</i>	<i>50</i>

2.1.4	<i>Data acquisition system (DAQ)</i>	51
2.2	Experimental Program	52
2.2.1	<i>Sand characteristics</i>	52
2.2.2	<i>Experimental procedure and test matrix</i>	54
2.3	Experimental Data	56
2.3.1	<i>Pump geometry and weight changes</i>	56
2.3.2	<i>Stage vibration</i>	71
2.3.3	<i>Stage photo</i>	74
2.3.4	<i>Pump performance degradation</i>	80
CHAPTER 3: THREE-DIMENSIONAL NUMERICAL SIMULATION		86
3.1	Geometry and Mesh	86
3.2	Numerical Schemes and Boundary Conditions	87
3.3	Results and Discussions	89
3.4.1	<i>Grid number and catalog curve validation</i>	89
3.4.2	<i>Stage effect</i>	91
3.4.3	<i>Transient simulation and steady-state DRWM simulation</i>	93
3.4.4	<i>Pump type effect</i>	96
3.4.5	<i>Particle diameter and density analysis</i>	99
3.4.6	<i>Turbulence model and wall function effect</i>	102
3.4.7	<i>Particle rebound model effect</i>	107
3.4.8	<i>Air-water-solid three-phase simulation</i>	109
3.4.9	<i>Erosion models comparison</i>	116
CHAPTER 4: MECHANISTIC MODELING AND RESULTS		122
4.1	Model Development	122
4.2.1	<i>Performance prediction</i>	122
4.2.2	<i>Erosion prediction</i>	127
4.2.3	<i>Abrasion prediction</i>	132
4.2	Mechanistic Modeling Results	135
4.3.1	<i>Abrasion validation</i>	136
4.3.2	<i>Performance validation</i>	136
CHAPTER 5: CONCLUSIONS AND RECOMMENDATIONS		138
5.1	Summary and Conclusions	138
5.1.1	<i>Experimental study</i>	138
5.1.2	<i>Numerical simulations</i>	141
5.1.3	<i>Mechanistic modeling</i>	143
5.2	Recommendations	144
5.2.1	<i>Experimental study</i>	144
5.2.2	<i>Numerical simulations</i>	144
5.2.3	<i>Mechanistic modeling</i>	145
NOMENCLATURE		146
BIBLIOGRAPHY		152

APPENDIX A: CALCULATION EQUATIONS FOR SINGLE-PHASE FLUID FLOW IN ESPS	168
APPENDIX B: PUMP GEOMETRY AND WEIGHT MEASUREMENT	177
B.1 Case-1 Water-Sand at $N = 3600$ rpm, $Q_L = 3100$ bpd	177
B.2 Case-2 Water-Sand at $N = 2400$ rpm, $Q_L = 3100$ bpd	185
B.3 Case-3 Air-Water-Sand at $N = 3600$ rpm, $Q_L = 3100$ bpd, $GVF = 15\%$.....	193
B.4 Case-4 Air-Water-Sand at $N = 3600$ rpm, $Q_L = 3100$ bpd, $GVF = 7.5\%$.....	200
B.5 Pump geometry comparison plots	208
APPENDIX C: ERROR ANALYSIS	211
APPENDIX D: GAS PROPERTY CALCULATION.....	216

LIST OF FIGURES

1.1 Wear type	3
1.2 Wear type ESP stage components and flow directions, (a) primary flow, (b) secondary flow and leakage	6
1.3 Single area of contact model.....	16
1.4 Schematic illustration of abrasion machine	19
1.5 Components of ESP, (a) entire ESP (http://www.franklinwater.com), (b) impeller front view, (c) diffuser front view	21
1.6 Eroded stages, (a) impeller, (b) diffuser, (c) scanned images of eroded impellers (Morrison et al., 2017)	23
1.7 Paint-removal tests, (a) compressor(Bertoneri et al., 2014; Falomi et al., 2016), (b) wind energy blade (Muhlbauer et al., and Wagner, 2018), (c) elbows (.....	24
1.8 Near-wall treatment, (a) subdivision of the near-wall region, (b) wall function and near-wall mesh refinement.....	34
1.9 Particle impact trajectory simulation, (a) fine grid near-wall boundary, (b) coarse grid near-wall boundary.....	35
1.10 particle rebound at the wall.....	36
1.11. Schematic of head curves and losses (a) head thrust and efficiency changes due to inter-stage leakage (Stepanoff, 1957), (b) head losses (Gülich, 2008), (c) head losses (Vieira et al., 2015).....	41

2.1 Schematic of TUALP ESP sand erosion flow loop	45
2.2 Skid for TUALP ESP sand erosion flow loop	48
2.3 MTESP components , (a) pressure ports and proximity probes, (b) 3D pump housing, (c) left view of pump housing, (d) 3D view of diffuser, (e) section view of MTESP, (f) combination of stages	49
2.4 Measured geometry on stages, (a) impeller, (b) diffuser	51
2.5 Sand particle size distribution (a) original, (b) after 2-hour circulation at 2 hours test, (c) after 2-hour circulation at 32 hours test, (d) after 2-hour circulation at 64 hours test	53
2.6 SEM scans, (a) original, (b) 2 hours, (c) 32 hours, (d) 64 hours	54
2.7 ESP erosion test procedure	55
2.8 Geometry changes in the inter-stage clearance.....	57
2.9 Geometry changes in the inter-stage clearance (diffuser-sleeve) clearance, (a) floater diffuser bore ID, (b) SCS diffuser bore ID, (c) steel sleeve OD, (d) carbide sleeve OD, (e) floater inter-stage clearance, (f) SCS inter-stage clearance	59
2.10 Geometry changes in the skirt ring clearance	60
2.11 Geometry changes in the skirt-ring clearance, (a) impeller skirt ring OD, (b) diffuser skirt bore ID, (c) skirt ring clearance.....	62
2.12 Geometry changes in the balance ring clearance	63
2.13 Geometry changes in the balance ring clearance, (a) impeller balance ring OD, (b) diffuser balance ring ID, (c) balance ring clearance	64
2.14 Geometry changes of three clearances for SCS and floater stages.....	65

2.15 Comparison of geometry changes of three clearance among four cases, (a) Case 1: water-sand, $Q_L=3100$ bpd, $N=3600$ rpm, (b) Case 2: water-sand, $Q_L=3100$ bpd, $N=2400$ rpm, (c) Case 3: water-air-sand, $Q_L=3100$ bpd, $N=3600$ rpm, $GVF=15\%$ (d) Case 4: water-air-sand, $Q_L=3100$ bpd, $N=3600$ rpm, $GVF=7.5\%$	66
2.16 Abrasion damage on sleeve OD.....	67
2.17 Geometry changes of sleeve OD, (a) Case 1: water-sand, $Q_L=3100$ bpd, $N=3600$ rpm, (b) Case 2: water-sand, $Q_L=3100$ bpd, $N=2400$ rpm, (c) Case 3: water-air-sand, $Q_L=3100$ bpd, $N=3600$ rpm, $GVF=15\%$ (d) Case 4: water-air-sand, $Q_L=3100$ bpd, $N=3600$ rpm, $GVF=7.5\%$	68
2.18 Average weight and weight loss of four cases (a) impeller weight, (b) diffuser weight, (c) impeller weight loss, (d) diffuser weight loss.....	69
2.19 Average weight loss of SCS stages and floater stages for four cases, (a) Case 1: water-sand, $Q_L = 3100$ bpd, $N = 3600$ rpm, (b) Case 2: water-sand, $Q_L = 3100$ bpd, $N = 2400$ rpm, (c) Case 3: water-air-sand, $Q_L = 3100$ bpd, $N = 3600$ rpm, $GVF = 15\%$ (d) Case 4: water-air-sand, $Q_L = 3100$ bpd, $N = 3600$ rpm, $GVF = 7.5\%$	70
2.20 FFT of vibration in vertical and horizontal direction, (a) Case 1: water-sand, $Q_L = 3100$ bpd, $N = 3600$ rpm, (b) Case 2: water-sand, $Q_L = 3100$ bpd, $N = 2400$ rpm, (c) Case 3: water-air-sand, $Q_L = 3100$ bpd, $N = 3600$ rpm, $GVF = 15\%$ (d) Case 4: water-air-sand, $Q_L = 3100$ bpd, $N = 3600$ rpm, $GVF = 7.5\%$	73
2.21 Impeller orbit, (a) Case 1: water-sand, $Q_L = 3100$ bpd, $N = 3600$ rpm, (b) Case 2: water-sand, $Q_L = 3100$ bpd, $N = 2400$ rpm, (c) Case 3: water-air-sand, $Q_L =$	

3100 bpd, $N = 3600$ rpm, $GVF = 15\%$ (d) Case 4: water-air-sand, $Q_L = 3100$ bpd, $N = 3600$ rpm, $GVF = 7.5\%$	74
2.22 Wear on MTESP, (a) 64 hours 1 st impeller of Case 1, (b) 64 hours 2 nd impeller of Case 1, (c) 64 hours diffuser of Case 1, (d) 64 hours diffuser of Case 3, (e) 64 hours steel sleeve of Case 1, (f) 64 hours straight carbide sleeve of Case 1, (g), 64 hours flanged carbide sleeve of Case 1, (h) 64 hours steel sleeve above the flange carbide sleeve of Case 4.....	75
2.23 Paint-removal photo of Case 2, (a) impeller-4 hours water, (b) impeller outlet- 4 hours water (c) impeller-4 hours slurry, (d) impeller inlet-4 hours slurry, (e) diffuser-4 hours water, (f) diffuser inlet-4 hours water, (g) diffuser 4-hours slurry, (h) diffuser inlet-4 hours slurry	77
2.24 Impeller paint-removal photos of four pumps, (a) Case 1: water-sand, $Q_L =$ 3100 bpd, $N = 3600$ rpm, (b) Case 2: water-sand, $Q_L = 3100$ bpd, $N = 2400$ rpm, (c) Case 3: water-air-sand, $Q_L = 3100$ bpd, $N = 3600$ rpm, $GVF = 15\%$ (d) Case 4: water-air-sand, $Q_L = 3100$ bpd, $N = 3600$ rpm, $GVF = 7.5\%$	78
2.25 Diffuser paint-removal photos of four pumps, (a) Case 1: water-sand, $Q_L =$ 3100 bpd, $N = 3600$ rpm, (b) Case 2: water-sand, $Q_L = 3100$ bpd, $N = 2400$ rpm, (c) Case 3: water-air-sand, $Q_L = 3100$ bpd, $N = 3600$ rpm, $GVF = 15\%$ (d) Case 4: water-air-sand, $Q_L = 3100$ bpd, $N = 3600$ rpm, $GVF = 7.5\%$	80
2.26 Pump performance curves in the 64-hour test, (a) Case 1: water-sand, $Q_L =$ 3100 bpd, $N = 3600$ rpm, (b) Case 2: water-sand, $Q_L = 3100$ bpd, $N = 2400$ rpm, (c) Case 3: water-air-sand, $Q_L = 3100$ bpd, $N = 3600$ rpm, $GVF = 15\%$ (d) Case 4: water-air-sand, $Q_L = 3100$ bpd, $N = 3600$ rpm, $GVF = 7.5\%$	81

2.27 Head decrease of four recorded stages after 64 hours at different flow rate, (a) Case 1: water-sand, $Q_L = 3100$ bpd, $N = 3600$ rpm, (b) Case 2: water-sand, $Q_L = 3100$ bpd, $N = 2400$ rpm, (c) Case 3: water-air-sand, $Q_L = 3100$ bpd, $N = 3600$ rpm, $GVF = 15\%$ (d) Case 4: water-air-sand, $Q_L = 3100$ bpd, $N = 3600$ rpm, $GVF = 7.5\%$	82
2.28 Average head, power, and efficiency decrease, (a) Case 1: water-sand, $Q_L = 3100$ bpd, $N = 3600$ rpm, (b) Case 2: water-sand, $Q_L = 3100$ bpd, $N = 2400$ rpm, (c) Case 3: water-air-sand, $Q_L = 3100$ bpd, $N = 3600$ rpm, $GVF = 15\%$ (d) Case 4: water-air-sand, $Q_L = 3100$ bpd, $N = 3600$ rpm, $GVF = 7.5\%$	83
2.29 Gas-liquid performance curves, (a) Pump performance at $GVF = 5\%$ (Case 3), (b) Pump performance at $GVF = 5\%$ (Case 4), (c) Pump performance at $GVF = 10\%$ (Case 3), (d) Pump performance at $GVF = 10\%$ (Case 4), (e) Pump performance vs. GVF at $Q_L = 3100$ bpd (Case 3), (f) Pump performance vs. GVF at $Q_L = 3100$ bpd (Case 4).....	85
3.1 Mesh (a) DN1750, (b) MTESP, (c) TE2700.....	87
3.2 Impact angle function of six erosion models	89
3.3 Head validation (a) optimum grid number analysis, (b) 3-stages MTESP head increment, (c) head increment error analysis (d) performance comparison between the simulated second stage and the test curve	91
3.4 MTESP stage erosion contour (a) 1st-stage impeller, (b) 2nd-stage impeller, (c) 3rd-stage impeller, (d) 1st-stage diffuser, (e) 2nd-stage diffuser, (f) 3rd-stage diffuser	92

3.5 3-stage MTESP transient simulation area-weighted average erosion rate (a)	
impeller, (b) diffuser	93
3.6 Steady-state DRWM and transient simulation (a) steady-state simulation with	
different DRWM tries number, (b) impeller average erosion rate vs. erosion	
flow time, (c) diffuser average erosion rate vs. erosion flow time	94
3.7 MTESP stage erosion contour (a) Steady state DPM impeller DRWM 1 tries,	
(b) Steady state DPM impeller DRWM 4 tries, (c) Transient DPM impeller	
DRWM 8 tries, (d) Transient DPM diffuser	95
3.8 Transient and steady state simulated area-weighted average erosion rate, (a)	
impeller, (b) diffuser	96
3.9 Impeller and diffuser erosion contour of different pumps using Oka et al. (2005)	
model (a) MTESP impeller, (b) TE2700 impeller, (c) DN1750 impeller, (d)	
MTESP diffuser, (e) TE2700 diffuser, (f) DN1750 diffuser	97
3.10 Impact information on impeller inside shroud of three pumps (a) impact angle,	
(b) impact speed, (c) hit times, (d) erosion rate	98
3.11 Particle size effect on the erosion patterns on impeller and diffuser (a) 50 μm	
impeller, (b) 200 μm impeller, (c) 1000 μm impeller, (d) 50 μm diffuser, (e)	
200 μm diffuser, (f) 1000 μm diffuser	100
3.12 Particle density effect to the erosion patterns on impeller and diffuser (a) 1500	
kg/m ³ impeller, (b) 2000 kg/m ³ impeller, (c) 3000 kg/m ³ impeller, (d) 1500	
kg/m ³ diffuser, (e) 2000 kg/m ³ diffuser, (f) 3000 kg/m ³ diffuser	101
3.13 Particle size and diameter effect (a) facet maximum erosion rate vs. particle	
diameter, (b) area-weighted average erosion rate vs. particle diameter, (c) facet	

maximum erosion rate vs. particle density, (d) area-weighted average erosion rate vs. particle density	102
3.14 Average erosion rate with different turbulence model (a) impeller, (b) diffuser....	103
3.15 Erosion contour (kg/m ² s) and velocity (m/s) contour of k- ϵ realizable, k- ω SST and RSM turbulence model (a) impeller erosion RSM, (b) impeller erosion k- ω SST, (c) impeller erosion k- ϵ realizable, (d) diffuser erosion RSM, (e) diffuser erosion k- ω SST, (f) diffuser erosion k- ϵ realizable, (g) stage velocity RSM, (h) stage velocity k- ω SST, (i) stage velocity k- ϵ realizable, (j) top-view of impeller paint-removal photo, (k) side view of impeller paint-removal photo (l) top view of diffuser paint-removal photo	104
3.16 Particle impact velocity and angle (a) impact angle on diffuser shroud, (b) impact angle on impeller hub, (c) impact velocity on diffuser shroud, (d) impact velocity on impeller hub	106
3.17 Wall function and curvature correlation effect (a) diffuser average erosion rate, (b) impeller average erosion rate, (c) impeller/diffuser erosion rate ratio, (d) head and torque at BEP by different models	107
3.18 Area-weighted average erosion rate and hits times by different rebound model, (a) erosion rate on diffuser shroud, (b) erosion rate on impeller hub, (c) erosion rate on impeller shroud	108
3.19 Gas-liquid flow performance validation at N = 3600 rpm, (a) Head of stage 3, 6, 9 and 12 vs. GVF at QL = 3100 bpd, (b) head, efficiency and power vs. flow rate at GVF = 5%, (c) head, efficiency and power vs. flow rate at GVF = 10%, (d) head, efficiency and power vs. GVF at QL = 3100 bpd	110

3.20 Gas bubble size effect, (a) Head vs. gas bubble diameter at GVF = 15%, (b) average erosion rate vs. gas bubble diameter at GVF = 15%, (c) modified 10% GVF pump curve, (d) modified head vs. GVF pump curve at QL = 3100 bpd.....	111
3.21 Gas phase distribution contour, (a) Steady state simulation GVF = 10%, (b) steady state simulation GVF = 15%, db = 0.000215 m, (c) Transient simulation GVF = 15%, db = 0.000215 m.....	112
3.22 Comparison of average erosion rate vs. GVF between test data, k- ϵ CFD and k- ω CFD simulations, (a) diffuser average erosion rate, (b) impeller average erosion rate.....	113
3.23 Average erosion rate of different stage surface vs. GVF, (a) erosion in diffuser by k- ϵ model, (b) erosion in impeller by k- ϵ model, (c) erosion in diffuser by k- ω model, (d) erosion in impeller by k- ω model.....	114
3.24 Erosion pattern comparison, (a) water-sand erosion pattern in diffuser, (b) gas-water-sand erosion pattern in diffuser at GVF = 15%, (c) impeller paint-removal photo at GVF = 15%, (d) water-sand erosion pattern in impeller, (e) gas-water-sand erosion pattern in impeller at GVF = 15%, (f) impeller outlet paint-removal photo at GVF = 15%,	115
3.25 MTESP impeller erosion contour (a) Haugen et al. (1995), (b) DNV (2015), (c) Zhang et al. (2007), (d) Oka et al. (2005), (e) Mansouri (2014), (f) Ahlert et al. (1994).....	116
3.26 MTESP diffuser erosion contour (a) Haugen et al. (1995), (b) DNV (2015), (c) Zhang et al. (2007), (d) Oka et al. (2005), (e) Mansouri (2014), (f) Ahlert et al. (1994).....	117

3.27 Facet maximum erosion rate and area-weighted average erosion rate on MTESP impeller and diffuser, (a) impeller maximum, (b) impeller average, (c) diffuser maximum, (d) diffuser average	118
3.28 Area-weighted average erosion rate comparison (a) diffuser, (b) impeller	120
3.29 Area-weighted average erosion rate error analysis	121
4.1 Velocity triangles at impeller outlet.....	123
4.2 Particle trajectory (a) main view (b) top view	129
4.3 Abrasion caused by particle between the sealing surface	132
4.4 Impeller orbit and force balance (a) top view (b) main view	134
4.5 Flow chart for pump performance degradation calculation	135
4.7 MTESP seals clearance validation, (a) skirt and balance ring clearance, (b) error analysis of seals clearance	136
4.8 MTESP performance degradation validation, (a) deteriorated head comparison between current study and Zhu et al. (2018) (a) head curve tested vs. calculated, (b) error analysis between calculated head and measured head	137
A.1 Schematic of the impeller flow channel.....	168
A.2 Velocity triangles at impeller outlet for $Q < Q_{BMP}$	169
A.3 Velocity triangles at impeller outlet for $Q > Q_{BMP}$	171
A.4 Flow chart for calculating ESP single-phase pressure increment	176
B.1 Case 1 performance degradation (a) head of stage 3, (b) head of stage 6, (c) head of stage 9, (d) head of stage 12, (e) average head, (f) pump efficiency, (g) average head degradation, (h), efficiency degradation	185

B.2 Case 2 performance degradation (a) head of stage 3, (b) head of stage 6, (c)	
head of stage 9, (d) head of stage 12, (e) average head, (f) pump efficiency	192
B.3 Case 3 performance degradation (a) head of stage 3, (b) head of stage 6, (c)	
head of stage 9, (d) head of stage 12, (e) average head, (f) Pump efficiency	200
B.3 Case 4 performance degradation (a) head of stage 3, (b) head of stage 6, (c)	
head of stage 9, (d) head of stage 12, (e) average head, (f) pump efficiency	208
B.2 Geometry changes in the inter-stage clearance, (a) Case 1: water-sand,	
$Q_L=3100\text{bpd}$, $N=3600\text{rpm}$, (b) Case 2: water-sand, $Q_L=3100\text{bpd}$, $N=2400\text{rpm}$,	
(c) Case 3: water-air-sand, $Q_L=3100\text{bpd}$, $N=3600\text{rpm}$, $GVF=15\%$ (d) Case 4:	
water-air-sand, $Q_L=3100\text{bpd}$, $N=3600\text{rpm}$, $GVF=7.5\%$	209
B.3 Geometry changes in the skirt-ring clearance, (a) Case 1: water-sand,	
$Q_L=3100\text{bpd}$, $N=3600\text{rpm}$, (b) Case 2: water-sand, $Q_L=3100\text{bpd}$, $N=2400\text{rpm}$,	
(c) Case 3: water-air-sand, $Q_L=3100\text{bpd}$, $N=3600\text{rpm}$, $GVF=15\%$ (d) Case 4:	
water-air-sand, $Q_L=3100\text{bpd}$, $N=3600\text{rpm}$, $GVF=7.5\%$	209
B.4 Geometry changes in the balance ring clearance, (a) Case 1: water-sand,	
$Q_L=3100\text{bpd}$, $N=3600\text{rpm}$, (b) Case 2: water-sand, $Q_L=3100\text{bpd}$, $N=2400\text{rpm}$,	
(c) Case 3: water-air-sand, $Q_L=3100\text{bpd}$, $N=3600\text{rpm}$, $GVF=15\%$ (d) Case 4:	
water-air-sand, $Q_L=3100\text{bpd}$, $N=3600\text{rpm}$, $GVF=7.5\%$	210

LIST OF TABLES

1.1: Constants used in Ahlert et al. model (1994).....	11
1.2: Empirical coefficient in Haugen model	11
1.3: Empirical coefficient in Oka et al. model (2005)	12
1.4: Empirical coefficient in Zhang et al. model (2007).....	12
1.5: Empirical coefficient in Mansouri model	13
1.6: Constants used in single area of contact	17
1.7: Abrasion constants	20
1.8: Affect parameters in erosion simulation	30
1.9: factors to calculate the restitution coefficient.	37
2.1 Experimental Matrix for Testing ESP Performance with Single-phase Water.....	47
2.2 Data Acquisition System Specifications of TUALP ESP Erosion Flow loop	52
2.3 Experimental Matrix for Testing ESP Sand Erosion	55
3.1: Input parameters of three ESPs.....	86
3.2: Empirical constants in six models	88
3.3: Input parameters of gas-liquid-solid simulation	110
B.1 Case 1: Diffuser position 1: diffuser skirt ring ID (in).....	177
B.2 Case 1: Diffuser position 2: diffuser hub ID (SCS diffuser bore of steel) (in)	177
B.3 Case 1: Diffuser position 3: diffuser balance ring ID (in).....	178
B.4 Case 1: Diffuser position 4: diffuser inside shroud ID (in).....	178
B.5 Case 1: Diffuser position 5: diffuser skirt ring depth (in)	178

B.6 Case 1: Diffuser position 6: diffuser hub ID (SCS diffuser bore by carbide) (in) ...	179
B.7 Case 1: Impeller position 1: impeller hub ID (in)	179
B.8 Case 1: Impeller position 2: impeller hub OD (in).....	179
B.9 Case 1: Impeller position 3: impeller balance ring OD (in).....	180
B.10 Case 1: Impeller position 4: impeller skirt ring OD (in)	180
B.11 Case 1: Impeller position 5: impeller outside shroud OD (in)	180
B.12 Case 1: Inter-stage clearance (SCS inter-stage of steel) (in).....	181
B.13 Case 1: Inter-stage clearance (SCS inter-stage of carbide) (in)	181
B.14 Case 1: Balance ring clearance (in).....	181
B.15 Case 1: Skirt ring clearance (in).....	182
B.16 Case 1: Sleeve/bushing OD (in)	182
B.17 Case 1: Impeller weight loss (g).....	183
B.18 Case 1: Diffuser weight loss (g).....	183
B.19 Case 1: Sleeve weight loss (g).....	183
B.20 Case 2: Diffuser position 1: diffuser skirt ring ID (in).....	185
B.21 Case 2: Diffuser position 2: diffuser hub ID (SCS diffuser bore of steel) (in)	185
B.22 Case 2: Diffuser position 3: diffuser balance ring ID (in).....	186
B.23 Case 2: Diffuser position 4: diffuser inside shroud ID (in).....	186
B.24 Case 2: Diffuser position 5: diffuser skirt ring depth (in)	186
B.25 Case 2: Diffuser position 6: diffuser hub ID (SCS diffuser bore of carbide) (in).....	187
B.26 Case 2: Impeller position 1: impeller hub ID (in)	187
B.27 Case 2: Impeller position 2: impeller hub OD (in)	187

B.28 Case 2: Impeller position 3: impeller balance ring OD (in).....	188
B.29 Case 2: Impeller position 4: impeller skirt ring OD (in)	188
B.30 Case 2: Impeller position 5: impeller outside shroud OD (in)	188
B.31 Case 2: Inter-stage clearance (SCS inter-stage of steel) (in).....	189
B.32 Case 2: Inter-stage clearance (SCS inter-stage of carbide) (in)	189
B.33 Case 2: Balance ring clearance (in).....	190
B.34 Case 2: Skirt ring clearance (in).....	190
B.35 Case 2: Sleeve/bushing OD (in).....	190
B.36 Case 2: Impeller weight loss (g).....	191
B.37 Case 2: Diffuser weight loss (g).....	191
B.38 Case 2: Sleeve weight loss (g).....	191
B.39 Case 3: Diffuser position 1: diffuser skirt ring ID (in).....	193
B.40 Case 3: Diffuser position 2: diffuser hub ID (SCS diffuser bore of steel) (in)	193
B.41 Case 3: Diffuser position 3: diffuser balance ring ID (in).....	193
B.42 Case 3: Diffuser position 4: diffuser inside shroud ID (in).....	194
B.43 Case 3: Diffuser position 5: diffuser skirt ring depth (in)	194
B.44 Case 3: Diffuser position 6: diffuser hub ID (SCS diffuser bore of carbide) (in).....	194
B.45 Case 3: Impeller position 1: impeller hub ID (in)	195
B.46 Case 3: Impeller position 2: impeller hub OD (in)	195
B.47 Case 3: Impeller position 3: impeller balance ring OD (in).....	195
B.48 Case 3: Impeller position 4: impeller skirt ring OD (in)	196
B.49 Case 3: Impeller position 5: impeller outside shroud OD (in).....	196

B.50 Case 3: Inter-stage clearance (SCS inter-stage of steel) (in).....	196
B.51 Case 3: Inter-stage clearance (SCS inter-stage of carbide) (in)	197
B.52 Case 3: Balance ring clearance (in).....	197
B.53 Case 3: Skirt ring clearance (in).....	197
B.54 Case 3: Sleeve/bushing OD (in).....	198
B.55 Case 3: Impeller weight loss (g).....	198
B.56 Case 3: Diffuser weight loss (g).....	199
B.57 Case 3: Sleeve weight loss (g).....	199
B.58 Case 4: Diffuser position 1: diffuser skirt ring ID (in).....	200
B.59 Case 4: Diffuser position 2: diffuser hub ID (SCS diffuser bore of steel) (in)	201
B.60 Case 4: Diffuser position 3: diffuser balance ring ID (in).....	201
B.61 Case 4: Diffuser position 4: diffuser inside shroud ID (in).....	202
B.62 Case 4: Diffuser position 5: diffuser skirt ring depth (in).....	202
B.63 Case 4: Diffuser position 6: diffuser hub ID (SCS diffuser bore of carbide) (in).....	202
Case 4: B.64 Impeller position 1: impeller hub ID (in)	203
B.65 Case 4: Impeller position 2: impeller hub OD (in)	203
B.66 Case 4: Impeller position 3: impeller balance ring OD (in).....	203
B.67 Case 4: Impeller position 4: impeller skirt ring OD (in).....	204
B.68 Case 4: Impeller position 5: impeller outside shroud OD (in).....	204
B.69 Case 4: Inter-stage clearance (SCS inter-stage of steel) (in).....	204
B.70 Case 4: Inter-stage clearance (SCS inter-stage of carbide) (in)	205
B.71 Case 4: Balance ring clearance (in).....	205

B.72 Case 4: Skirt ring clearance (in).....	205
B.73 Case 4: Sleeve/bushing OD (in).....	206
B.74 Case 4: Impeller weight loss (g).....	206
B.75 Case 4: Diffuser weight loss (g).....	206
B.76 Case 4: Sleeve weight loss (g).....	207
C.1 Instrument specification	213
C.2 Uncertainty and relative uncertainty	214
D.1 Coefficients for gas property calculation.....	217

INTRODUCTION

As one of the most widely used artificial lift methods, electrical submersible pumps (ESPs) are suitable for high production rates and for high water cut wells. However, the ESP performance and run life are affected by many problematic factors such as high gas-liquid ratio (GLR), high-temperature, corrosion, and erosion. With the development of horizontal well drilling and multistage hydraulic fracturing, sand production from unconsolidated sandstone and proppant backflow often cause severe damage to ESPs resulting in reduced operating lifespan.

Two types of wear occur in ESPs and deteriorate the pump's boosting capacity. Erosion can be found on the diffusers and impellers hub, walls, blades, and vanes that shape the primary flow path of the pump, as well as impellers balance holes that are in the pump's secondary flow paths. Abrasion takes place on the pump bearings, bushings, impeller seals and their corresponding diffuser stators, opening the clearances and reduces the stiffness of the entire system. This type of wear directly impacts the secondary flow paths of the pump (Morrison et al., 2015).

In this study, six tests were conducted under water-sand and water-air-sand conditions with different rotation speeds. In each test, a 64-hour experiment was divided into several short periods (8, 8, 16 and 32 hours). After each period test, gas-liquid flow rate, temperature, pump performance (pressure increment, thrust, and torque), stage imbalance and vibration were measured. The pump was then disassembled and the wear rate was measured. The sand was reused in the loop and replaced every 2 hours. CFD simulations

were carried out to better understand the internal flow structure, especially the gas-liquid-sand three-phase flow. Finally, a comprehensive mechanistic model for predictions of solid trajectory, wear rate, geometry change and pump performance degradation was developed.

CHAPTER 1

LITERATURE REVIEW

Wear by hard particles occurs in many different kinds of equipment such as on earth-moving equipment, slurry pumps or pipelines, rock drilling, rock or ore crushers, pneumatic transport of powders, dies in powder metallurgy, and extruders or chutes. According to Figure 1.1, the wear processes may be classified by different modes depending on the kinematics and by mechanisms depending on the physical and chemical interactions between the elements of the tribosystem, which results in detaching of material from the solid surfaces (Gahr, 1998).

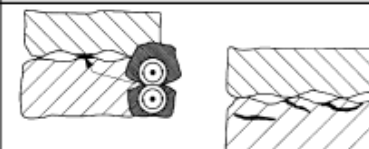
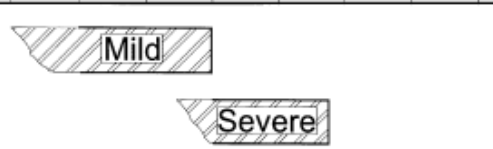
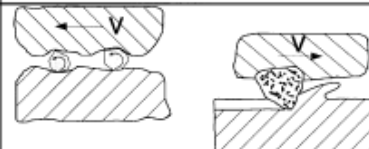
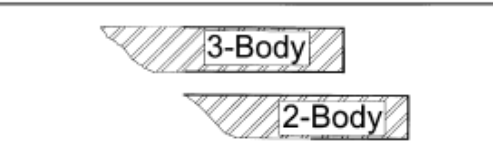
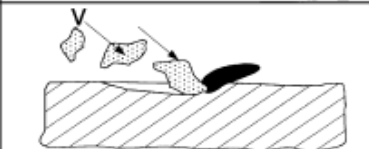
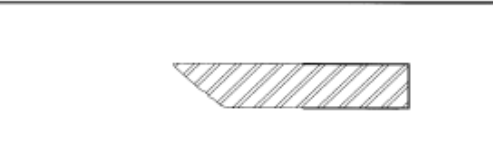
Wear Mode	Wear Mechanism	Wear Coefficient $k = \frac{W_v \cdot H}{F_N \cdot s}$
		10 ⁻⁷ 10 ⁻⁶ 10 ⁻⁵ 10 ⁻⁴ 10 ⁻³ 10 ⁻² 10 ⁻¹ 10 ⁰
Sliding Wear		
Abrasive Wear		
Erosive Wear		

Figure 1.1 Wear type

In the petroleum industry, sand wear causes damage to downhole equipment, increases the load and stress, and reduces the system's stability (Meng et al, 2019a; Zhang et al., 2016 and 2017). Therefore, it is very important to predict the damage of sand wears. The mechanism of erosion has been well studied and many prediction models have been developed from direct impingement experiments and elbow/tee slurry experiments (Parsi et al., 2014). In those applications, erosion is described as a surface attacked by solid particles entrained in the fluid. In abrasion, the material is displaced or detached from a solid surface by hard particles between or embedded in one or both of the two solid surfaces in relative motion, or by the presence of hard protuberances on a counterface sliding with the a relative velocity (King et al., 1983). Only simple physics-based empirical abrasion prediction models were developed for certain geometries. The empirical coefficients need to be corrected for an ESP.

As shown in Figure 1.2 (a) and (b), the flow field in an ESP is composed of the primary flow in channels created by impeller blades and diffuser vanes, and the secondary flow region created by the balance chamber and seals clearances. The raised pressure is imparted by rotating impellers (rotor), while the diffusers (stator) is designed to connect the flow between two impellers with the minimum turning and friction pressure loss. An axial thrust force is created by pressure differences on impeller surfaces. The secondary flow region between rotors and stators, which is shown in circles in Figure 1.2 (b), is designed to balance the thrust forces, especially in unsteady flow conditions. The secondary flow region is sealed by annular seals, whose clearance is usually less than a thousandth of the stage radius. Therefore, mass flux through the secondary flow region can be ignored for a new pump (Zhu et al., 2018d). The thrust force accumulates stage by stage

in a fixed-rotor multi-stage compression type ESP and can cause severe damage to the pump shaft and bearings. Therefore, the rotors are usually floated between stators and supported by thrust washers. When sand presents, the total axial thrust of the pump increases gradually with the decrease of the thrust washers thickness.

Wear inside an ESP can be classified by different modes of mechanisms. Two-body erosive wear in Figure 1.1 can be observed in the primary flow channel of the impeller (rotor) and diffuser (stator). Particle strike shroud surfaces and the scratched material is flushed away by fluids. Various semi-mechanistic erosion correlations are available to be coupled with Computational Fluid Dynamics (CFD) software to predict the erosion in ESPs. However, there are not enough data to validate the simulation results. In the secondary flow region, three-body abrasive wear shown in Figure 1.1 is believed to dominate the wearing process in the balance chamber and sealing ring clearances where particles present between the clearance of stator and the rotating rotor (Hashish, 1988; Morrison et al., 2015). The pump boosting capacity and efficiency will be gradually reduced by abrasion on seals, while the pump suffers more in the future if the blades and vanes are damaged by erosion in the primary flow channel (Zhu, et al., 2019c). In this 64-hour run, we believe the pump performance degradation is dominated due to the increased leakage through eroded seals. The leakage flow direction is shown in Figure 1.2 (b). Along the primary flow direction, leakage flows through the skirt ring clearance to the impeller eye. The flow is prevented by skirt rings and down-thrust washers. Then, leakage goes to the balance chamber through balance ring clearance and inter-stage clearance and flows back through balance holes. Balance holes have no sealing ability compared to the aforementioned geometries since their diameter is much larger than the seal clearance's

hydraulic diameter. This study aims to fill the gaps of erosion and abrasion test in a mixed type ESP in which carbide flanged sleeves are interval-installed.

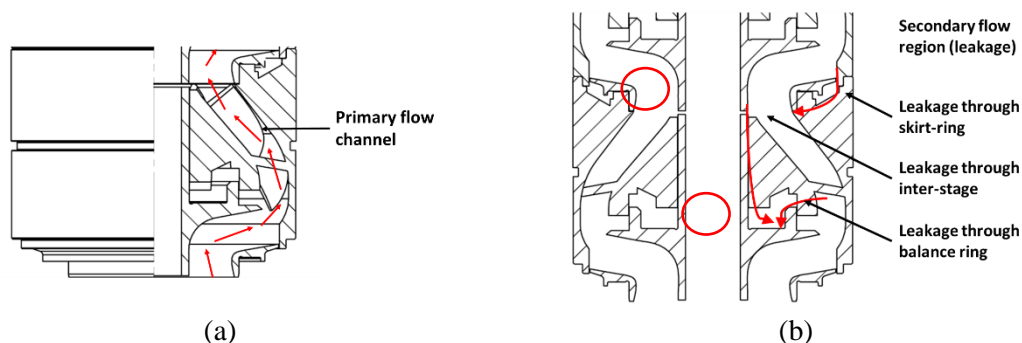


Figure 1.2 Wear type ESP stage components and flow directions, (a) primary flow, (b) secondary flow and leakage

1.1 Erosion Wear

Erosion can be observed and cause damage to various industrial applications. The simple API RP 14E erosion/corrosion criteria are widely used in the oil and gas industry. However, failure cases collected by Salama (2000) show that the API equations is not conservative enough. Erosion prediction in different applications are widely studied and empirical, semi-empirical (Ahlert, 1994), semi-mechanistic (Haugen et al., 1995; Oka and Yoshida, 2005; DNV GL, 2015; Zhang, 2018; Zhang et al, 2018a and 2018b) and mechanistic (Bitter, 1963a and 1963b) erosion equations were developed considering particle and target surface materials. Sand erosion is influenced by several factors, including fluid characteristics (flow rate, composition, density, viscosity), sand characteristics (concentration, impact velocity, impact angle, number of particles hitting the surface, shape/sharpness, hardness, size distribution, density) and component geometries (bend, tee, choke, joint, material properties hardness, and microstructure) etc. Therefore, the erosion mechanism and affecting factors require careful analyses.

1.1.1 Erosion mechanism

Consider a spherical body with only elastically deformable impinges. As soon as the sphere touches the flat body, stress concentrations are set up as a result of elastic deformation, which is called deformation wear (Bitter, 1963a):

$$W_D = \frac{1}{2} \frac{M (V_P \sin \theta - D_k)^2}{\varepsilon_D} \quad (1.1)$$

and

$$D_k = \frac{\pi^2}{2\sqrt{10}} y^{\frac{5}{2}} (\rho_P)^{-\frac{1}{2}} \left[\frac{1 - \nu_P^2}{E_P} + \frac{1 - \nu_s^2}{E_s} \right]^{\frac{1}{2}}, \quad (1.2)$$

where W_D is erosion in units volume loss, M and V_P are total mass and velocity of impinging particles respectively, θ is impact angle, ε describes the plastic-elastic behavior of the substance, ν_P and ν_s are respectively poisson's ratio of sphere and flat body, E_P and E_S represent Young's modulus of sphere and flat body respectively, D_K is deformation characteristic velocities. The equation is valid if $V_P \sin \theta \geq D_K$. Otherwise, no deformation wear occurs as the collisions are purely elastic.

If a particle strikes a horizontal surface at an acute angle, the material is subjected to shear over an area equal to the vertical cross-section of that part of the particle, which has penetrated into the surface. If the shearing strength is exceeded, the destruction occurs, which is referred to as cutting wear. Two possibilities are considered: the particle leaves body surface with and without a horizontal velocity component (Bitter, 1963b):

$$W_{C1} = 2M \frac{C_K (V_P \sin \theta - D_k)^2}{\sqrt{V_P \sin \theta}} \left(V_P \cos \theta - \frac{C_K (V_P \sin \theta - D_k)^2}{\sqrt{V_P \sin \theta}} \varepsilon_C \right), \quad (1.3)$$

$$W_{C2} = \frac{1}{2} \frac{M \left[V_P^2 \cos^2 \theta - K_1 (V_P \sin \theta - D_K)^{\frac{3}{2}} \right]}{\varepsilon_C}, \quad (1.4)$$

and

$$C_K = \frac{0.288}{y} \sqrt{\frac{\rho_P}{y}}, \quad (1.5)$$

where W_{C1} and W_{C2} refer to the two cases above, y is elastic load limit, θ_0 is the impact angle at which the horizontal velocity component has just become zero when leaving the body, C_K is cutting characteristic velocities. Equation (1.3) is valid if $\theta \leq \theta_0$. Otherwise, Equation (1.4) must be used. In practice, two forms of wear generally occur simultaneously. Therefore, the total wear at every instant is

$$W_T = W_D + W_{C1} \quad \theta \leq \theta_0 \quad (1.6)$$

and

$$W_T = W_D + W_{C2} \quad \theta > \theta_0. \quad (1.7)$$

Since Bitter's model did not take into account the wall material yield stress, Finnie summarized cutting and deformation wear into a new model that can be applied to a wider variety of wall materials (Finnie, 1960).

$$ER = \frac{cV_P^2 \rho_w}{8\sigma_y} \left(\cos \theta - \frac{3 \sin \theta}{2} \right) \sin \theta \quad \theta \leq 18.5^\circ \quad (1.8)$$

and

$$ER = \frac{c\rho_w (V_P \sin \theta)^2}{24\sigma_y} \cot \theta \quad \theta > 18.5^\circ, \quad (1.9)$$

where c is a constant, suggested being 0.5 for most applications. σ_0 represents the wall yield stress of target.

Edwards (2000) then combined erosion models presented by Hashish (1988) and Bitter (1963) to a new one including both cutting and deformation wear:

$$ER_{cutting} = \frac{75}{2\sqrt{29}} \left(\frac{V}{C_k} \right) \frac{\rho_w}{\rho_p} \sqrt{\sin \theta} \sin \theta \quad (1.10)$$

and

$$ER_{deformation} = \frac{\rho_w (V \sin \theta - D_k)^2}{2\varepsilon}, \quad (1.11)$$

where ρ_p is the particle density, D_k is given in Equation (1.2), C_k is given as follow:

$$C_k = \sqrt{\frac{3\sigma_y R_r^{0.6}}{\rho_p}}, \quad (1.12)$$

where R_r is a particle roundness factor with value $0.1 \leq R_r \leq 1$. The overall erosion ratio is the sum of the two components:

$$ER_{cutting} = ER_{cutting} + ER_{deformation}. \quad (1.13)$$

The local erosion on a surface, which can be converted to the local penetration rate, is calculated by summing the mass loss resulted from each impingement on the computational cell:

$$P_j = \frac{\pi d_p^3}{6A_j} \sum_i ER_{i,j} \left(\frac{N_p}{N} \right) \left(\frac{\rho_p}{\rho_w} \right), \quad (1.14)$$

where d_p is the diameter of the particle, A_j denotes the area of the impinged computational cell face, N_p represents the number of particles per second flowing, N is the total number of particles simulated. The subscript i refers to the impingement under consideration, and j denotes the computational cell of interest.

1.1.2 Erosion prediction model

A fully empirical erosion model for a certain flow domain requires four primary parameters: solids concentration, velocity, particle size, and material hardness. However, it is expensive and time-consuming to run erosion test for all conditions and equipment.

Thanks to the development of computing speed, those parameters can be obtained by CFD simulations. Therefore, more attention can be paid to secondary parameters, for example, material hardness, density, etc. Semi-empirical erosion models were developed based on the direct impingement test, which controls primary parameters and studies the effect of secondary parameters. Most of the semi-empirical erosion equations have similar formulas and can be summarized as an empirical correlation with the help of extensive databases as below.

$$ER = KV_p^n F(\theta), \quad (1.15)$$

where K and n are experimentally determined constants that depend on the material properties. $F(\theta)$ is a function depending on the impact angle and the target material ductile/brittle behavior. The value of $F(\theta)$ is maximum for ductile materials such as steel at impact angles of 20° to 40° , and for brittle materials such as ceramics at 90° . With the development and application of a machine learning approach in oil and gas industry (Meng et al, 2019; Tang, et al, 2019; Zhu et al., 2019f), it is possible to improve the erosion prediction model by applying machine learning methods on published erosion tests data.

The Ahlert et al. (1994) empirical erosion model was established by TUECR/C and has been used in the ANSYS manual as a reference. The correlation starts from Equation (1.15) and uses the impact angle function as Equation (1.16):

$$F(\theta) = \begin{cases} a\theta^2 + b\theta & \theta \leq \theta_0 \\ x \cos^2 \theta \sin(w\theta) + y \sin^2 \theta + z & \theta > \theta_0 \end{cases}. \quad (1.16)$$

Table 1.1: Constants used in Ahlert et al. (1994) model

Empirical constant	Material	
	Carbon Steel	Aluminum
K	$1559e-9BH^{0.59}$	$2.388e-7$
θ_0	15	10
a	-38.4	34.79
b	22.7	12.3
w	1	5.205
x	0.3147	0.147
y	0.03609	-0.745
z	0.2532	1
n	1.73	1.73

Haugen et al. (1995) model has the same formulas compared as the ANSYS Fluent erosion equations:

$$ER = Ke^{-9}V_p^n F(\theta) \quad (1.17)$$

$$F(\theta) = \sum_{i=1}^8 A_i \left(\frac{\theta\pi}{180} \right)^i \quad (1.18)$$

where K is $2e-9$, n is 2.6, θ is in degree and A_i can be found in Table 1.2.

Table 1.2: Empirical coefficients in Haugen et al. (1995) model

A1	A2	A3	A4	A5	A6	A7	A8
9.37	-42.295	110.864	-175.804	170.137	-98.298	31.211	-4.17

Oka et al. (2005) used E_{90} as a reference erosion rate from their tested results (Oka et al., 2005; Oka and Yoshida, 2005).

$$ER = e^{-9} E_{90} F(\theta), \quad (1.19)$$

$$E_{90} = K (Hv)^{K_1} \left(\frac{V_p}{V^*} \right)^{K_2} \left(\frac{d_p}{d^*} \right)^{K_3}, \quad (1.20)$$

$$n_1 = S_1 (Hv)^{q_1}, \quad (1.21)$$

$$n_2 = S_2 (Hv)^{q_2}, \quad (1.22)$$

$$K_2 = 2.3 (Hv)^{0.038}, \quad (1.23)$$

and

$$F(\theta) = [\sin(\theta)]^{n_1} \{1 + Hv[1 - \sin(\theta)]\}^{n_2}, \quad (1.24)$$

where V^* and d^* are reference velocity and particle diameter, 104 m/s and 326 μm for SiO₂, respectively. Hv is Vicker's hardness in GPa.

Table 1.3: Empirical coefficients in Oka et al. (2005) model

K	K_1	K_3	S_1	S_2	q_1	q_2
60	-0.12	0.19	0.71	2.4	0.14	-0.94

Zhang et al. (2007) model was derived from Ahlert et al. (1994) model with a polynomial impact angle function. Particle shape coefficient F_s was included, 1.0 for sharp (angular), 0.53 for semi-rounded, or 0.2 for fully rounded sand particles (Zhang et al., 2007).

$$ER = 2.17e^{-7} (BH)^{-0.59} F_s V_p^{2.41} F(\theta) \quad (1.25)$$

and

$$F(\theta) = \sum_{i=1}^5 A_i \left(\frac{\theta\pi}{180} \right)^i. \quad (1.26)$$

Table 1.4: Empirical coefficients in Zhang et al. (2007) model

A_1	A_2	A_3	A_4	A_5
5.4	-10.11	10.93	-6.33	1.42

Mansouri (2014) from TUE/CRC developed another erosion model by further improving the previous study with a trigonometric impact angle function:

$$ER = C (BH)^{-0.59} F_s V_p^n F(\theta) \quad (1.27)$$

and

$$F(\theta) = A [\sin(\theta)]^{n_1} \{1 + Hv^{n_3} [1 - \sin(\theta)]\}^{n_2}. \quad (1.28)$$

Table 1.5: Empirical coefficients in Mansouri (2014) model

	A	n	n_1	n_2	n_3	C
Air	0.6536	2.41	0.20	0.85	0.65	4.62e-07
Water	0.0534	2.41	1.52	8.9	0.01	2.45e-07

DNV (2015) model used Haugen et al. (1995) model as a reference. A new impact angle function was developed for both brittle and ductile materials.

$$ER = Ke^{-9}V_p^n F(\theta), \quad (1.29)$$

$$F(\theta) = \frac{2\theta}{\pi}, \quad (\text{Brittle}) \quad (1.30)$$

and

$$F(\theta) = 0.6 \left[\sin(\theta) + 7.2(\sin(\theta) - \sin^2(\theta)) \right]^{0.6} \left[1 - \exp\left(-\frac{\theta\pi}{9}\right) \right]. \quad (\text{Ductile}) \quad (1.31)$$

Based on equations of motion of particles in horizontal and vertical directions originally developed by Finnie et al. (1960), Arabnejad et al. (2015) developed a new mechanistic erosion equation for cutting wear:

$$ER_c = \begin{cases} \frac{mV_p^2 \sin(\theta) [2K \cos(\theta) - \sin(\theta)]}{2K^2 BH} & \theta \leq \theta_0 \\ \frac{mV_p^2 \cos(\theta)^2}{2BH} & \theta > \theta_0 \end{cases}, \quad (1.32)$$

where K is an empirical coefficient that depends on shape of the particle and material deformation behavior, and m is the mass of the particle. The deformation wear is calculated by Equation (1.11) developed by Bitter (1963). Then the total erosion can be calculated by the following equation:

$$ER = F_s \rho \frac{CER_c + ER_D}{m}, \quad (\text{Ductile}) \quad (1.33)$$

where ρ is the material density to convert volumetric loss to mass loss, and C is the cutting erosion coefficient.

1.1.3 Erosion prediction procedure

The erosion prediction model cannot be accurate without a precise particle impact velocity V_p . McLaury and Shirazi (1995) developed a simplified mechanistic procedure to predict erosion in elbows and tees, which obtained V_p from the equation of the motion of a solid particle moving in a flowing stream:

$$mV_s \frac{dV_s}{dx} = 0.5\rho_f(V_f - V_s)|V_f - V_s|C_D \frac{\pi d_p^2}{4}, \quad (1.34)$$

where m is the mass of the particle, V_s denotes the particle velocity, ρ_f represents the fluid density, V_f expresses the fluid velocity, d_p is the particle diameter and C_D represents the drag coefficient, which is assumed to be given by a simple correlation:

$$C_D = 0.5 + \frac{24}{Re_f}, \quad (1.35)$$

After the flow fields are calculated, particles are introduced into the flow field at the plane of the inlet. Then, particle trajectories are obtained by solving the 2-D version of the equation of motion. If a particle impinges the pipe wall, the particle impact speed, and angle are recorded. The erosion from each individual particle is calculated by empirical erosion equations.

Edwards (2000) improved the model and gave a generalized procedure that contains three steps: flow modeling, particle tracking, and erosion calculation. A flow model (or a CFD code) is usually used to determine the flow field. Then, the Lagrangian particle tracking model is used to determine the particle trajectories. Finally, empirical erosion equations are used to predict erosion rates. The method is widely used in commercial software like ANSYS Fluent.

1.2 Abrasion Wear

1.2.1 Abrasion mechanism

In the 1860s, the energy dissipative hypothesis was proposed that the volume of the removed debris due to wear is proportional to the work done by friction forces. Then, a simple model to represent the surfaces and to the theoretical deductions was developed as below (Archard, 1953).

The radius a of the circular area of contact formed when a sphere of radius R is pressed against a flat surface under a load P is given by

$$a = 1.1 \left[\frac{1}{2} PR \left(\frac{1}{E_1} + \frac{1}{E_2} \right) \right]^{\frac{1}{2}}. \quad (1.36)$$

When the deformation is elastic, E_1 and E_2 are Young's moduli of the materials of the contacting members, and

$$a = \left(\frac{P}{\pi p_m} \right)^{\frac{1}{2}}, \quad (1.37)$$

if the deformation is plastic, p_m is the flow pressure (assumed constant) of the deformable member.

The conductance G at contact is given by

$$G = 2a\sigma, \quad (1.38)$$

when the contact is purely metallic, the resistance of the contact is the "constriction resistance". σ is the specific conductivity of the two materials (assumed equal). When the

resistance of the contact is due to a film of resistance ρ per unit area, the “constriction resistance” is negligible. Thus,

$$G = \frac{\pi a^2}{\rho}. \quad (1.39)$$

Equation (1.36) to (1.39) can be used to calculate the contact area and conductance as a function of the load for both a single contact (representing a sphere pressed against a flat surface) and the multiple areas of contact model (representing two flat surfaces in contact).

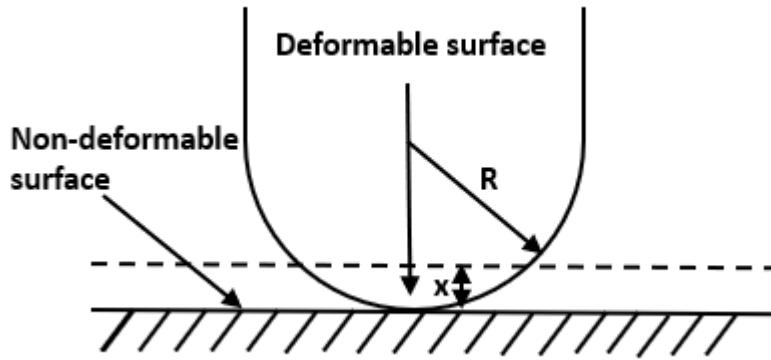


Figure 1.3 Single area of contact model

For a single area of contact shown in Figure 1.3, it consists of a perfectly flat non-deformable surface and a deformable spherical surface with curvature radius R . Changes in the area of contact A_I , the load P_I carried by the contact, and the contact conductance G_I , are considered for a movement of the non-deformable surface through a distance x . A_I , P_I and G_I are given by the following general equations:

$$A_I = bx, \quad (1.40)$$

$$P_I = cx^p, \quad (1.41)$$

and

$$G_l = dx^m . \quad (1.42)$$

By Equation (1.36) to (1.39) above,

$$b = 2\pi R . \quad (1.43)$$

Table 1.6: Constants used in single area of contact

	P	c	m	d
Plastic deformation	1	$2\pi R\rho_m$	/	/
Elastic deformation	1.5	$4.25ER^{0.5}$	/	/
Film resistance	/	/	1	$2\pi R/\rho$
Constriction resistance	/	/	0.5	$(8R)^{0.5}\sigma$

These results give the following generalized relationships between the contact area or conductance and the load:

$$A_l = b \left(\frac{P_l}{c} \right)^{\frac{1}{P}} \quad (1.44)$$

and

$$G_l = d \left(\frac{P_l}{c} \right)^{\frac{m}{P}} . \quad (1.45)$$

Then, two simple assumptions can be made regarding the volume δV of a given wear particle:

$$\delta V = \beta a^2 , \quad (1.46)$$

where β is a constant. This implies that the depth of the material removed is constant; more specifically, it is independent of the load or the radius of the contact area.

$$\delta V = \gamma a^2 , \quad (1.47)$$

where γ is a constant. This implies that the depth to the torn material is proportional to the radius of the contact area. That means the shape of the wear particles is independent of their size statistically.

Not every contact results in a wear particle. It is assumed that a proportion K , which is independent of size, does so. If the wear rate i.e., the total wear per unit sliding distance for the whole surface, is W and the contribution from the area under consideration is δW , then one can derive

$$\delta W = \frac{K\delta V}{2a}. \quad (1.48)$$

The wear rate is given by

$$W = \sum \delta W. \quad (1.49)$$

1.2.2 The empirical abrasion prediction model

Assuming hemispherical wear particles of the same radius as the contact areas, Achard (1953) gave an abrasion prediction equation:

$$W = \frac{KP}{3a}. \quad (1.50)$$

Holm (1967) assumed that the real area of contact is formed by the plastic deformation of contacting asperities and considered wear as an atomic process (Holm, 1967). On this basis, the worn volume per unit sliding distance W is given by

$$W = \frac{ZP}{p_m}, \quad (1.51)$$

where Z is the number of atoms removed per atomic encounter. Assuming that the total real area of contact consists of N circular “ a spots,” then:

$$Z = \frac{\xi\alpha}{2a}, \quad (1.52)$$

where α is the interatomic spacing.

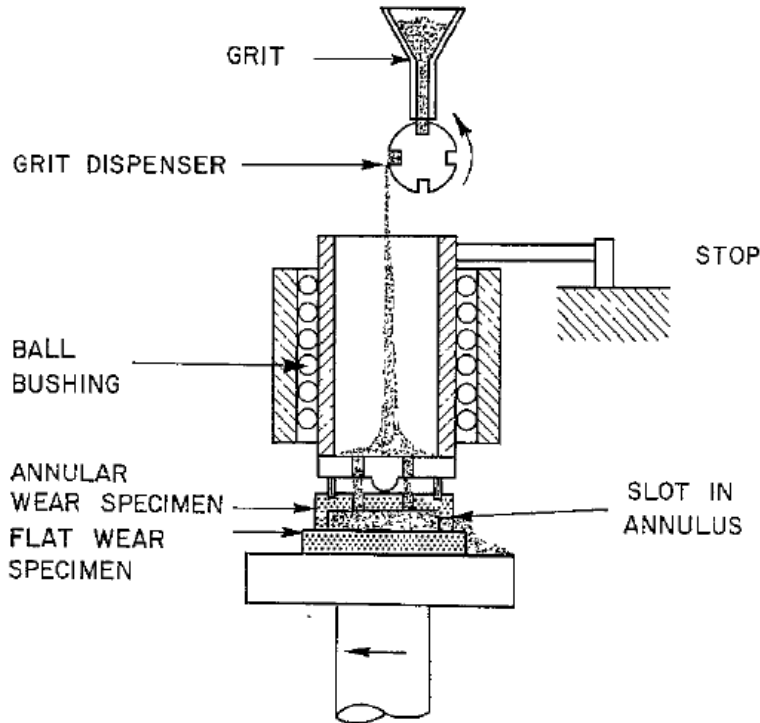


Figure 1.4 Schematic illustration of abrasion machine

Shown in Figure 1.4, Rabinovicz et al. (1961) conducted an abrasive three-body wear experiment, which essentially consisted of a vertically mounted loading cylinder that pressed a stationary annular specimen against a rotating flat plate, while abrasive particles passed through the space between the wearing surfaces. Based on the experimental results, they developed and validated an abrasion prediction model that is similar in form to Archard (1953). The difference is that the Archard equation is for adhesive wear, where the coefficient K is the non-dimensional probability, per contact, of forming a wear particle. However, in the abrasive wear system, it represents the cotangent of the average angle of the abraders

$$W = \frac{KP}{BH}, \quad (1.53)$$

where BH is target material hardness. Table 1.7 shows the coefficients calculated from the wear data of other investigators.

Table 1.7: Abrasion constants

Investigator	Wear type	Abrasive	Size (μm)	Material	K (e^{-3})
Spurr et al. (1957)	2-body	Files (shallow)	-	Many	180
Spurr et al. (1957)	2-body	Emery paper	110	Many	150
Avient et al. (1960)	2-body	Emery paper	40-150	Many	120
Lopa (1956)	2-body	Al_2O_3 grinding wheel	260	Steel	80
Khrushov et al. (1960)	2-body	Electrocorudum paper	80	Many	24
Samuels (1956)	2-body	SiC paper	70	Brass	16
Toporov (1951)	3-body	Al_2O_3	150(?)	Steel	6(?)
Rabinovicz et al. ((1961)	3-body	Al_2O_3	80	Steel	4-5
Rabinovicz et al. (1961)	3-body	Al_2O_3	40	Many	2

From those data, Rabinovicz et al. (1961) concluded that abrasive grains in three-body conditions spend 90% of the time rolling, thus producing no abrasion particles, and only about 10% of the time sliding and abrading the surfaces, which could explain the low coefficient of friction measured in three-body abrasion tests.

1.3 Wear in ESPs

The components shown in Figure 1.5 are used to describe wear locations in ESPs. Erosion takes place on the primary flow region in ESP impeller and diffuser flow channel and abrasion can be observed on pump bearings, bushings, seals and sleeves. (Hashish, 1988; Morrison et al., 2015). The pump boosting capacity and efficiency will be gradually reduced by abrasion on seals, while the erosion on the primary flow channel can eventually destroy the pump.

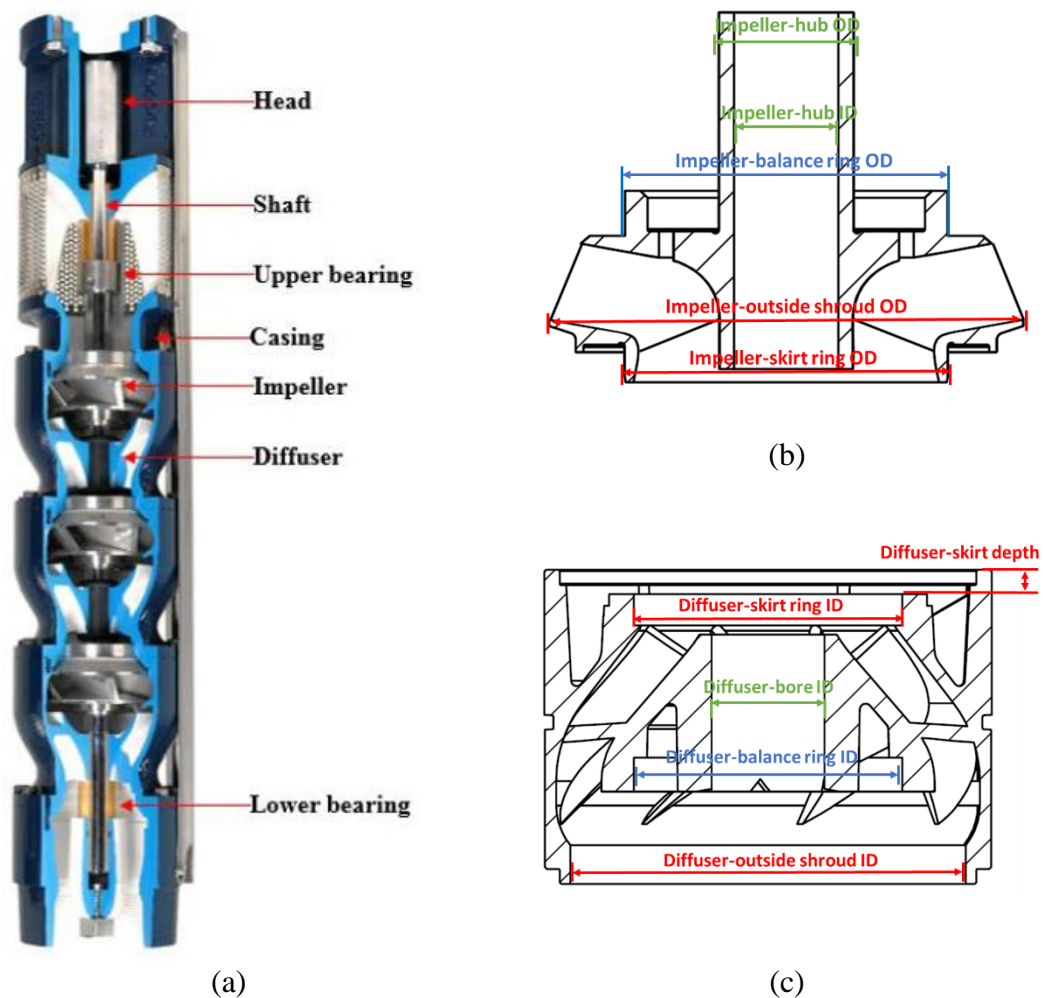


Figure 1.5 Components of ESP, (a) entire ESP (<http://www.franklinwater.com>), (b) impeller front view, (c) diffuser front view

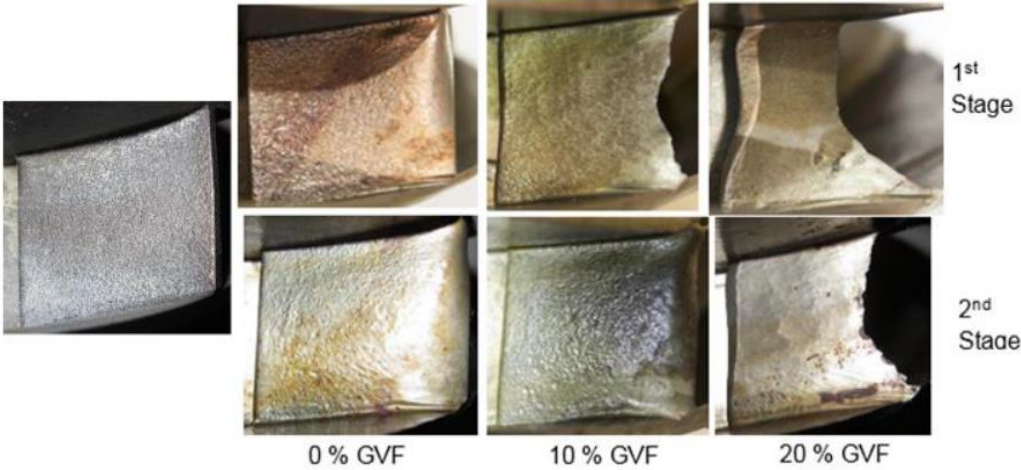
1.3.1 Erosion in ESPs

1.3.1.1 Erosion experiments on turbomachinery and pumps

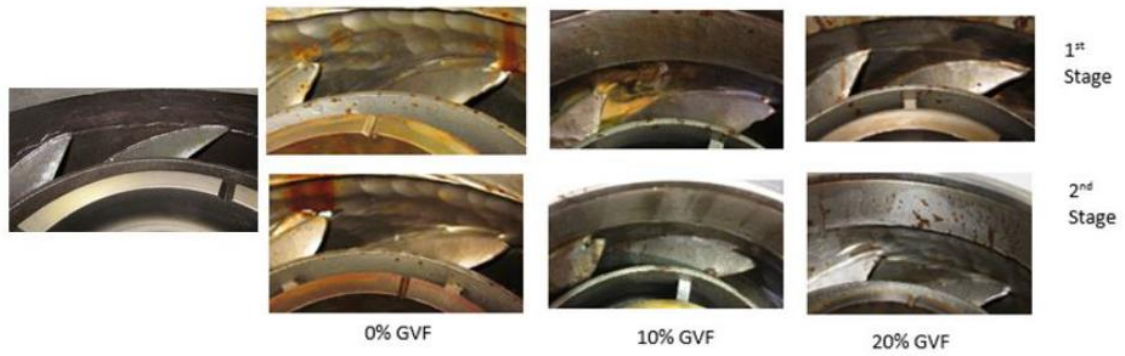
Erosion is very common in tubing, piping, fittings and other equipment. The mechanism of the wear has been studied extensively with prediction models being developed from the direct impingement experiments and slurry flow testing (Parsi et al., 2016; Parsi et al., 2014). Erosion tests on a mixed type ESP-WJE1000 were conducted by

Morrison et al. (2015). From their observation, the erosion on ESPs was caused by impinging sand particles that affect the diffusers and impellers hub, walls, and blades that shape the primary flow paths of the pump. It can also be observed on the impeller balance holes, thrust plate and the spacers that are in the pump's secondary flow paths. The amount of balance hole wear after 117 hours' test was small at the first stage impeller and grew larger at the second stage impeller, which became much larger in the third stage impeller. They concluded that the variation in the amount of wear from one stage to the other was caused by the difference in pressure rise across the secondary flow paths. The higher the pressure rise can result in more backflow.

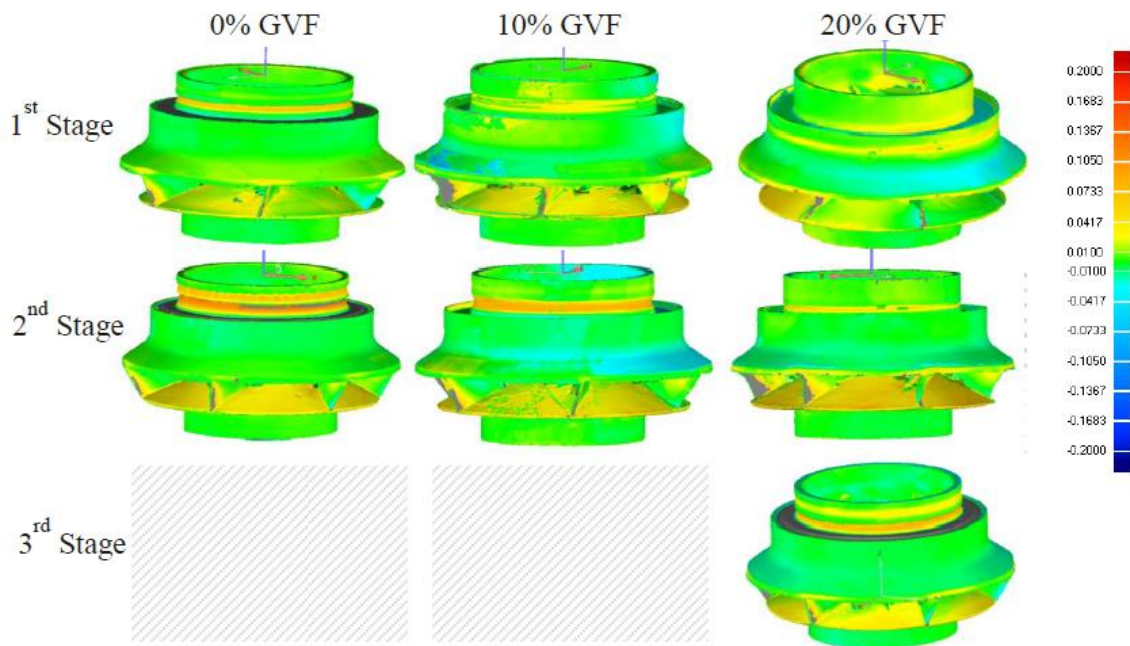
Later on, Morrison et al. (2017) conducted an erosion test on a split-vane ESP. As shown in Figure 1.6, in liquid-sand flow, the erosion was not obvious and the pump head slightly and gradually deteriorated due to the increase of leakage between eroded seals caused by abrasion. However, ESP blades will be worn out rapidly due to the erosion by the liquid-gas-sand flow, which leads to the pump boosting capacity completely deteriorated (Morrison et al., 2017).



(a)



(b)



(c)

Figure 1.6 Eroded stages, (a) impeller, (b) diffuser, (c) scanned images of eroded impellers (Morrison et al., 2017)

The pictures of erosion pattern on ESP in Figure 1.6 (a) and (b) taken by Morrison et al. (2015) and Basaran (2017) are not clear enough to show the erosion pattern details. In addition, it is difficult to apply a profilometer to a complex geometry like ESPs. Scans taken by Morrison et al. (2017) in Figure 1.6 (c) can only show the abrasion wear on seals. Therefore, paint-removal and weight-loss are used to validate the erosion prediction models and CFD simulations in this study.

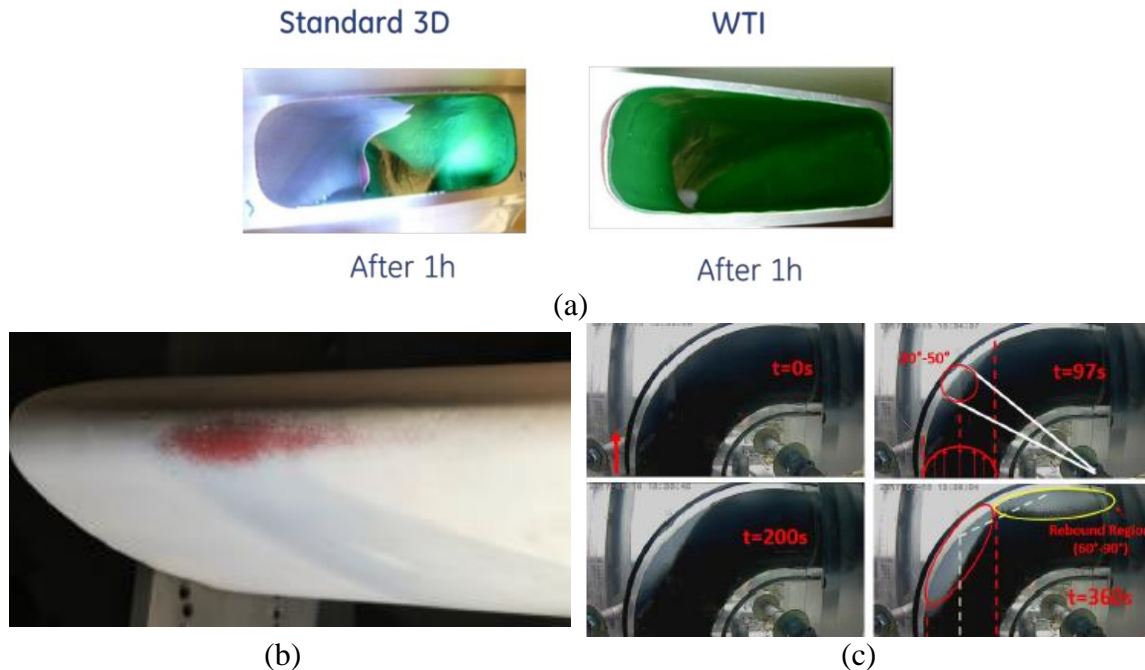


Figure 1.7 Paint-removal tests, (a) compressor (Bertoneri et al., 2014; Falomi et al., 2016), (b) wind energy blade (Muhlbauer et al., and Wagner, 2018), (c) elbows (Asgharpour et al., 2018)

Similar measurement techniques have been used in literature. Zheng (2013) measured the geometry changes and weight-loss of a mixed type ESP under multi-phase slurry flow conditions. The abrasion wear on the contact surface of seals was believed to have the dominant effect. Bertoneri et al. (2014) and Falomi et al. (2016) conducted paint-removal tests on centrifugal compressors under gassy flow with limited liquids, shown in Figure 1.7 (a). They concluded the significance of the liquid presents in compressor erosion and corrosion. Muhlbauer et al. (2018) evaluated the respective rain erosion on wind turbine blades using a protective coating, as shown in Figure 1.7 (b). Zahedi (2018) conducted paint experiments on elbows, as shown in Figure 1.7 (c), which was used to validate CFD simulations (Sedrez et al., 2018). As seen, using paint-removal sequence photos correctly can help investigate the maximum erosion location and patterns, as well as validate CFD simulations.

1.3.1.2 Centrifugal pump erosion simulations

Zhong and Minemura (1995) investigated the wear in pump casings for wear-resistant materials. Applying Bitter's erosion model, the effects of particle impingement angle, velocity, concentration, and size were studied. The spinning of particles after a collision with the wall makes it possible to measure the particle impingement velocity (Minemura et al., 1995).

Krüger et al. (2010) studied the erosion of a radial centrifugal pump. The authors considered two main erosion processes, which are shock-like and friction-like processes. In the friction-like process, solid particles rub against the solid surface under pressure with low impingement angle and high near-wall tangential velocity. On the other hand, the shock-like process happens due to the particles with a high normal velocity and a higher impingement angle (Krüger et al., 2010). According to the authors, the key parameters affecting the pump erosion are particle concentration, impingement angle, particle size, hardness and shape, flow velocity, turbulence, vortices, and secondary flow. Krüger used the empirical models developed by Gülich (2008) along with CFD simulations (Euler-Euler approach) to predict the erosion in centrifugal pumps. CFD simulations were performed on both non-eroded and eroded pumps to understand the flow change due to the erosion in the pump. Using the flow results obtained from CFD, the empirical quantitative erosion factor (Gülich, 2008) was used to predict the erosion rate in different parts of the pump.

Marsis and Russell (2013) applied Discrete Phase Models (DPM) and Eulerian-Granular models to above CFD erosion models to predict erosion rates inside an ESP. A

transient analysis of the pump was implemented using the moving mesh. Eulerian-Granular models have better accuracy based on CFD simulation results. In their study, the moving mesh simulation was more accurate than moving reference frame simulation in turbomachinery. In addition, the DPM model appeared to be more sensitive to the near-wall gradients and less accurate than the Eulerian-Eulerian Granular model in erosion simulation.

Pirouzpanah and Morrison (2014) conducted experimental and CFD studies of the ESP-WJE1000 pump. The erosion depth for the first and second stages is measured and provided by utilizing clay casting measurements and 3D laser scanning measurements respectively. The Eulerian-Granular model is used in ANSYS Fluent and a new empirical-numerical model was developed to predict the erosion rate on the ESP as follows:

$$EF = (\alpha_s)^{0.08} \left(\frac{V_s}{V_{s0}} \right)^{0.07} \left(\frac{k_w}{k_{w0}} \right)^{1.25}, \quad (1.54)$$

where V_s and V_{s0} are sand velocity and reference sand velocity (m/s), respectively; k_w and k_{w0} represent reference turbulent kinetic energy (m^2/s^2).

Using the results computed from the erosion factor, the erosion rate is obtained by employing the measured erosion depth from experimental results as below:

$$ER = 0.0163EF^2 + 0.8774EF. \quad (1.55)$$

1.3.2 Abrasion on ESPs

A five-year investigation of sand abrasion phenomena in conventional electrical submersible pumps (ESP) was conducted by King et al. (1983). From their investigation and tests, the three-body abrasion of pumps operating under abrasive conditions is the most

destructive cause of downhole equipment failure. Worn pumps cause vibration and shaft seal leakage, which eventually leads to electrical failure of the motor or power cable. Wear on down-thrust washers and stages seals can be substantially reduced by the use of special sleeves and inserts without prohibitively increasing the manufacturing costs of the pump. In addition, erosion is a problem only under severe corrosion and abrasive conditions, which can also be controlled using cast irons with good fluid channel design. The material can be expensive but it is worthy if workover costs are high.

Wilson (1990) conducted a set of experiments on ESPs to analyze the size and quantity of abrasives with fluid flow through the pump. The experiment was conducted with cast iron sleeves and hard material sleeves with the particles ranged from 2.3 μm to 70 μm under 0.25wt% sand concentration flow for 4 hours. Sleeves with hard materials can help reduce the wear on impeller hubs, stage seal rings (skirt and balance rings) and thrust washers. However, small particles (2.3 μm) increased the wear on thrust washers during the 4-hour tests (Wilson, 1990). In his study, the shaft was stabilized by hard sleeves. Large particles were too big to migrate into the thrust washer and lubricant seal rings, resulting in low abrasion. However, when the pump was running under low thrust conditions, the seal's clearance between impellers and diffusers was enough to allow larger abrasive grains to enter. In addition, the pump started rotating eccentrically when the impeller hub and sleeves were worn out. Then, particles larger than the lubrication layers were wedged under the edge of the thrust washer, causing high abrasion.

Zheng (2013) conducted 117 hours of water-sand tests followed by 68 hours of water-air-sand tests on a 3-stage WJE1000 ESP. Abrasion was observed in the secondary flow field, including seals, impeller hubs and diffuser bores. Besides, erosion was also

observed in the main flow field. Vibration signals and orbit sizes went through a considerable change due to increased bearing clearance. Each stage had different levels of abrasion and the largest was in the third stage. The impeller blades were sharpened by erosion, which had a different curved pattern on the leading edge. Erosion became more obvious under gas-liquid-sand three-phase conditions. In summary, WJE1000 had severe abrasions in the secondary flow region. Although the erosion in the main flow field was detected on all components, it did not reach the failure level (Zheng, 2013).

Based on the erosion test results by Zheng (2013), Morrison et al. (2015) concluded that the abrasion took place on the pump bearings, and corresponding bushings, impeller downstream seals, impeller upstream seals, and their corresponding diffuser stators, which reduced the stiffness of the entire system. The amount of abrasion on the bearings and impeller downstream seals was higher at the pump intake, which gradually decreases across the stages to the pump discharge. Three reasons were summarized by Morrison et al. (2015):

1. Sand at the pump intake is sharpest and most aggressive as it is crushed in the first stage. As the sand moves from one stage to the other, the sand loses its sharpness causing lesser shear wear to the final stage components.
2. The pump is vertically placed under the motor. The system is stiffer at the drive end of the pump, which also happens to be the pump discharge. On the other hand, the pump intake is hanging free and has less stiffness. This variation in stiffness directly resulted in a smaller amount of wear and clearances near the drive end, but larger amounts of wear away from the drive end.

3. At the pump intake, more sand is trapped between stators and rotors due to the low-pressure difference across the first stage. The entrapment of sand allows more wear to occur in the components affected. As the pressure differences increase from one stage to another, less sand is trapped in the discharge stage between stators and rotors so less wear takes place at the pump's third stage.

1.4 Gas-Liquid-Solid CFD Simulation

As described in section 1.1.3, the accuracy of a semi-empirical erosion prediction model depends on the calculation of particle impact velocity and impact angle. With the development of computer speed and commercial Computational Fluid Dynamic (CFD) software, the impact information can be obtained more easily than before. The three-step simulation procedure proposed by Edwards (2000) is widely used with CFD software. Chen et al., (2004) conducted CFD erosion simulation on elbows and plugged tees. Zhang (2007) validated his erosion equations by simulating erosion of an impingement testing with air and liquid flow. Marsis and Russell (2013) predicted erosion rates in a single-stage ESP by using erosion models presented by Russell et al., (2004). Pirouzpanah and Morrison (2014) developed a new ESP erosion empirical-numerical model related to turbulence kinetic energy and examined it with a single-stage ESP simulation. Pirouzpanah (2014) and Basaran (2017) conducted 2-stages ESP erosion simulations under different viscosity fluid and gas void fraction. The head increment and erosion patterns are different between the first and the second stage, especially when gas presents. Zhu et al. (2018a) conducted 2-stage mixed and radial type ESPs simulations to investigate the particle density, size, and pump type effects on erosion in ESPs. Zhang (2018) conducted a comprehensive CFD erosion simulation for elbows, sudden contractions and expansions, sharp bend under gas

dominant multiphase flows to analyze the near-wall modeling approach, grid refinement, turbulence models and rebound models.

The CFD erosion simulation is collaboratively affected by many factors in Table 1.8. Comprehensive background knowledge is required to accomplish the complex process and factors below will be analyzed in this study.

Table 1.8: Affecting parameters in erosion simulation

Affecting factor	Flow field	Particle tracking	Erosion prediction
Mesh type (Hex or Tetra)	✓	✓	
Grid number	✓	✓	
Near-wall refinement	✓	✓	
Multiphase flow model	✓	✓	
Turbulence model	✓	✓	
Wall function	✓	✓	
Particle tracking method		✓	
Rebound model		✓	✓
Drag law		✓	✓
Particle rotation		✓	✓
Turbulent dispersion		✓	✓
Particle interaction		✓	✓
Particle property		✓	✓
Target surface property			✓
Erosion equation			✓

1.4.1 Rotating turbomachinery methodology

Two methods can be applied to the rotating turbomachinery, frame motion and mesh motion. Mesh motion, which is also referred to as sliding meshes, imitate the real rotation by moving mesh, geometry, and boundaries together. Therefore, high-quality meshes and transient simulation, which requires more computational power, are needed. On the other hand, frame motion simplifies this procedure by adding a centrifugal force term in the momentum equations, which is applicable to steady-state simulation. In

addition, the frame motion is further divided into mixing plane, which can couple any number of fluid zones or passages by applying interface formulation to both vectors and scalars, and frozen rotor, which only applies interface formulation to vectors and cannot be applied if fluid zones are different, for example, ESP pump with different numbers of impeller blade and diffuser vane.

Usually the frozen rotor method is accurate enough for single-phase and gas-liquid two-phase CFD studies on different types of turbomachinery (Shi et al., 2017; Shi et al., 2018; Zhu et al., 2016; Zhu et al., 2019i; Zhu et al., 2019h). However, the simulations with the frozen rotor method show a non-concentric but y-z plane symmetrical erosion pattern, which is mainly due to the different blade numbers between impeller and diffuser (Zhu et al., 2018a; Zhu et al., 2019b). The erosion rate and erosion pattern can still be qualitatively analyzed but the accuracy needs to be compared to the mesh motion method. In this paper, the frozen rotor method is used in most simulations to reduce the computational cost.

1.4.2 Turbulence model

In order to accurately obtain the flow field, several turbulence models are considered to handle the irregular flow characteristics. By simply solving kinetic energy (k) and dissipation rate (ε), the standard k - ε model, which is accurate in high-Reynolds number flow, is the most widely used method among all turbulence models. Using an analytical formula of Prandtl number, the RNG k - ε model increases the accuracy in low-Reynolds number flow and swirling flows. The turbulent viscosity and dissipation rate in the realizable k - ε model is modified based on Reynolds stresses. Compared to others, the realizable k - ε model has better accuracy on single moving reference frame systems, but

still is questionable in multiple moving frames and may produce non-physical turbulent viscosities. To improve the $k-\varepsilon$ model, streamline curvature, swirl, rotation and rapid changes in strain rate are accounted in Reynolds Stress Model (RSM) by solving the Reynolds stresses and dissipation (Zhu et al., 2019a; Zhu et al., 2017a). Since seven additional transport equations are solved in 3D geometries, the computational cost and accuracy improvement may not be proportional. Both the $k-\varepsilon$ and RSM models require near-wall treatment. The result and convergence are highly depended on y^+ and wall functions. In general, the enhanced wall function is suggested for rotating simulations. On the other hand, the default near-wall treatment of the $k-\omega$ model is close to that of the $k-\varepsilon$ model and RSM model with enhanced wall function. Therefore, the default shear-stress transport (SST) $k-\omega$ model is good at boundary layer simulations and rotating equipment simulations.

Different turbulence models usually have a limited effect on ESP performance prediction, but its importance to boundary layer velocity profile and particle impact information in ESPs is not clear. According to its obvious influence in other geometries (Darihaki et al., 2019; Zhang et al., 2019a and 2019b; Chen et al., 2019; Jiang et al., 2015, Wang, et al., 2019a and 2019b), the turbulence model effect will be incorporated with different wall functions in the CFD simulation section.

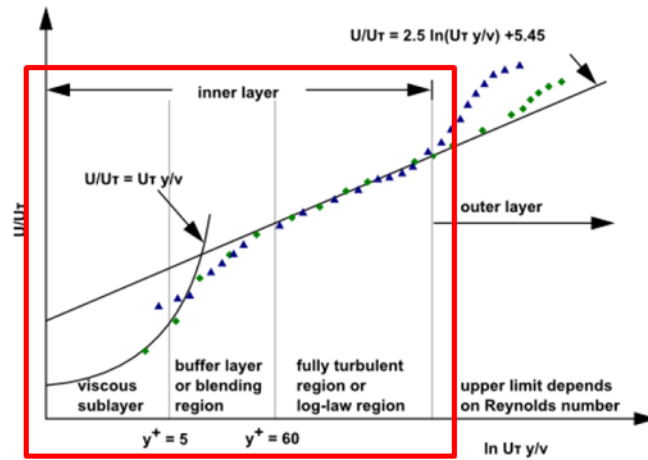
1.4.3 Near wall treatment

In wall-bounded turbulent flows, the fidelity of the simulation is influence by different near-wall treatment methods since the variables have a large gradient in the wall boundaries. The three layers of near-wall inner layer region are proved by various

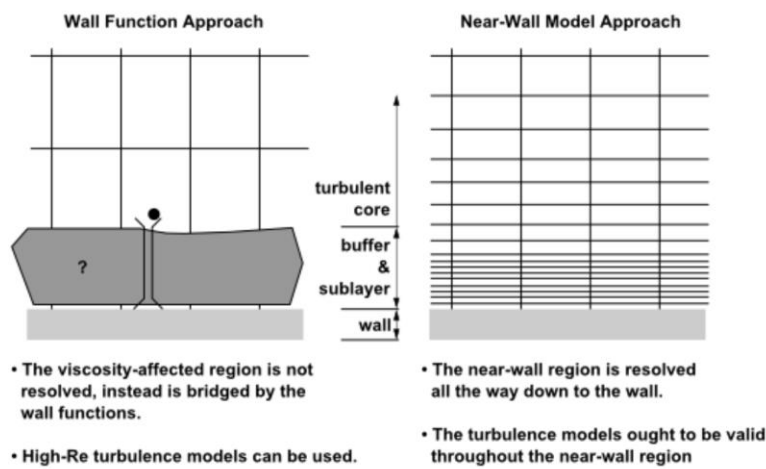
experiments. The molecular viscosity plays the most important role in the viscous sublayer region, while the turbulence dominates the flow in the fully turbulent region. The buffer layer represents the transition zone as shown in Figure 1.8 (a). There are two ways to solve this problem. The first one is very straight forward. The turbulence model is modified to be able to solve the viscous sublayer that is usually in the laminar flow regime, for example, using Large Eddy Simulation (LES) approach. However, these method requires a very fine near-wall grid in order to precisely solve the high Reynolds number flow. Besides, the model itself requires a high computational cost. Besides of the high computational cost, the refined near-wall mesh also has a strong effect on particle tracking simulation as shown in Figure 1.9, which will be discussed in the next section.

The second way is more commonly used in most simulations, choosing wall functions based on different applications. The wall functions are semi-empirical equations that can be incorporated with the turbulence model to predict the near-wall region flow field as shown in plot and equations in Figure 1.8 (a). Several wall functions are provided for both the $k-\varepsilon$ model and RSM model, standard wall function, scalable wall function, non-equilibrium wall function, and enhanced wall treatment. The standard wall function is one of the most widely used equations and works well for a wide range of wall-bounded flows. However, its accuracy deteriorates with low y^* (dimensionless velocity) and the solution may be hard to converge if y^* is less than 11.225. Then, the scalable wall function is developed to avoid the effect of arbitrary near-wall refinement. If y^* is less than 11.225, the model will set it to be 11.225. Usually, the simulation converges much faster, but its accuracy is obviously questionable. In addition to the standard wall function, the non-equilibrium wall function partly accounts for the pressure gradient effect and is

recommended for use in complex flows involving separation, reattachment, and impingement. However, the model still lacks enough accuracy in ESP simulations, where the strong body force (rotating centrifugal force) deviates significantly from the inertial conditions. Then, the enhanced wall treatment function is provided.



(a)



(b)

Figure 1.8 Near-wall treatment, (a) subdivision of the near-wall region, (b) wall function and near-wall mesh refinement

As described at the beginning of this section, one way to improve the accuracy of the near-wall region is to refine the near-wall grid and use the LES model. However, near-wall mesh refinement has a significant effect on particle trajectory simulation, especially

on particle impact information. By using ANSYS Fluent, the solid is treated to be a point without a diameter in the simulation and the trajectory is calculated layer by layer. Therefore the particle trajectory will be over calculated if the particle diameter is larger than the near-wall layer thickness as shown in Figure 1.9 (a). In other word, the particle does not impact the surface in the simulation while it already hits the surface in reality. As a result, the impact velocity and angle may be lower than the reality. On the other hand, the impact velocity and angle may be larger if the particle diameter is smaller than the near-wall layer thickness. The near-wall mesh refinement and LES simulation will be hard to be incorporated together in an ESP erosion simulation if the mesh layer thickness has a strong effect on the results.

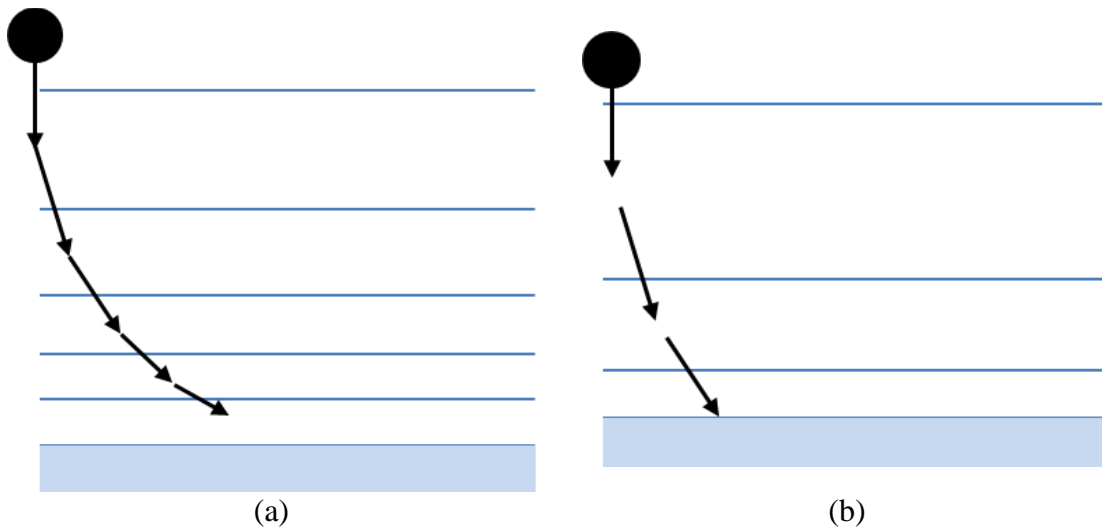


Figure 1.9 Particle impact trajectory simulation, (a) fine grid near-wall boundary, (b) coarse grid near-wall boundary

1.4.4 Particle rebound model

The particle impact velocity and angle are highly dependent on the flow field in near-wall boundary layers. In addition, the particle velocity and direction after

impingement (as shown in Figure 1.10) are also important factors, which is controlled by the particle rebound model.

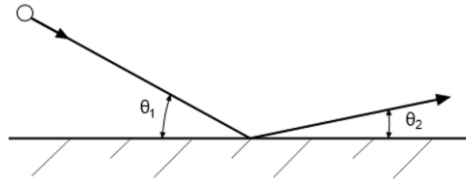


Figure 1.10 particle rebound at the wall

The coefficient of rebound restitution can be calculated by particle velocity before and after the impingement.

$$e_N = \frac{V_{2N}}{V_{1N}} \quad (1.56)$$

and

$$e_T = \frac{V_{2T}}{V_{1T}}, \quad (1.57)$$

where e is the restitution coefficient, V is particle velocity, subscript 1 and 2 represent before and after impingement, subscripts N and T represent normal and tangential directions.

The perfect elastic rebound applies unity to both the restitution coefficient. Then, a coefficient relationship for turbomachinery as well as a stochastic relationship in a statistical sense was proposed (Grant and Tabakoff, 1975; Wakeman and Tabakoff, 1982). Moreover, Forder et al., (1998) proposed an empirical relationship for AISI 4130. All equations assume that the restitution coefficient has a polynomial relationship with the particle impact angle as:

$$e = A_1 + A_2 \times \theta + A_3 \times \theta^2 + A_4 \times \theta^3 + A_5 \times \theta^4 + A_6 \times \theta^5, \quad (1.58)$$

where A_i is shown in Table 1.9:

Table 1.9: Factors to calculate the restitution coefficient.

		A1	A2	A3	A4	A5	A6
Perfect elastic	e_N	1					
	e_T	1					
Tabakoff	e_N	0.993	-1.76	1.56	-0.49		
	e_T	0.988	-1.66	2.11	-0.67		
Tabakoff	σ_N	-5e-5	0.2	-0.535	0.089		
Stochastic	σ_T	2.15	-5.02	4.05	-1.085		
Forder et al.	e_N	0.988	-0.78	0.19	-0.024	0.0027	
	e_T	1	-0.78	0.84	-0.21	0.028	-0.022

According to the rebound model formulas, the rebound effect is more obvious with a larger impact angle. On the other hand, its effect can be neglected in low impact angle simulations (Zhang, 2018; Haider, 2017, Haider et al., 2017, Moses et al., 2019). In this study, the impact information, including velocity, angle and hits number, will be extracted. Then the particle rebound model effect can be well understood in ESP erosion simulations.

1.4.5 Particle tracking method

Two commonly used methods, Euler-Lagrange and Euler-Euler approaches, are provided to solve the multiphase flows. By using the Euler-Euler method, the Navier-Stokes equations for both continuous and dispersed phases are solved together. However, the method requires much more computational time and the improvement is not obvious for low particle concentration. On the other hand, the discrete phase particle tracking method (DPM), a Euler-Lagrange approach, only treats the fluid phase as a continuum and saves computational time. The particle is solved separately as a discrete phase by Equation

(1.59) after the fluid flow field is obtained without considering particles. As a result, the flow field for water-sand DPM simulation is still a single-phase simulation, where the sand trajectory is simulated after the single-phase water flow field is calculated. For high particle concentration, the particle interaction effect is included by using the dense discrete phase method (DDPM), where particle concentration term is added to the mass and momentum conservation equations for the primary phase.

$$\frac{du_p}{dt} = F_D (\vec{u} - \vec{u}_p) + \frac{\vec{g}(\rho_p - \rho)}{\rho_p} + \vec{F} \quad (1.59)$$

where F_D is drag force and other forces, including virtual mass and pressure gradient force, moving reference frames force, thermophoretic force, Brownian force, Saffman's lift force, are included in F . In this study, thermophoretic force is not considered since the energy model is not enabled, and Brownian force and Saffman's lift force for sub-micron particles can be ignored since most of the particles are large than 50 μm .

The Euler-Lagrange method is widely used in erosion simulation (Pirouzpanah and Morrison, 2014; Wang et al., 2019c; Zhu et al., 2018a; Zhu et al., 2019e) with acceptable accuracy. Although the Euler-Euler method is investigated by some researchers in pump erosion simulations (Krüger et al., 2010; Marsis and Russell, 2013), the studies lacks details in the numerical methodology introduction and experimental validation. It is questionable if they have used the Euler-Euler approach to solve the particle trajectory and erosion rate or only incorporated DDPM with the Eulerian multiphase model, in which the particle trajectory is still solved by Lagrangian approach. Since the particle concentration in the ESP field application is usually much lower than 0.1wt% and the test condition in this study

is 1wt%, the particle interaction effect is neglected in the following CFD simulations. The DPM method is incorporated in both water-sand and air-water-sand simulations.

1.4.6 Gas-liquid multiphase simulation

It should be noted that “multiphase” refers to gas-liquid two-phase rather than gas-liquid-solid three-phase in this study, since the solid phase is treated to be a discrete phase and is solved after the gas-liquid flow field is obtained. Therefore, a converged gas-liquid phase flow field is required for both steady and unsteady ESP simulations before injecting particles.

In order to accurately capture the flow field of the gas-liquid phase in detail, three multiphase flow models, including VOF, Mixture, and Eulerian methods, are provided in ANSYS Fluent. The VOF model can model several immiscible fluids by solving a single set of momentum equations, while both the mixture model and the Eulerian multiphase model use a Eulerian treatment for each phase, where the mixture model is a substitute for the Eulerian model when some flow information is not available. The complexity increases along with, VOF, mixture, and Eulerian models and more fluid flow information are required, for example, particle size and drag laws. Although the Eulerian model should theoretically be the most accurate multiphase flow model, its performance can be significantly affected if a wrong fluid flow property is used. Therefore, VOF and mixture model are still very popular in practical if some important flow detail is missing, for example, applying the VOF model to simulate motions of large bubbles, and mixture model in low bubble flow with low gas concentration.

According to previous studies, the Eulerian model is suggested in air-water ESP simulation with the proposed gas bubble diameter equation (Zhu et al., 2017a; Zhu and Zhang, 2016; Zhu, et al., 2018e). When using the steady state simulation in ESP with low GVF, three more options are available in the Eulerian steady state simulation for different applications. The mixture method is suggested to be used in stratified flow, which is not suitable for this study. The dispersed method is good for low GVF conditions, including dispersed bubble and bubble flow. The Per Phase method is more comprehensive but requires more computational time. As a result, it is possible to use the dispersed method with low GVF in ESP simulation. In this study, the ESP starts to suffer from the intermittent flow region when GVF reaches 10%, where the Per Phase method is applied in the corresponding simulation.

1.5 Mechanistic Modeling

In general, the prediction of ESP head curve starts from Euler equations. Besides friction loss in the pump, other losses like hydraulic loss, shock loss, leakage loss, and recirculation loss are considered individually. From Gülich's (2008) study, as shown in Figure 1.11 (b), recirculation loss is higher at lower flow rates, where high turbulence is generated by high velocity and pressure gradients. Incidence loss is caused when the flow angle is different than the blade angle. Vieira et al. (2015) combined recirculation loss and incidence loss together as shock loss, as shown in Figure 1.11 (c).

Leakage loss is considered separately in centrifugal pump performance prediction models. Figure 1.11 (a) shows a test of a 2-inch two-stage pump with normal and worn inter-stage clearance (0.060") by Stepanoff (1957). Leakage is believed to result in loss of efficiency and head at a high flow rate since the flow rate in the flow channel is increased

compared to that through the entire pump. On the contrary, Gülich (2008) believes the head loss due to leakage is approximately similar for any flow rate, while Vieira et al. (2015) believe more head loss can be observed at low flow rate.

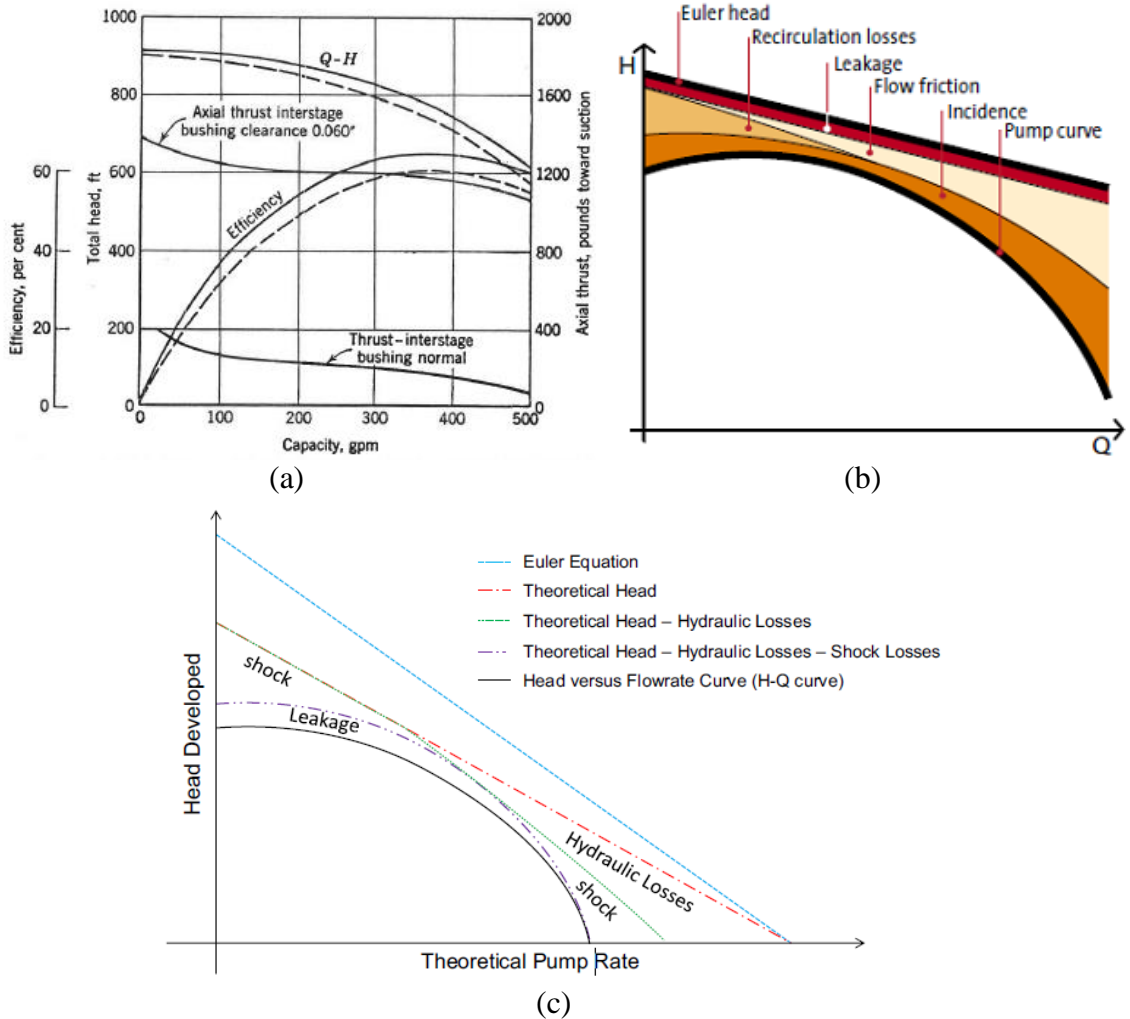


Figure 1.11. Schematic of head curves and losses (a) head thrust and efficiency changes due to inter-stage leakage (Stepanoff, 1957), (b) head losses (Gülich, 2008), (c) head losses (Vieira et al., 2015)

Aungier (1995) and Bing et al. (2012) proposed a similar leakage loss equation from a forced vortex in centrifugal compressors, as shown below:

$$H_{LK} = \frac{Vol_{LK} U_{LK} U_2}{2Q^* g} \quad (1.60)$$

where H_{LK} is leakage head loss, Vol_{LK} is leakage channel volume, U_2 and U_{LK} are tangential velocity at impeller outlet and seal clearance and Q^* is the ideal flow rate of the pump. However, the flow in the secondary flow region in an ESP is different from a compressor. In the mechanistic model developed by Zhu et al. (2018c) and Zhu et al. (2019j), the leakage flow rate is calculated from the head generated by the impeller and the head difference across the seal clearances. Leakage head loss is included in other head losses and will not be calculated separately.

The head difference between leakage inlet and outlet can be estimated as

$$H_{LK} = H_E - H_R - H_{FI} - H_{TI} - \frac{U_2^2 - U_{LK}^2}{8g}, \quad (1.61)$$

where H_E is Euler head, H_R is recirculation loss, H_{FI} is friction loss in the impeller flow channel and H_{TI} is turning loss in the impeller.

The head loss across the leakage consists of contraction, expansion and friction components as shown below:

$$H_{LK} = 0.5 \frac{V_{LK}^2}{2g} + 1.0 \frac{V_{LK}^2}{2g} + f_{LK} \frac{V_{LK}^2 L_G}{2g S_{LK}}, \quad (1.62)$$

where L_G is the leakage channel length, S_{LK} is the leakage clearance width, V_{LK} is fluid velocity in the leakage channel. However, only leakage through the impeller outlet to the skirt ring is included in the model. The predicted head curve is unreliable once the pump is damaged by solids.

Equations (1.60) to (1.62) work fine in a new ESP, whose leakage effect can be neglected. However, for a pump working under sandy flow condition, seal clearances increase with time and leakage effect becomes more important. Both the head loss due to the turbulence in eroded seal regions and the increased flow rate in the flow channel should

be considered. A new method to calculate leakage head loss is proposed and validated by experiments in this study.

In order to predict the pump boosting pressure under gas-liquid two-phase conditions, the mechanism of multiphase flow in pipelines (Chi et al., 2018 and 2019; Daraboina et al., 2019; Zhou et al., 2018; Dubey et al., 2017) is borrowed and applied in ESPs. Thereafter, Zhu et al. (2019i and 2019j) proposed a unified ESP performance prediction model for gas-liquid multiphase flow. The single-phase and two-phase ESP prediction model is based on the previous study. The abrasion prediction model is incorporated to predict new pump geometry. Then, the leakage flow prediction and its effect on pump head loss are revised based on experimental data. According to the inverse prediction methods (Liu and Reynolds, 2019, and Liu et al., 2018), it is also possible to predict the downhole pump working conditions by using the surface production data. Thereafter, the pump and choke management can be optimized (Liu and Forouzanfar, 2018 and Liu et al., 2019a and 2019b) in the future study.

CHAPTER 2

EXPERIMENTAL SETUP AND RESULTS

The flow loop for ESP sand erosion test is a newly designed and constructed experimental multi-phase flow loop at the Tulsa University Artificial Lift Projects (TUALP). The experimental facility consists of 2” carbon steel pipes and a 12-stage mixed type ESP. Intake pressure was maintained at 150 psig in the flow loop to avoid cavitation. Four pumps were tested to investigate sand wear in ESPs under different rotation speeds and gas volumetric fractions. Gas-liquid flow rate, fluid density, temperature, pump performance (pressure increment and torque) and stage vibration were recorded in the test. Sand particles were replaced every two hours, which were monitored by Scanning Electron Microscopy (SEM) analysis and Advanced First-trimester Screening (AFS) test. For each pump, a 64-hour erosion test was conducted and subdivided into several time-period tests (8, 8, 16, and 32 hours). After each period test, the pump was disassembled and the geometries were measured. Once a 64-hour experiment was completed, a new test was conducted with a new pump.

The effects of pump rotation speed and gas volume fraction were investigated in this study under water-solid and water-air-sand flow conditions. Fracture sand SDS from a local company with a specific density of 2.637 was used in the experiments. The mean diameter of original particles is 150 microns with a range of 50 to 250 microns. Sand particle size, density, and sharpness were compared before and after 2 hours’ recirculation

time. The sharpness is similar, while the mean diameter reduced to 100 microns from SEM and AFS tests.

2.1 Experimental Facility

The facility specifications and the schematic of the facility layout for the TUALP ESP sand erosion flow loop are shown in Table 2.1 and Figure 2.1, respectively. As can be seen, the sand erosion flow loop is composed of a main flow loop, a gas injection loop, and a disposal tank, and a water supply.

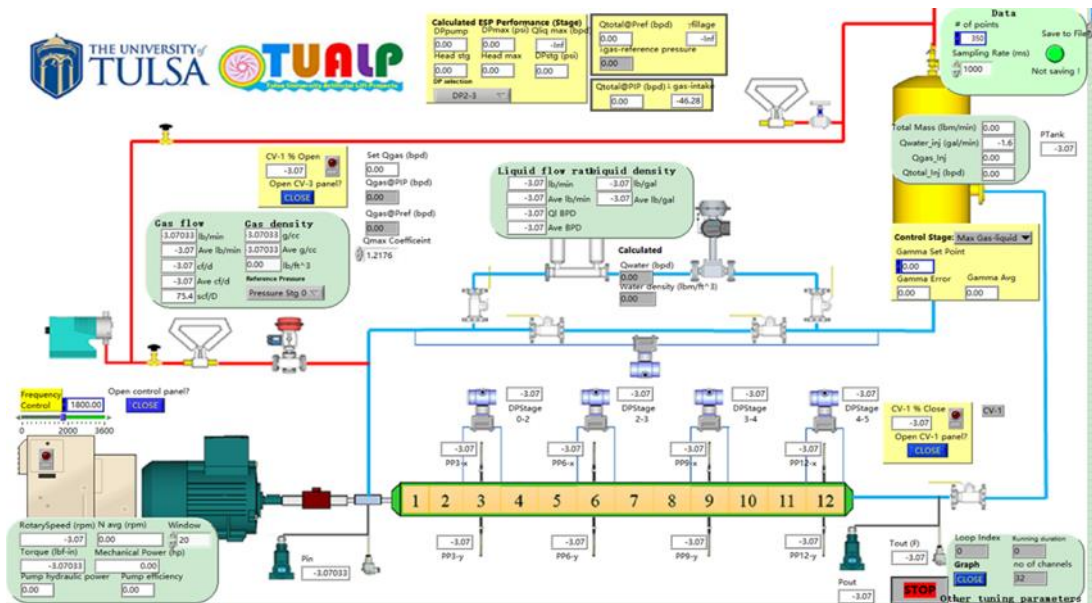


Figure 2.1 Schematic of TUALP ESP sand erosion flow loop

2.1.1 Water-air and water-air-sand flow loops

As shown in Figure 2.1, pure water is supplied by the water tank and recycled in the main flow loop. The sand was added at the top of the gas separator. Absolute pressure and differential pressure transmitters, temperature transmitters, vibration proximity probes, and a torque sensor were installed on the ESP bench. After each time-period test, pump

geometry changes (seal clearance increase and weight loss), performance degradation (pressure increment, torque, efficiency) and vibration were measured and recorded. Pump stages were painted to visualize the most severely eroded location. In each time-period test, sand was added through the separator and replaced every 2 hours. After a 2-hours recirculation, the wasted sand was drained and the loop was washed with pure water. SEM and AFS tests were done to monitor the average sand properties. The process was repeated until all the time-period tests were finished.

The slurry flow rate was controlled by a downstream manual gate valve after the ESP, which can be replaced easily if eroded. The gas flow rate was regulated by a pneumatic globe control valve in the gas injection loop. Gas and slurry flow rates were measured by two Coriolis flowmeters (Micro Motion CMF025 and Endress Hauser Promass 80F). The in-situ air density at the ESP intake and separator outlet was calculated using correlations for wet air properties based on the local pressure and temperature. The pump intake pressure was maintained by a gas pressure regulator that connect the gas separator to the gas injection loop. In water-air-sand three-phase experiments, most of the air was separated by the gas separator and the GVF was less than 1% at the separator outlet. Thereafter, the volume of carried air was calculated from the measured mixture density by the Coriolis flowmeter (Endress Hauser Promass 80F) in the main flow loop. The liquid Coriolis flowmeter was protected by a bypass line. At the beginning of the test, the relationship between the total boosting pressure gain of the pump and flow rates was recorded, then the flowmeter is bypassed and the pressure drop was used to indicate flow rates.

Table 2.1 Experimental equipment list

Equipment/Instrument	Model	Capacity/Range
ESP pump	MTESP	BEP: 3100 bpd, 3500 rpm
Electric motor	WEG 05036EG3E326TS-W22	50 hp
Variable speed drive	FUJI ELECTRIC FRN050G1S-4U	50 hp, 380 ~ 480 V, 70 A
ESP thrust chamber	HSG, Thrust chamber 1.x series horizontal	–
Air compressor	Kaeser CSD60	186 cfm, 217 psi
Liquid control valve	Manually gate valve	–
Gas control valve	Emerson 24588SB	–
Temperature transmitter	Endress Hauser TMT82	-20-200 ^o C
Absolute pressure transmitter	Endress Hauser PMC71	6 ~ 600 psig
Differential pressure transmitter	Endress Hauser PMD75	0.45-45 psig
Coriolis liquid flowmeter	Endress Hauser Promass 80F	0 ~ 10000 bpd
Coriolis gas flowmeter	Micro Motion CMF025	0 ~ 40 lb/min
Proximity probe	GE 3300 NSV	10-90 mils
Proximitior	GE 3300 XL NSV	Output: 200 mV/mil, 100 KHz
Pressure regulator	NORGREN 1/2" NPT Regulator	10-250 psig, 212 cfm
POP safety valve	APOLLO Bronze POP safety valve	400 psig
Torque sensor	S.Himmelstein MCRT28004T(5-3)NFA	0 ~ 8500 rpm 0 ~ 5000 lbf-in
Torque sensor monitor	S.Himmelstein model 721	2000 samples/sec

2.1.2 ESP test bench

The ESP motor, thrust chamber and other equipment needed for the operation were assembled on an ESP test bench. The skid for the ESP test bench is shown in Figure 2.2. The torque sensor was installed between the motor and thrust chamber, and 8 vibration proximity probes were mounted on pump stages. Performance, torque and vibration signals were recorded to reflect the pump condition. A 12-stage MTESP, which is designed to resist erosion in practical field conditions, was installed. The best efficiency point (BEP) is $Q = 3100$ bpd and $N = 3600$ rpm with the boosting pressure of 9.8 psig per stage. The

maximum open flow rate at $N = 3500$ rpm is 5000 bpd, while the maximum shut-in pump head is 16.7 psi.

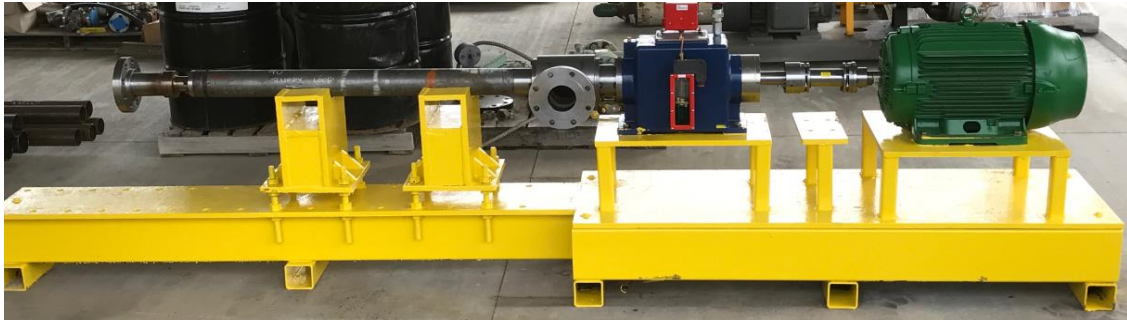


Figure 2.2 Skid for TUALP ESP sand erosion flow loop

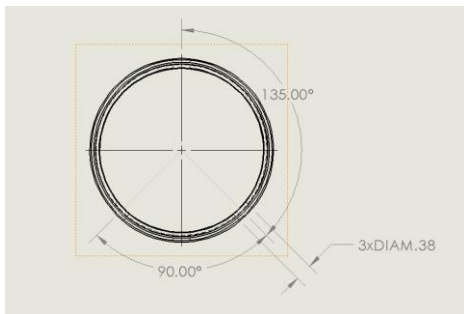
The MTESP ESP delivers unmatched performance for flow rates from 4000 bpd to 1200 bpd. As shown in Figure 2.3. (f), the MTESP is composed of two types of stages, SCD stages and floater stages (general stages). The pump is made of NI-Resist Type-1 Iron steel with a Brinell/Vickers hardness of 130-180. All stages have the same type of impellers. In an SCD stage, Tungsten carbide flanged sleeve with a Vickers hardness of 2600 is used, and the corresponding diffuser bore is also made by carbide material. On the other hand, other components of the special carbide stage, for example, impeller and diffuser except diffuser bore, are also made by Ni-Resist Type-1 Iron steel. Both bottom and top bearings have carbide straight sleeve bearings. The geometry of all stages and sleeves were measured in this study, and the performance and vibration of four selected stages in the dashed box in Figure 2.3 (f) are recorded



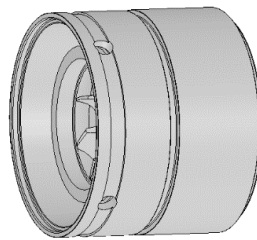
(a)



(b)



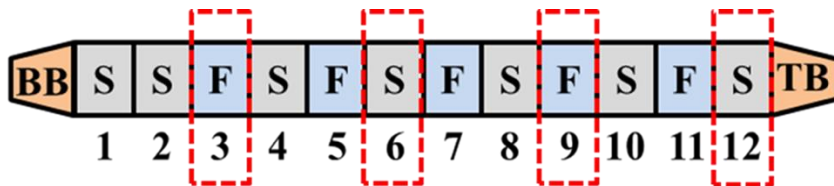
(c)



(d)



(e)



BB: Bottom bearing
S: Special carbide stage

TB: Top bearing
F: General floater stage

(f)

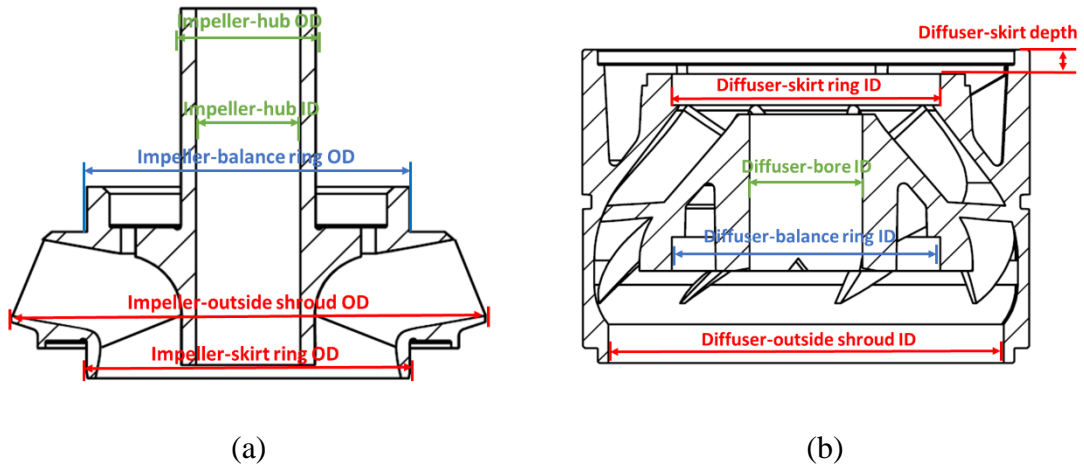
Figure 2.3 MTESP components , (a) pressure ports and proximity probes, (b) 3D pump housing, (c) left view of pump housing, (d) 3D view of diffuser, (e) section view of MTESP, (f) combination of stages

As shown in Figure 2.3 (a), 13 quarter-inch holes were drilled and threaded on the pump housing to install pressure transmitter and proximity probes. Two 3/8"×5/8" slots

per diffuser, shown in Figure 2.3 (c), (d) and (e), were drilled to mount the proximity probe. Thereafter, the required distance between the probe tip and the target impeller surface can be reached. Another hole 135° to the slots was drilled to allow the communication between the pressure transmitters and the working fluids. Teflon O-rings were installed to block fluid communication between stages. Quick connectors (Swagelok QTM2) were tightened through pressure holes to connect pressure transmitters. A $1/4''$ UNF thread was machined in the center of a $1/4''$ pipe hex plug to install and seal proximity probes, which were mounted at the stagnation area between impeller and diffuser.

2.1.3 Stage geometry and seals clearance

As shown in Figure 2.4 and Figure 2.8, the inside diameter (ID) and outside diameter (OD) of the hub, bottom shroud, balance ring and skirt ring on impellers and diffusers were measured after every time-period test. In addition, the outer diameter of the sleeves and weight of impeller, diffusers, and sleeves were also recorded in the test. Skirt ring clearance can be calculated by subtracting the impeller skirt ring OD from diffuser skirt ID. Similarly, balance ring clearance is the difference between impeller balance ring OD and diffuser balance ring OD. It should be noted that the inter-stage clearance is obtained from impeller hub OD and diffuser bore ID.



(a) (b)
Figure 2.4 Measured geometry on stages, (a) impeller, (b) diffuser

2.1.4 Data acquisition system (DAQ)

The data acquisition system was originally programmed with the Compact FieldPoint module from National Instruments (NI) (Zhu et al., 2017b). However, FieldPoint modules were replaced by CompactDAQ modules to obtain a high updating rate. NI 9208 was used for pressure, flow rate and temperature signals with a range of 4~20 mA. The internal control signals (4~20mA) generated by NI 9265 output module were sent to VSD and control valves. In addition, NI 9228, a high updating rate voltage input module, was used for proximity probes and torque sensor, which requires high scanning frequency. The data processing center is a Dell computer (Optiplex 9020). The DAQ program was written in the graphic-programing language Labview.

Table 2.2 Data acquisition system specifications of TUALP ESP erosion flow loop

Equipment/Instrument	Model	Capacity/Range
Fieldpoint chassis	NI cFP-1804	–
Fieldpoint analog input	NI cFP-AI-111	16 channels; input ranges 0-20 mA/4-20 mA \pm 20 mA; updating rate 0.83-3 Hz
Fieldpoint output	NI cFP-AO-200	8 channels, current output, 200 Hz
Fieldpoint voltage input	NI cFP-AI-100	8 channels; input range \pm 1V, \pm 5V, \pm 15V, \pm 30V, 0-1V, 0-5V, 0-15V, 0-30V, 0-20 mA/4-20 mA \pm 20 mA; updating rate 360 Hz
Fieldpoint supply	NI cFP-CB-1	–
CompactDAQ analog output	NI 9265	0 to 20mA, 16-Bit, 100 kS/s, 4-Ch AO module
CompactDAQ voltage input	NI 9228	8-Ch +/-60 V, 1 kS/s/ch, 24-Bit, Ch-to-Ch Isolated AI module
CompactDAQ chassis	NI 9939	Backshell for 16-pos connector block (qty 1)
CompactDAQ analog input	NI 9208	24-bit current input module with D-Sub
CompactDAQ chassis	NI 9923	Front-mount terminal block for 37-pin D-Sub Modules
Power supply	AutomationDirect	–
Terminal blocks	AutomationDirect	–
Circuit protection blocks	AutomationDirect	–
Konnect-It terminal block jumper	AutomationDirect	–
Electrical enclosure	Hoffman	–
Computer	Dell	–
Terminals tubular cable lug	YONGCUN	–

2.2 Experimental Program

2.2.1 Sand characteristics

The sand used in our experiment is fracture sand SDS from a local company with a specific density of 2.637. The mean diameter of particles is 150 microns with a range of 50 to 250 microns as shown in Figure 2.5 (a).

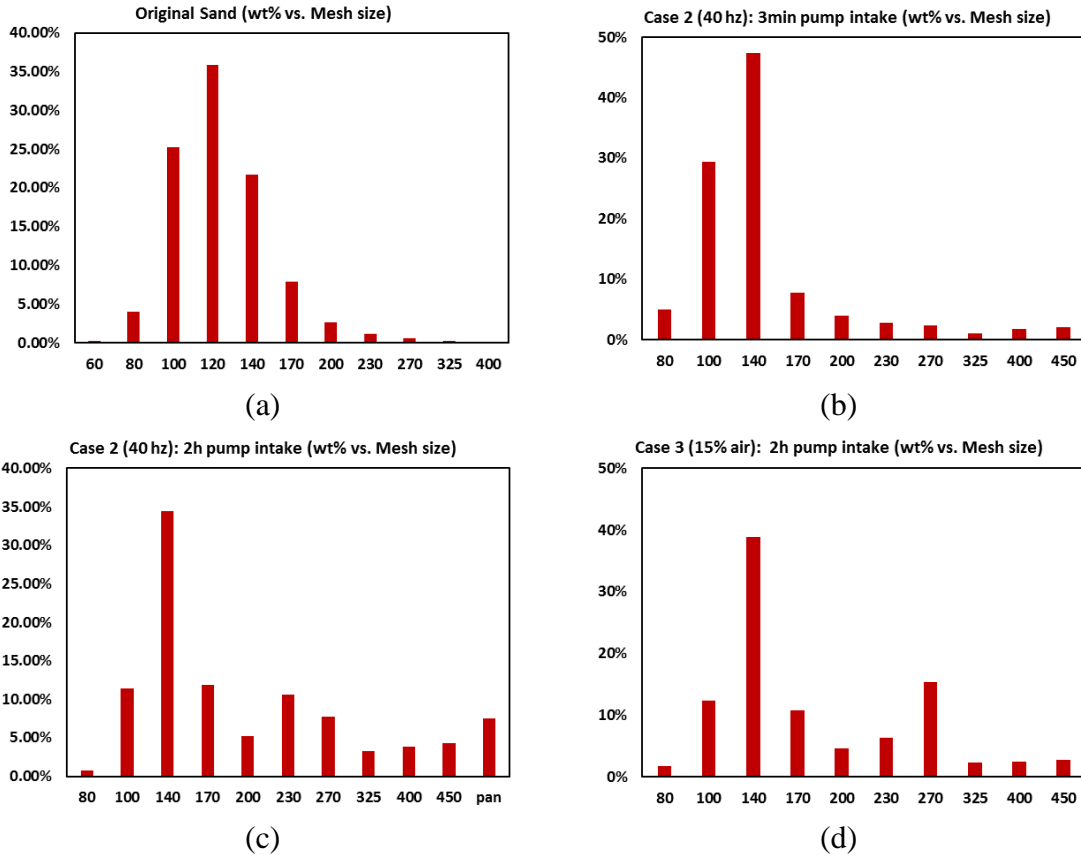


Figure 2.5 Sand particle size distribution (a) original, (b) Case 2 (40 Hz): after 3 min circulation at pump intake, (c) Case 2 (40 Hz): after 2 hours circulation at pump intake, (d) Case 3 (15% air): after 2 hours circulation at pump intake

The sand in the flow loop was replaced every 2 hours during the 64-hour long test. Therefore, sand was replaced 32 times for 1 64-hour erosion test. Samples were collected during the tests. Three samples that collected during or after 2-hour circulation were compared with the original sand sample. As shown in Figure 2.5 (a), (b) and Figure 2.6 (a), (b), some dirt (rust and steel debris) exists in the loop. But the sand size distribution at the beginning of the test is comparable to the original sand particles. In Figure 2.5 (c), (d) and Figure 2.6 (c), (d), some sand particles are damaged into small pieces, the sand mean diameter decreases from 140 μm to 70-80 μm (AFS mesh size from 100-110 to 170-200). However, the sand size distribution after 2-hour circulations of different cases is comparable, indicating that half of the original particles were broken into smaller pieces.

In addition, solids in Figure 2.6 are still very sharp, which indicates the sharpness keeps consistent. Therefore, it is presumable that the averaged sand characteristics are identical in all tests. AFS number of 150 (diameter $100\ \mu\text{m}$) and the sharpness factor of 1 (1 is sharp particle, 0.53 is semi-rounded particle, and 0.2 is fully-rounded particle) are used in this study.

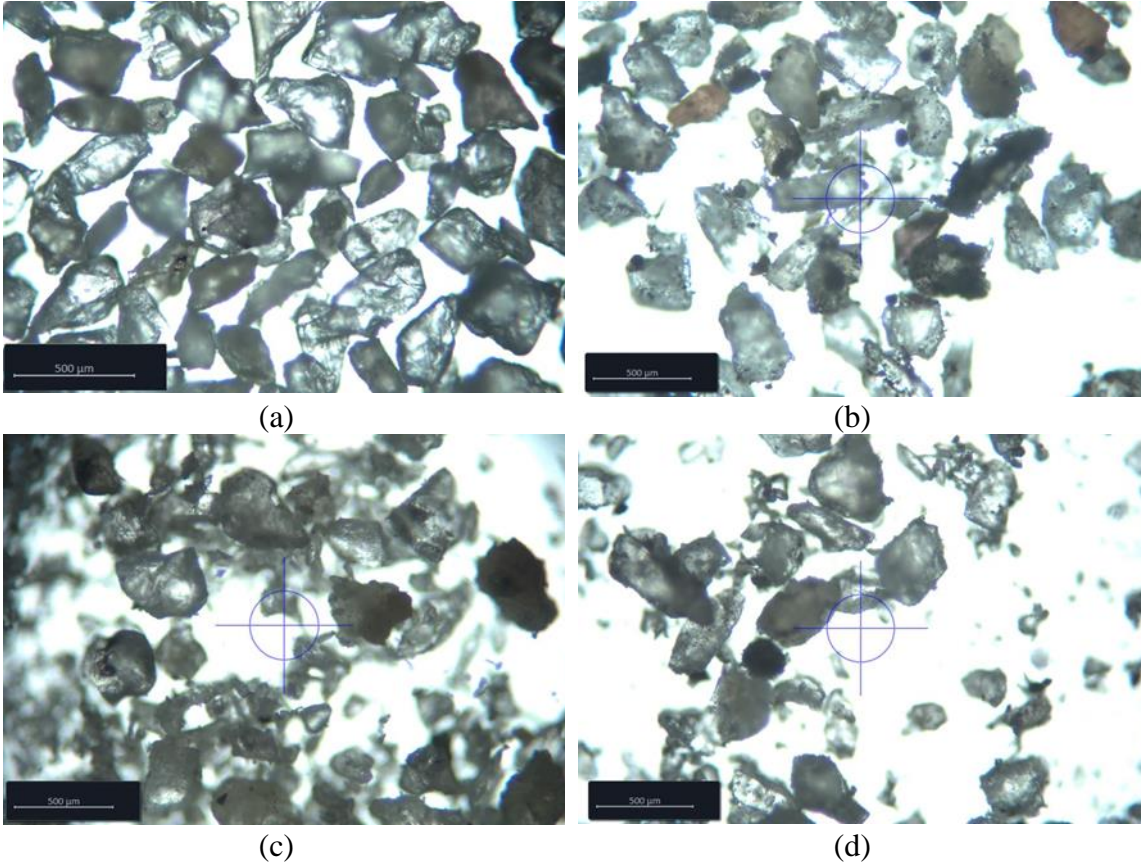


Figure 2.6 Sand photos, (a) original, (b) 3 mins (40 hz), (c) 2 hours (40 hz), (d) 2 hours (60 hz)

2.2.2 Experimental procedure and test matrix

Four tests were conducted under water-sand and water-air-sand flow conditions with rotation speed $N = 2400$ and 3600 rpm to investigate the rotation speed effect and gas effect on sand erosion in ESPs. The test matrices are listed in Table 2.3.

Case	1	2	3	4
Sand concentration(%)	1%	1%	1%	1%
Rotation speed (Hz)	40Hz	60Hz	60Hz	60Hz
Liquid flow rate (bpd)	3100	3100	3100	3100
Gas volume fraction (%)	0	0	15%	7.5%

The worn parts of each pump, including impellers, diffusers, shaft, sleeves, and bearings, were replaced after every 64 hours erosion test, while the rest of the pump components were kept. A simplified procedure chart for the 64-hour test is shown in Figure 2.7. The ESP erosion tests, including pump performance, vibration, geometry changes, and sand properties measurements, were accomplished at the University of Tulsa (TU). Impeller imbalance tests, thrust tests, and profilometry scans were conducted at sponsor company.

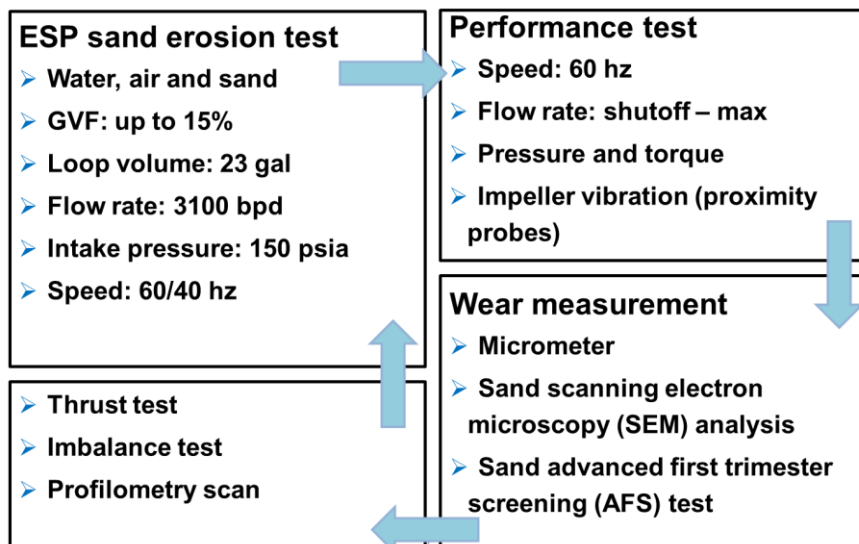


Figure 2.7 ESP erosion test procedure

The 64-hour erosion test was divided into several time-period tests (8, 8, 16 and 32 hours). The detailed procedure in a period test is shown below.

1. Measure the original pump geometry and weight.

2. Install the pump onto the flow loop and acquire the original pump performance with water, including head increment, efficiency and vibration, and geometries.
3. Fill the main loop with water-sand slurry under low rotation speed.
4. Increase the separator pressure to 200 psig.
5. Increase the rotation speed and change the water-sand mixture flow rate to the designed conditions. Inject gas if required.
6. Replace the slurry and collect sand particles after 2 hours of circulation.
7. Repeat steps 2 to 4 until the period test is finished.
8. Replace the slurry with pure water and measure the deteriorated pump performance.
9. Disassemble the pump and measure the weight and geometry changes.
10. Send the pump to company to conduct an imbalance test and thrust test.
11. Send sand samples to the Biology Department or Chemical Engineering Department for SEM and AFS tests.
12. Take back the pump for the next period test.

2.3 Experimental Data

2.3.1 Pump geometry and weight changes

In this section, the pump geometry changes due to the three-body abrasion wear in seal clearances and total weight loss of impeller, diffuser, and sleeves are recorded and compared. The flanged carbide sleeve can help the pump resist the abrasion wear. However, the damage to SCS and floater stages are comparable. In the following sections, abrasion damage will be discussed according to the different seal geometry. For the sake

of convenience, all the dash curves in Figure 2.8 to Figure 2.19 refer to the average dimension of general floater stages and the solid curves refer to that of the SCS stages. All the raw measurements are listed in Appendix B.

2.3.1.1 Inter-stage clearance

The whole inter-stage clearance can be divided into two sections. The first one is the clearance between the impeller hub (green lines in Figure 2.8) and the corresponding diffuser bore (red lines), whose surface material is steel for both SCS and floater stages. The second one is the clearance between sleeve (purple lines) and the corresponding diffuser bore (red lines), which is made by Tungsten carbide in SCS stages and steel in floater stages. The outlet of the inter-stage clearance is impeller balance holes, which is not designed to resist leakage and was not damaged by abrasion in the tests. Therefore, it was not recorded in the test.

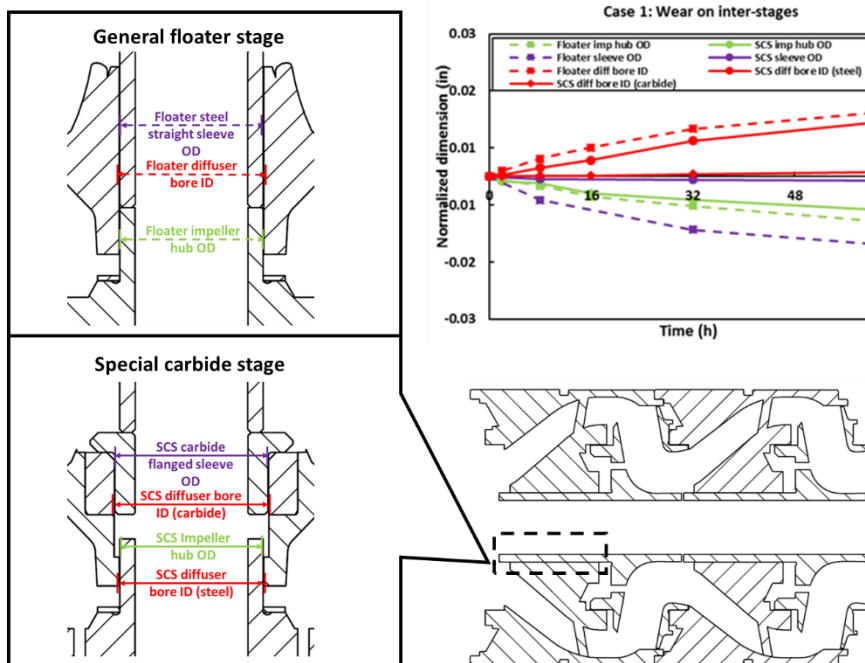


Figure 2.8 Geometry changes in the inter-stage clearance

The original geometry dimension is subtracted from all the measurements in order to compare the damage to different geometries. As shown in the chart of Figure 2.8, there is almost no damage on carbide sleeves and carbide diffuser bores, which means that the inter-stage clearance between carbide sleeves and diffuser bore in the SCS stage maintains its integrity and helps resist leakage in this flow domain. It is presumable that the leakage in the inter-stage clearance of SCS stages is lower than floater stages and the damage on the impeller hub is caused by trapped solids. As a result, the abrasion damage on the impeller hub and the corresponding diffuser bore in SCS stages is slightly lower than that of the floater stages.

Although difference exists in other inter-stage geometries, the overall trend and value are comparably similar. Therefore, only the sleeve OD, the corresponding diffuser bore ID, and the clearance between them for the four tested pumps is shown in Figure 2.9 to analyze the stage type and surface material effect. More detailed geometry change measurements for the four tested pump are shown in Appendix B.

As shown in Figure 2.9, the abrasion damage gradually decreases during the first 16 hours and becomes stable after that. It is clear that carbide material can help resist damage by comparing Figure 2.9 (a), (c), (e) and (b), (d), (f). The overall geometry changes of the four tested pumps are comparable, which indicates that the rotation speed and gas fraction do not significantly affect the abrasion damage in the tested ESPs. Although the difference between four test cases is limited, lower rotation speed and higher GVF slightly reduce the abrasion damage according to the measurements at 32-hour and 64-hour. The difference may become more obvious if we increase the testing time. The total testing time was kept as 64 hours since the performance of the pump deteriorated about 10%, which is

significant in field application. The slight deviation of pump 1 geometry before 32 hours, when a caliper is used to measure the geometry before new micrometers were ordered, may be caused by a higher measurement uncertainty of the caliper shown in Appendix C.

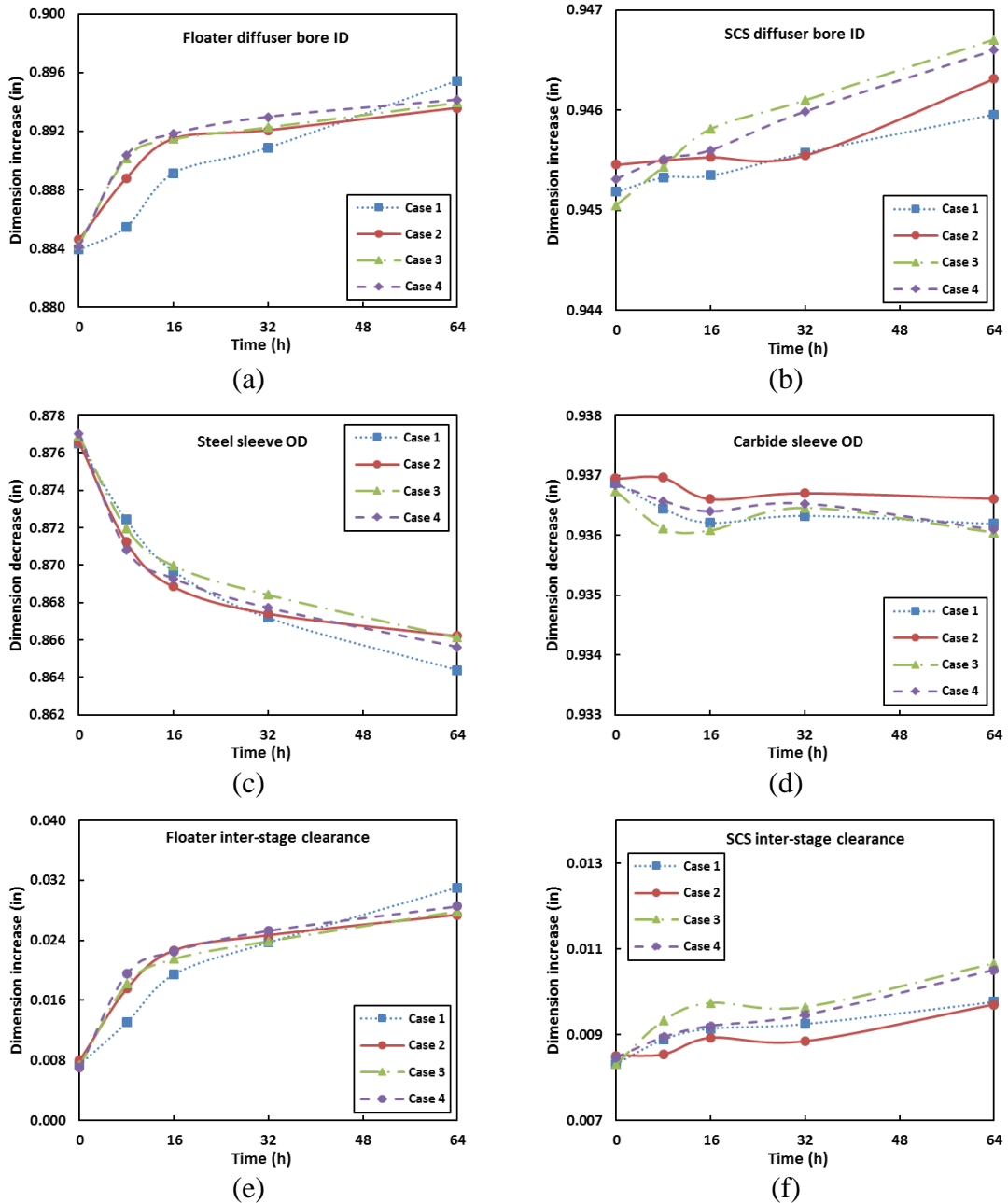


Figure 2.9 Geometry changes in the inter-stage clearance (diffuser-sleeve) clearance, (a) floater diffuser bore ID, (b) SCS diffuser bore ID, (c) steel sleeve OD, (d) carbide sleeve OD, (e) floater inter-stage clearance, (f) SCS inter-stage clearance

2.3.1.2 Skirt ring clearance

As shown in Figure 2.1, the inlet is skirt seal clearance between impeller skirt OD (green) and diffuser skirt bore ID (red) and the outlet is shroud clearance between impeller outside shroud OD (purple) and diffuser outside shroud ID (orange). In general, the thrust force for a floated ESP is always pointed downward, which can cause more damage to the impeller skirt ring top surface and diffuser skirt bore bottom surface. Therefore, a thrust washer made by softer material is always embedded on to impeller skirt rings to protect this seal geometry. According to the four tested pumps, those thrust washers were completely worn out quickly between 8-16 hours. Since the impeller skirt ring depth is hard to be obtained, only the diffuser skirt bore depth was measured and shown in blue lines

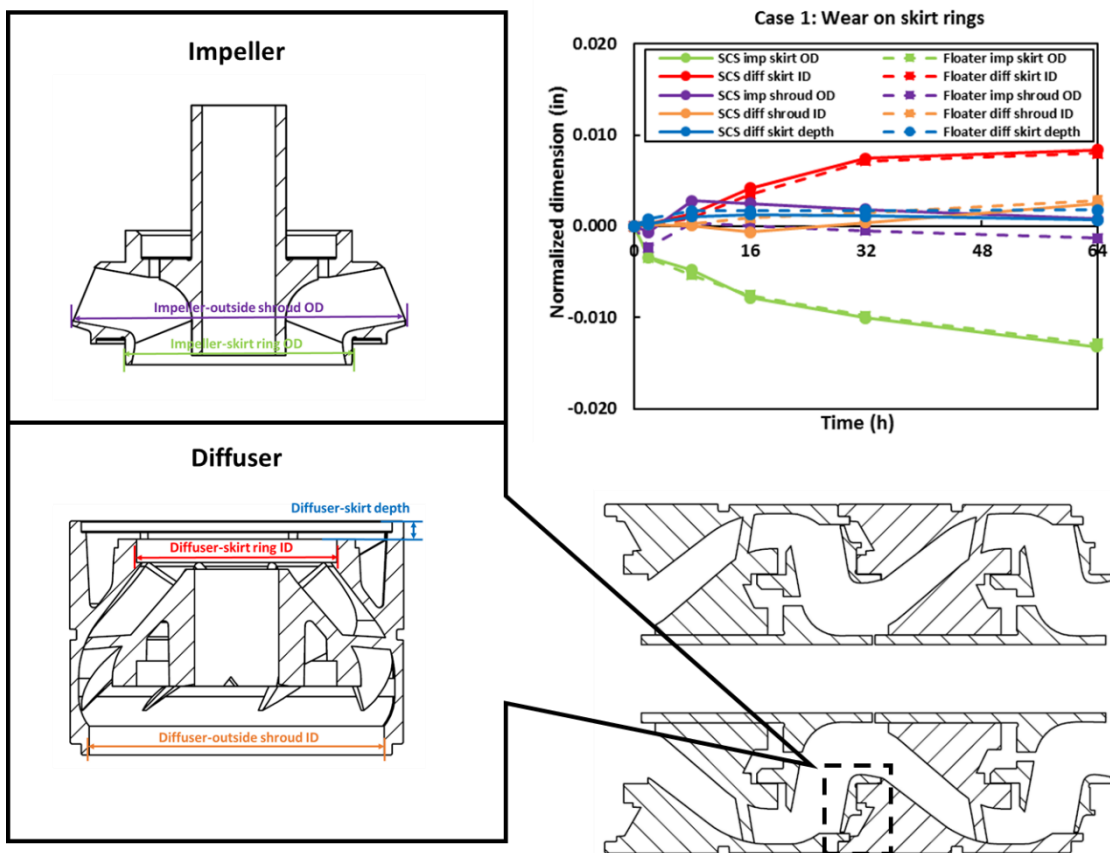


Figure 2.10 Geometry changes in the skirt ring clearance

As shown in the chart of Figure 2.10, the damage on SCS and floater stage are almost identical, which indicates that the carbide sleeve do not help resist damage on the skirt rings. In addition, the damage on the outside shroud diameter of the impeller and diffuser can be ignored compared to that on the skirt ring. However, the stage photos in Figure 2.22 (d) in Section 2.3.3.1 indicate that the damage on the diffuser outside shroud is still obvious. Due to the limitation of the measuring tools, the damage on the shroud cannot be accurately recorded and will not be compared in Figure 2.11. Finally, the diffuser skirt ring bore depth also keeps its original size for the following reason. The impeller position depends on axial thrust force hydraulic design and sleeve design. Besides the thrust washer, the sleeves between the impeller and diffuser are also designed to hold the impeller to prevent tightly touching the diffuser under high thrust force condition. Once the thrust washers are completely worn out, most of the thrust force is offset by sleeves and the length of the sleeve can be reduced during the test. When flanged carbide sleeves are used, the steel sleeve above them suffers more damage under high thrust force conditions. According to Figure 2.22 in Section 2.3.3.1, the steel sleeve above the flanged carbide sleeve does suffer obvious damage. Therefore, the diffuser skirt bore depth is firstly protected by thrust washer, then by sleeves. Similarly, the depth measurement will not be shown in Figure 2.11 since it is not obviously damaged compared to the balance ring diameter.

Similar to inter-stage clearance, the damage gradually decreases during the first 16 hours, and gas fraction and rotation speed effects on abrasion damage on skirt rings are limited in Figure 2.11. As discussed previously, the measurement of case 1 has higher

uncertainty before 32 hours. Besides case 1, the damage for cases 2, 3, and 4 looks quite similar before 16 hours. After that, lower rotation speed and higher GVF give slightly lower the damage on the skirt rings. Especially for case 1 (GVF 0%), 3(GVF 15%), and 4(GVF 7.5%), the trend that higher GVF gives slightly lower abrasion damage is obvious after 16 hours.

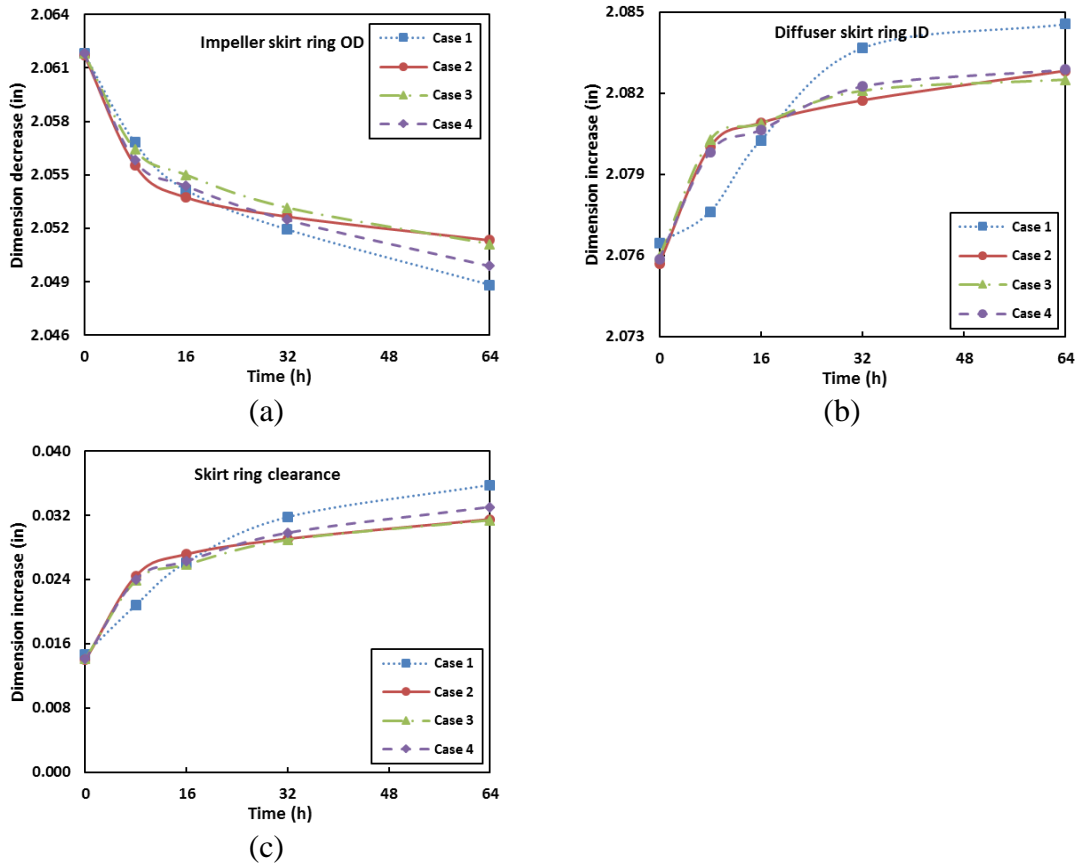


Figure 2.11 Geometry changes in the skirt-ring clearance, (a) impeller skirt ring OD, (b) diffuser skirt bore ID, (c) skirt ring clearance

2.3.1.3 Balance ring clearance

Before analyzing the experimental data, it should be noted that the diffuser balance ring ID is measured by a caliper with lower accuracy and higher uncertainty shown in Appendix C since the micrometer cannot be used due to the complex pump geometry and

limited measuring space. Therefore, the accuracy of the diffuser balance ring ID and balance ring clearance is lower. Similar to the inter-stage clearance, the outlet of this secondary flow passage is the impeller balance hole, which is not damaged by three-body abrasion wear. Then, the geometry of balance ring clearance becomes very clean that only diffuser balance ring ID and impeller balance ring OD are recorded in Figure 2.12 and Figure 2.13. Similar to the skirt ring geometries, using carbide sleeves does not help prevent the damage on this clearance.

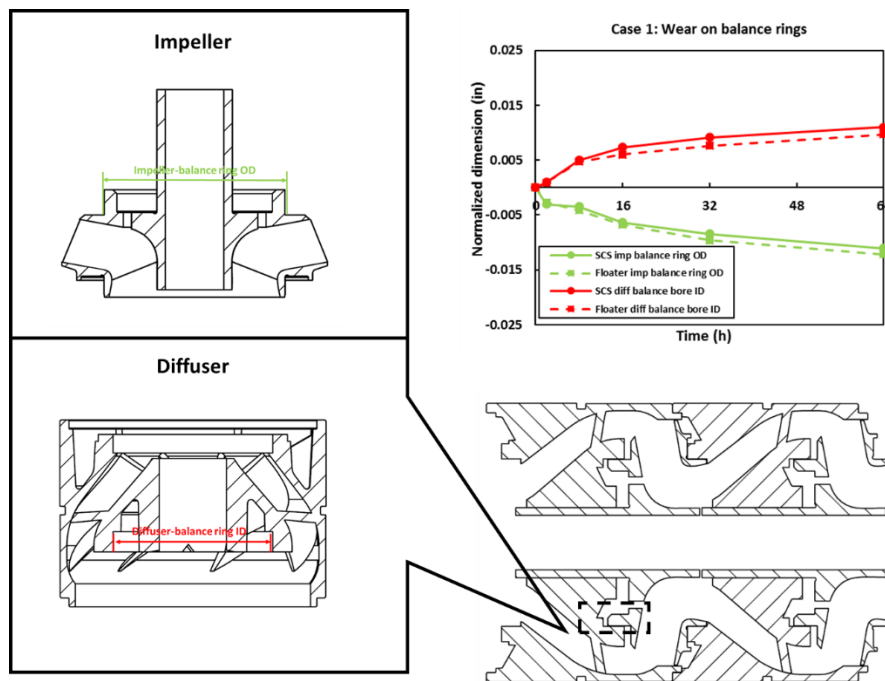


Figure 2.12 Geometry changes in the balance ring clearance

Similarly, comparison among four tested pumps is shown in Figure 2.13 and more data are available in Appendix B. Overall, the rotation speed and gas fraction effects are still limited. Different from the previous two clearances, the gas fraction has almost no effect on the abrasion on the impeller balance ring, while lower rotation speed gives slightly lower damage at 64 hours.

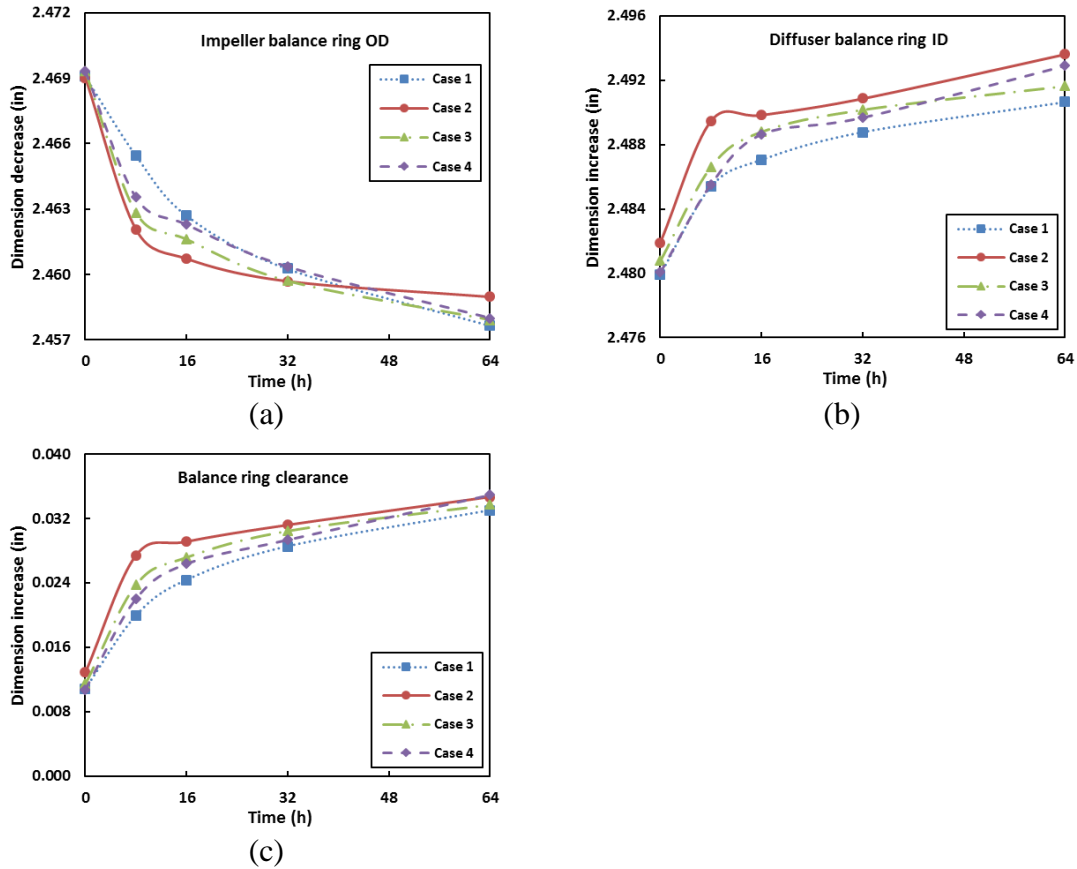


Figure 2.13 Geometry changes in the balance ring clearance, (a) impeller balance ring OD, (b) diffuser balance ring ID, (c) balance ring clearance

2.3.1.4 Comparison of three clearances

Figure 2.14 shows the three clearance changes according to different stage types, where dash lines represent the average dimension changes of general floater stages and solid lines are that of SCS stages. Blue curves are for balanced ring clearance and red curves are for skirt-ring clearance. Similarly in Figure 2.15, SCS stages do not help reduce the damage on these two clearances. As introduced in Section 2.3.1.1, the inter-stage clearance can be divided into diffuser-impeller inter-stage (orange), where SCS and floater stages are similar, and diffuser-sleeve inter-stage (green), where carbide material is used in SCS stages. Obviously, the carbide diffuser-sleeve inter-stage (solid green line) didn't

suffer from solid due to its higher hardness and kept the seal function. As a result, the SCS diffuser-impeller inter-stage has less damage since the leakage flow is lower.

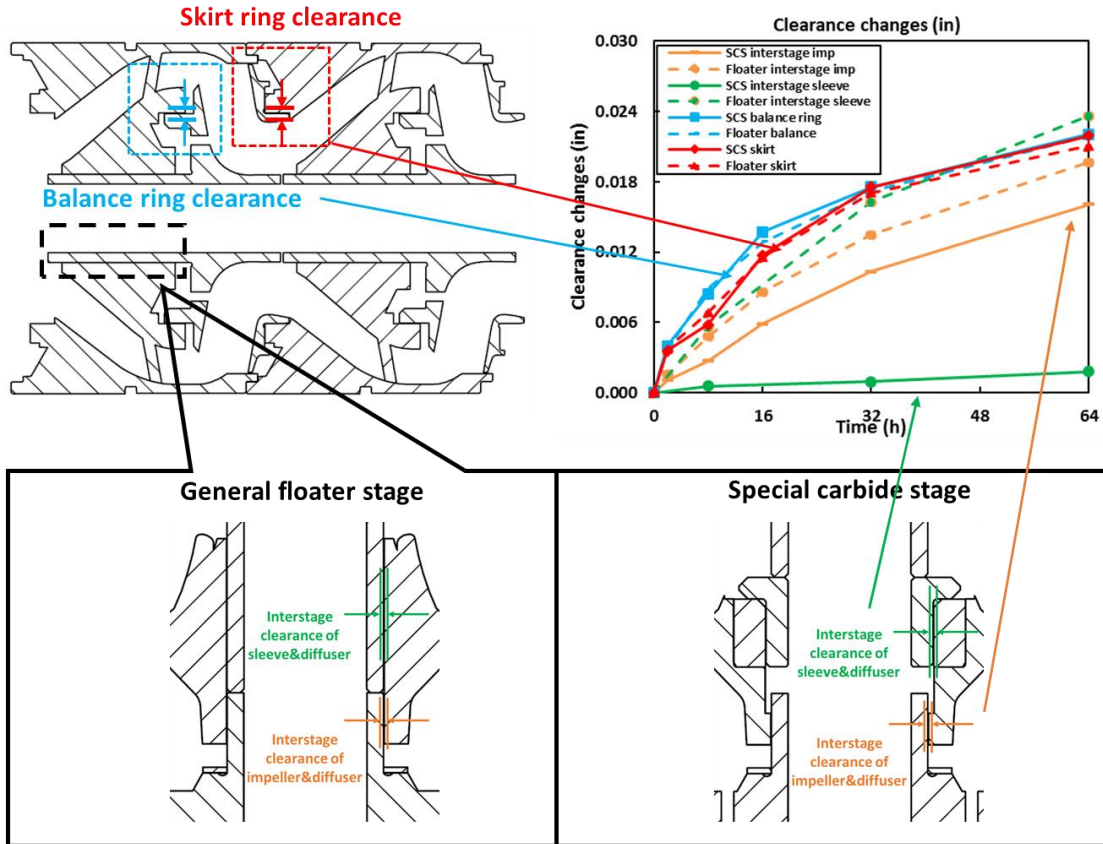


Figure 2.14 Geometry changes of three clearances for SCS and floater stages

The diffuser-impeller inter-stage clearance is not shown in Figure 2.15, and the difference among diffuser-sleeve inter-stage clearances of four cases is limited. All the carbide parts kept their original shapes and sizes. On the other hand, damage on the balance ring slightly increased and that on the skirt ring slightly decreased as shown in cases 1, 3, and 4. It may be caused by gas bubbles trapped in the impeller inlet region as shown in the CFD simulation in this study in Figure 3.21. The trapped gas bubbles can cause more turbulence and pressure loss for flow through skirt ring clearance. On the other hand, fewer

gas bubbles can be found close to the impeller balance holes, which makes its leakage flow similar to single-phase water flow condition.

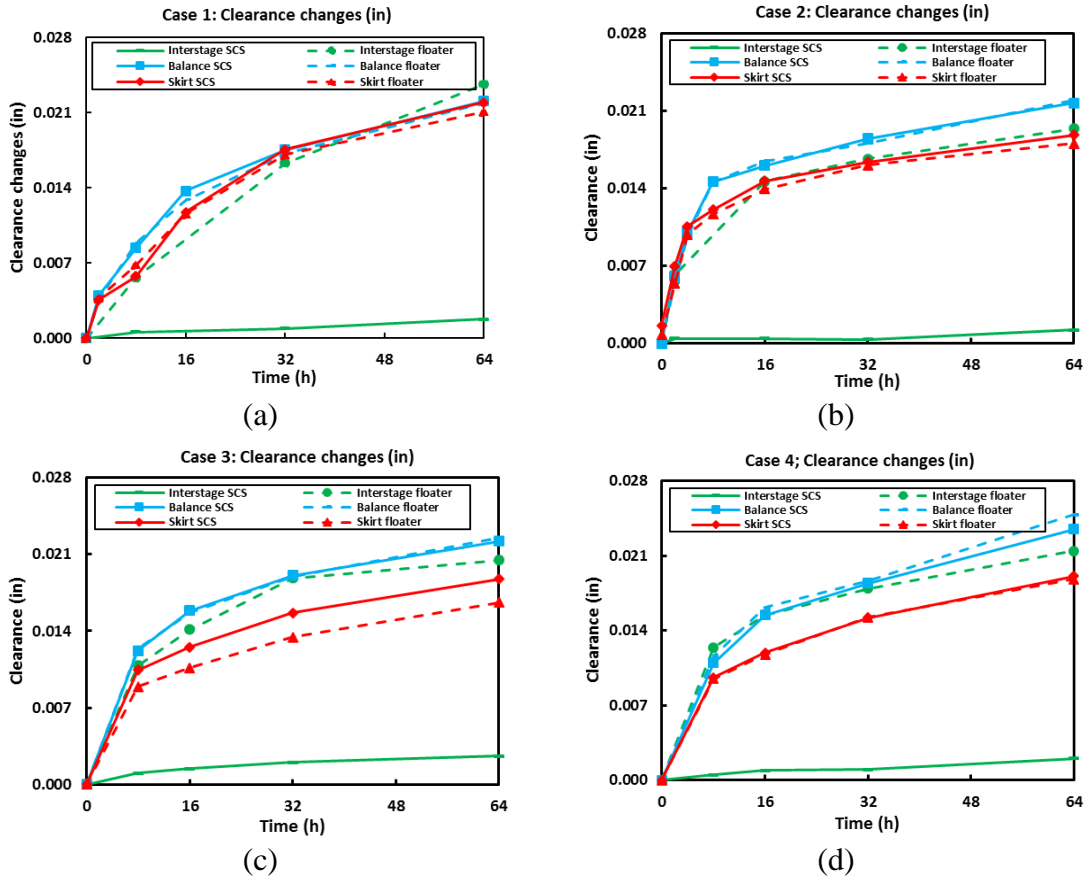


Figure 2.15 Comparison of geometry changes of three clearance among four cases, (a) Case 1: water-sand, $Q_L = 3100$ bpd, $N = 3600$ rpm, (b) Case 2: water-sand, $Q_L = 3100$ bpd, $N = 2400$ rpm, (c) Case 3: water-air-sand, $Q_L = 3100$ bpd, $N = 3600$ rpm, $GVF = 15\%$ (d) Case 4: water-air-sand, $Q_L = 3100$ bpd, $N = 3600$ rpm, $GVF = 7.5\%$

2.3.1.5 Sleeves

Three different types of sleeves were used in the pump. Straight steel sleeves were used in general floater stages, flanged carbide sleeves were used in SCS stages, and straight carbide sleeves were used in the top, bottom bearing and the last pump stage. As shown in Figure 2.16, abrasion damage on steel sleeves is much severer than that of carbide sleeves.

Meanwhile, the damage on straight carbide sleeves is slightly higher than that on flanged carbide sleeves. It is believed that the flanged shape can efficiently reduce the leakage in the inter-stage clearance.

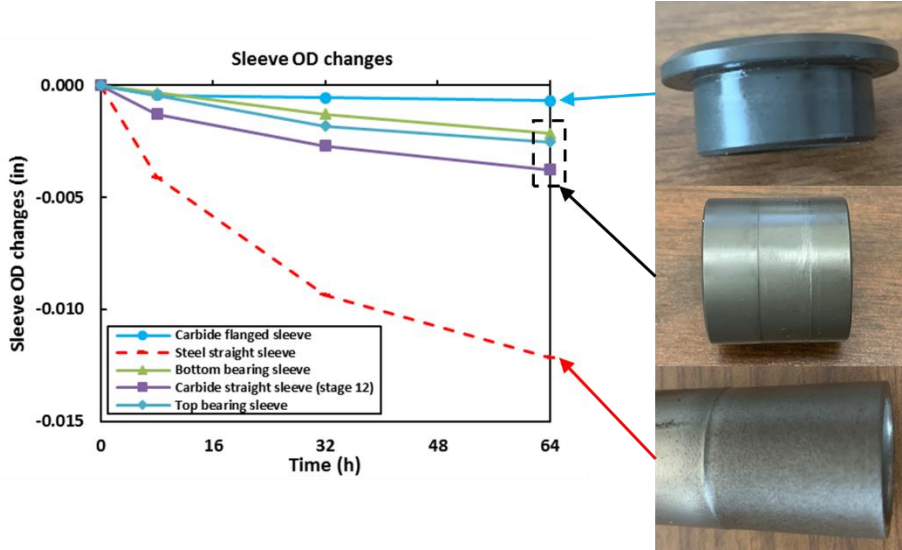


Figure 2.16 Abrasion damage on sleeve OD

According to the comparison in Figure 2.17, the steel sleeves always have higher damage. In addition, more damage can be observed either on the sleeves of the last stage, or the top bearing near the outlet. According to Morrison’s study, the stiffness of the pump system influences the abrasion rate (Bai et al., 2019; G. L. Morrison et al., 2015). The pump inlet has higher stiffness since it is locked by thrust chamber coupling and skid holder, while the outlet is only locked by skid holder. It is presumable that lower stiffness of the outlet caused more damage to those carbide sleeves.

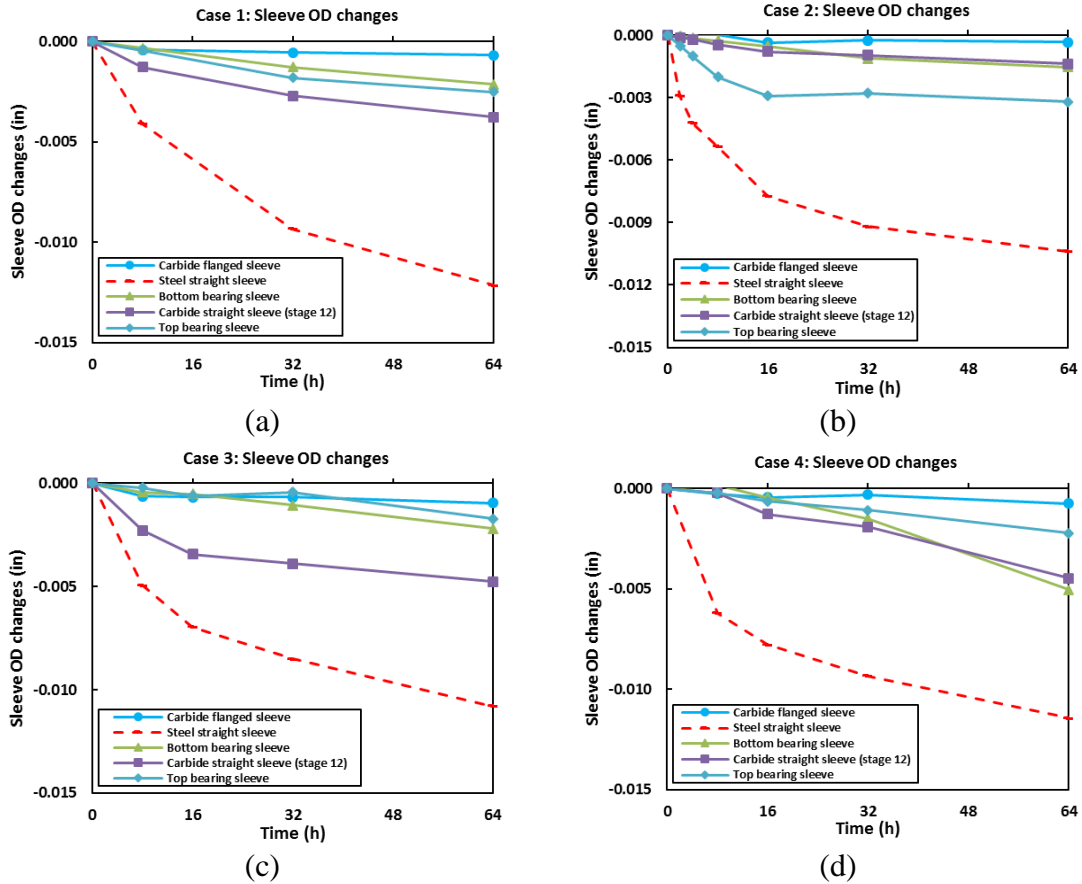


Figure 2.17 Geometry changes of sleeve OD, (a) Case 1: water-sand, $Q_L = 3100$ bpd, $N = 3600$ rpm, (b) Case 2: water-sand, $Q_L = 3100$ bpd, $N = 2400$ rpm, (c) Case 3: water-air-sand, $Q_L = 3100$ bpd, $N = 3600$ rpm, $GVF = 15\%$ (d) Case 4: water-air-sand, $Q_L = 3100$ bpd, $N = 3600$ rpm, $GVF = 7.5\%$

2.3.1.6 Weight losses

The comparison of the average impeller and diffuser weight and weight loss among the four pumps is shown in Figure 2.18. The big difference between Figure 2.18 (b) is caused by manually drilled holes for pressure and vibration measurement. As shown in Figure 2.18 (c) and (d), case 2, with lower rotational speed, has lower weight loss for both impeller and diffuser. Therefore, the erosion damage is obviously reduced since only a slight difference of abrasion damage among the four cases can be observed. On the other hand, the weight losses are similar under different GVF. However, the paint-removal

photos in Section 2.3.3.2 shows that the erosion becomes more concentrate on blade edges and impeller inside shrouds. In short, the average weight loss of impellers and diffusers of the four tested pumps are similar, but the erosion becomes more concentrate when more gas presents.

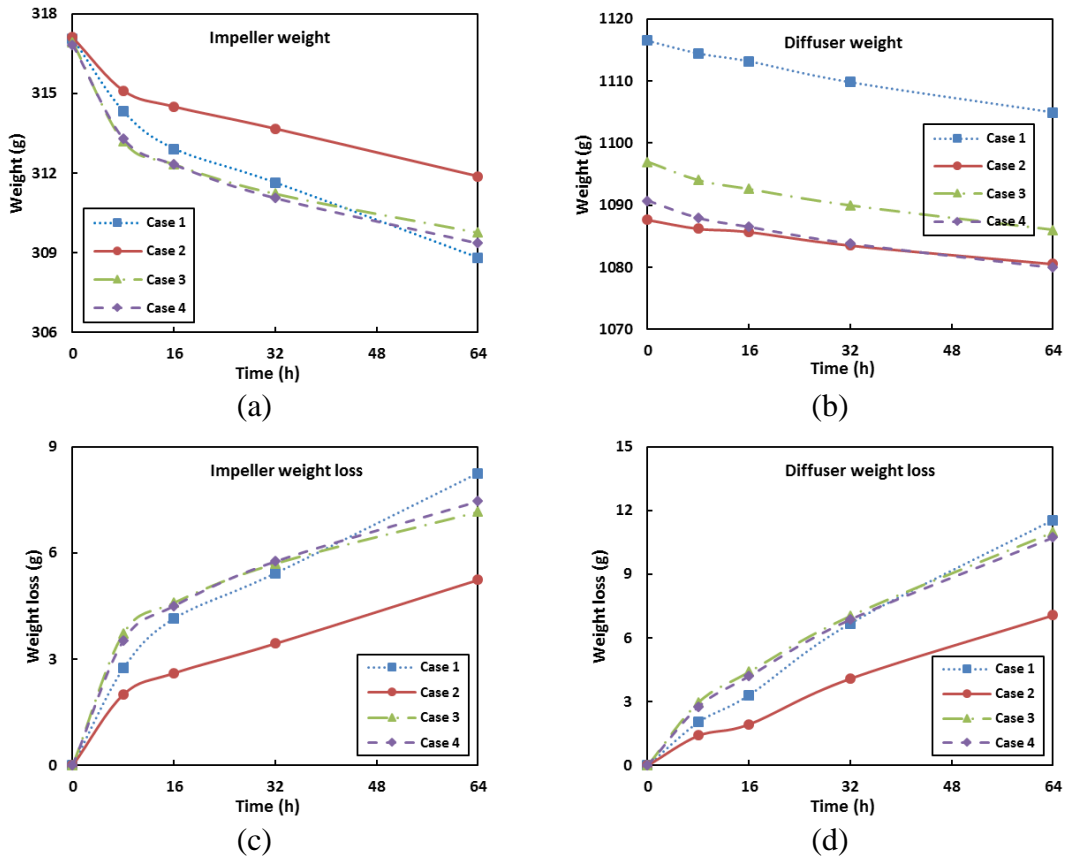


Figure 2.18 Average weight and weight loss of four cases (a) impeller weight, (b) diffuser weight, (c) impeller weight loss, (d) diffuser weight loss

Average weight loss is further separated by stages types, where dash lines represent general floater stage and solid lines are SCS stages. Clearly, steel sleeves of general floater stages have higher weight loss in four cases. However, the diffuser weight loss of SCS stages is surprisingly much lower than that of floater stages. Although there is less abrasion on the inter-stage clearance of SCS stages, the roughly calculated abrasion weight loss difference should be much less than 1 g, which does not cause a big deviation in Figure

2.19. The lower weight loss of SCS stage is caused by less leakage flows through the inter-stage clearance. As a result, the real in-situ liquid flowrate in the SCS impeller is lower than that in the floater impeller. Therefore, the particle impact velocity and erosion damage are lower in SCS stages. As shown in Figure 2.19, weight losses have a more linear relationship with time, which is different from the abrasion damage shown before. The higher weight loss of the impeller is due to the worn thrust washer at the beginning of the test (2 g per stage). Subtracting the thrust washer weight loss, the pure impeller weight loss is also linear with time.

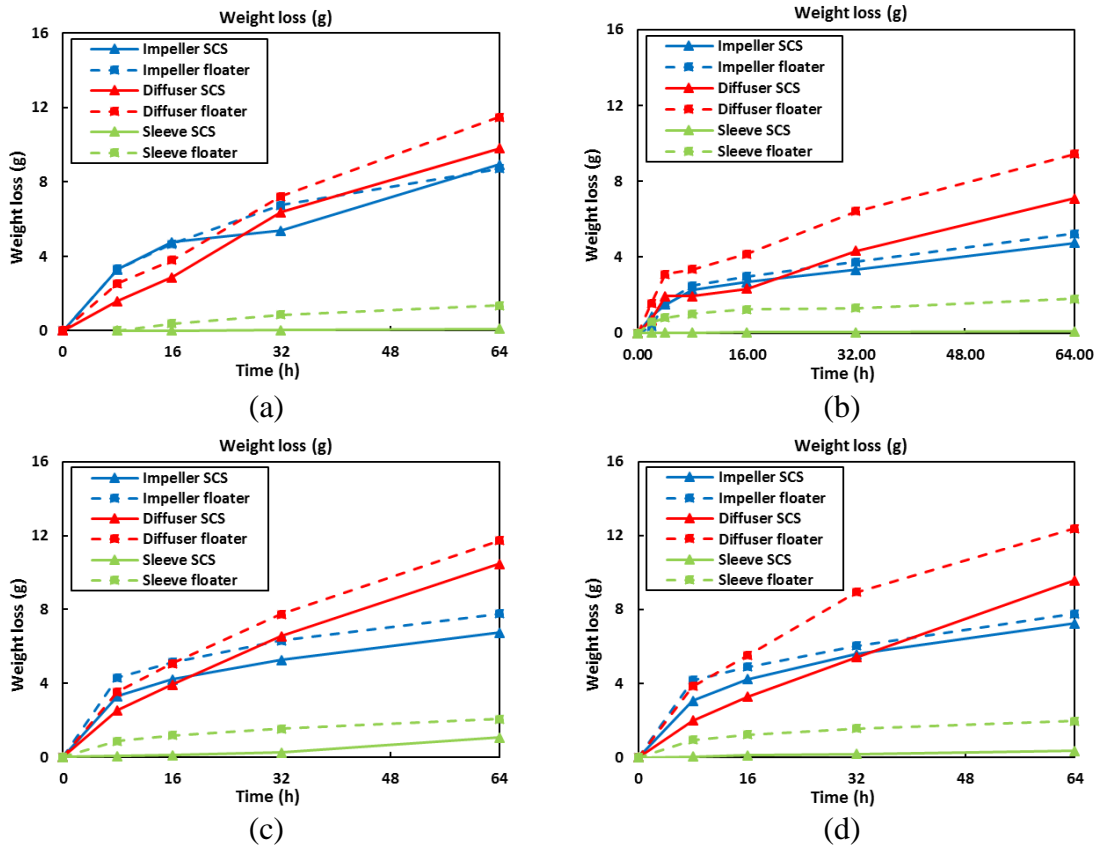


Figure 2.19 Average weight loss of SCS stages and floater stages for four cases, (a) Case 1: water-sand, $Q_L = 3100$ bpd, $N = 3600$ rpm, (b) Case 2: water-sand, $Q_L = 3100$ bpd, $N = 2400$ rpm, (c) Case 3: water-air-sand, $Q_L = 3100$ bpd, $N = 3600$ rpm, $GVF = 15\%$ (d) Case 4: water-air-sand, $Q_L = 3100$ bpd, $N = 3600$ rpm, $GVF = 7.5\%$

2.3.2 Stage vibration

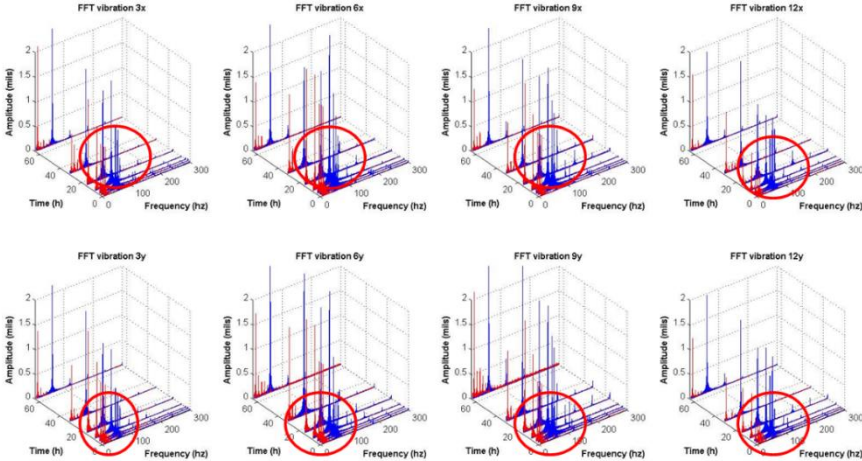
2.3.2.1 Stages vibration

The vibration signals of the four tested cases are shown in Figure 2.20. Fast Fourier Transform (FFT) was used to process the vibration signals and reduce the noises (Chen et al, 2018). The peak of an FFT curve is the stage vibration amplitudes (mils). It should be noted that the thrust chamber seals were severely damaged after Case 1 due to misalignment between motor, thrust chamber, and pump. Then, we replaced the thrust chamber and re-aligned the pump system. Therefore, the vibration of Pump 1 in Figure 2.20 (a) is slightly higher than that of Pumps 2, 3, and 4.

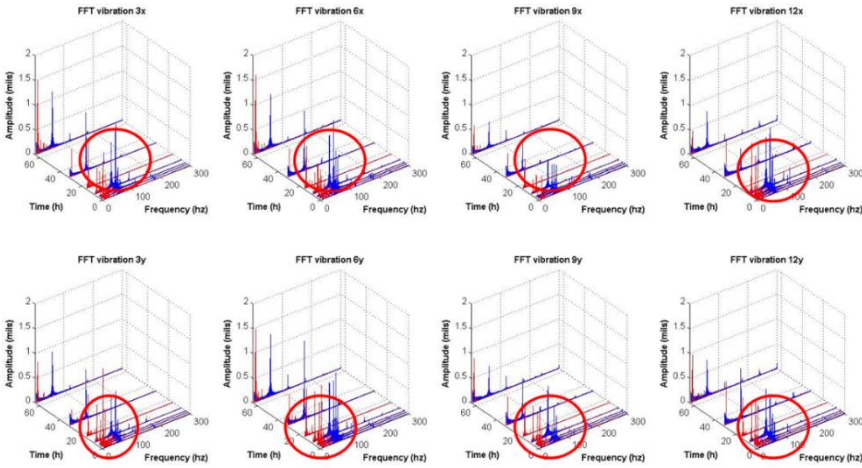
Although wear measurements of stages are similar, the vibration signals are different. The vibration amplitudes of stages 6 and 9 are slightly higher than that of stages 3 and 12 since the pump inlet and outlet were locked to the pump skid, which makes them stiffer. On the other hand, the stage type effect does not have an obvious effect since stages 3 and 9 are general floater stages and stages 6 and 12 are SCS stages. The vibration signal shows different results compared to Morrison's study, where the subharmonic of the vibration signal increased and became dominant during the test (Morrison et al., 2015). In this study, the primary vibration is always at the pump speed (60 Hz) and the subharmonic vibration is not distinguishable, which again indicates that the carbide sleeves help sustain the pump rotation.

The increased stage vibration is mainly caused by the damage on stage seal clearance. The vibration of stages increases rapidly at the beginning and becomes flat after a 16-hour test. Firstly, stage vibration was affected by all clearance geometry together. Later on, only the SCS inter-stage helped maintain the rotation since it was not damaged

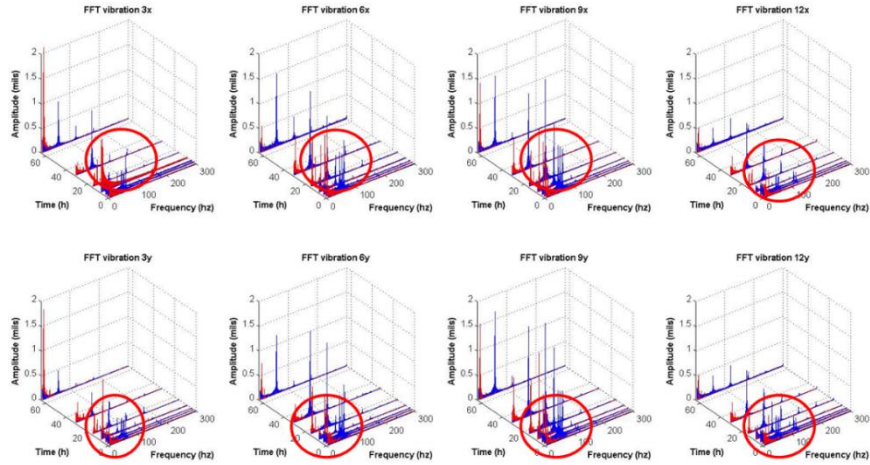
during the test. Since the hard Tungsten carbide material performed very well under the sandy conditions and almost kept its geometry, the stage vibration stopped increasing. As a result, the load on particles decreased due to expanded clearances, which could reduce the abrasion damage. At some point, the abrasive wear in the seal clearance would switch to erosive wear when the clearance was large enough. Therefore, the interval-installed SCS stages help sustain the stability of high-speed rotation and protect both SCS and general floater stages.



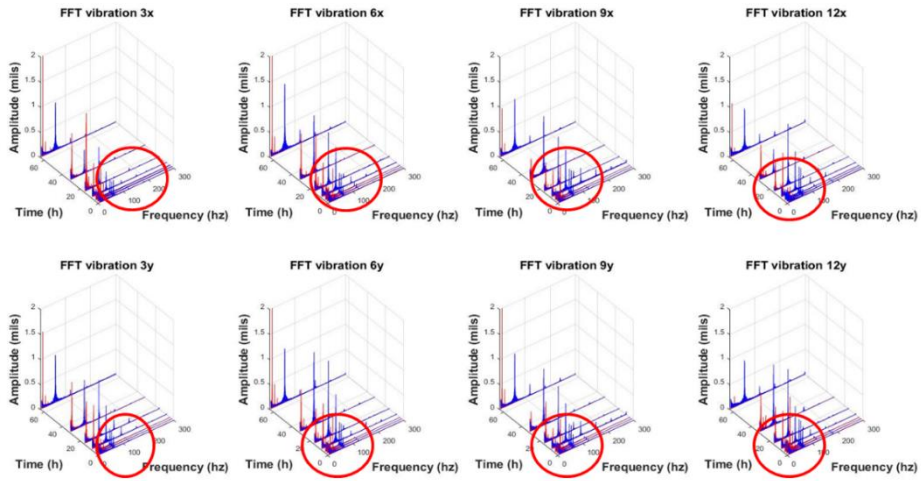
(a)



(b)



(c)



(d)

Figure 2.20 FFT of vibration in vertical and horizontal direction, (a) Case 1: water-sand, $Q_L = 3100$ bpd, $N = 3600$ rpm, (b) Case 2: water-sand, $Q_L = 3100$ bpd, $N = 2400$ rpm, (c) Case 3: water-air-sand, $Q_L = 3100$ bpd, $N = 3600$ rpm, $GVF = 15\%$ (d) Case 4: water-air-sand, $Q_L = 3100$ bpd, $N = 3600$ rpm, $GVF = 7.5\%$

2.3.2.2 Stages orbit

Similar as the vibration data, orbits of stages 3, 6, 9 and 12 increased gradually at the first 16-hour slurry test as shown in Figure 2.21. In addition, the original orbits had an irregular shape with sharp edges, which became round circles later. It is presumable that

extruded points on the original sealing rings and sleeves were smoothed after a few hours of testing. The results are different from Morrison's tests, in which the orbit keeps increasing. Our vibration and orbit data agree well with our pump geometry measurement, which again proves the importance of using carbide sleeves.

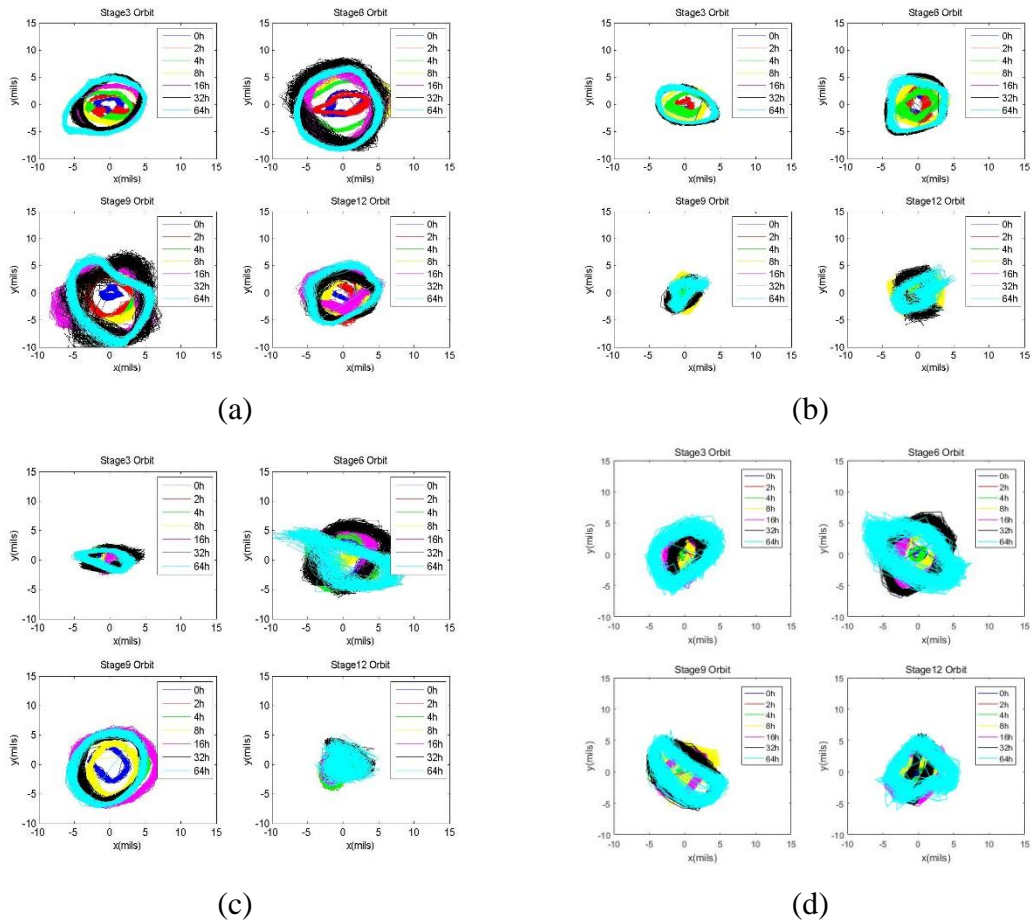


Figure 2.21 Impeller orbit, (a) Case 1: water-sand, $Q_L = 3100$ bpd, $N = 3600$ rpm, (b) Case 2: water-sand, $Q_L = 3100$ bpd, $N = 2400$ rpm, (c) Case 3: water-air-sand, $Q_L = 3100$ bpd, $N = 3600$ rpm, $GVF = 15\%$ (d) Case 4: water-air-sand, $Q_L = 3100$ bpd, $N = 3600$ rpm, $GVF = 7.5\%$

2.3.3 Stage photo

2.3.3.1 Erosion and abrasion damage

After 64 hours, obvious erosion (blue circles) and abrasion (red circles) damage in ESP impellers and diffusers are shown in Figure 2.22. The impeller skirt suffered more in the test and the down-thrust washers were completely worn out after 16 hours. Compared to other stages, the abrasion on skirt ring and erosion on blade leading edges are more severe in the first stage as shown in Figure 2.22 (a) and (b). Besides the first stage, the erosion pattern can hardly be identified in the impeller flow channel. On the other hand, a clear erosion pattern can be found on the diffuser outside shroud in Figure 2.22 (c), which indicates a higher erosion rate. Compared to water-sand tests, the shape of the diffuser vanes' leading edge was eroded severely when gas presents in Figure 2.22 (d).

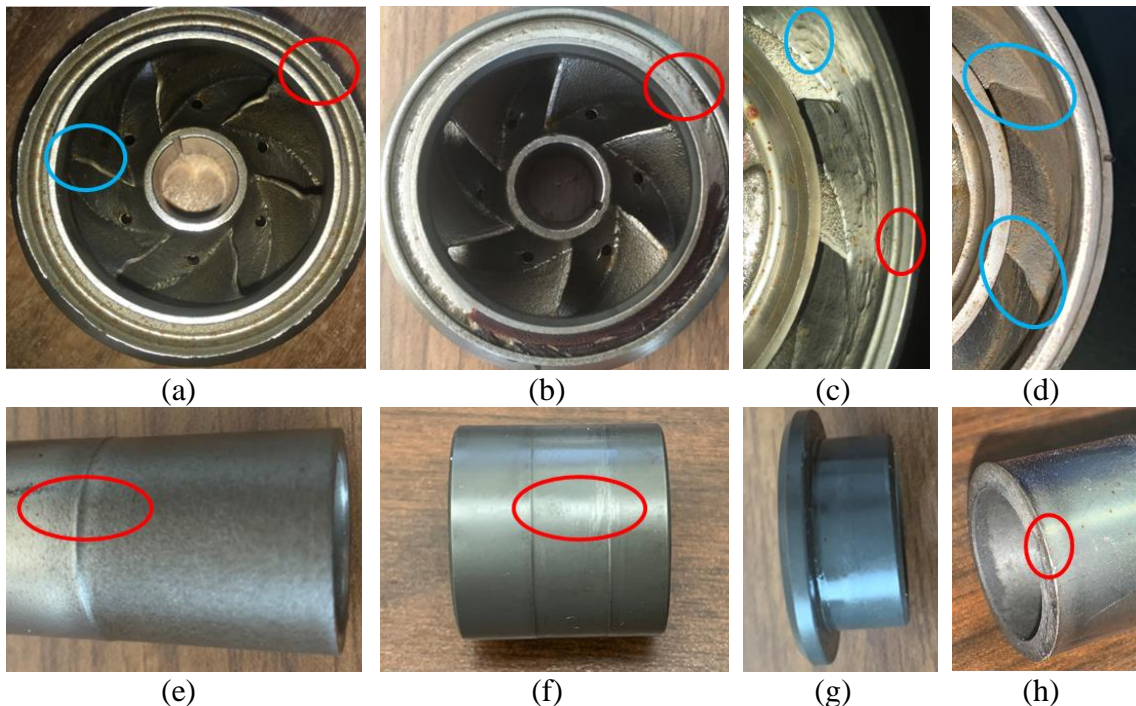


Figure 2.22 Wear on MTESP, (a) 64 hours 1st impeller of Case 1, (b) 64 hours 2nd impeller of Case 1, (c) 64 hours diffuser of Case 1, (d) 64 hours diffuser of Case 3, (e) 64 hours steel sleeve of Case 1, (f) 64 hours straight carbide sleeve of Case 1, (g) 64 hours flanged carbide sleeve of Case 1, (h) 64 hours steel sleeve above the flange carbide sleeve of Case 4

As shown in Figure 2.22 (e), (f), and (g), steel straight sleeves were severely worn out during the test, while no obvious abrasion pattern can be observed on carbide flanged

sleeves. Although the same Tungsten material is used, abrasion can still be recognized on carbide straight sleeves used in the last stage, bottom bearings, and top bearings. It is presumable that the flanged sleeves help prevent particles from passing through inter-stage clearances. However, the steel sleeves used above the carbide sleeves will be slowly deformed and worn by carbide sleeves in Figure 2.22 (h). It was stuck to pump shaft tightly, especially in Case 4 (GVF = 7.5%). As the sleeve is shortened and the impeller position is lower due to the down thrust force, more damage should be observed on skirt ring clearances theoretically. However, it was not shown in the measurement of the diffuser skirt bore depth. Therefore, it is convincing that the damage to the steel sleeves by using carbide sleeves will not strongly affect the sand wear on skirt rings.

2.3.3.2 Paint-removal photos

To capture the detailed erosion pattern and detect the most severe erosion location, stages were coated and tested under different flow conditions. A four-hour water test was conducted before the erosion test to check the reliability of the paint as shown in Figure 2.23 (a), (b), (e) and (f). Then, a four-hour slurry test was performed to obtain a clear erosion pattern as presented in Figure 2.23 (c), (d), (g) and (h).

From Figure 2.23 (c), the paint lost on impeller blade edges and impeller inside shroud are more prominent. The slight paint-removal pattern can also be detected on the outside shroud and blade surfaces in Figure 2.23 (d). As shown in Figure 2.23 (g) and (h), the erosion in the diffuser is obviously located on the outside shroud and the pressure side of vanes. More paint is eroded in the diffuser throat region compared to the inlet.

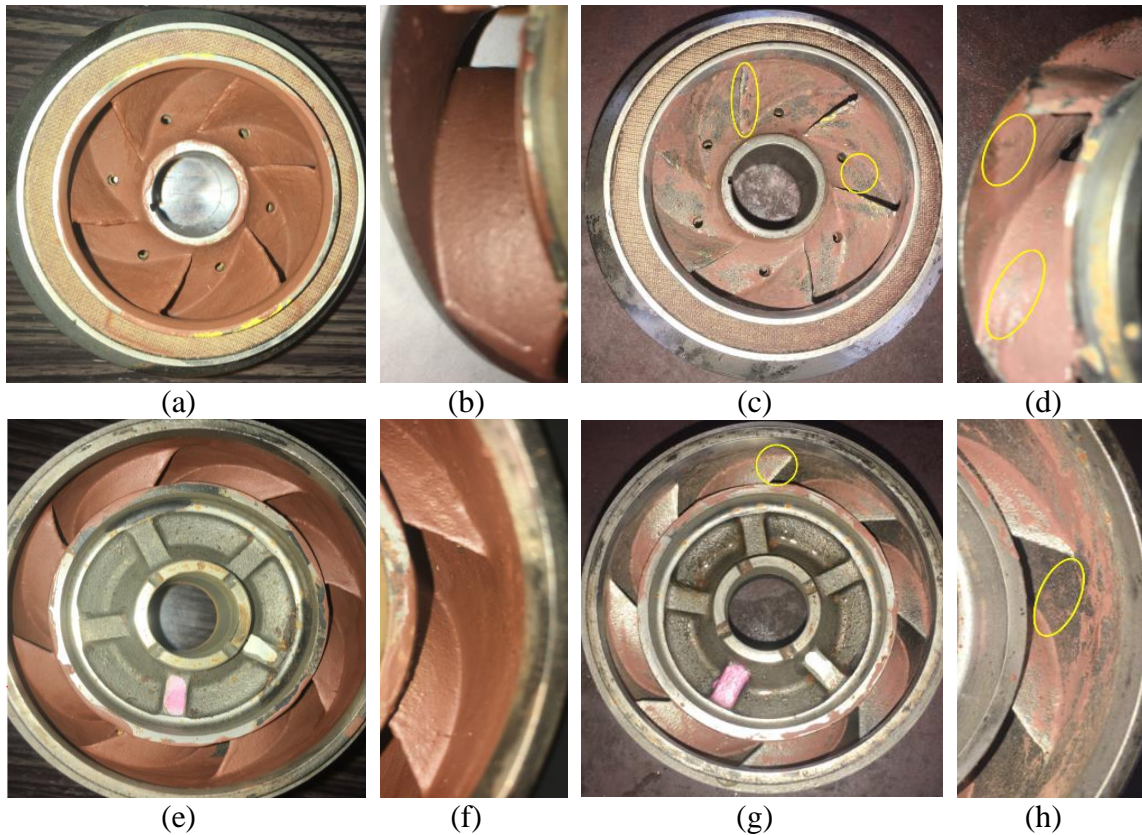


Figure 2.23 Paint-removal photo of Case 2, (a) impeller-4 hours water, (b) impeller outlet-4 hours water (c) impeller-4 hours slurry, (d) impeller inlet-4 hours slurry, (e) diffuser-4 hours water, (f) diffuser inlet-4 hours water, (g) diffuser 4-hours slurry, (h) diffuser inlet-4 hours slurry

The liquid flow rate of 3100 bpd is used for all four cases. By keeping the liquid flow rate the same and decreasing the rotation speed, more particles will hit the impeller inside shroud and less will hit the outside shroud due to the decrease of the centrifugal force. As a result, more erosion damage can be observed on the impeller inside shroud surface as shown in Figure 2.24 (b), while that on the outside shroud surface is higher in Figure 2.24 (a).

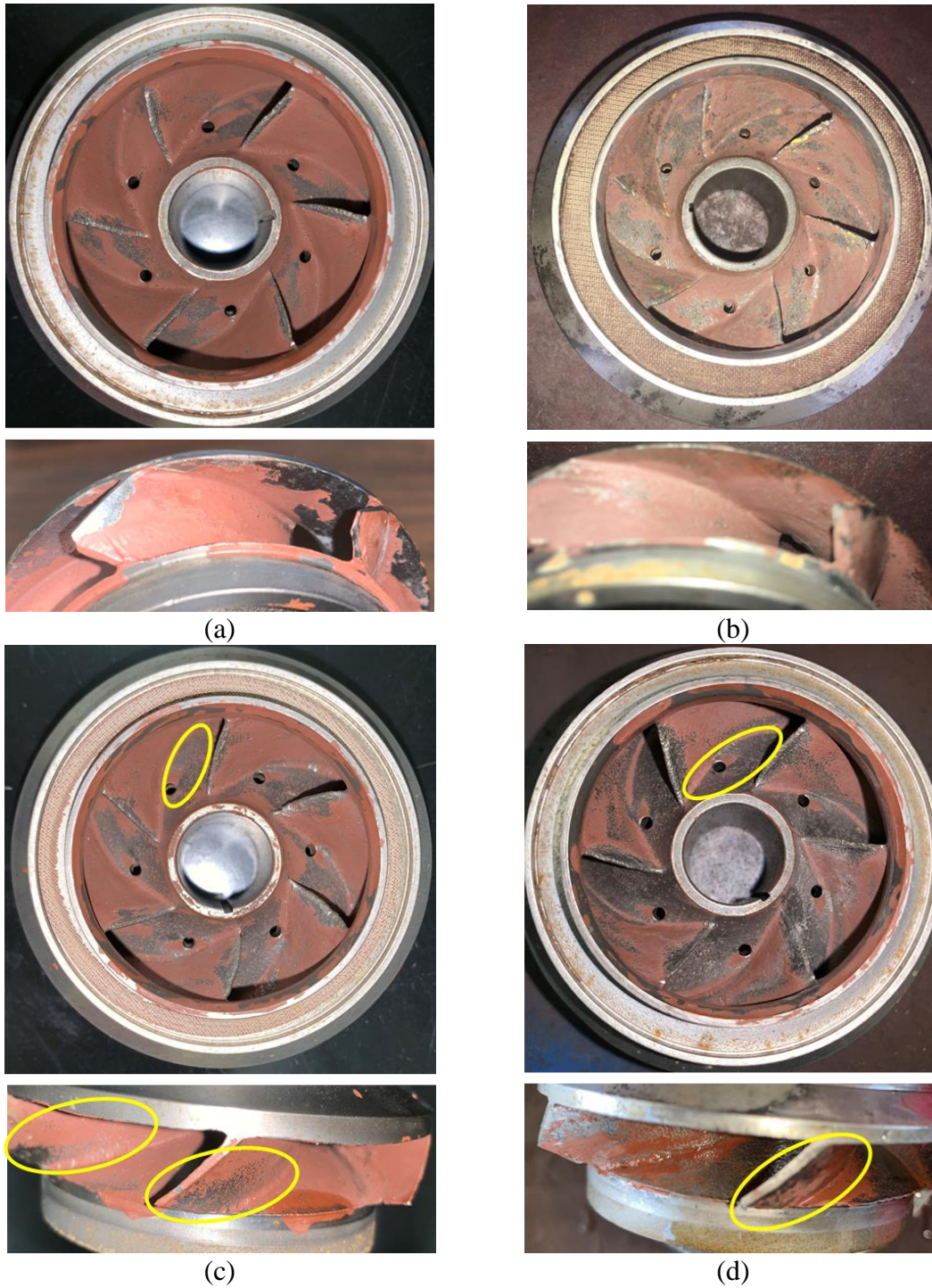
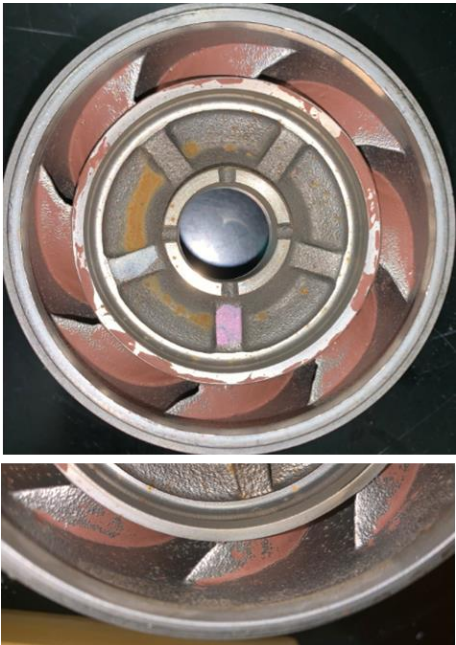


Figure 2.24 Impeller paint-removal photos of four pumps, (a) Case 1: water-sand, $Q_L = 3100$ bpd, $N = 3600$ rpm, (b) Case 2: water-sand, $Q_L = 3100$ bpd, $N = 2400$ rpm, (c) Case 3: water-air-sand, $Q_L = 3100$ bpd, $N = 3600$ rpm, $GVF = 15\%$ (d) Case 4: water-air-sand, $Q_L = 3100$ bpd, $N = 3600$ rpm, $GVF = 7.5\%$

If big gas bubbles present, they will be trapped in the impeller inlet area as shown in Figure 3.21, which will cause more turbulence and a sharp increase of liquid in-situ velocity. Since particles are commonly believed to flow with the continuous liquid phase, the particle impact velocity and impact angle will increase with more gas. Therefore, the erosion damage on the impeller inside shroud surface of Pumps 3 and 4 are more obvious. More details can be found in the CFD simulation section.

The erosion damage in the diffuser is similar for four pumps. The diffuser vane seems to suffer more damage in Pump 2 than Pump 1. This is also due to a lower centrifugal force. More particles impact diffuser outside shroud of Pump 1 due to a higher centrifugal force. The blade suffers more damage in Pumps 3 and 4 than Pump 1. This is mainly due to higher turbulence and a higher liquid in-situ velocity.



(a)



(b)

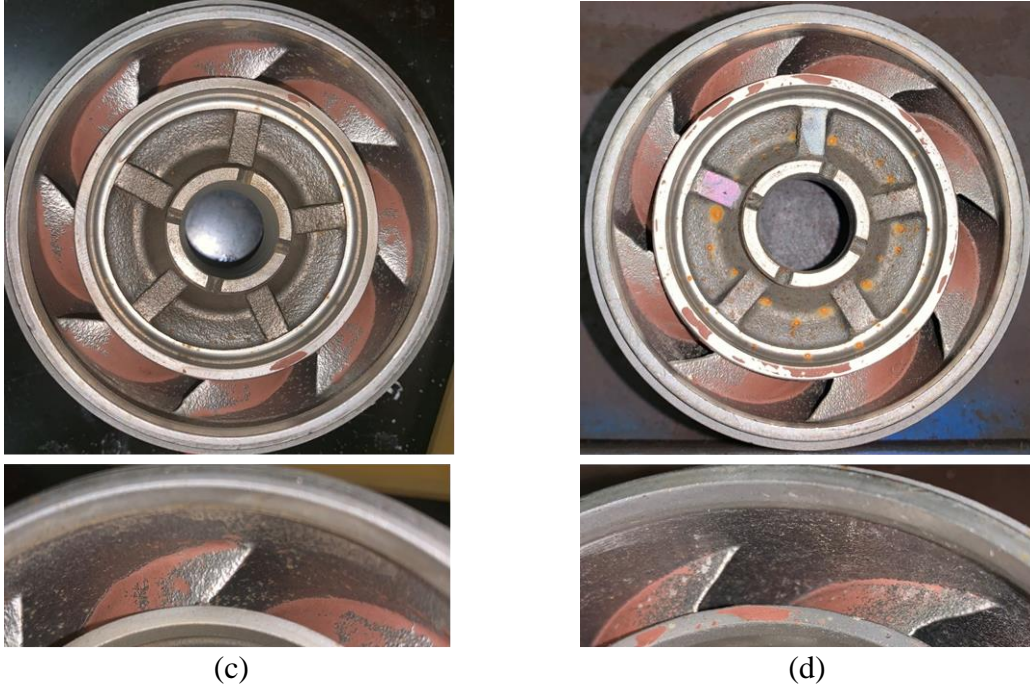


Figure 2.25 Diffuser paint-removal photos of four pumps, (a) Case 1: water-sand, $Q_L = 3100$ bpd, $N = 3600$ rpm, (b) Case 2: water-sand, $Q_L = 3100$ bpd, $N = 2400$ rpm, (c) Case 3: water-air-sand, $Q_L = 3100$ bpd, $N = 3600$ rpm, $GVF = 15\%$ (d) Case 4: water-air-sand, $Q_L = 3100$ bpd, $N = 3600$ rpm, $GVF = 7.5\%$

2.3.4 Pump performance degradation

2.3.4.1 Water curve

No obvious differences can be found in four recorded stages as shown in Figure 2.27 and Appendix B. Therefore, only averaged head, power and efficiency curves are shown in Figure 2.26. As can be seen, an obvious decrease is shown on both head and efficiency curves, while the power consumption curves are almost identical. The unobvious change of power consumption curves could be due to higher relative uncertainty of torque measurements as shown in Appendix C.

The obvious decrease in both the stage head increment and pump efficiency in Figure 2.26 is caused by more leakage through the secondary flow region. All types of head

losses increase with the increase of the real in-situ flow rate. The leakage itself also generates more turbulence in the turning area between impeller and diffuser and results in extra leakage head loss. Pump boosting capacity deteriorates more at low flow rate due to more leakage generated by higher pressure increment.

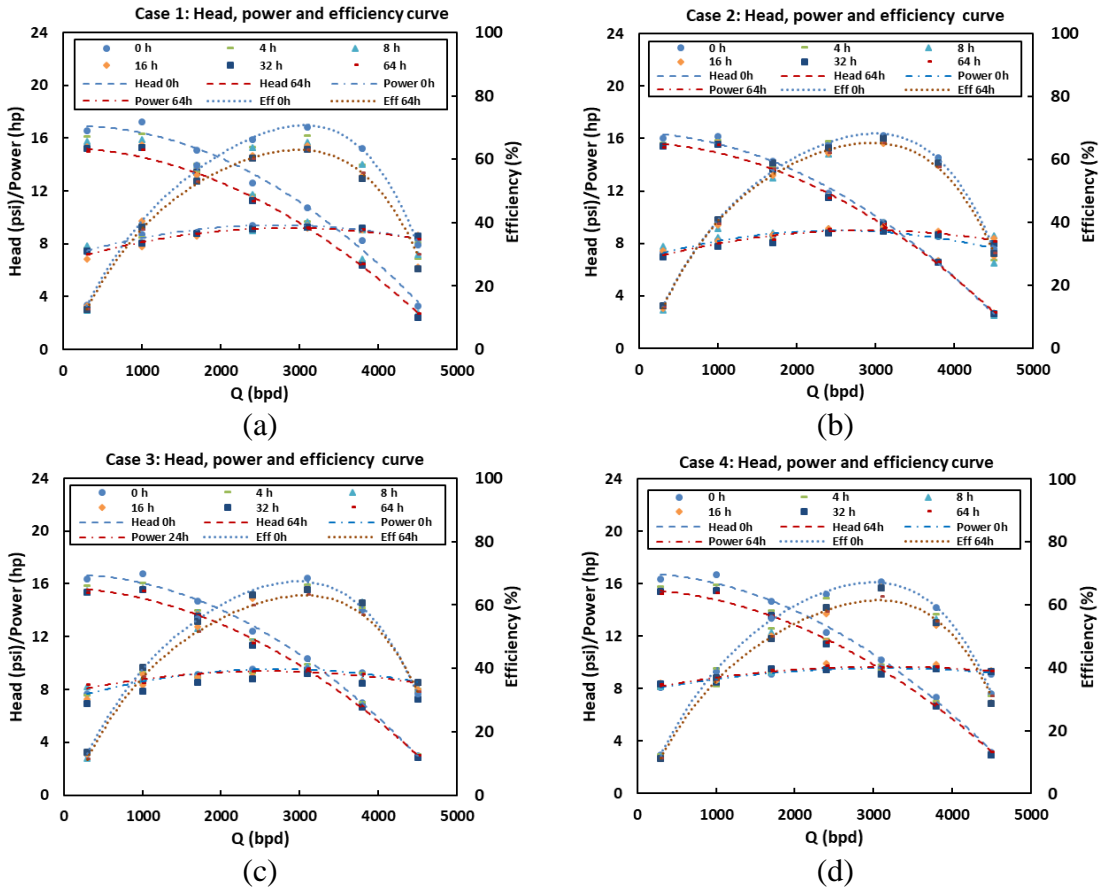


Figure 2.26 Pump performance curves in the 64-hour test, (a) Case 1: water-sand, $Q_L = 3100$ bpd, $N = 3600$ rpm, (b) Case 2: water-sand, $Q_L = 3100$ bpd, $N = 2400$ rpm, (c) Case 3: water-air-sand, $Q_L = 3100$ bpd, $N = 3600$ rpm, $GVF = 15\%$ (d) Case 4: water-air-sand, $Q_L = 3100$ bpd, $N = 3600$ rpm, $GVF = 7.5\%$

As shown in Figure 2.27, the head deteriorated ratios after 64 hours for four recorded stages are similar. Besides the high flow rate region that is above the operation range (2480–3720 bpd), the head loss for most flowrates are around 10%. The head decrease of Pump 2 is a little lower, which might be caused by lower erosion damage

according to the weight loss measurement. In Figure 2.27, red (Stage 3) and purple (Stage 9) columns are floater stages, while green (Stage 6) and blue (Stage 12) are SCS stages.

There is no distinguishable difference between the two types of stages.

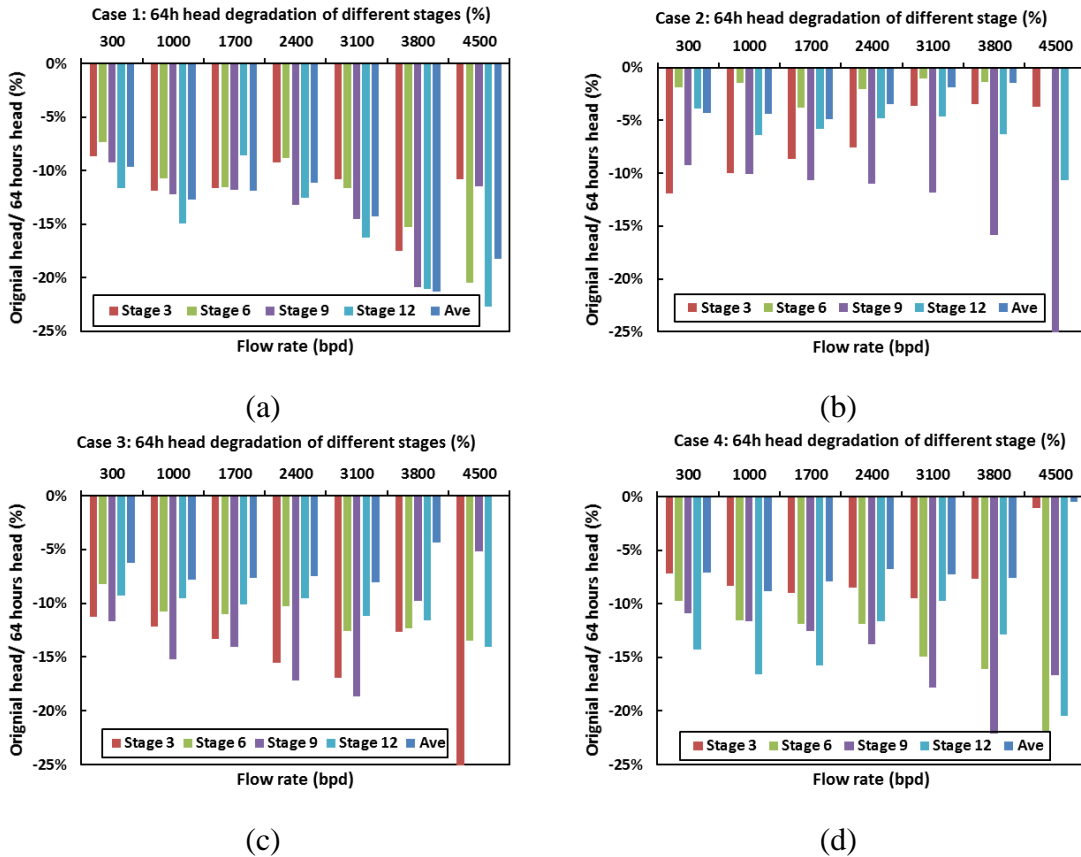


Figure 2.27 Head decrease of four recorded stages after 64 hours at different flow rate, (a) Case 1: water-sand, $Q_L = 3100$ bpd, $N = 3600$ rpm, (b) Case 2: water-sand, $Q_L = 3100$ bpd, $N = 2400$ rpm, (c) Case 3: water-air-sand, $Q_L = 3100$ bpd, $N = 3600$ rpm, $GVF = 15\%$ (d) Case 4: water-air-sand, $Q_L = 3100$ bpd, $N = 3600$ rpm, $GVF = 7.5\%$

Figure 2.28 shows the average head, power and efficiency loss after 64 hours of four cases. As can be seen, the power loss can be ignored compared to head and efficiency loss. As a result, the decrease in efficiency is mainly originated from the deteriorated head. Overall, the head and efficiency decrease ratios for most flowrates decrease about 5-10% for all cases.

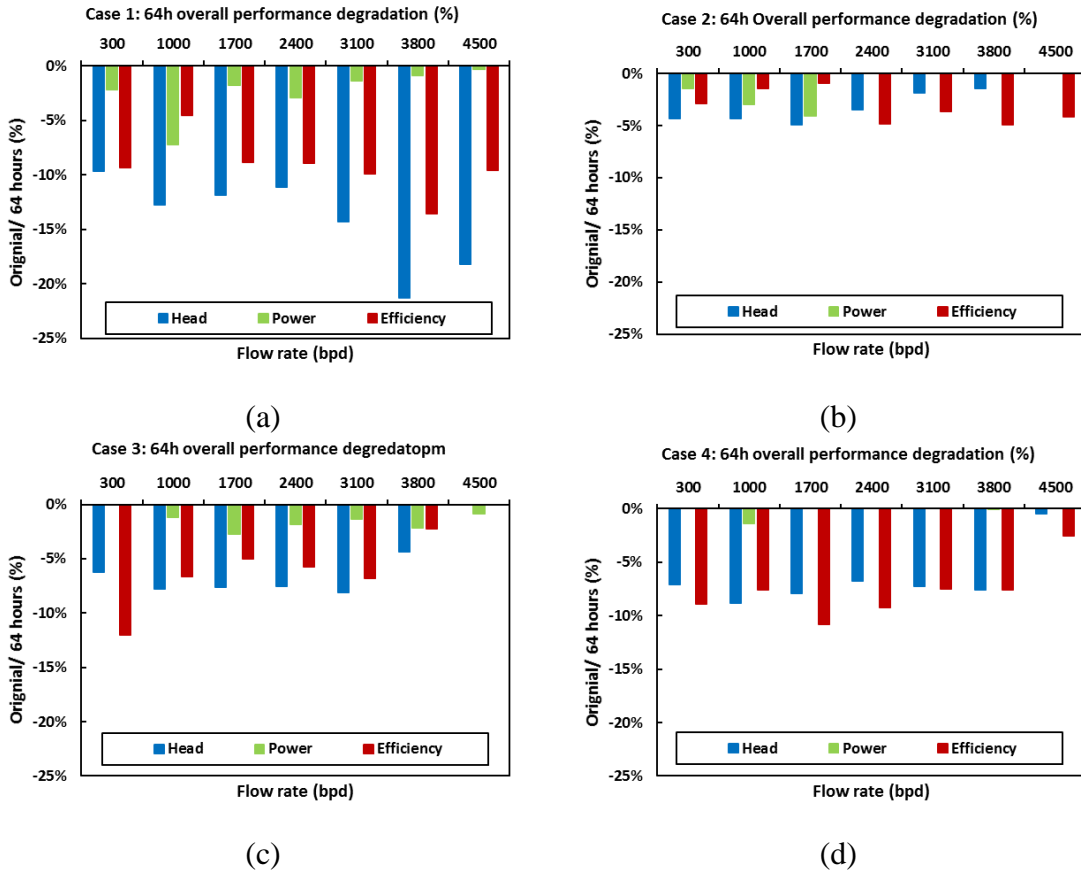
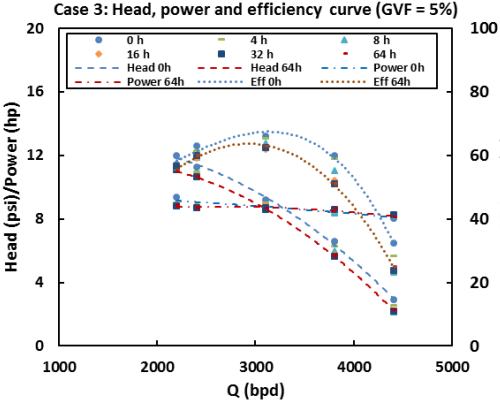


Figure 2.28 Average head, power, and efficiency decrease, (a) Case 1: water-sand, $Q_L = 3100$ bpd, $N = 3600$ rpm, (b) Case 2: water-sand, $Q_L = 3100$ bpd, $N = 2400$ rpm, (c) Case 3: water-air-sand, $Q_L = 3100$ bpd, $N = 3600$ rpm, $GVF = 15\%$ (d) Case 4: water-air-sand, $Q_L = 3100$ bpd, $N = 3600$ rpm, $GVF = 7.5\%$

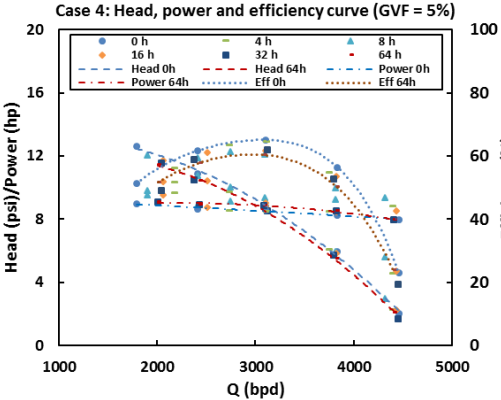
2.3.4.2 Air-water curve

In addition to the default water curve, gas-liquid pump performance curves of 5% and 10% GVF and pump performance vs. GVF curve at $Q_L = 3100$ bpd were obtained after each time-period test of the Cases 3 and 4. Comparing to the original non-eroded pump curve, performance curves of 10% GVF decrease more than that of 5% GVF , while the change of the power consumption is not remarkable. An interesting result is shown in Figure 2.29 (e) and (f). Comparing to the original pump curve, the pump head at $Q_L = 3100$ bpd after 64-hour tests deteriorated less with more gas when GVF is less than 5%. It is

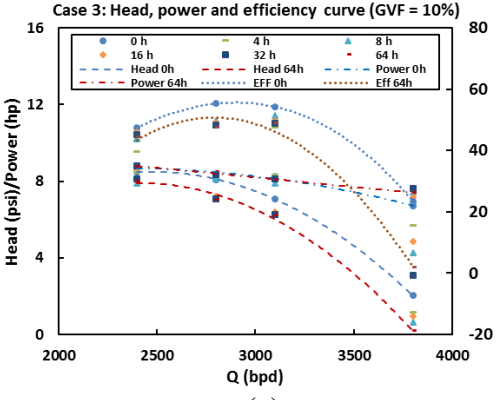
presumable that increasing inlet GVF helps resist the leakage under dispersed-bubble and bubble flow condition. At the same time, the downward axial thrust force is reduced with more gas. Further increasing the gas fraction, the impeller position can move upward and more leakage can flow through skirt ring clearances especially when down thrust washers are worn out. As a result, comparing to the original pump head, the head of the eroded pump at $Q_L = 3100$ bpd deteriorated more with more gas when GVF is higher than 5%.



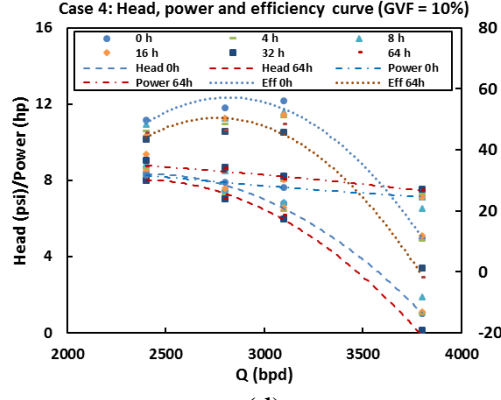
(a)



(b)



(c)



(d)

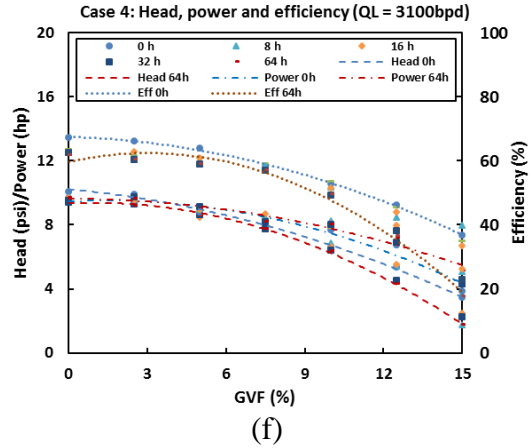
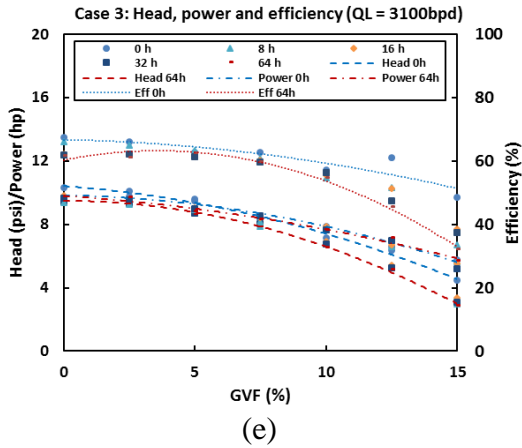


Figure 2.29 Gas-liquid performance curves, (a) Pump performance at $GVF = 5\%$ (Case 3), (b) Pump performance at $GVF = 5\%$ (Case 4), (c) Pump performance at $GVF = 10\%$ (Case 3), (d) Pump performance at $GVF = 10\%$ (Case 4), (e) Pump performance vs. GVF at $Q_L = 3100$ bpd (Case 3), (f) Pump performance vs. GVF at $Q_L = 3100$ bpd (Case 4)

CHAPTER 3

THREE-DIMENSIONAL NUMERICAL SIMULATION

In this section, the erosion affecting factors were numerically studied using commercial Computational Fluid Dynamics (CFD) software ANSYS Fluent. For each pump, the flow domain of two stages was built and the high-quality structured meshes, comprising around 1.2 to 1.8 million hexahedral grids per stage, were generated. Six erosion models, including Ahlert et al. (1994), Haugen et al. (1995), Oka et al. (2005), Zhang et al. (2007), Mansouri (2014) and DNV (2015), were implemented into CFD simulations to obtain the most accurate one in predicting the ESP erosion rates. By using the selected erosion model, pump type effects and sand characteristic effect are analyzed.

3.1 Geometry and Mesh

MTESP is a mixed type 4-inch OD multi-stage centrifugal pump with a specific speed of $N_s = 1200$. There are 6 blades in the impeller and 8 vanes in the diffuser. The pump is designed to resist solid particle wear using abrasion-resistant material within the flow rate range of 1200-4000 bpd and the rotational speed at 60 Hz. The best efficiency point (BEP) is $Q_L = 3100$ bpd, $N = 3600$ rpm. TE2700 is a radial type pump that has 5 impeller blades and 9 diffuser vanes. The BEP is $Q_L = 3000$ bpd, $N = 3600$ rpm rotational speed. DN1750 is another mixed type ESP with 6 blades and 9 vanes in the impeller and diffuser, respectively. The BEP is $Q_L = 1800$ bpd and $N = 3600$ rpm. A sand mass concentration of 1wt% is used in all simulations. Detailed input parameters can be found

in

Table 3.1.

Table 3.1: Input parameters of three ESPs

Pump	Q_{BEP} (m^3/s)	Head (m)	Blade	Vane	OD (m)	N	Pump type
MTESP	5.7e-3	7.38	6	8	0.1016	2000	Mixed

TE2700	5.5e-3	16.17	5	9	0.127	1100	Radial
DN1750	3.3e-3	5.62	6	8	0.1016	1900	Mixed

The stage mesh grid number was gradually increased until the simulated pressure increment becomes stable and the y^+ meets the requirement. Besides, the near-wall grid layers were refined and mesh quality is above 0.3. Totally, a mesh number around 1.5 million per stage was generated by ICEM in Figure 3.1 (c) and (b). More details of grid number effect can be found in Section 3.4.1.

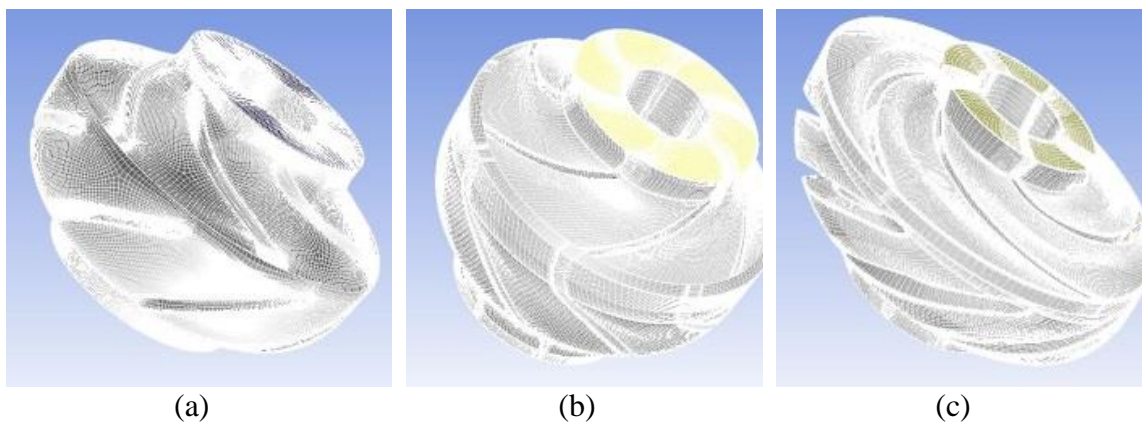


Figure 3.1 Mesh (a) DN1750, (b) MTESP, (c) TE2700

3.2 Numerical Schemes and Boundary Conditions

In this study, the boundary conditions of parametric studies were set to be the same as testing conditions according to the tested cases. Sand particle properties were set according to average sand properties. The simulations applied an individual frame of reference to each component in the computational domains. By doing this, the relative orientation can be kept at the interface. This method requires the least amount of computational effort compared to other interface models (Zhu, 2017). The general connection interface model was employed in a pair of impeller and diffuser interfaces, which was to apply a frame change and connect non-conformal grids. In the cell zone, the

properties of diffuser cells were kept as the default, while the frame motion was selected for impeller cells. The rotation-axis direction was set to the global Z-axis and the rotational velocity was at 3600 rpm. The mesh interfaces were created at the connections of rotating and stationary parts in order to apply the moving reference of the frame (MRF) algorithm.

Sand particles with a density of 2637 kg/m^3 were used in DPM simulations. The Rosin-Rambler method with a mean diameter of $1\text{e-}4 \text{ m}$ was used. The Discrete Random Walk Model and Random Eddy Lifetime Model were enabled to analyze the random particle distributions. Parametric studies on particle diameters and densities were simulated with the MTESP pump. The simplec and coupled methods were selected for different cases to achieve convergence criteria.

With the same boundary conditions and sand properties, the particle trajectories are similar. Different erosion rates and patterns are originated by erosion models. From empirical erosion correlation, the experimentally determined parameters K and n are constant for the selected particles and target surface material. Assuming the target surface is carbon steel and the solid particle is sharp, K and n values for six models, shown in Table 3.1, are different by one order of magnitude.

Table 3.2: Empirical constants in six models

Model	Ahlert et al. (1994)	Haugen et al. (1995)	Oka et al. (2005)	Zhang et al. (2007)	Mansouri (2014)	DNV (2015)
$C(dP)$	7.3e-8	2e-9	6.23e-9	1.02e-8	2.17e-8	2e-9
n	1.73	2.6	2.35	2.41	2.41	2.6

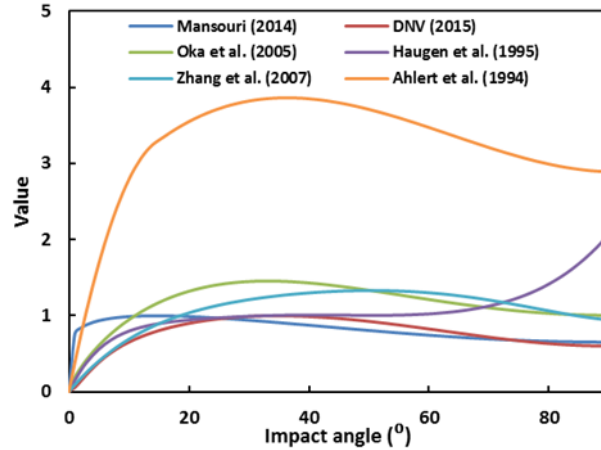


Figure 3.2 Impact angle function of six erosion models

The trend of impact angle function $F(\theta)$ is shown in Figure 3.2. As can be seen, the impact angle functions of six erosion models have comparably similar trends and values. However, the values given by Ahlert et al. (1994) erosion equations are three times higher than that computed by other models. Therefore, it is possible to assume the erosion patterns, regarding the magnitude, generated by six erosion models are similar in ESPs.

3.3 Results and Discussions

First, for the MTESP, a three-stage geometry is employed to investigate the inlet and outlet effect. Thereafter, a two-stage pump geometry is applied in CFD simulations to compare the transient and steady state DPM simulations. Erosion pattern, average erosion rate, particle impact velocity and angle (extracted by a UDF) are compared with tested weight loss and paint-removal in this section to study the effect listed in Table 1.8.

3.4.1 Grid number and catalog curve validation

The optimum grid number was obtained by comparing pressure increment and hydraulic efficiency results from 1-stage MTESP. As shown in Figure 3.3 (a), both parameters become stable when the grid number reaches 1.5 million. Therefore, the mesh number of MTESP is 1.863 million per stage as shown in Figure 3.1 (a). Thereafter, DN1750 and TE2700 were meshed in the same way with the quality above 0.3 and near-wall grid refinement. The mesh with a grid number around 1.5 million per stage was generated as shown in Figure 3.1 (a) and (c).

Then, a three-stage geometry of MTESP was created to eliminate the inlet and outlet effects (Shi et al., 2018). The boosting pressure accuracy of each stage was compared with catalog curves in Figure 3.3 (b) and (c). As can be seen, the calculated head deviates from catalog data at the first stage, but the difference disappears at the second stage. In Figure 3.3 (d), the simulated head and efficiency agree well with pump catalog curves. The over-predicted efficiency is caused by under-predicted torque due to ignoring the mechanical loss and leakage flow in the second flow region.

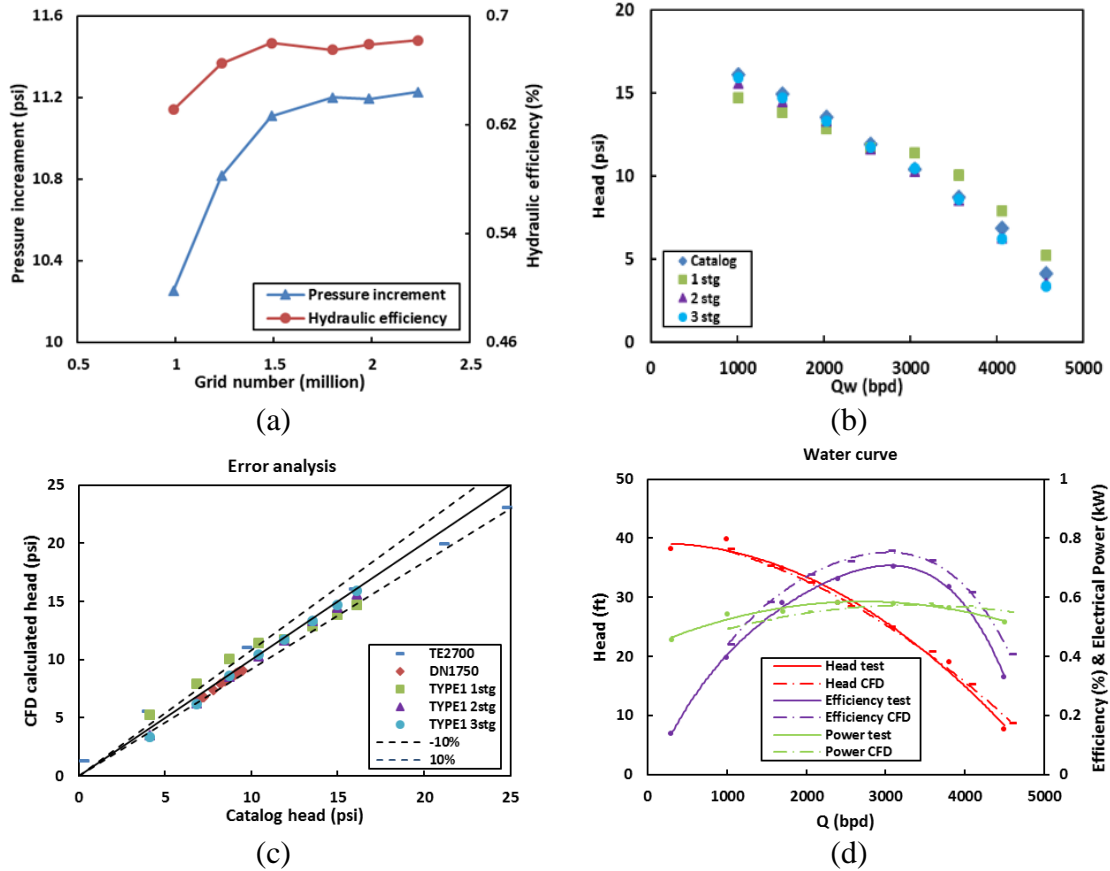


Figure 3.3 Head validation (a) optimum grid number analysis, (b) 3-stages MTESP head increment, (c) head increment error analysis (d) performance comparison between the simulated second stage and the test curve

3.4.2 Stage effect

In CFD simulations of ESP performance, great attention has been paid to the inlet effect. Even in test conditions, the erosion rate of the first stage was different compared to downstream stages (Pirouzpanah, 2014; Basaran, 2017). To eliminate inlet and outlet effects, the extruded inlet pipe section or multi-stage were incorporated in CFD simulations by Shi et al. (2017), Zhu et al. (2017a) and Zhu et al. (2018b). Therefore, the three-stage pump geometry with steady-state and transient erosion simulation of MTESP is conducted in this study.

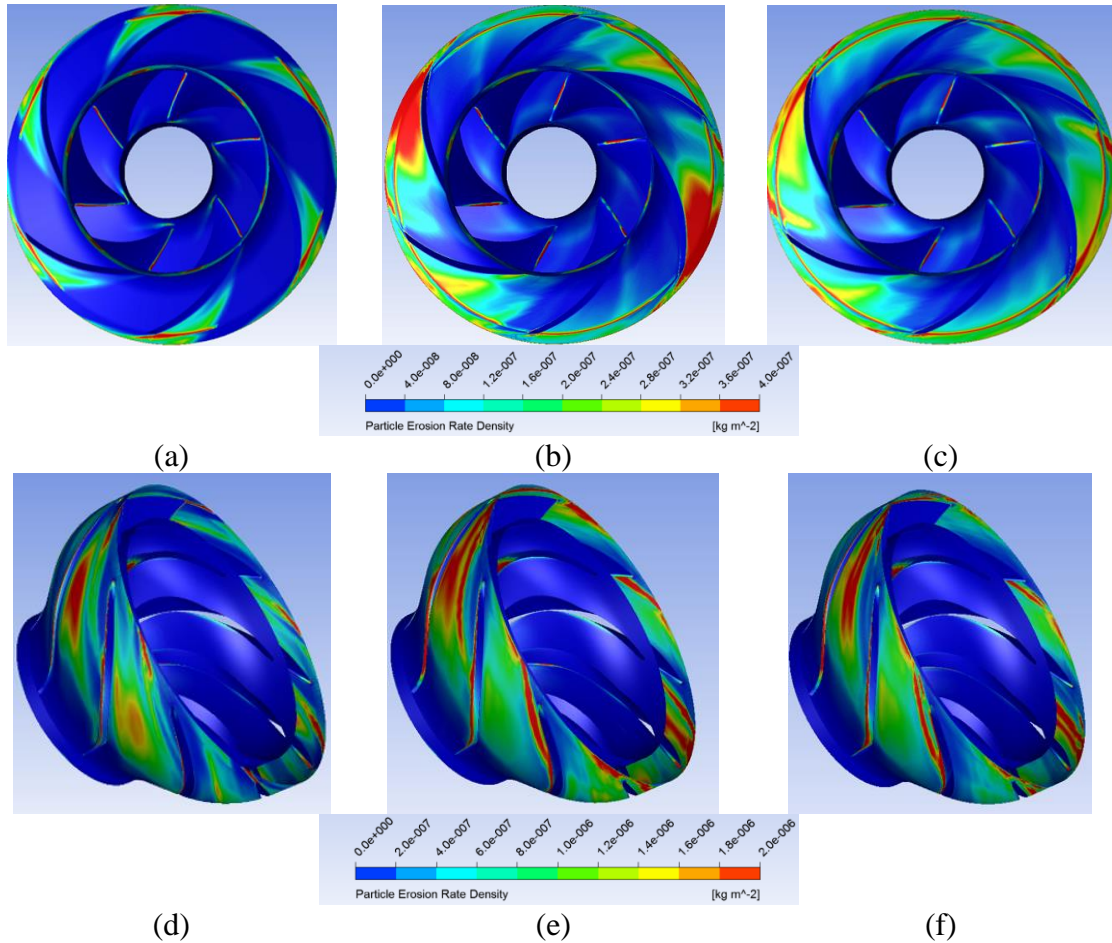


Figure 3.4 MTESP stage erosion contour (a) 1st-stage impeller, (b) 2nd-stage impeller, (c) 3rd-stage impeller, (d) 1st-stage diffuser, (e) 2nd-stage diffuser, (f) 3rd-stage diffuser

As shown in Figure 3.3, the head curve of Stage-1 differs from that of Stage-2 and 3. In addition, the area-weighted average erosion rate of the first stage is almost 50% lower than that of the second and third stages in Figure 3.5. The erosion contour of Stage-1, especially that of the impeller, derive a lot from the downstream two stages in Figure 3.4. Therefore, the inlet effect is more important than the outlet effect since the homogeneous inlet velocity profile and sand particle distribution is unrealistic. The un-concentric erosion pattern of Stage-2 and 3 is mainly caused by using a frozen rotor method. Due to the comparable simulation results at the downstream two stages, a 2-stage geometry was selected in order to save the computation time. Using the same methodology, the 2-stage

computational domains of TE2700 and DN1750 were generated by ICEM and TurboGrid separately.

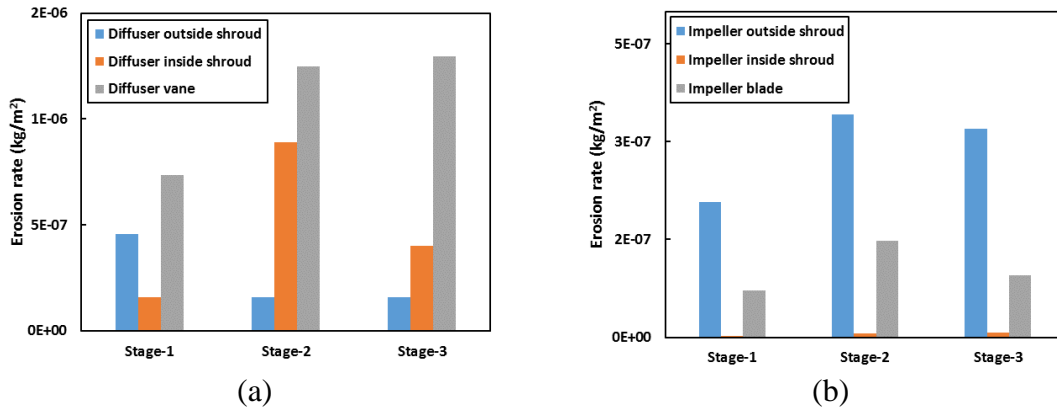
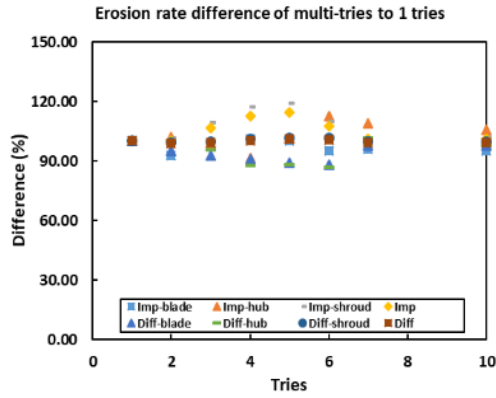


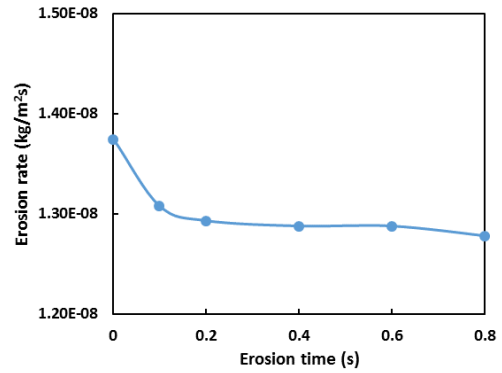
Figure 3.5 3-stage MTESP transient simulation area-weighted average erosion rate (a) impeller, (b) diffuser

3.4.3 Transient simulation and steady-state DRWM simulation

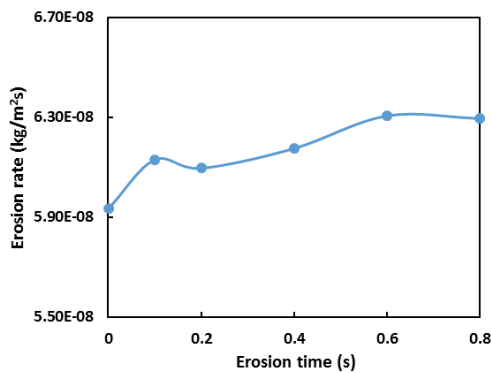
The default DPM simulations only inject one particle per inlet facet. Therefore, the injected particle number may not be enough to capture a proper erosion result. In order to consider the interaction of a particle with discrete stylized fluid phase eddies, the tries of DRWM increased from 1 to 10. As shown in Figure 3.6 (a), increase tries of DRWM don't have an obvious influence on area-weighted average erosion rate on the different wall surface. When tries number is around 5, the erosion rate increases on impeller wall surfaces and decreases on diffuser wall surfaces. However, the differences are within 20%. As shown in Figure 3.7 (a), (b) and (c), after the number of tries increased, erosion contour becomes smoother, but the maximum erosion location doesn't change. In the following studies, the number of tries is set to be 5 to obtain a better erosion contour.



(a)



(b)



(c)

Figure 3.6 Steady-state DRWM and transient simulation (a) steady-state simulation with different DRWM tries number, (b) impeller average erosion rate vs. erosion flow time, (c) diffuser average erosion rate vs. erosion flow time

In the transient simulation, particles are injected at each time step within the erosion flow time (injection end time – start time). To investigate the stable transient erosion flow time, the Oka et al. (2005) erosion equation was incorporated in CFD simulations. The DPM simulation started at 0.2 s when the flow field was fully developed. In order to compare the transient erosion rate (kg/m^2) to the steady-state erosion rate ($\text{kg/m}^2\text{s}$), the erosion rate (kg/m^2) of transient DPM simulation shown in Figure 3.6 to Figure 3.8 is divided by erosion flow time. It should be noted that this calculation procedure may slightly over predict the erosion rate ($\text{kg/m}^2\text{s}$) of transient simulation since slip exists between the

solid and liquid phases. The real erosion flow time should be slightly higher than the simple calculation above. However, the effect will be lower with a longer erosion flow time. The slippage effect can be neglected when the flow time is long enough. Figure 3.6 (b) and (c) **Error! Reference source not found.** show that area-weighted average erosion rates become comparably similar after 0.1 s DPM flow time. Therefore, a total simulation time of 0.5 s with the DPM simulation time between 0.2 s to 0.3 s was used in the transient simulations.

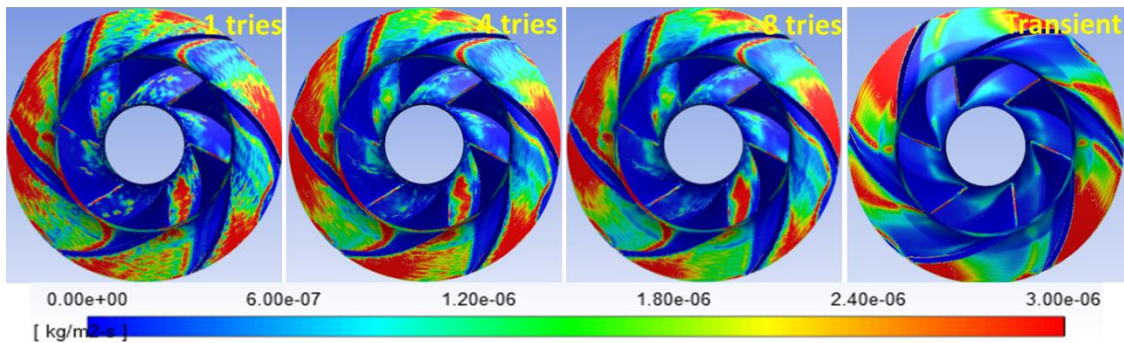


Figure 3.7 MTESP stage erosion contour (a) Steady state DPM impeller DRWM 1 tries, (b) Steady state DPM impeller DRWM 4 tries, (c) Transient DPM impeller DRWM 8 tries, (d) Transient DPM diffuser

The simulated erosion contours were compared in Figure 3.7. As can be seen, both simulation schemes have similar erosion trends, the transient DPM simulation and steady-state DPM with more DRWM tries to result in a more continuous erosion pattern. On the other hand, the area-weighted average erosion rate of impeller and diffuser shown in Figure 3.8 proves that the erosion rate magnitudes of the two simulation schemes are identical. In this paper, the steady state DPM simulation is adopted in the parametric study for the sake of saving computation time, while the transient DPM simulation is incorporated in the comparison between the tested paint-removal pattern and CFD simulated erosion pattern.

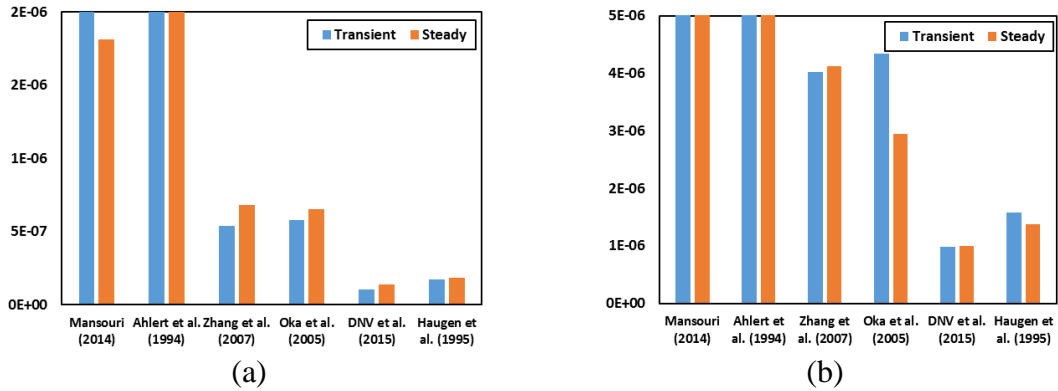


Figure 3.8 Transient and steady state simulated area-weighted average erosion rate, (a) impeller, (b) diffuser

3.4.4 Pump type effect

Since two types of ESPs were simulated in this study, mixed (DN1750 and MTESP) and radial type (TE2700) ESPs, the pump type effect on erosion damage can be studied. For simplicity, the Oka et al. model is incorporated in CFD simulations. The preliminary results are shown in Figure 3.9. Erosion is likely to be observed on blade tips and on the outside shroud in the mixed type ESPs, MTESP and DN1750. In the radial type ESP (TE2700), a higher erosion rate is predicted on the impeller inside the shroud surface in Figure 3.9 (b). The erosion pattern on radial type ESP impeller is analogous to sand and cavitation erosion patterns in other studies (Coutier-Delgosha et al., 2003; Grant and Tabakoff, 1975).

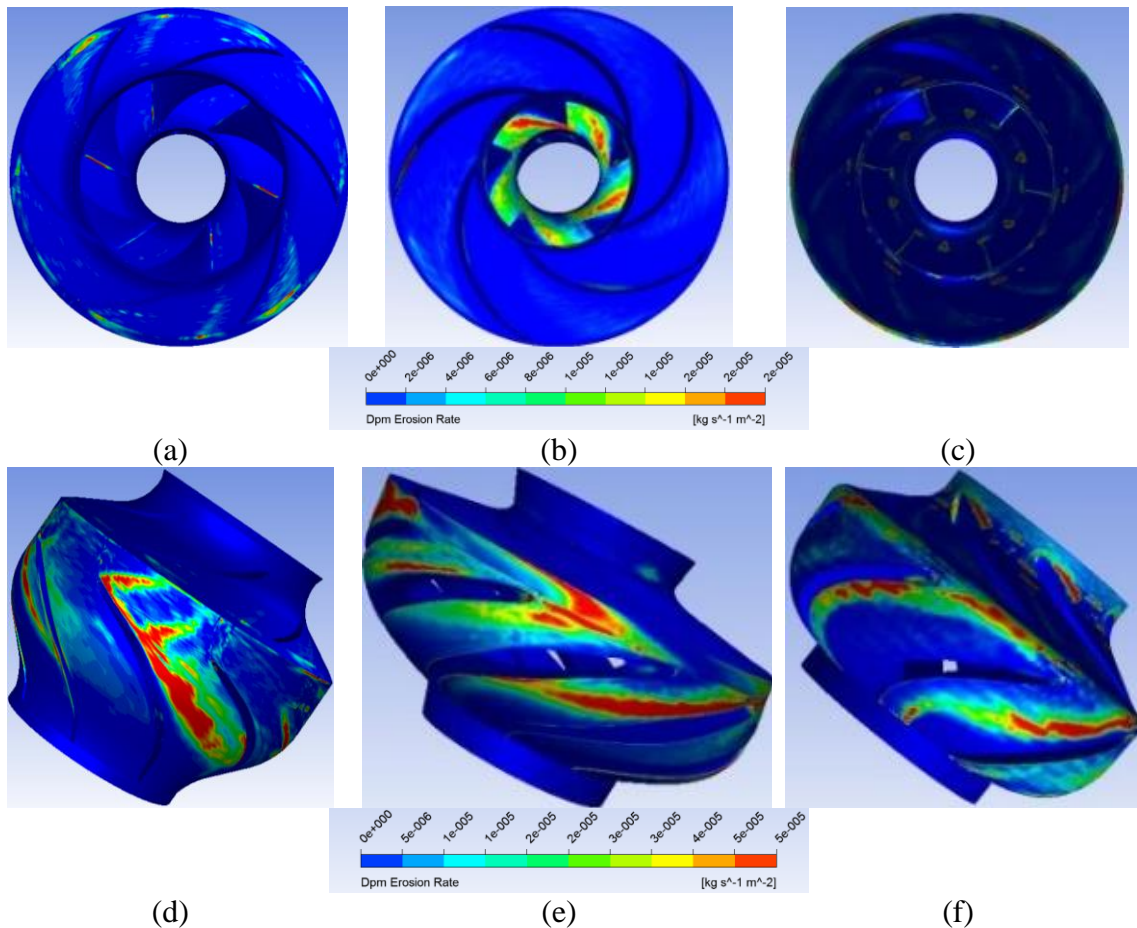


Figure 3.9 Impeller and diffuser erosion contour of different pumps using Oka et al. (2005) model (a) MTESP impeller, (b) TE2700 impeller, (c) DN1750 impeller, (d) MTESP diffuser, (e) TE2700 diffuser, (f) DN1750 diffuser

As mixed type ESPs, DN1750 and MTESP have similar erosion patterns in the impeller. The lower boosting capacity gives lower erosion rates in the DN1750 as shown in Figure 3.10 (c) and (d). On the other hand, Figure 3.9 (a) to (f) illustrate significant differences in erosion patterns and magnitudes between MTESP (mixed) and TE2700 (radial). With close boundary conditions, the erosion is more prominent in TE2700, especially on the inside shroud surface. TE2700 possesses a flatter impeller, which results in a sudden change of flow direction. Therefore, the solid particles are more prone to collide with the impeller inside the shroud surface.

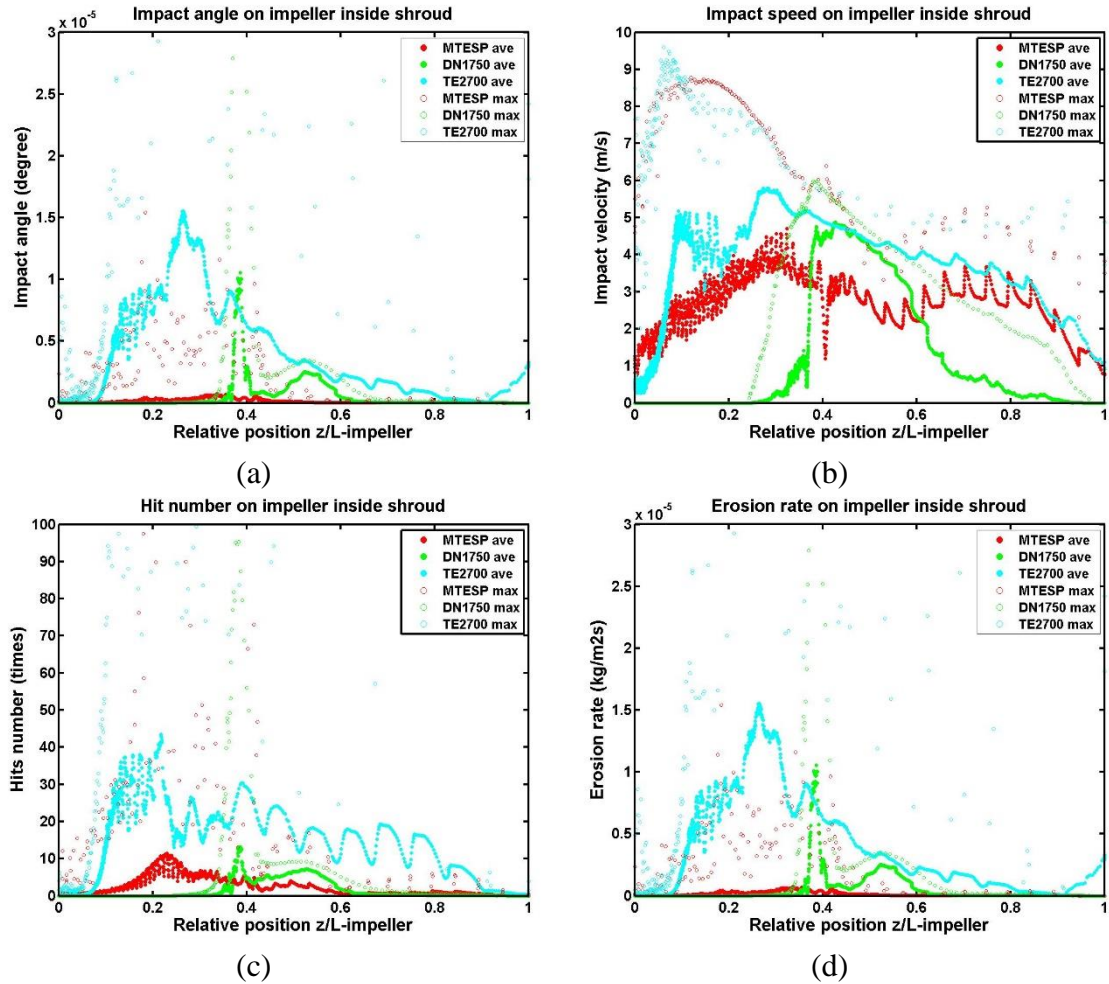


Figure 3.10 Impact information on impeller inside shroud of three pumps (a) impact angle, (b) impact speed, (c) hit times, (d) erosion rate

The relative position in the vertical direction (z -axis) is used in Figure 3.10, where 0 and 1 represent outlet and inlet. Both maximum and moving average impact parameters are calculated within a range of 0.01. In Figure 3.10 (a), the average impact angle varies from 0° to 5° for two mixed-type pumps (MTESP and DN1750) and 0° to 10° for the radial-type pump (TE2700). The maximum impact angle is around 14° for the two mixed-type pumps and 25° for the radial-type pump. Similarly, in Figure 3.10 (b) and (c), the impact velocity and hit times of TE2700 are much higher. As a result, the erosion rate is much higher on TE2700 than others in Figure 3.10.

3.4.5 Particle diameter and density analysis

As discussed above, the solid size and density are the key factors in CFD simulations DPM coupling. The erosion rate increases with the particle size before a more flat and stable relationship is reached, as concluded in erosion tests results of Tilly (1973). Normally, the particle density is closely related to its hardness. However, particle hardness may have no effect on erosion once the particle hardness is several times higher than that of the target surface, whereas the sand density has the dominant effect (Levy and Chik, 1983). With the larger size and higher density, the grains possess more inertia to resist the flow direction changes in ESPs, and higher impact velocities when colliding with the target surfaces. On the contrary, the particle number decreases with the larger size and density, which in turn reduces the wear rate. The sand erosion phenomenon is more complicated for complex geometry, e.g. ESPs. Therefore, the particle size and density effect on ESP erosion are accounted for in this section.

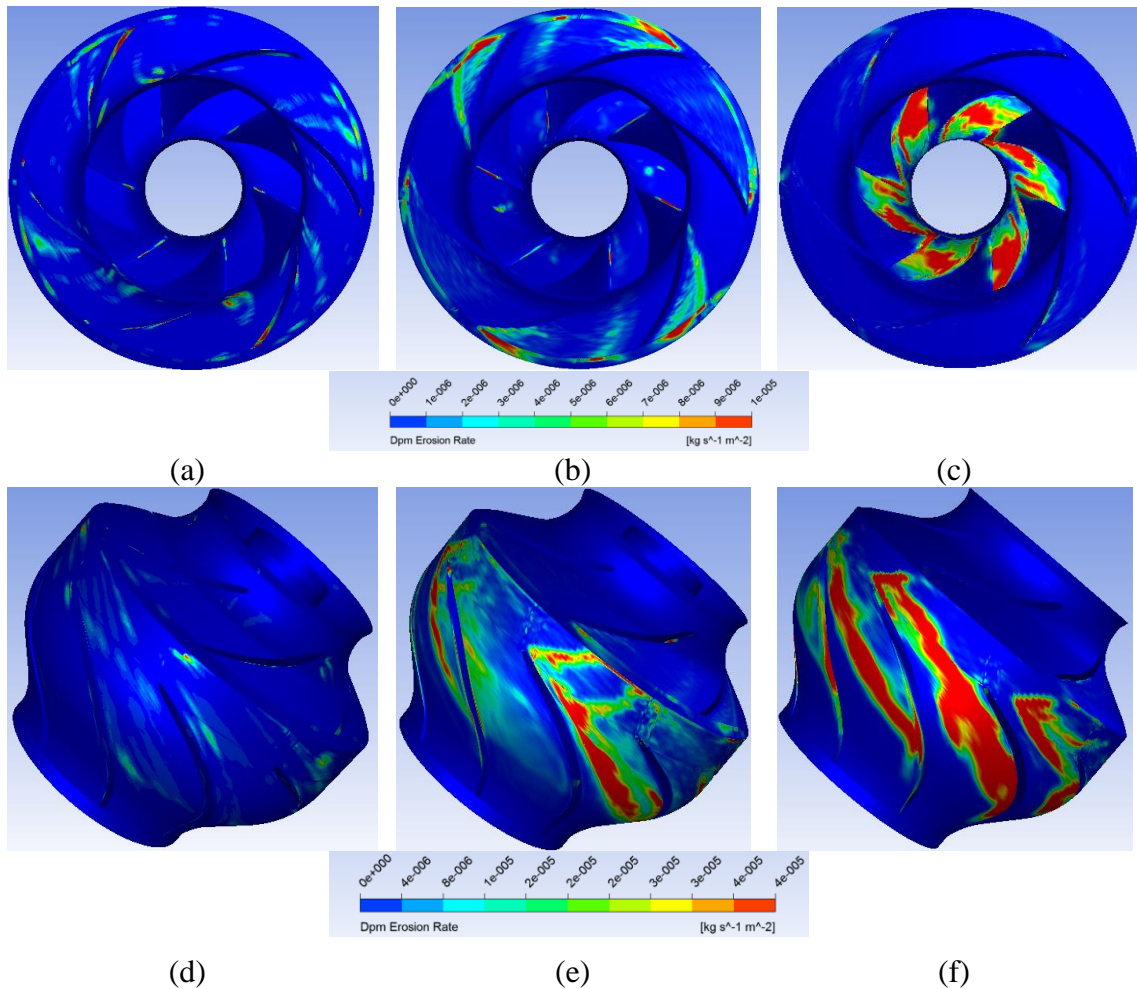


Figure 3.11 Particle size effect on the erosion patterns on impeller and diffuser (a) 50 μm impeller, (b) 200 μm impeller, (c) 1000 μm impeller, (d) 50 μm diffuser, (e) 200 μm diffuser, (f) 1000 μm diffuser

Comparing erosion patterns in Figure 3.11, it is convincing that erosion rate increases on the impeller outside shroud surface. On the contrary, further increase in the particle diameter to 1000 μm can reduce the erosion on the impeller outside shroud surface, but increase that on the impeller inside shroud surface. In addition, the erosion rate on diffuser increases and becomes more evenly distributed with larger particles. The facet maximum erosion rates and area-weighted average erosion rates shown in Figure 3.13 (a) and (b) illustrate that the larger particles cause more wear when the sand diameter is smaller than 300 μm . Thereafter, opposite changes can be observed depending on erosion surfaces.

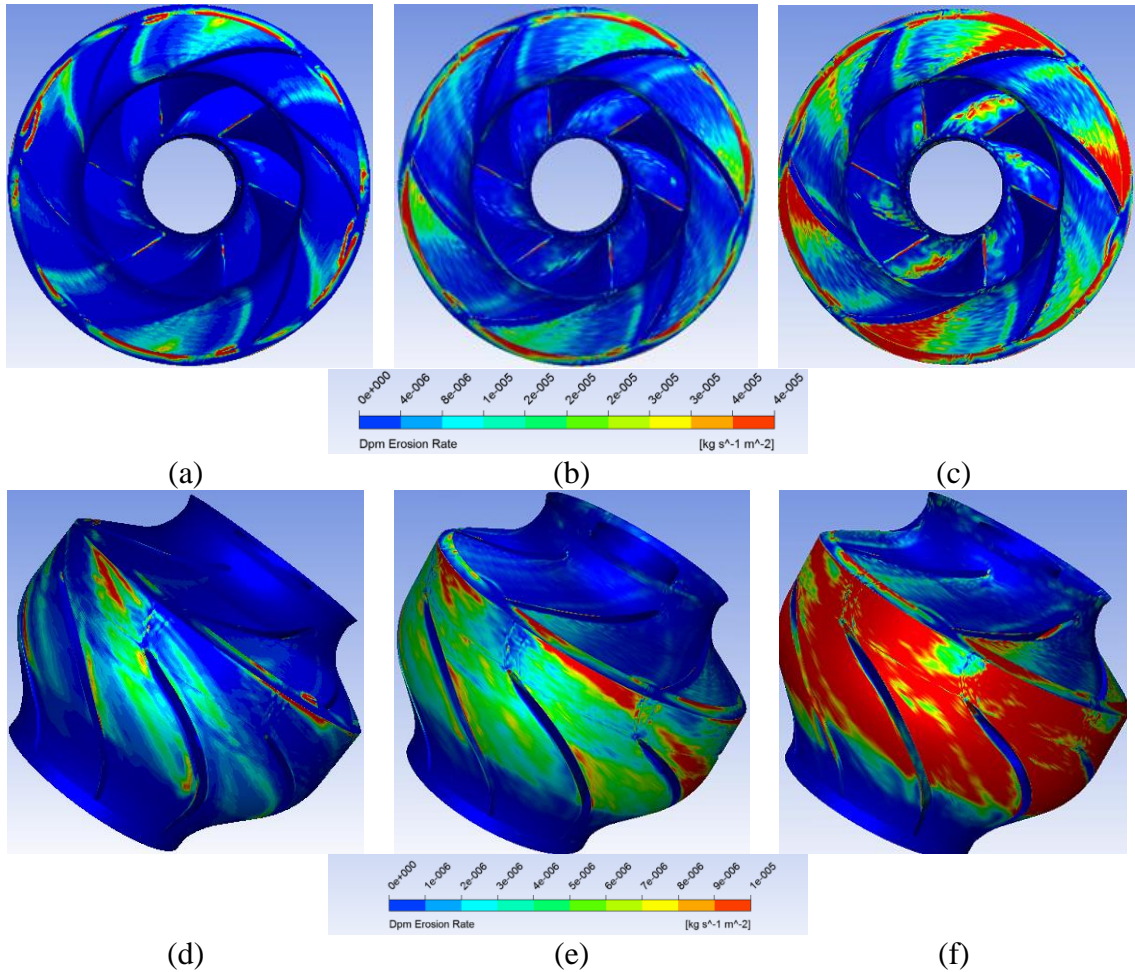


Figure 3.12 Particle density effect to the erosion patterns on impeller and diffuser (a) 1500 kg/m³ impeller, (b) 2000 kg/m³ impeller, (c) 3000 kg/m³ impeller, (d) 1500 kg/m³ diffuser, (e) 2000 kg/m³ diffuser, (f) 3000 kg/m³ diffuser

As shown in Figure 3.12, the outside shroud of both impeller and diffuser suffers from the most severe erosion with different particle densities. Both facet maximum and area-weighted average erosion rates, shown in Figure 3.13, increase with particle density when it is relatively small. The relation becomes flat and stable when the density is higher than 3000 kg/m³. Particle density and size in ESPs are usually within 1500 – 3000 kg/m³ and 10 – 300 μm . Therefore, it is important to study the particle size and density effects on erosion in ESPs.

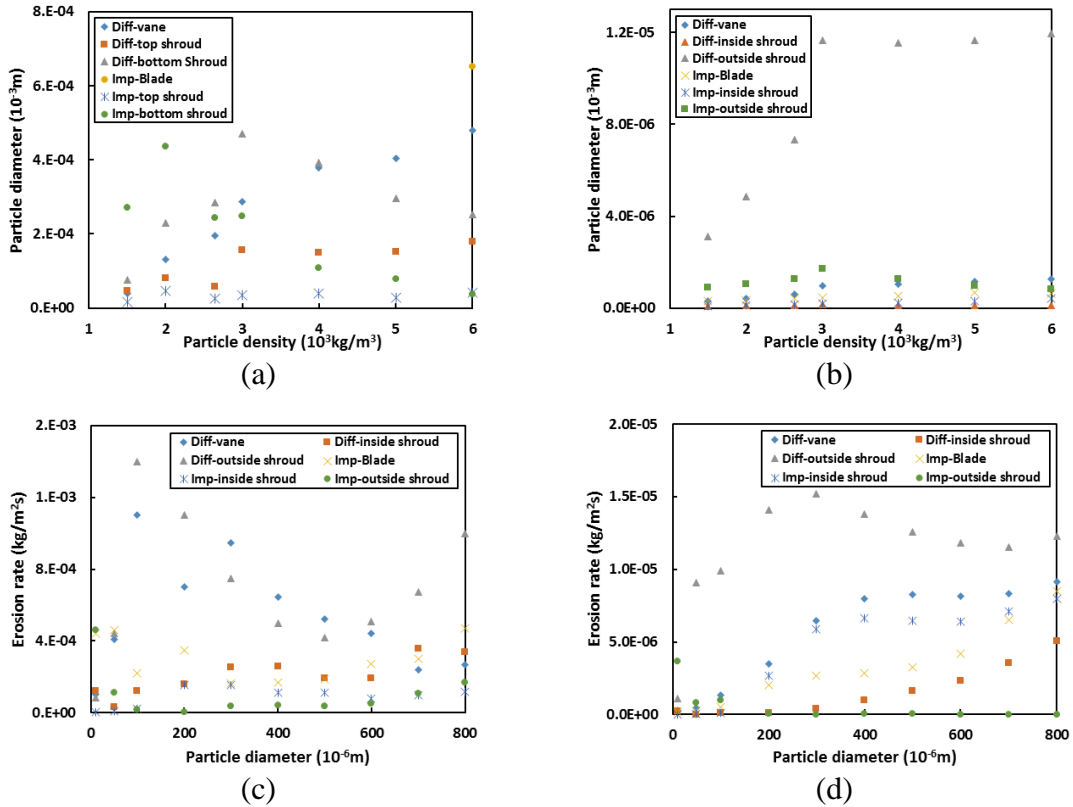


Figure 3.13 Particle size and diameter effect (a) facet maximum erosion rate vs. particle diameter, (b) area-weighted average erosion rate vs. particle diameter, (c) facet maximum erosion rate vs. particle density, (d) area-weighted average erosion rate vs. particle density

3.4.6 Turbulence model and wall function effect

Figure 3.19 shows the comparison between the calculated erosion rate and tested erosion rate (black column in Figure 6) by different turbulence models. As can be seen, different models have less effect on the impeller compared to that on the diffuser. RSM model predicts a slightly higher erosion rate on both the impeller and diffuser. Overall, the $k-\omega$ SST agrees best with the measured weight loss. Besides, the erosion ratio between the impeller and diffuser of the $k-\omega$ SST model is also the closest to the test results.

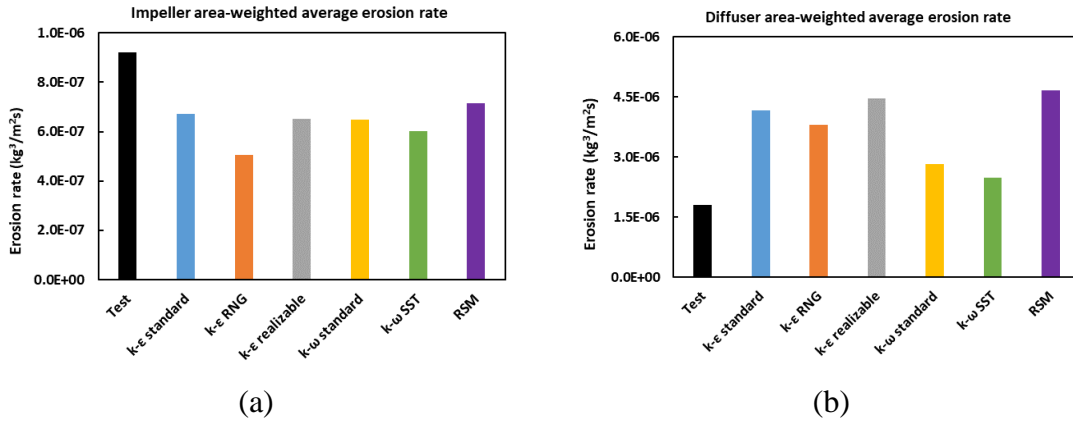


Figure 3.14 Average erosion rate with different turbulence model (a) impeller, (b) diffuser

The contour of the $k-\epsilon$ realizable model, $k-\omega$ SST model, and RSM model are compared in Figure 3.15. As shown in Figure 3.15 (g), (h) and (i), the velocity contour in the primary flow channel calculated by the $k-\epsilon$ realizable model is much smoother than others. The high-velocity layers of the $k-\omega$ SST model is thicker, which can be the reason for the lower erosion rate shown above. The impeller erosion contours are shown in Figure 3.15 (a), (b) and (c). As can be seen, the RSM model gives the most evenly distributed erosion patterns. The erosion on the impeller shroud is lower calculated by $k-\omega$ SST than others. Overall, the erosion contour matches the paint-removal photo shown in Figure 3.15 (i) and (j). The extremely concentrated erosion on the impeller shroud outlet is caused by neglecting the leakage between the impeller and diffuser shroud. Ignoring the clearance results in direct impact from a high rotational domain to the stationary wall surface. On the other hand, the leakage flow can create a liquid film between the rotor and stator, which can reduce the impact velocity. Future studies may focus on considering the clearance effect. The erosion contour on diffuser walls is shown in Figure 3.15 (d) to (f), where the contour of the RSM model shows a higher and concentrated erosion contour.

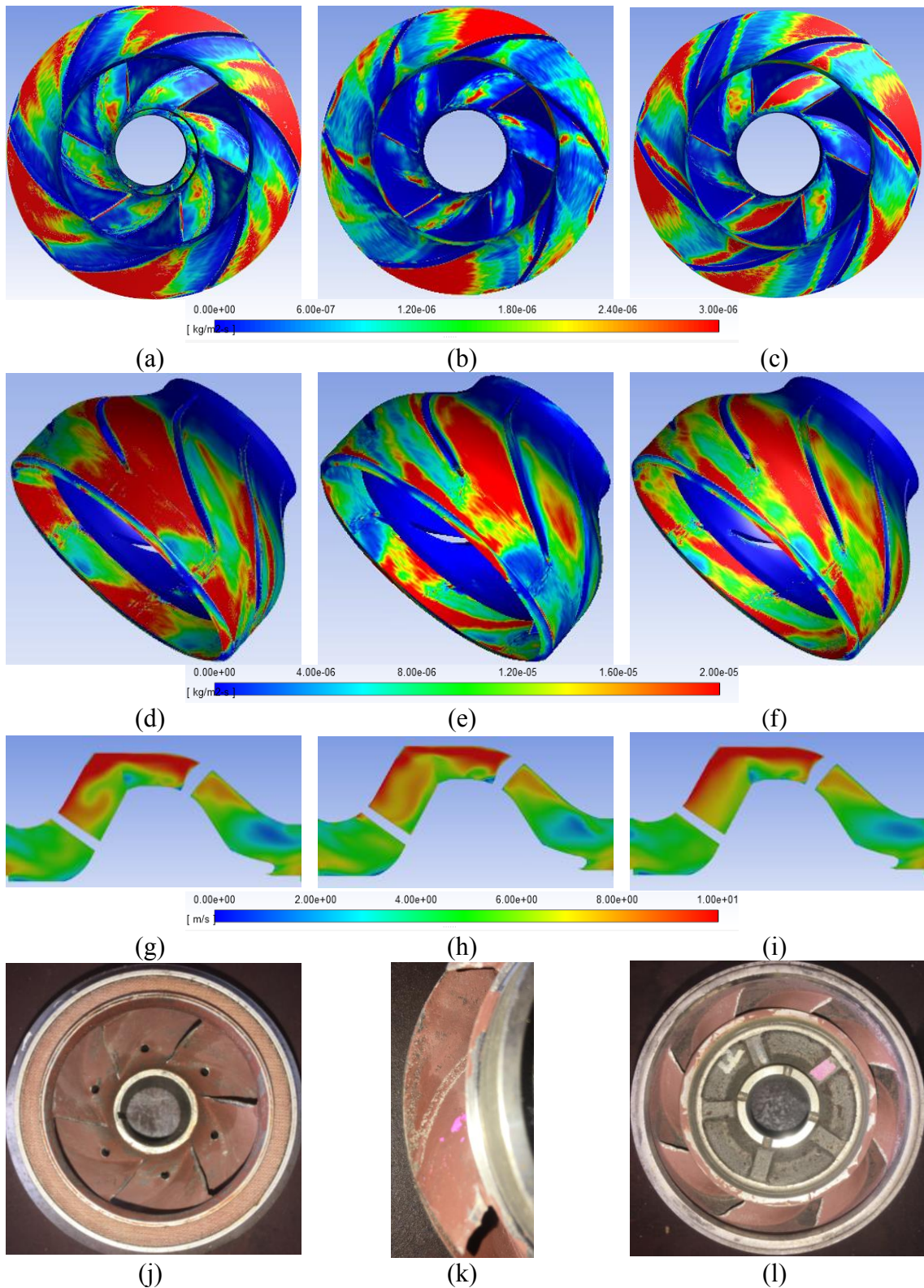


Figure 3.15 Erosion contour ($\text{kg}/\text{m}^2\text{s}$) and velocity (m/s) contour of $k-\epsilon$ realizable, $k-\omega$ SST and RSM turbulence model (a) impeller erosion RSM, (b) impeller erosion $k-\omega$ SST, (c) impeller erosion $k-\epsilon$ realizable, (d) diffuser erosion RSM, (e) diffuser erosion $k-\omega$ SST, (f) diffuser erosion $k-\epsilon$ realizable, (g) stage velocity RSM, (h) stage velocity

k- ω SST, (i) stage velocity *k- ϵ* realizable, (j) top-view of impeller paint-removal photo, (k) side view of impeller paint-removal photo (l) top view of diffuser paint-removal photo

Particle impact angle on diffuser shroud and impeller hub are shown in Figure 3.16. As shown, the maximum impact velocity and angle have a similar trend and magnitude with different turbulence models. The difference in erosion rate and pattern can be better indicated by the moving average trend shown in Figure 3.16 solid dots. The average impact angle on the diffuser shroud and impeller hub is about 5° . The average impact velocity is higher on diffuser shroud, which is 6 to 10 m/s. Compared to other models, the lower erosion rate of the *k- ω* SST model is caused by lower average impact angle and velocity.

The peak shown in Figure 3.16 shows the particle rebound trajectory, which is more obvious on the impeller hub due to sharp flow changes from axial to the radial direction. The rebound is denser on diffuser due to a decreased radius along the flow path.

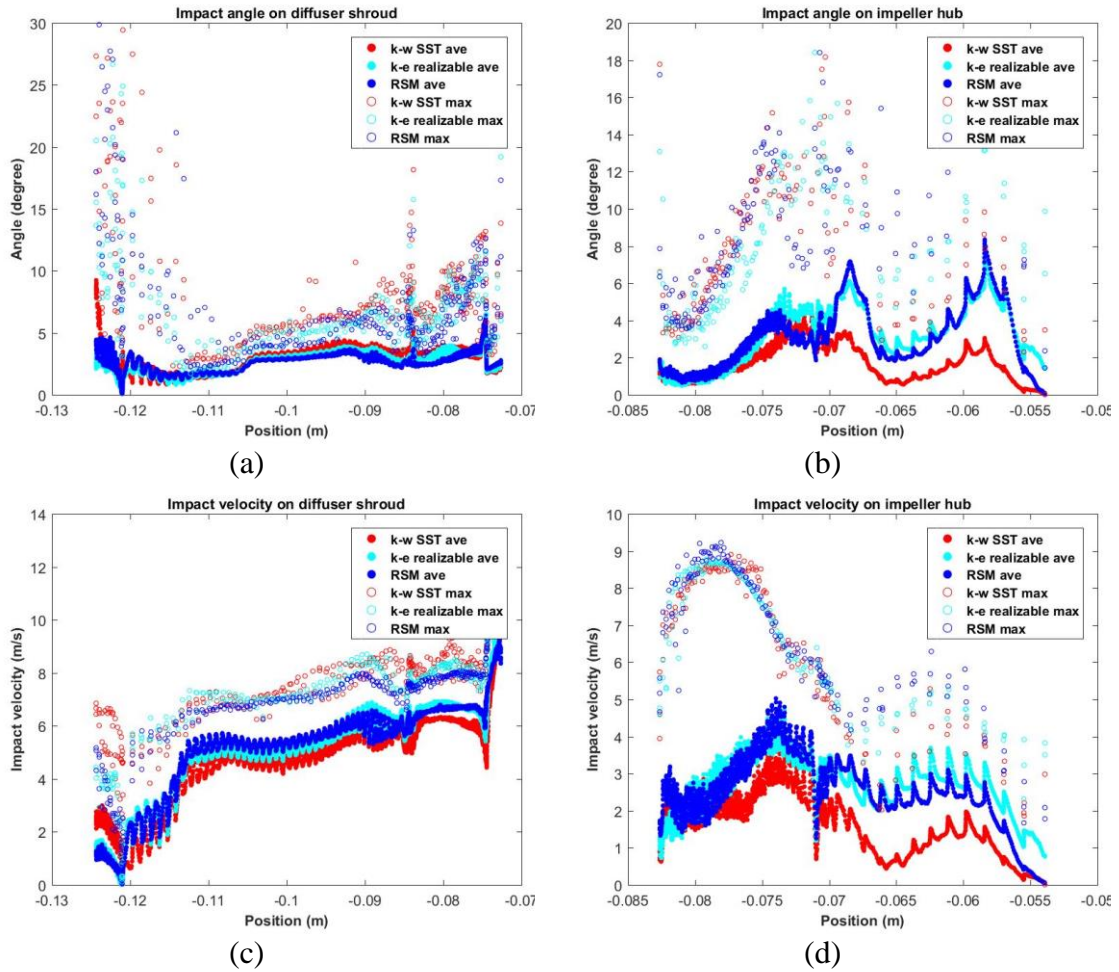


Figure 3.16 Particle impact velocity and angle (a) impact angle on diffuser shroud, (b) impact angle on impeller hub, (c) impact velocity on diffuser shroud, (d) impact velocity on impeller hub

As mentioned in Section 1.4.3, theoretically *k-ε* model should behave better by using the enhanced wall function in ESP simulation. As shown in Figure 3.17, the *k-ε* model with enhanced wall function does help increase the accuracy in both erosion rate value and ratio compare to the *k-ε* model with scalable wall function and becomes more close to that of *k-ω SST* model. In addition, the curvature correction effect is studied in Figure 3.17 since the erosion ratio still deviates a lot from the measured data. As shown, the curvature correction does affect the erosion rate prediction, but the changed erosion ratios become worse. The potential reasons for the mismatch could be an error in erosion

equations, additional weight loss that cannot be measured shown in Section 2.3.3.1, high relative uncertainty of roughly calculated average erosion rate, neglecting the secondary flow region, and first layer grid thickness. Further study needs to focus on these effect factors to increase the accuracy of the CFD simulation.

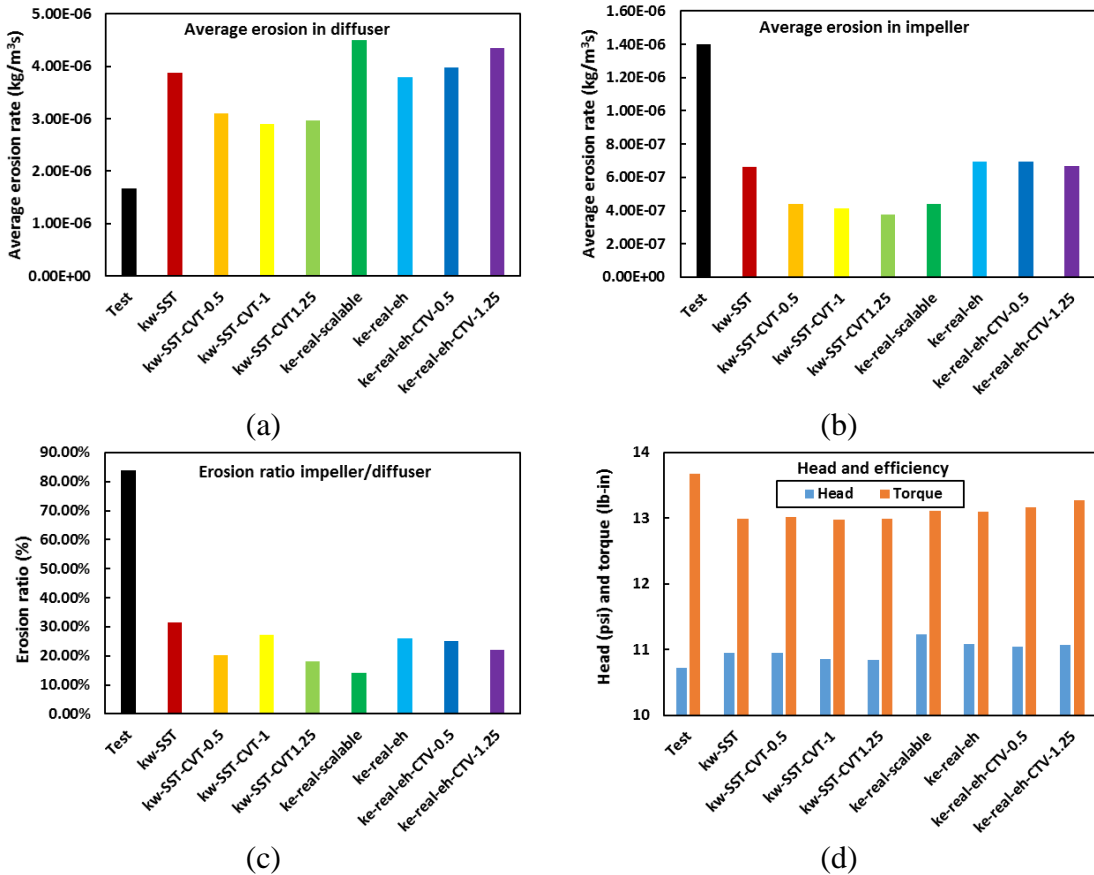


Figure 3.17 Wall function and curvature correlation effect (a) diffuser average erosion rate, (b) impeller average erosion rate, (c) impeller/diffuser erosion rate ratio, (d) head and torque at BEP by different models

3.4.7 Particle rebound model effect

Figure 3.18 (a) and (b) shows the erosion rate along the axial direction of diffuser shroud and impeller hub and shroud by different particle rebound model, where 1 represents perfect elastic model which doesn't consider the rebound effect, 2 is Tabakoff rebound model, 3 is Tabakoff Stochastic rebound model, and 4 is Forder et al. rebound

model. As can be seen, erosion on the impeller hub is higher when flow direction changes (close to balance hole area). In addition, more erosion can be observed in the interaction zone between the impeller outlet and diffuser inlet. The peak on impeller and diffuser shroud is generated due to ignoring the leakage as shown before. Besides some extremum points, the particle rebound effect on erosion simulation inside an ESP is ignorable, especially on average erosion rate. Considering the low impact angle shown previously, the restitution coefficients are close to 1 no matter which rebound model is used.

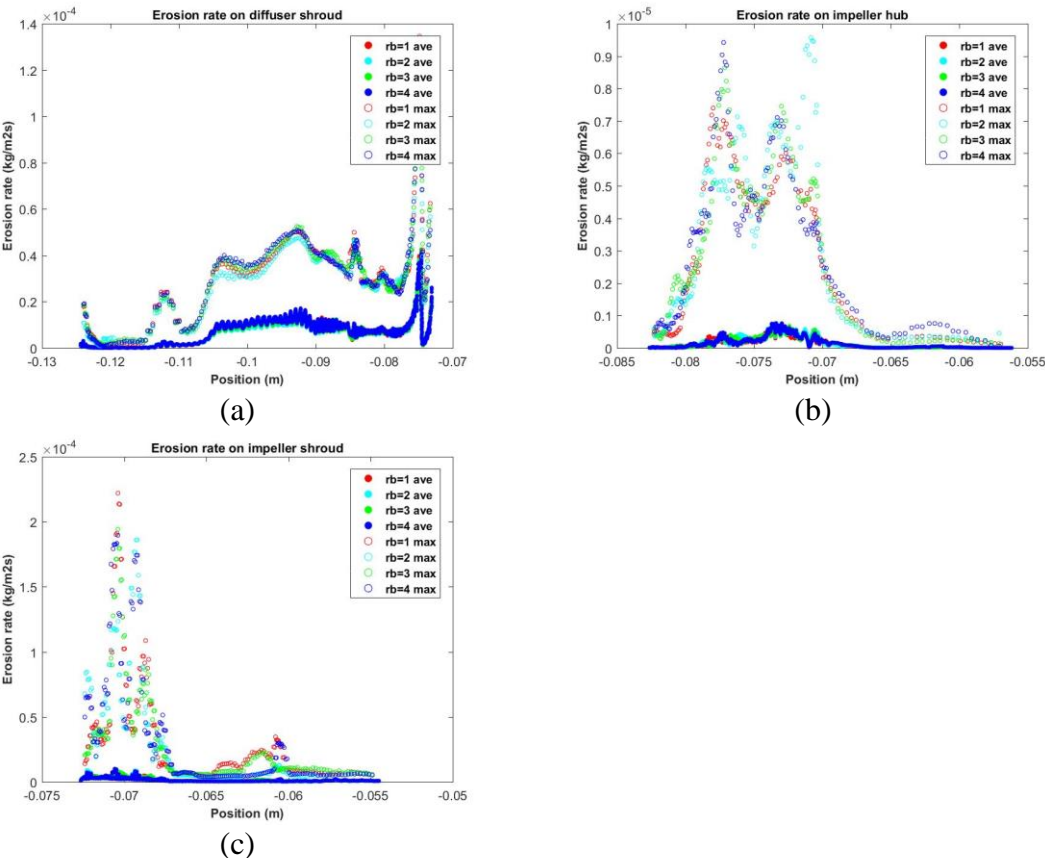
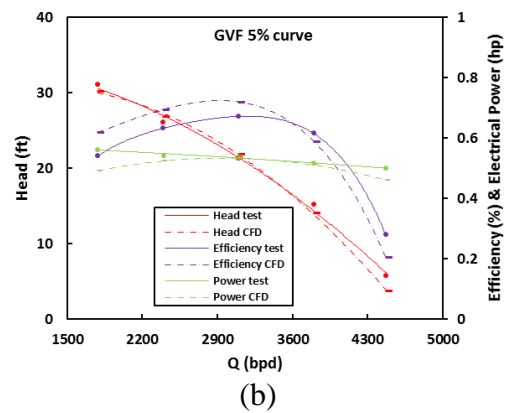
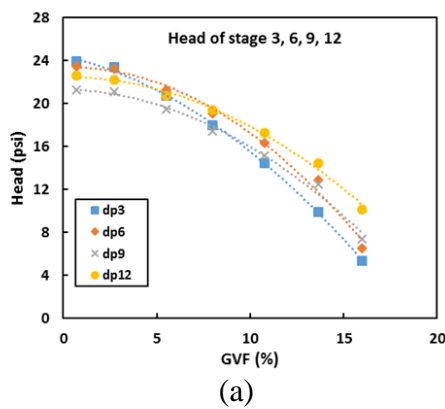


Figure 3.18 Area-weighted average erosion rate and hits times by different rebound model, (a) erosion rate on diffuser shroud, (b) erosion rate on impeller hub, (c) erosion rate on impeller shroud

3.4.8 Air-water-solid three-phase simulation

Pump performance under different $GVFs$ was recorded for Cases 3 and 4. Figure 3.19 (a) shows the head changes of Stages 3, 6, 9, and 12 according to different $GVFs$ at $Q_L = 3100$ bpd. The head curve of Stage-3 has a sharper decrease, followed by Stage-6, which indicates that the pump performance becomes better stage by stage in a mixed type ESP. In order to save the computation time, the steady-state Eulerian Per Phase method was first incorporated in the simulation. The particle diameter is calculated using the proposed equation (Zhu et al., 2018d; Zhu and Zhang, 2014). The calculated gas bubble diameter and other input parameters are shown in Table 3.3. As shown in Figure 3.19 (b) and (c), the simulated head curve of $GVF = 5\%$ matches with the tested curve of Stage-3, while that of $GVF = 10\%$ is higher than the test data. Similar results can be observed in Figure 3.19 (d), the over-prediction of the head curve is mainly due to an under-estimated gas bubble diameter. The simulated efficiency curve for most cases is higher than the test curve. The slightly under-predicted 15% GVF efficiency point in Figure 3.19 (d) indicates that the steady-state Eulerian method starts to lose its accuracy if GVF further increases.



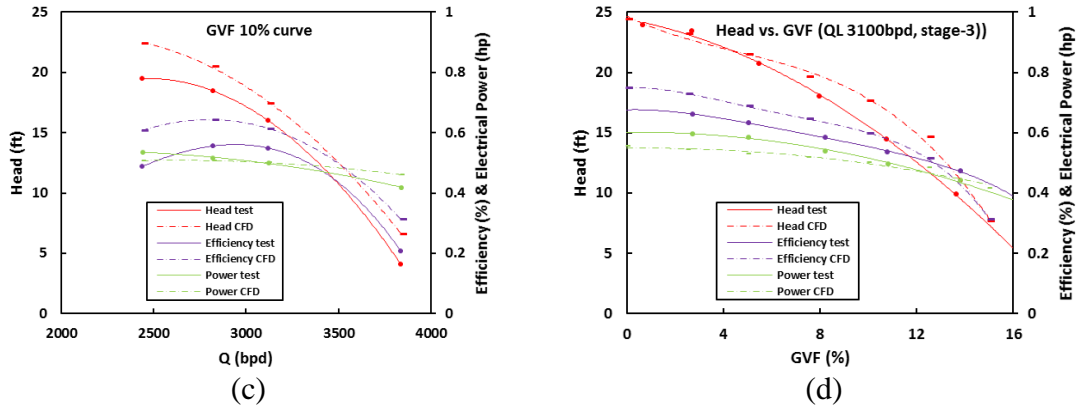


Figure 3.19 Gas-liquid flow performance validation at $N = 3600$ rpm, (a) Head of stage 3, 6, 9 and 12 vs. GVF at $Q_L = 3100$ bpd, (b) head, efficiency and power vs. flow rate at $GVF = 5\%$, (c) head, efficiency and power vs. flow rate at $GVF = 10\%$, (d) head, efficiency and power vs. GVF at $Q_L = 3100$ bpd

Table 3.3: Input parameters of gas-liquid-solid simulation

Case	GVF (%)	d32 (m)	Revised d32 (m)	Liquid mass flow (kg/s)	Gas mass flow (kg/s)	Solid inlet velocity (m/s)
1	5.00	5.33E-05	/	3.21	2.13E-03	1.93
2	5.00	5.08E-05	/	4.31	2.86E-03	2.60
3	5.00	4.97E-05	/	5.57	3.70E-03	3.35
4	5.00	5.24E-05	/	6.83	4.54E-03	4.11
5	5.00	7.29E-05	/	8.03	5.34E-03	4.83
6	10.00	1.13E-04	1.36E-04	4.38	6.15E-03	2.64
7	10.00	1.09E-04	1.31E-04	5.07	7.11E-03	3.05
8	10.00	1.11E-04	1.33E-04	5.61	7.87E-03	3.38
9	10.00	1.77E-04	2.13E-04	6.90	9.68E-03	4.15
10	0	/	/	5.57	0.00	3.35
11	2.5	2.46E-05	2.46E-05	5.57	1.80E-03	3.35
12	5	4.92E-05	5.00E-05	5.57	3.70E-03	3.35
13	7.5	7.88E-05	8.00E-05	5.57	5.70E-03	3.35
14	10	1.12E-04	1.36E-04	5.57	7.81E-03	3.35
15	12.5	1.55E-04	1.68E-04	5.57	1.00E-02	3.35
16	15	2.15E-04	/	5.57	1.24E-02	3.35
17	15	1.10E-04	/	5.57	1.24E-02	3.35
18	15	1.50E-04	/	5.57	1.24E-02	3.35

Before changing the gas bubble diameter, a simple parametric study on bubble diameter effect on pump head and erosion rate was conducted and the results are shown in Figure 3.20 (a) and (b). Decreasing gas bubble diameter can obviously increase pump head and decrease the erosion rate. It is convincing that an accurate fluid field of gas-liquid flow

is required before DPM and erosion simulation. Therefore, the mean particle diameter is revised as shown in Table 3.3. As a result, the simulated head curves match well with the test curves in Figure 3.20 (c) and (d).

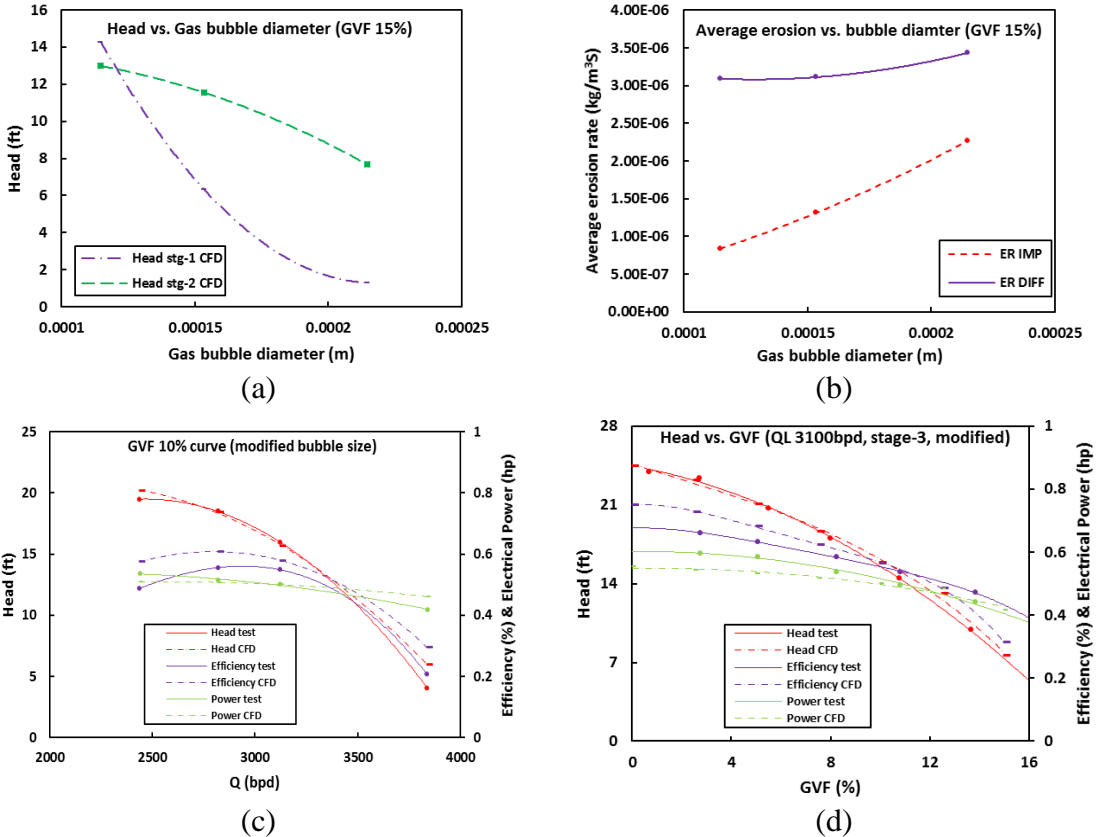


Figure 3.20 Gas bubble size effect, (a) Head vs. gas bubble diameter at $GVF = 15\%$, (b) average erosion rate vs. gas bubble diameter at $GVF = 15\%$, (c) modified 10% GVF pump curve, (d) modified head vs. GVF pump curve at $Q_L = 3100$ bpd

Before we analyze the erosion prediction, a brief comparison between steady state and transient gas-liquid simulations was made since the efficiency of the 15% GVF point in Figure 3.20 (d) is un-realistically lower than the test point. The head of transient simulation is close to that in Figure 3.20 (d), but the efficiency increases to 51.42%, which is higher than the test point. According to gas distribution patterns in Figure 3.21, steady-state gas-liquid CFD simulation predicts a lower in-situ gas void fraction in a diffuser, and

the gas bubble shape is an un-realistic cubic shape. For a lower GVF (10%), big gas bubbles are not completely formed, and the results shown before are acceptable.

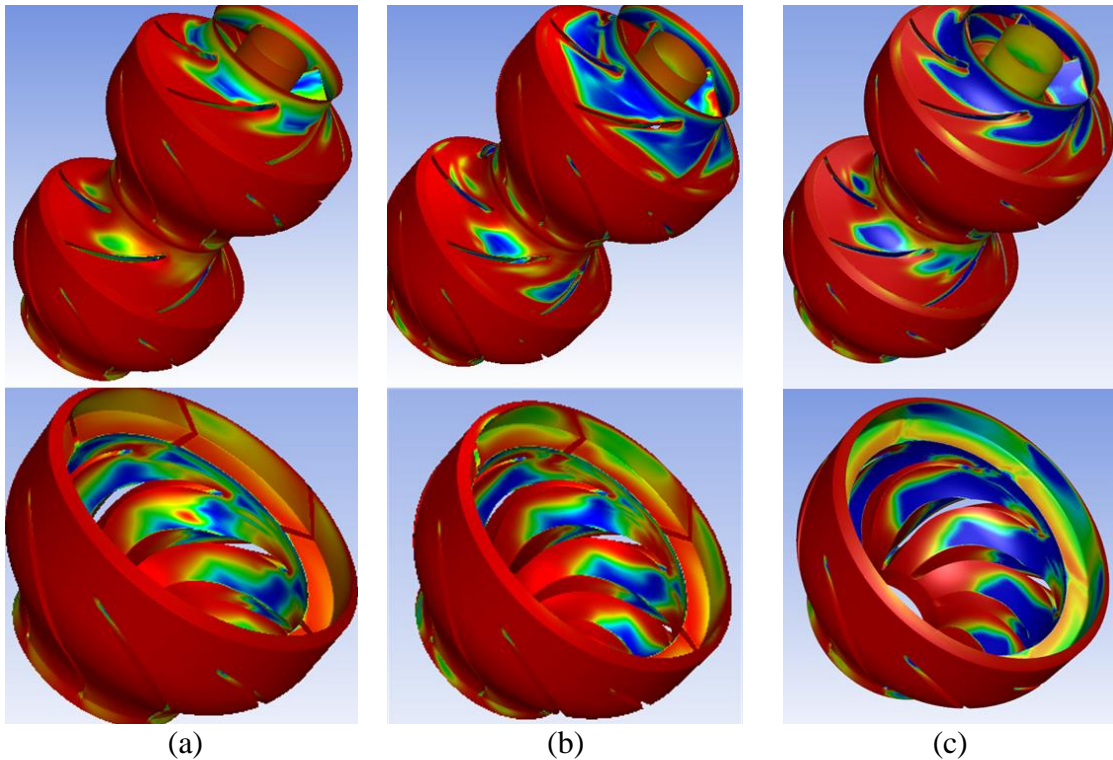


Figure 3.21 Gas phase distribution contour, (a) Steady state simulation $GVF = 10\%$, (b) steady state simulation $GVF = 15\%$, $d_b = 0.000215$ m, (c) Transient simulation $GVF = 15\%$, $d_b = 0.000215$ m

Although the transient simulation is more accurate at 15% GVF , steady-state erosion simulation is analyzed in Figure 3.22 to keep the consistency of the numerical methodology since the steady-state head prediction is still acceptable. Similar to water-sand erosion simulation, the calculated erosion rate in the diffuser is higher than the measured erosion rate, while that in the impeller is lower. However, the trend of the GVF effect from the simulation behaves similar as the test results.

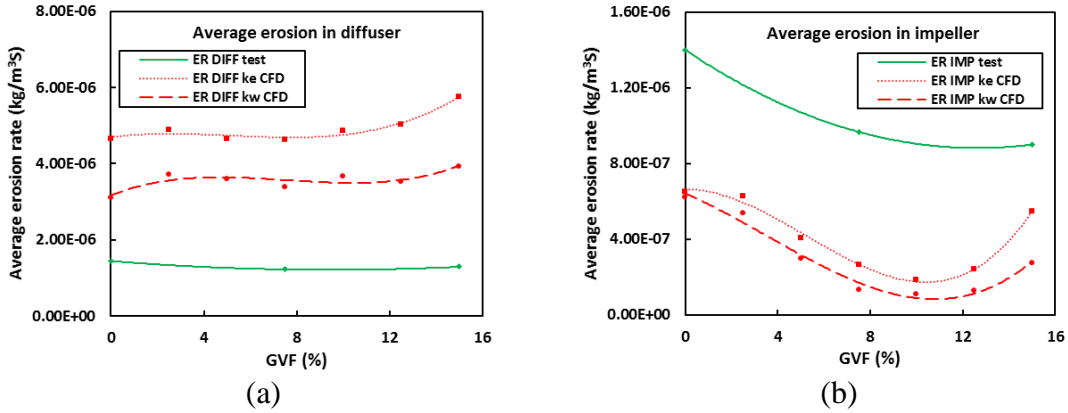


Figure 3.22 Comparison of average erosion rate vs. *GVF* between test data, *k-ε* CFD and *k-ω* CFD simulations, (a) diffuser average erosion rate, (b) impeller average erosion rate

An interesting result comes out from both CFD simulation and test weight loss data: increasing pump intake *GVF* has no obvious effect on erosion damage in the diffuser and can decrease the average weight loss and surface erosion rate in the impeller, which is opposite to the most commonly accepted understanding. Therefore, the average erosion rate of different stage surfaces is shown in Figure 3.23. The erosion damage on three surfaces simulated by the *k-ε* model slightly increased with *GVF*, while that on diffuser vane simulated by *k-ω* has an obvious increase. In addition, erosion rate on impeller outside shroud surface simulated by both *k-ε* and *k-ω* decreases with *GVF*, while that on the inside shroud surface and blade surface increases. It is presumable that gas can help prevent erosion on impeller outside shroud, but cause more damage on impeller blades, diffuser vanes and inside shroud.

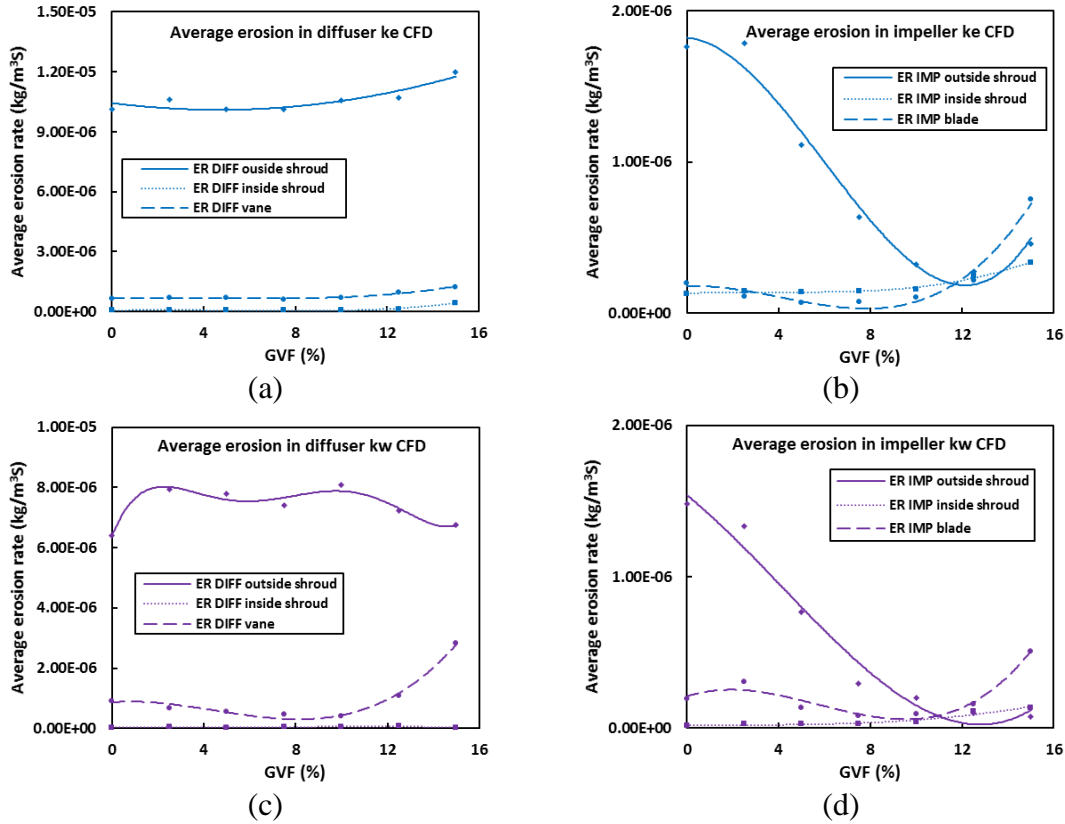


Figure 3.23 Average erosion rate of different stage surface vs. *GVF*, (a) erosion in diffuser by *k-ε* model, (b) erosion in impeller by *k-ε* model, (c) erosion in diffuser by *k-ω* model, (d) erosion in impeller by *k-ω* model

The erosion contours of water-sand simulation and air-water-sand (15% *GVF*) are shown in Figure 3.24. The CFD simulated erosion pattern becomes more concentrated with the presence of gas, and erosion damage on impeller inside surface is more obvious. The simulation results are very close to the paint-removal photos shown in Figure 3.24 (c) and (f). Besides, the increased damage on blade edges also agrees well to the photo in Figure 2.22 (d). Therefore, it is convincible that the erosion damage becomes more concentrated with more gas, but the average erosion rate and weight loss of the whole stages decrease in this study when *GVF* is less than 15%. According to the trend in Figure 3.22 and Figure 3.23, the weight loss and average erosion rate may increase if more gas presents.

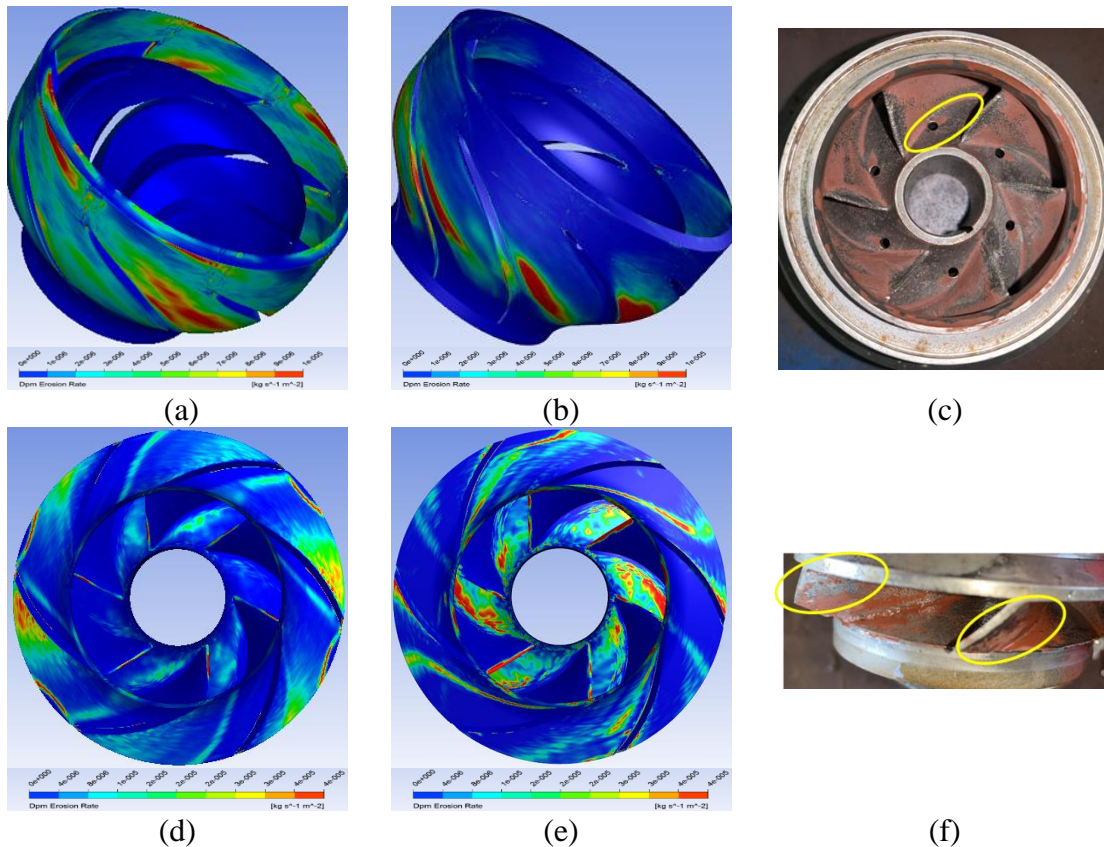


Figure 3.24 Erosion pattern comparison, (a) water-sand erosion pattern in diffuser, (b) gas-water-sand erosion pattern in diffuser at $GVF = 15\%$, (c) impeller paint-removal photo at $GVF = 15\%$, (d) water-sand erosion pattern in impeller, (e) gas-water-sand erosion pattern in impeller at $GVF = 15\%$, (f) impeller outlet paint-removal photo at $GVF = 15\%$,

3.4.9 Erosion models comparison

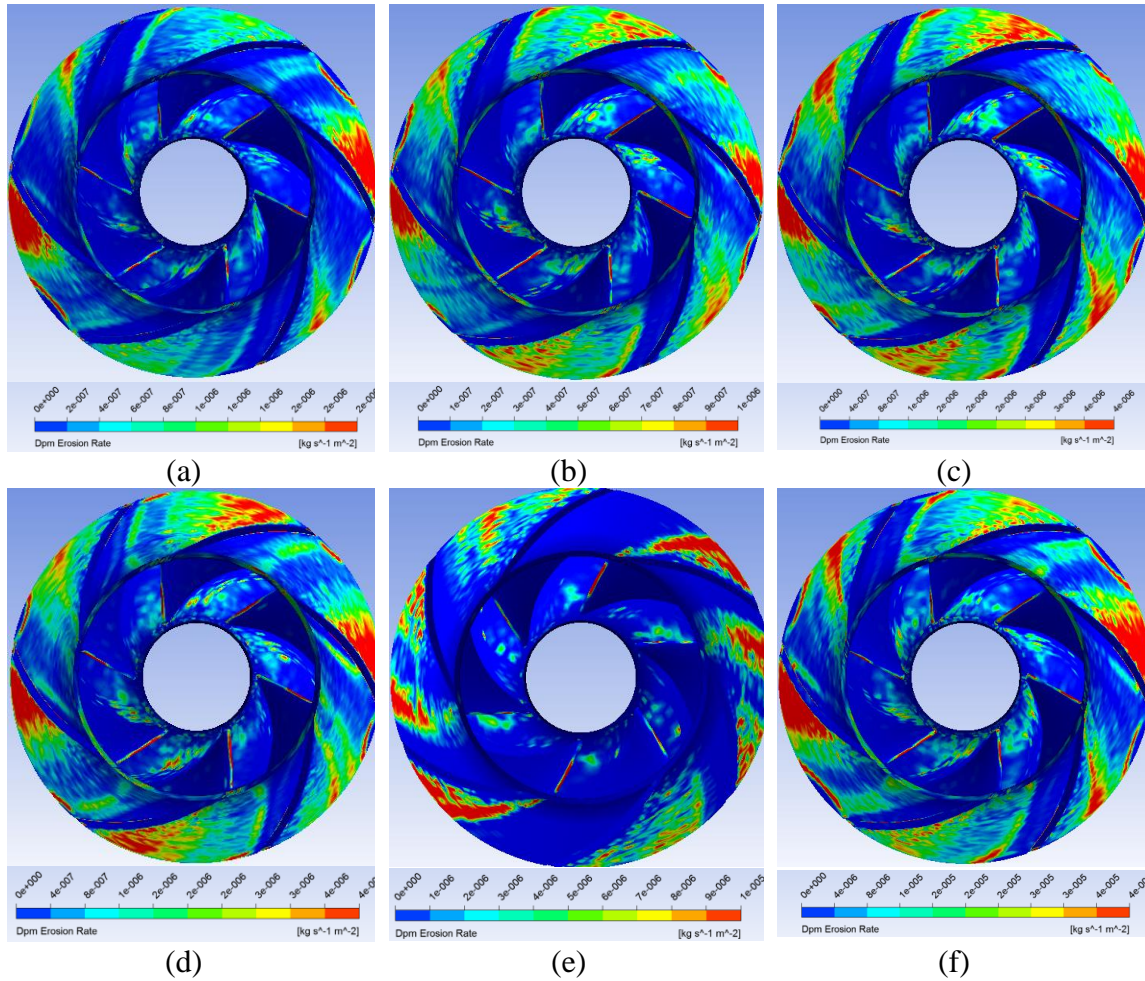


Figure 3.25 MTESP impeller erosion contour (a) Haugen et al. (1995), (b) DNV (2015), (c) Zhang et al. (2007), (d) Oka et al. (2005), (e) Mansouri (2014), (f) Ahlert et al. (1994)

As shown in Figure 3.25, the erosion patterns of six erosion models in the impellers have similar trends, although the severity differences can be found in the erosion rate magnitude. Severe wear on impeller blades and the outside shroud are observed. The impeller blades suffer the highest erosion rate, which can be detected on both blades leading and trailing edges in Figure 3.27 (b) and (d) under current flow condition, $Q_L = 3100$ bpd, $N = 3600$ rpm. Compared to the diffuser, the magnitude of erosion rate on ESP impeller is several times lower. However, the pump boosting pressure of ESP is mainly

generated by the impeller rotation (Shi et al., 2018) due to the conversion of fluid kinetic energy to pressure head. According to the mechanistic model to predict ESP hydraulic performance developed by Zhu et al. (2018c), the impeller blade length and projection angle are the key factors affecting pump-boosting pressure. Thus, it seems more important to study the erosion inside ESP impellers.

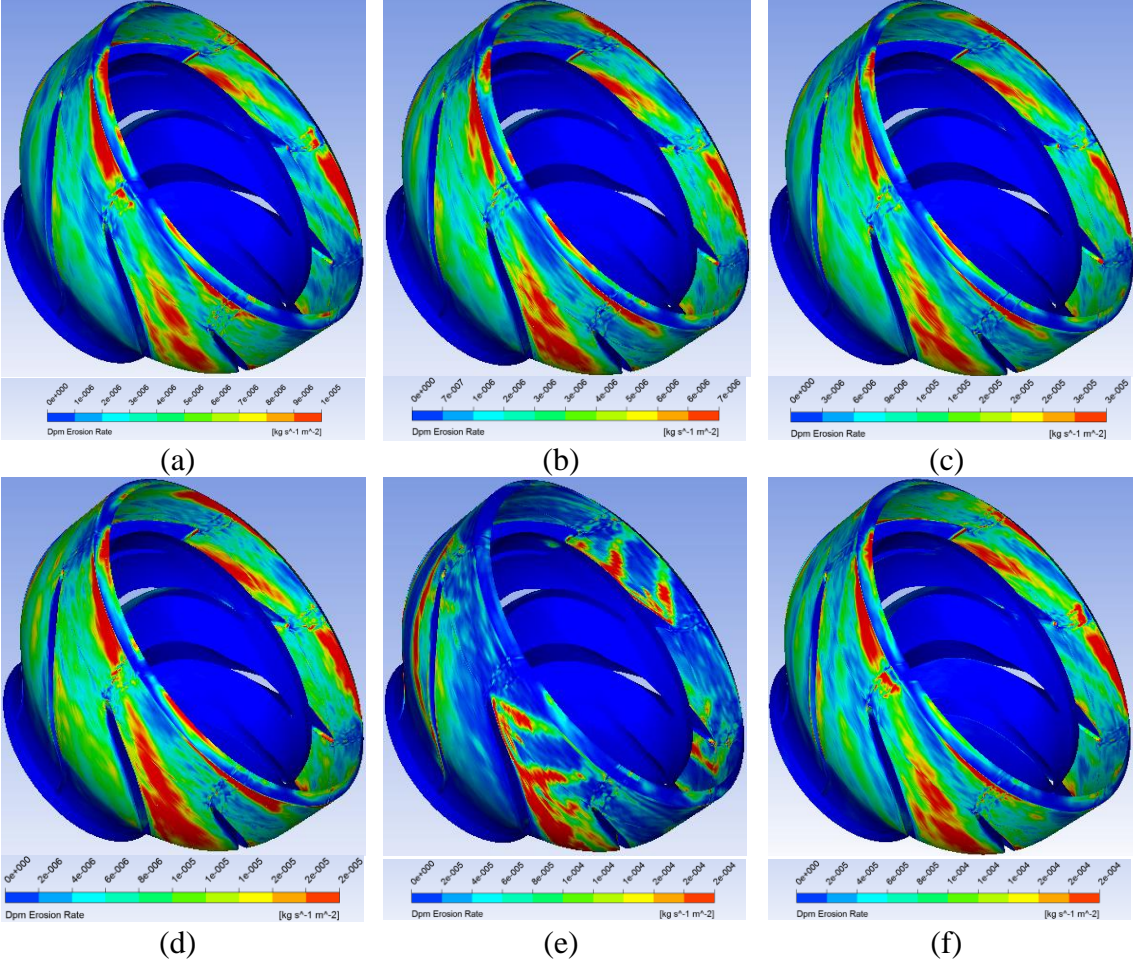


Figure 3.26 MTESP diffuser erosion contour (a) Haugen et al. (1995), (b) DNV (2015), (c) Zhang et al. (2007), (d) Oka et al. (2005), (e) Mansouri (2014), (f) Ahlert et al. (1994)

Similarly, the wear patterns on the diffuser are comparably similar and the severe wear region is located in diffuser vanes, flow channels and the interaction zones between impeller and diffuser. The maximum erosion is detected near the diffuser vanes and outside

shroud according to the histograms in Figure 3.26. The area-weighted average erosion rate in Figure 3.27 (b) shows high wear conditions on outside shrouds and relatively low conditions on vanes. It is consistent with the simulated erosion patterns that only the pressure side of the blades and interaction area between the impeller and diffuser suffer from severe erosions.

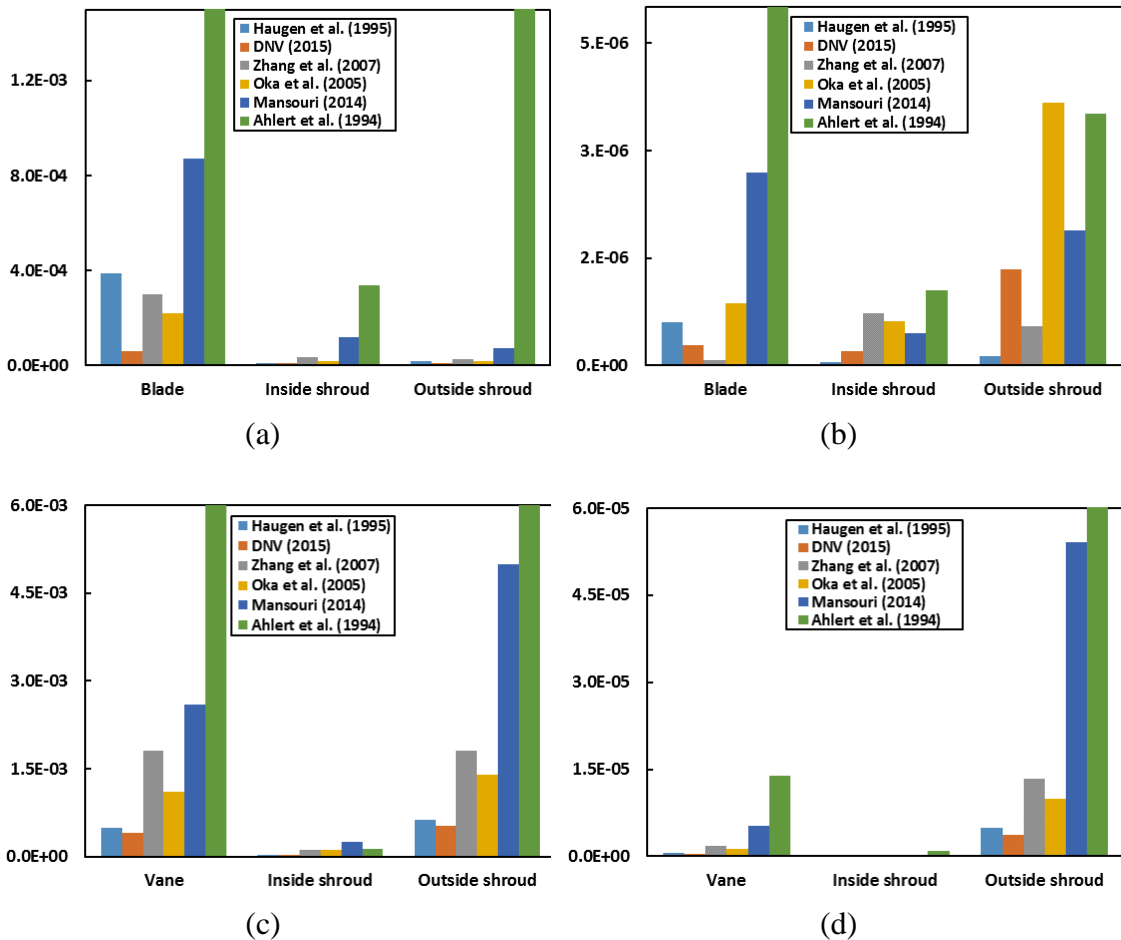
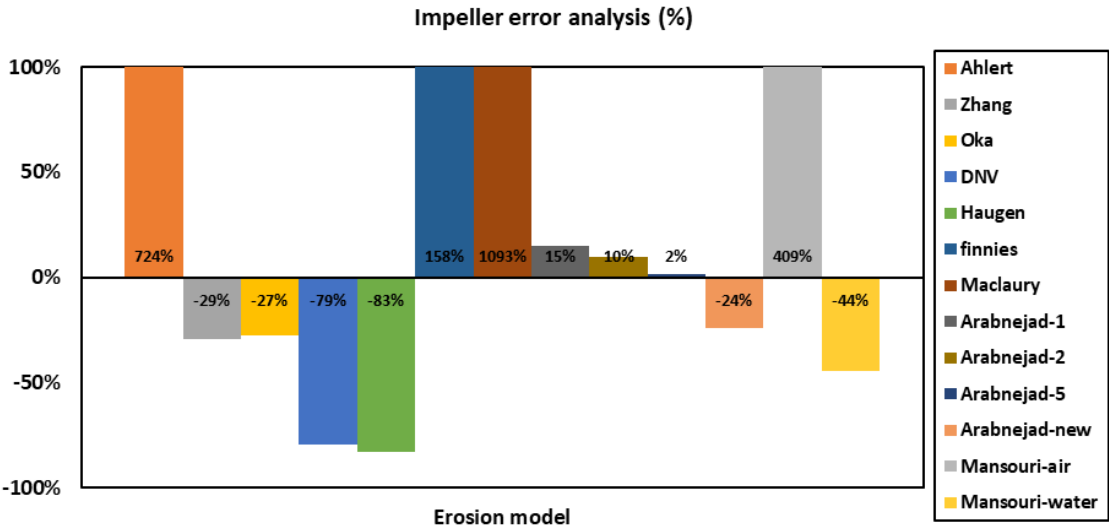


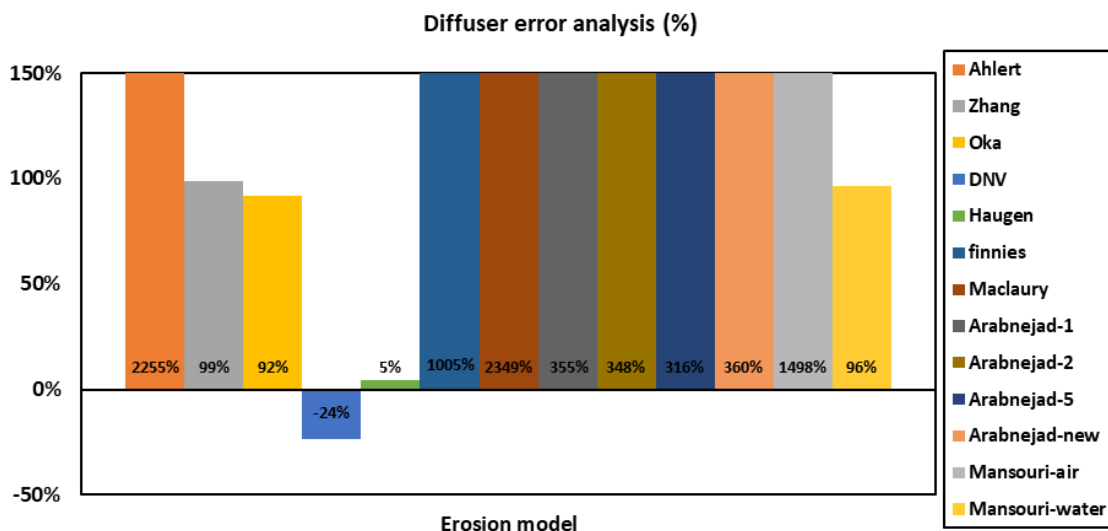
Figure 3.27 Facet maximum erosion rate and area-weighted average erosion rate on MTESP impeller and diffuser, (a) impeller maximum, (b) impeller average, (c) diffuser maximum, (d) diffuser average

The weight-loss rate was validated with a 64-hour erosion test on MTESP under liquid-sand condition. The working condition corresponds to sand concentration at 1wt%, mixture flow rate $Q_L = 3100$ bpd, rotation speed $N = 3600$ rpm and pump intake pressure

at 150 psig. The average clearance of seal geometry and weight-loss of stages were measured and shown in Section 2.3.1.3. Weight-loss caused by abrasion wear on seals was calculated using the clearance changes. It should be noted that the impeller down-thrust washers were completely worn out after 16 hours during the first test, whose weight is 2 g per stage. The erosion weight-loss was obtained by subtracting the abrasion and washer losses from the total loss. The average weight-loss caused by abrasion was 1.07 g and 1.53 g for impeller and diffuser, respectively, while the corresponding erosion weight-loss was 6.26 g and 13.55 g. Accordingly, the area-weighted average erosion rates on impeller and diffuser were calculated to be $1.31 \times 10^{-6} \text{ kg/m}^2\text{s}$ and $1.09 \times 10^{-6} \text{ kg/m}^2\text{s}$.



(a)

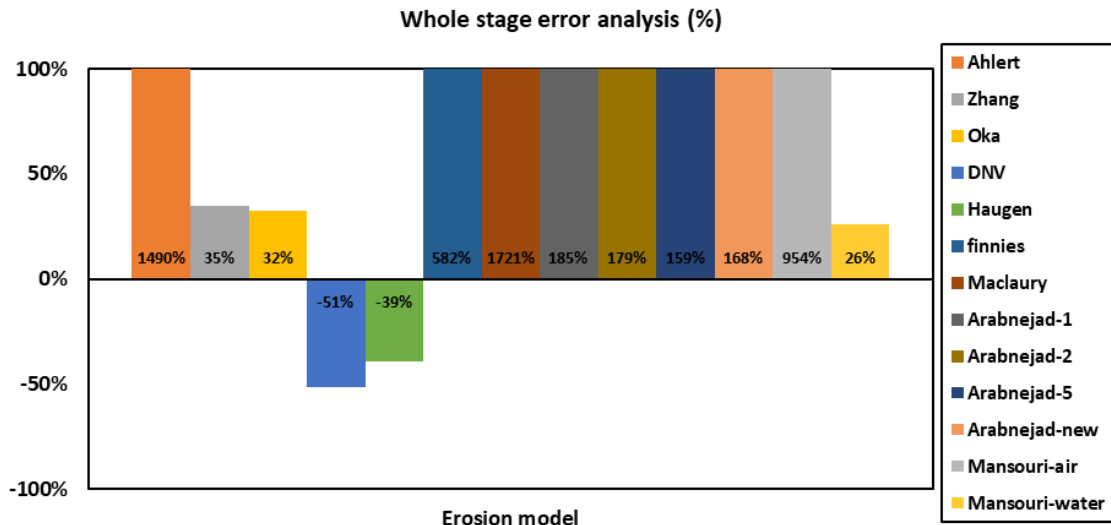


(b)

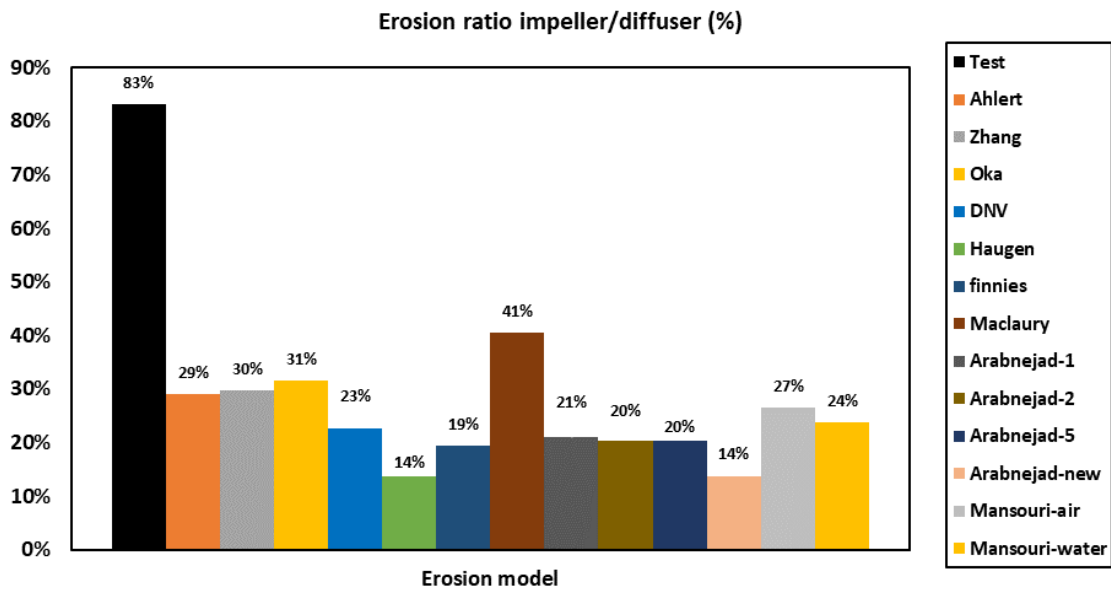
Figure 3.28 Area-weighted average erosion rate comparison (a) diffuser, (b) impeller

Figure 3.28 and Figure 3.29 below show the comparison of the area-weighted average erosion rate among six erosion models. The number behind Arabnejad model (2015) represents different materials, where 1 is 1018 carbon steel, 2 is 4130 carbon steel, and 5 is 316 stainless steel. Although these models were derived from air impingement erosion tests, some models perform surprisingly well inside the complex ESP geometries under liquid-sand flow. As shown in Figure 3.29, Some models work fine in the simulation, for example: Zhang et al. (2007) model, Haugen et al. (1995) model, Oka et al. (2005) model, DNV (2012) model, and Mansouri et al. (2014) water model. It should be noted that most models are developed in air-solid conditions. Corrections might be necessary for water-solid simulation. As a result, the accuracy of Mansouri-water (2015) is much higher than Mansouri-air (2015). The erosion rate ratio of diffuser/impeller is shown in Figure 3.29 (b), which is under-predicted by all erosion models. It is presumable that the deviation is caused by the near-wall grid refinement and ignoring the leakage flow. Overall, Mansouri-water model (2015) is suggested with the lowest average error of impeller and

diffuser. In addition, it is also possible to use Arabnejad-5 model (2015) in the impeller (2% error) and Haugen et al. (1995) model in the diffuser (5% error).



(a)



(b)

Figure 3.29 Area-weighted average erosion rate error analysis

CHAPTER 4

MECHANISTIC MODELING AND RESULTS

In oil production, screens and filters are used in the well completion to prevent large solids flowing into the ESP intake. However, small particles, especially sand production from unconsolidated sandstone and proppant backflow in fracturing wells often cause severe damage. The performance and lifespan of ESPs are severely reduced by erosion on blades and abrasion on seals.

Pump performances for single phase, multiphase and emulsion flows have been modeled in previous researches as listed in Appendix A. Only erosion, abrasion, and improved leakage loss models, from which the eroded pump geometry can be generated, are included in this section.

4.1 Model Development

4.2.1 *Performance prediction*

The model in this study is developed from the previously proposed mechanistic ESP performance model (Zhu et al., 2019c). Starting from Euler equation, the head loss due to recirculation, turning, friction and leakage are detached from theoretical head increment. More detailed impeller velocity triangle calculations for gas-liquid flow, high viscosity oil flow, and oil-water emulsion flow can be found in the published paper (Zhu et al., 2019d; Zhu et al., 2019g; Zhu et al., 2018h)

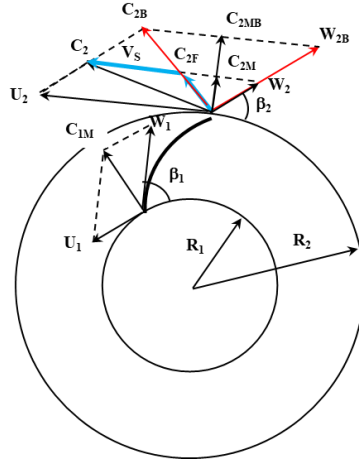


Figure 4.1 Velocity triangles at impeller outlet

Assuming there is a best match flow rate Q_{BM} that matches the designed flow direction. Then, C_{2B} is the absolute fluid velocity at the impeller outlet corresponding to Q_{BM} . Recirculation occurs when the flow rate is different from the best match flow rate. For example, if the flow rate is lower than Q_{BM} and C_2 is the actual absolute fluid velocity as shown in Figure 4.1. Then, C_2 can be divided into a shear velocity component V_S and a velocity component C_{2F} in the best match velocity direction. Derived from Euler head equation, the theoretical head can be expressed as:

$$H_E = \frac{U_2^2}{g} - \frac{U_2 C_{2M}}{g \tan \beta_2}, \quad (4.1)$$

where U_2 is the outlet peripheral velocity, β_2 is the blade angle from the tangential direction at impeller outlet, C_{2M} is meridional velocity at the impeller outlet as below

$$C_{2M} = \frac{Q}{(2\pi R_2 - Z_I T_B) y_{I2}}, \quad (4.2)$$

where Q is the liquid flow rate (leakage flow rate should be added), R_2 is the impeller outlet radius, Z_I is the impeller blade number, T_B is the blade thickness projected to the radial direction, and y_{I1} is the impeller inlet height.

Then, the recirculation loss caused by shear velocity can be calculated as:

$$H_R = \frac{C_2^2 - C_{2E}^2}{2g}, \quad (4.3)$$

$$C_{2E} = C_{2F} + \sigma(C_{2P} - C_{2F}), \quad (4.4)$$

$$C_{2F} = C_{2B} \frac{Q}{Q_{BMP}}, \quad (4.5)$$

$$C_{2P} = \frac{C_2^2 + C_{2F}^2 - V_S^2}{2C_{2F}}, \quad (4.6)$$

$$V_S = U_2 \frac{Q_{BEP} - Q}{Q_{BEP}}, \quad (4.7)$$

and

$$\sigma = \frac{\left(\frac{\mu_W}{\mu_L}\right)^{0.5}}{1 + 0.02 Re_C^{0.2}}, \quad (4.8)$$

where H_R is recirculation head loss, C_{2E} is the effective velocity of C_{2F} due to viscosity effect, σ denotes the viscosity effect, C_{2P} is the projected velocity of C_2 in the direction of C_{2B} , μ_L and μ_W are liquid and water viscosity.

The friction loss in the impeller and diffuser primary flow channel can be calculated using pipe flow friction loss equation as shown below:

$$H_{FI} = f_{FI} \frac{V_I^2 L_I}{2gD_I} \quad (4.9)$$

and

$$H_{FD} = f_{FD} \frac{V_D^2 L_D}{2gD_D} \quad (4.10)$$

where H_F is the friction loss, f_F is the friction factor, V is the representative fluid velocity, L is the channel length, and D is the representative (hydraulic) diameter of the channel. Subscripts I and D represent impeller and diffuser, respectively.

The turning head loss occurs when the flow direction has a rapid change. Two turning loss are included: turning effect in the impeller and and turning effect in the diffuser. Turing losses can be estimated as:

$$H_{TI} = f_{TI} \frac{V_I^2}{2g} \quad (4.11)$$

and

$$H_{TD} = f_{TD} \frac{V_D^2}{2g}, \quad (4.12)$$

similarly, subscripts I and D represent impeller and diffuser, respectively. H_T is turning loss, f_T is turning loss factor determined from experiments.

To calculate the leakage head loss, the leakage flow rate needs to be first determined. As shown in Figure 2.10 and Figure 2.12, the pressure at impeller balance hole and skirt ring is close to the impeller inlet and the pressure at balance ring and the clearance between the outside shroud of impeller and diffuser is close to the impeller outlet pressure. Therefore, the pressure head difference across leakage regions can be estimated by Equation (4.13) and (4.15):

$$H_{LKB} = H_E - H_R - H_{FI} - H_{TI} - \frac{U_2^2 - U_{LKB}^2}{8g}, \quad (4.13)$$

$$H_{LKS} = H_E - H_R - H_{FI} - H_{TI} - \frac{U_2^2 - U_{LKS}^2}{8g}, \quad (4.14)$$

and

$$H_{LKIT} = H_P - \frac{U_1^2 - U_{LKIT}^2}{8g}, \quad (4.15)$$

where H_{LKB} , H_{LKS} and H_{LKIT} represent pressure head difference across the balance, skirt and inter-stage leakage region, respectively. U_{LKB} , U_{LKS} , and U_{LKIT} are the peripheral velocities at the outlet of the balance, skirt and inter-stage leakage regions, respectively.

The pressure loss across the leakage region is due to contraction, expansion, turning, and friction. The friction coefficient is derived below (Childs, 1983):

$$H_{LK_i} = \frac{f_{LK_i} V_{LK_i}^2}{g} + \sum \frac{E_{LK_i} V_{LK_i}^2}{2g}, \quad (4.16)$$

$$f_{LK_i} = \frac{L_{G_i}}{S_{LK_i}} \left[0.066 \times Re_{LK_{ai}}^{-0.25} \left(1 + \frac{\Omega^2 R_{LK_i}^2}{4V_{LK_i}^2} \right)^{0.375} \right], \quad (4.17)$$

and

$$Q_{LK_i} = 2\pi R_{LK_i} S_{LK_i} V_{LK_i}, \quad (4.18)$$

where E_{LK} defines head loss coefficients due to geometry changes ($E_{LK} = 0.5$ for contraction, $E_{LK} = 1$ for expansion and $E_{LK} = 3$ for turning), f_{LK} is the friction loss coefficient in leakage regions, L_G is the length of leakage region, R_{LK} is leakage radius, Q_{LK_i} is leakage flow rate, $Re_{LK_{ai}}$ is nominal axial leakage Reynolds number, subscript i represents different regions ($i = B$ for balance region, $i = S$ for skirt region, $i = IT$ for inter-stage region). The pressure losses in three leakage regions should be calculated based on corresponding geometry parameters.

Solving Equation (4.1) to (4.18), the leakage flow rate in the corresponding region can be obtained. Previously the leakage loss was included in other loss using Q_{LK} . However, the calculated head curve with eroded geometries does not have a similar trend with experimental curves. The higher leakage can generate severe turbulence in the

interaction zones between impellers and diffusers. Therefore, ESP head loss due to leakage flow H_{LLK} is calculated as

$$H_{LLKi} = \frac{f_{LLK}}{2g} \left(\frac{Q_{LK_i}}{Z_I \times A_I} \right)^2, \quad (4.19)$$

where f_{LLK} is the leakage head loss coefficient determined from experiments ($f_{LLK} = 20$ in this study), Z_I is the impeller blade number, A_I is the representative impeller channel cross-sectional area, Q_{LK} is the leakage flow rate. Then, the final pump head is calculated by:

$$H_P = H_{EE} - H_{FI} - H_{FD} - H_{TI} - H_{TD} - \sum H_{LLKi} \quad (4.20)$$

By dividing the total erosion time into several smaller time steps, erosion on the blade surface, and abrasion on sealing area and pump performance degradation can be calculated using the flow chart in Figure 4.5.

4.2.2 Erosion prediction

In this section, sand particles are assumed to be uniformly distributed in the liquid phase at impeller inlet. Particle trajectory in the primary flow passage can be solved from Newton's second law of motion by considering large pressure gradients, buoyancy, added mass, centrifugal and Coriolis forces. The squeeze film and restitution effects are included at near-wall boundary to include fluid protection effect. With impact angle and velocity, erosion can be calculated using existing models developed from the gas impingement test in Section 1.1.2.

4.2.2.1 Particle trajectory

Assuming solids are gathered at the outside shroud and no-slip between liquid and solid particles at the impeller inlet, particle trajectory can be solved based on Newton's second law of motion:

$$F = m_p \frac{dV_p}{dt}, \quad (4.21)$$

where F is the total force on the particle, V_p is the particle velocity and m_p is particle mass.

Five body forces, i.e. pressure gradient force F_p , particle buoyancy force F_B , gravity force F_G , added mass force F_A , rotating coordinates force F_R , and fluid drag force F_D are considered as follows:

$$F_p = -\frac{\pi d_p^2}{4} \nabla P, \quad (4.22)$$

$$F_B = \frac{\pi d_p^2 \rho_f}{4} g, \quad (4.23)$$

$$F_B = \frac{\pi d_p^2 \rho_p}{4} g, \quad (4.24)$$

$$F_A = -\frac{m_p \rho_f}{2 \rho_p} \frac{dV_p}{dt}, \quad (4.25)$$

$$F_R = -m_p \left[2\Omega \times V_p + \Omega \times (\Omega \times V_p) \right], \quad (4.26)$$

and

$$F_p = \frac{\pi d_p^2 \rho_p C_D (V_p - V_f)^2}{8}, \quad (4.27)$$

where V_f and V_p are fluid and particle velocities, ρ_f , and ρ_p are fluid and particle densities.

The drag coefficient C_D is given by

$$C_D = \frac{24}{Re_s} (1 + 0.15 Re_s^{0.687}) \quad (4.28)$$

and

$$Re_s = \frac{\rho_f (V_p - V_f) d_p}{\mu_f} \quad (4.29)$$

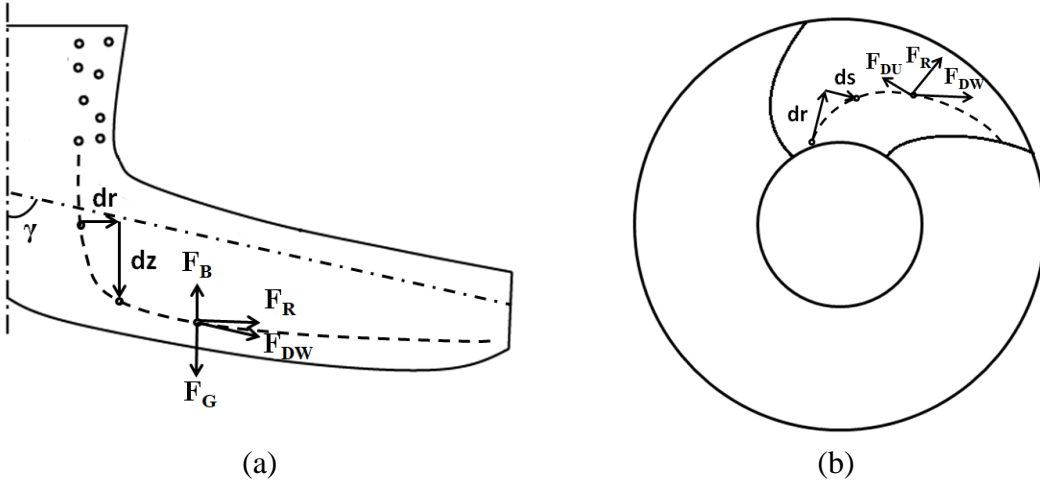


Figure 4.2 Particle trajectory (a) main view (b) top view

$$Re_s = \frac{\rho_f (V_p - V_f) d_p}{\mu_f} \quad (4.30)$$

the pressure gradient force, added mass force and Coriolis force. Newton's second law can be applied in three directions at position i : Z direction in Figure 4.2 (a), tangential U direction and flow passage W direction in Figure 4.2 (b). Then, the total force in three directions will become:

$$F_z = F_G - F_B + F_{DW} \cos \gamma \quad (4.31)$$

$$F_U = F_{DU} \quad (4.32)$$

$$F_W = F_{DW} + F_R \sin \beta_i \quad (4.33)$$

and

$$\beta_i = \beta_1 + \frac{(\beta_2 - \beta_1)(R_i - R_1)}{R_2 - R_1}, \quad (4.34)$$

where F_{DW} and F_{DU} correspond to the drag force in blade projection and blade tangential direction, β_i is the blade projection angle, R_i is the radius at position i , γ is the angle between the blade and z-axis. For a mixed type pump with a non-zero γ , β needs to be calibrated with β_H , the blade angle projection in the horizontal plane.

$$\beta = \arccos(\cos \beta_H \sin \gamma) \quad (4.35)$$

At impeller inlet, assuming particle velocity in the z -direction is same as fluid velocity, the relative particle velocity along impeller blade projection area is zero and tangential velocity is

$$U_t = R_t \Omega \quad (4.36)$$

Dividing the flow passage into several interval sections, particle position and velocity can be obtained. Once a particle touches the blade surface, the squeeze film effect needs to be included:

$$Re_p = \frac{\rho_p V_t d_p}{\mu_f}, \quad (4.37)$$

$$Re^* = \frac{12 \xi^2}{a}, \quad (4.38)$$

and

$$a = 8 \left[2 \left(\frac{\rho_p}{\rho_f} \right) + f_{av} \right], \quad (4.39)$$

where ξ , suggested as 10, is a dimensionless constant that depends on particle shape and f_{av} is suggested to be 1.0. Only if $Re_p > Re^*$, the particle can possess sufficient momentum

to penetrate the squeeze film and thus impinge the wall. Then, the particle velocity component normal to the wall is calculated by a factor Γ :

$$V_{P+} = \Gamma V_{iU} \sin \beta_i \quad (4.40)$$

$$V_{P//} = V_{iU} \cos \beta_i + V_{iW} \quad (4.41)$$

and

$$\Gamma = \frac{a}{a + \xi} \left(1 - \frac{Re^*}{Re_p} \right), \quad (4.42)$$

where V_{iU} is particle tangential velocity and V_{iW} is particle velocity along the blade projection direction at position i . Impact angle is:

$$\theta = \arctan \left(\frac{V_{P\perp}}{V_{P//}} \right), \quad (4.43)$$

Finally, the restitution effect on particle impact velocity is included as:

$$e_+ = 0.988 - 0.78\theta + 0.19\theta^2 - 0.024\theta^3 + 0.027\theta^4 \quad (4.44)$$

$$e_{//} = 1 - 0.78\theta + 0.84\theta^2 - 0.21\theta^3 + 0.028\theta^4 - 0.022\theta^5 \quad (4.45)$$

4.2.2.2 Erosion model

Erosion models based on wear mechanism have similar formulas and can be summarized into an empirical correlation that is widely used to evaluate erosion rate with the help of extensive databases using the following equation:

$$ER = KV_p^n F(\theta) \quad (4.46)$$

where K and n are experimentally determined constants that depend on the material properties. $F(\theta)$ is a function of the impact angle. Six models, including Ahlert et al. (1994), Haugen et al. (1995), Oka et al. (2005), Zhang et al. (2007), Mansouri (2014) and DNV (2015), reviewed in Section 1.1.2.

4.2.3 Abrasion prediction

4.2.3.1 Abrasion model

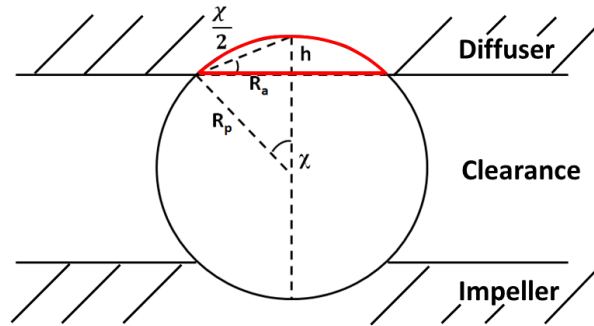


Figure 4.3 Abrasion caused by particle between the sealing surface

Figure 4.3 shows a particle between the sealing surfaces of the impeller and diffuser. The penetrated depth in Figure 4.3 is h , and the radius of the penetrated surface is R_a . Then R_a can be calculated by local load dP and target surface Brinell hardness BH .

$$R_a = \left(\frac{dP}{BH\pi} \right)^{\frac{1}{2}}. \quad (4.47)$$

If $R_a > R_p$, the total volume of fragments removed from the target surface is close to particle volume by a distance of $2R_p$. Therefore, total abrasion rate AR (volume per unit length) becomes

$$AR = K \sum \frac{1}{3} \pi R_p^2, \quad (4.48)$$

where K is a dimensionless constant, being suggested as 0.01

If $R_a < R_p$, the penetrated depth h and fragments removed by the particle can be obtained as:

$$\chi = \arcsin\left(\frac{R_a}{R_p}\right), \quad (4.49)$$

$$h = R_a \tan(\chi), \quad (4.50)$$

and

$$dV = \frac{1}{3} \pi (3R_a - h) \times h^2. \quad (4.51)$$

Since the above volume is formed by the distance of $2R_a$, then total abrasion rate AR can be calculated as follows:

$$AR = K \sum \frac{dV}{2Ra}, \quad (4.52)$$

where K is a dimensionless constant, P is the total normal load, BH is target surface Brinell hardness. The value of K is suggested to be $1e-4$.

The fraction of particles that present between the sealing surface is assumed to be equal to the ratio of leakage flow rate and inlet flow rate. Then, abrasion can be roughly predicted by Archard (1953) equation. Finally, pump geometry inputs are modified and head degradation can be calculated.

4.2.3.2 Load calculation

Figure 4.4 shows the impeller force balance in the radial direction, the blue area is leakage area between diffuser and impeller, the dash line is impeller rotation orbit. The rotation radius is the same as the elastic deflection δ of the shaft.

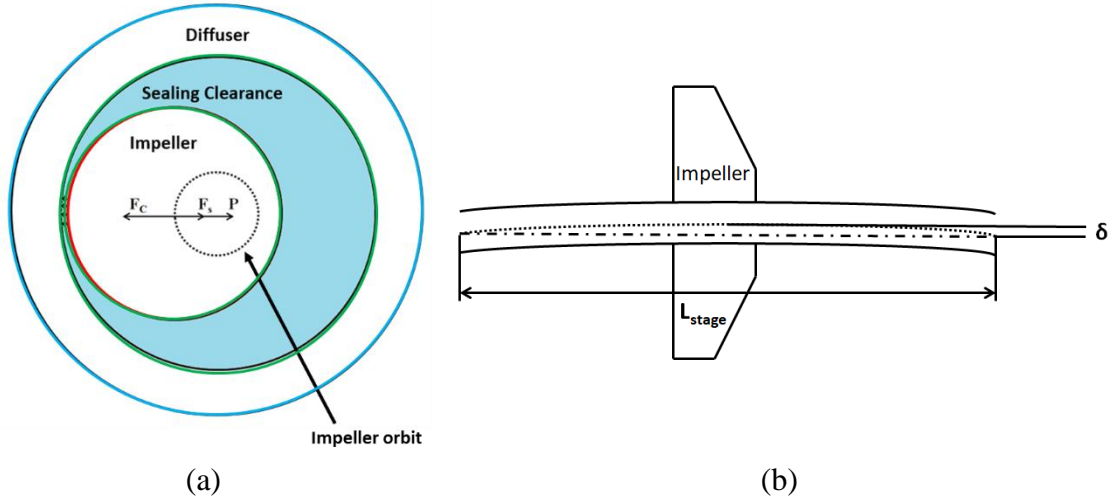


Figure 4.4 Impeller orbit and force balance (a) top view (b) main view

$$P = F_C - F_s, \quad (4.53)$$

$$F_C = m_{impeller} \Omega^2 \delta, \quad (4.54)$$

$$F_s = \frac{48\delta EI}{L_{stage}^3}, \quad (4.55)$$

and

$$\delta = S_L - R_p, \quad (4.56)$$

where E is the modulus of elasticity, I is moment of inertia of the shaft's cross-section, L_{stage} is the length of one stage, $m_{impeller}$ is impeller weight, S_L is leakage width. Once load P is obtained from Equation (4.53), the abrasion erosion rate can be calculated. Leakage width can be updated at each time step, and the reduced performance can be calculated with increased leakage width.

Based on the mechanistic models, the calculation flow chart for ESP slurry flow is shown in Figure 4.5.

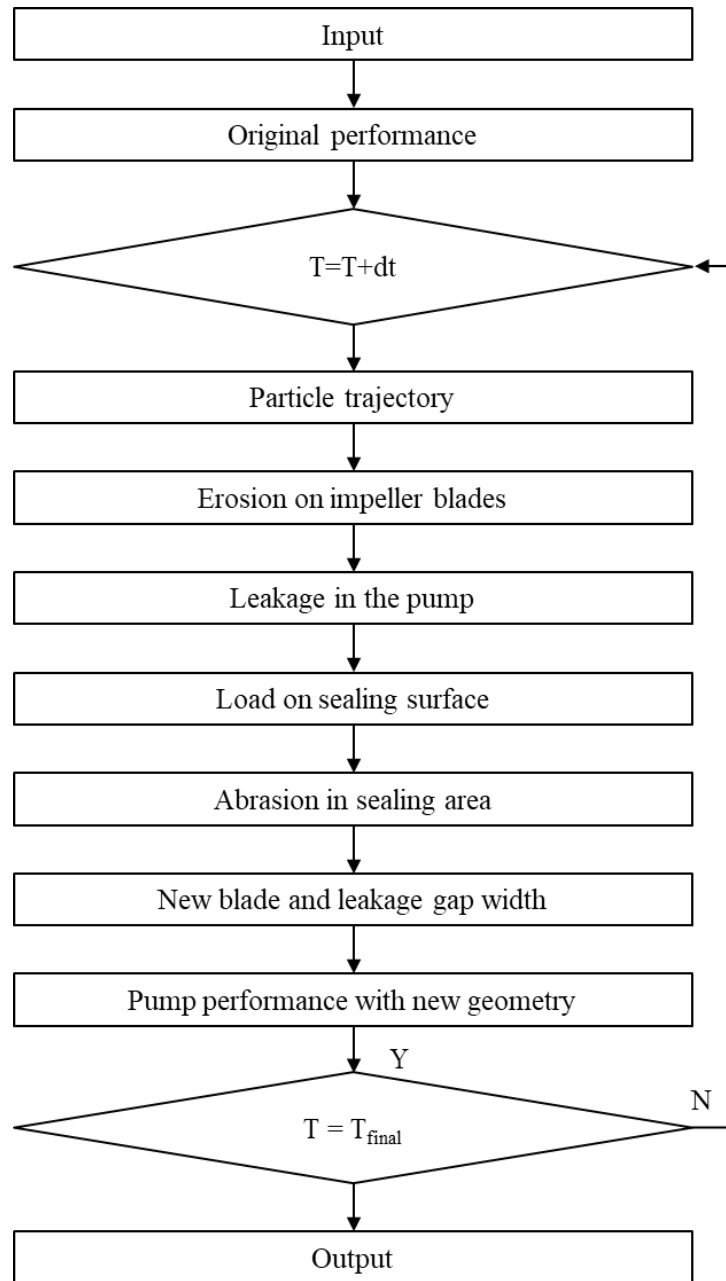


Figure 4.5 Flow chart for pump performance degradation calculation

4.2 Mechanistic Modeling Results

The mechanistic models for ESP performance predictions with modified leakage loss equations under single-phase and gas/liquid two-phase flow conditions are coded into

computer programs with the Fortran programming language. Thereafter, erosion and abrasion equations are included for wear calculations.

4.3.1 Abrasion validation

The dots in Figure 4.6 (a) are measured clearance after each time-period test and lines are the calculated clearance. As can be seen, the trend of the calculated clearance versus time, as well as the obtained values, match well with measured data. The error in Figure 4.6 (b) is less than 10%, which shows good accuracy.

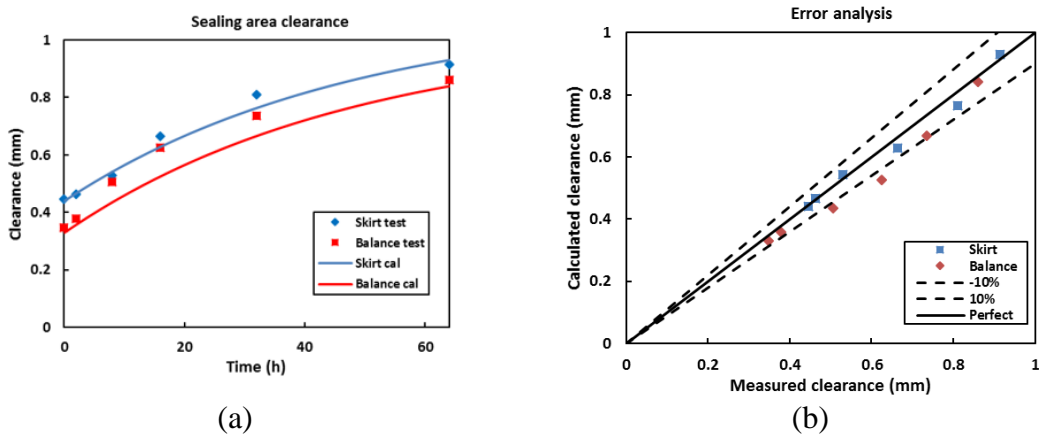


Figure 4.6 MTESP seals clearance validation, (a) skirt and balance ring clearance, (b) error analysis of seals clearance

4.3.2 Performance validation

Deteriorated head curves calculated by Zhu et al. (2018) and current study are shown in Figure 4.7 (a). The head curve by Zhu et al. (2018) has a similar trend to the experimental results of Stepanoff (1957), in which only inter-stage leakage was considered. According to sufficient Computational Fluid Dynamic (CFD) study on pressure and velocity profile inside ESPs (Zhu et al. 2018a, Shi et al 2017 and Shi et al. 2018), the pressure and velocity field of the inter-stage inlet and outlet is more stable and smooth than

that of other leakage regions. Therefore, it is presumable that the addition pump head loss due to turbulence around inter-stage clearance can be neglected. The pump head loss due to leakage flow in the inter-stage area can be added into other head losses due to the increased flow rate in the flow channel as described by Stepanoff (1957). However, in a complex mixed-type ESP geometry, ESP head loss due to leakage flow through skirt ring and balance ring clearances should be calculated as shown in this study.

Figure 4.7 (b) and (c) show the comparison and accuracy of tested and calculated head increment. Figure 8 (b) is a solid proof that the proposed method can capture the trend of the head curve in an eroded ESP. Besides a slight deviation at high flow rate region, the predicted head perfectly matches tested data within 5% error.

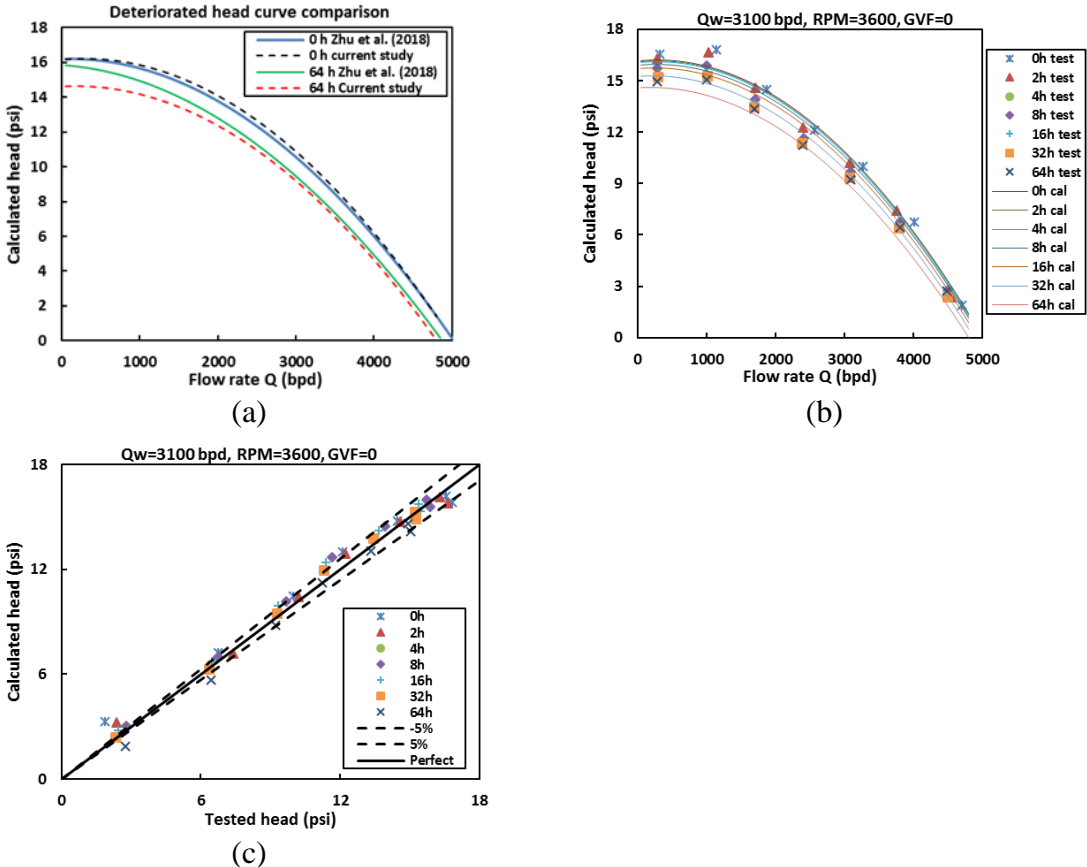


Figure 4.7 MTESP performance degradation validation, (a) deteriorated head comparison between current study and Zhu et al. (2018) (a) head curve tested vs. calculated, (b) error analysis between calculated head and measured head

CHAPTER 5

CONCLUSIONS AND RECOMMENDATIONS

In this section, the conclusions of three research methods, including experimental tests, numerical simulation, and mechanistic modeling are summarized separately to perform a comprehensive study on sand wear in ESPs and its effect on pump performance. In addition, recommendations for future studies are also provided separately.

5.1 Summary and Conclusions

5.1.1 *Experimental study*

1. In erosion tests, most of the impeller down-thrust washers for pumps 1, 3, and 4 were completely worn out after 8-16 hours, while some of pump 2's washers still remained after 64 hours. Obvious abrasion damage could be found and measured on sealing rings except that made by Tungsten carbide material.
2. The pump vibration amplitude and impeller orbits increased rapidly at the beginning and then became stable. The primary vibration is always at the pump rotation speed, which indicates the un-eroded carbide sleeves help sustain the pump rotation. As a result, the wear damage rate gradually decreased during 8-16 hours and became stable after 16 hours.
3. When carbide sleeves sustain the stage rotation, the load applied on solids gradually decreases as the clearance increases, which reduces the abrasion on

seal rings. In addition, the wear damage mechanism on stage seal rings is believed to gradually change from three-body abrasive wear to two-body erosive wear.

4. The gas and pump rotation speed effects on abrasion damage in ESPs are not significant in this study. However, lower rotation speed and higher *GVF* slightly decrease the abrasion damage on seal rings according to the geometry measurement after 64 hours. We stopped the test in this study since the 10% loss of the pump performance is already significant enough for some field applications.
5. From the paint-removal on the selected stage of MTESP, the erosion is more likely to be observed on impeller blade tips, the inside impeller shroud close to the balance hole, and the outside impeller shroud close to impeller outlet. High turbulence and shear flow in ESP can be the reason. In addition, the obvious erosion also locates on diffuser vane tips, flow channels and interaction zones between the impeller and diffuser.
6. The weight loss of diffusers is higher than that of the impeller, which is believed due to the higher impact velocity and angle from the simulated results with ANSYS Fluent.
7. Decreasing the pump rotation speed can decrease erosion damage on the whole stage. At the same time, more particles tend to hit the impeller inside shroud surface due to a lower centrifugal force.
8. In Cases 3 and 4, the erosion becomes more concentrated on impeller inside shroud surface and blade edges of impeller and diffuser when gas presents.

9. The erosion weight loss due to erosion damage surprisingly decreases in Cases 3 and 4 when gas presents. According to the paint-removal photos and CFD simulated erosion rate and pattern, the overall erosion damage and weight loss decrease with the presence of gas since it protects the impeller outside shroud of the tested pump.
10. On the other hand, the erosion damage becomes more concentrated and the blade shapes of impellers and diffusers change obviously in the test, which is same to field applications. The damage of the pump blade caused by gas presence may help explain the pump failure in field cases.
11. The abrasion damage in this study is much more obvious than the erosion damage. It is believed that most of the head loss is due to the abrasion damage on the seal rings in this study. Both pump head and efficiency deteriorate with the liquid-sand and gas-liquid-sand flow. The significant decrease in pump efficiency and boosting capacity is caused by increased leakage flow.
12. Additional head loss may be related to the turbulence caused by the increased leakage flow. The water performance at rotation speed $N = 3600$ rpm of the pump 1, 3 and 4 all decreased by about 10% due to the similar abrasion damage and erosion weight loss. The gas-liquid performance curves of Pumps 3 and 4 are also comparable.
13. Under low GVF condition (less than 5%), gas is believed to help resist leakage through stage seal rings. Compared to no-erosion ESP, the decrease of gas-liquid performance of the eroded pump at $Q_L = 3100$ bpd is less with more gas.

14. Further increasing *GVF* (more than 5%), the downward axial thrust force will not be strong enough to sustain the original impeller position. As a result, the impeller moves upward and more leakage flows through skirt rings especially when the down thrust washer is completely worn out. Therefore, the head of the eroded pump at $Q_L = 3100$ bpd deteriorated more with more gas compared to the no-erosion pump when *GVF* is higher than 5%.

5.1.2 Numerical simulations

1. Among the erosion models studied, Mansouri-water (2014) erosion equation has the best accuracy on overall erosion prediction of a complete stage. In addition, it is also possible to use Arabnejad-5 model (2015) in the impeller (2% error) and Haugen et al. (1995) model in the diffuser (5% error).
2. Since the inlet velocity and particle distribution of the first stage are different, the simulated flow field and erosion pattern differ significantly from the downstream stages.
3. Compared to transient DPM simulation, the predicted erosion rate and pattern by steady state DPM simulation with the DRWM method are acceptable when *GVF* is lower than 15%.
4. In air-water-solid simulations, the gas bubble diameter not only has a strong effect on pump performance calculation but also on the erosion prediction. Although head increment of the second stage calculated by different turbulence models agrees well with the correspondent catalog curve, the difference can still be found in erosion rates and patterns.

5. Compared with paint-removal photos and stage weight losses, the $k-\omega$ SST model can capture the erosion trend more accurately, especially the ratio between erosion on impeller and diffuser, while the accuracy of the $k-\varepsilon$ model simulation increases by using the enhanced wall function.
6. The impact area is more concentrated for the SST $k-\omega$ model, and the impact velocity and angle are slightly lower than the $k-\varepsilon$ model and RSM model. The average impact angle on both impeller and diffuser is $0-5^\circ$, and the average impact velocity is higher on diffuser outside shroud (5-10 m/s) and is lower on impeller inside shroud (1-4 m/s). The maximum impact angle and velocity can be as high as $30^\circ-50^\circ$ and 15 m/s on the diffuser shroud and impeller hub for MTESP separately.
7. Due to the low particle impact angle, the particle rebound effect can be neglected.
8. In general, the produced sand has a density between $1500 - 3000 \text{ kg/m}^3$ and a diameter of less than $300 \text{ }\mu\text{m}$. Within the above range, the erosion rate of the tested pump increased linearly with solid size and density.
9. The pump erosion tolerance depends on pump types. Higher erosion is found in radial type ESPs, especially on the impeller inside shroud surface, while erosion in mixed ESPs is not significant under water-sand flow. The average impact angle of the radial-type TE2700 increases to $0-10^\circ$ and the average impact velocity increases to 1-6 m/s on impeller inside shroud surface at the best efficiency point. The impact angle and velocity are 50-100% higher than that in a mixed type ESP with the same diameter.

10. Considering the significant effect of the velocity exponential factor, which is usually higher than 2, and the impact angle function, whose value increases sharply when the angle is less than 30° for ductile material, in erosion prediction models, the predicted erosion rate of the radial type ESP is much higher than the two simulated mixed type ESP.

5.1.3 Mechanistic modeling

1. By using the proposed model, both three-body abrasion rate and pump performance degradation can be accurately predicted.
2. According to the tested results in this study, the boosting head of a mixed-type ESP deteriorated more at a low flow rate under sandy flow condition, which is different from experiments conducted by Stepanoff (1957). A detailed leakage flow region figure is proposed and leakage flow through skirt and balance leakage are studied.
3. The improved mechanistic ESP performance prediction model can capture the trend of the decreased head curve under sandy flow conditions with acceptable accuracy. However, it should be noted that most ESPs have floated stages, whose impeller position changes according to the flow rate and axial thrust.
4. In most conditions, ESPs work in a down-thrust condition and impellers are pushed downwards to the diffusers ahead. Leakage through the skirt seals can be restrained with the presence of a down-thrust washer. As a result, most down-thrust washers were worn out rapidly during the test. On the contrary, up-

thrust washers are protected by the fluid and the clearance between the impeller balance ring top surface and diffuser balance bore is expanded.

5. Therefore, under the recommended working condition, leakage should have a tendency to flow through balance leakage regions. Since the impeller position is not considered in the proposed model, it is possible that the predicted head curve may have a little deviation in extreme working conditions.

5.2 Recommendations

5.2.1 Experimental study

1. Testing time may be increased to obtain a more prominent trend of pump geometry changes. Then, the effect of rotational speed and *GVF* can be better understood.
2. Erosion tests for NI-Resist Type-1 Iron may be conducted to develop the corresponding coefficients and improve the accuracy of CFD simulations.
3. More ESP sand wear tests may be conducted for different sand sizes, sand concentrations, and pump configurations.

5.2.2 Numerical simulations

1. In order to save the computation time, the frozen rotor method, which can predict pump performance with adaptable accuracy, is used in this study. However, the erosion contour is not centrosymmetric without considering the

real rotation. Therefore, sliding mesh method should be incorporated to validate the accuracy of the frozen rotor method.

2. Near wall mesh inflation grid layer thickness and pump inner domain mesh size effect to ESP erosion simulation need to be investigated
3. More attention needs to be paid to gas bubble size estimation, body force effect on the secondary phase and discrete phase, and more turbulence models.
4. The effect of the secondary flow region (leakage flow) needs to be analyzed. The over predicted erosion rate on diffuser throat area might be caused by neglecting the leakage flow effect, which can create additional vortex, reduce the particle speed, and protect the diffuser outside shroud surface.

5.2.3 *Mechanistic modeling*

1. The abrasion coefficient in the mechanistic model needs more data to be improved.
2. The additional leakage head loss coefficient needs to be validated with more experimental data.
3. The proposed model needs to be improved and validated under more gas-liquid multiphase flow conditions.

NOMENCLATURE

a	Circular area of contact formed when a sphere is pressed against a flat surface, L^2 , m^2
A	Annular area, L^2 , ft^2
AR	Abrasion rate, L^2 , m^3/m
B_g	Gas formation volume factor, ft^3/scf
B_o	Oil formation volume factor, bbf/STB
B_w	Water formation volume factor, bbf/STB
BH	Brinell hardness, ML^{-2} , $[kg/mm^2]$
BHP_{vis}	Brake horse power for viscous fluid flow, ML^2T^{-3} , hp
BHP_w	Brake horse power for water flow, ML^2T^{-3} , hp
C_{BHP}	Brake horse power correction factor
C_{drift}	Drift size of casing, L , in
C_h	Head correction factor
C_k	Characteristic velocities in cutting wear
C_q	Flow rate correction factor
C_t	Temperature correction factor
C_η	Efficiency correction factor
d	Pump diameter, L , m
d_{cable}	Cable diameter, L , in

d_{em}	Motor diameter, L, ft
d_{ic}	Motor casing diameter, L, ft
d_t	Tubing internal diameter, L, in
D_k	Characteristic velocities in deformation wear
D	Pipe diameter, L, mm
d_p	Particle diameter
e_{\perp}	Restitution effect in vertical direction
$e_{=}$	Restitution effect in horizontal direction
E	Young's modulus of sphere, $ML^{-1}T^{-2}$, grf/cm ²
ER	Erosion rate, target surface material removed by one particle kg/kg
E_{LK}	Friction loss factor by geometry changes
Eu	Euler number
F_A	Added mass force, MLT^{-2} , N
F_B	Particle buoyance force, MLT^{-2} , N
F_D	Fluid drag force, MLT^{-2} , N
F_{DW}	Drag force in blade projection, MLT^{-2} , N
F_{DU}	Drag force in blade projection and blade tangential direction, MLT^{-2} , N
F_G	Gravity force, MLT^{-2} , N
F_P	Pressure gradient force, MLT^{-2} , N
Fr	Froude number
F_R	Rotating coordinates force, MLT^{-2} , N

F_s	Particle shape factor, 1 for sharp, 0.53 for semi-round, or 0.2 for fully rounded sand particles or shear force caused by shaft deformation, N
$F(\theta)$	Particle impact angle function
F_{av}	Dimensionless constant for squeeze film effect
f_{Moody}	Moody friction factor
g	Gravity acceleration, LT^{-2} , ft/s^2
G	Conductance
GOR	Production gas/oil ratio, scf/STB
h	Penetration rate, LT^{-1} , mm/yr
H_{req}	Pump required total dynamic head, L, ft
H_{stg}	Pump dynamic head of each stage, L, ft
H_{vis}	Pump head at BEP, L, ft
H_w	Head for viscous fluid flow, L, ft
H_{wBEP}	Head for water flow, L, ft
HP_h	Hydraulic horsepower, ML^2T^{-3} , hp
HP_{pump}	Pump motor load, ML^2T^{-3} , hp
H_v	Vicker's Hardness, [GPa]
K	Empirical erosion parameter constant
L_{stage}	Length of one stage, L, m
$m_{impeller}$	Impeller weight, M, kg
m_p	Particle mass, M, kg
M	Total mass of impinging particles, M, g

N_S	Specific speed
N	Rotational speed, T^{-1} , rpm
n	Empirical impact velocity exponential constant
P	load on abrasion particle, M, kg
p_m	Flow pressure of the deformable member (hardness), MLT^{-2} , N
p_{pr}	Pseudo-reduced pressure, MLT^{-2} , psia
p_{pc}	Critical pressure, MLT^{-2} , psia
Pr	Prandtl number
Re	Reynolds number
Rr	Particle roundness factor from 0.1 to 1.
St	Strouhal number
V	Velocity, LT^{-1} , cm/s
V_P	Particle impact velocity, LT^{-1} , cm/s
V_f	Fluid velocity, LT^{-1} , m/s
V_{iU}	Particle tangential velocity at position I, LT^{-1} , m/s
V_{iW}	Particle velocity along the blade projection direction at position I, LT^{-1} , m/s
V_{pi}	Particle impact velocity, LT^{-1} , m/s
W	Worn volume per unit sliding distance, L^3 , cm^3/m or m^3/m
W_C	Work done by centrifugal force, MLT^{-2} , N
y	Elastic load limit, MLT^{-2} , gf/cm^2
Z	Number of atoms removed per atomic encounter

Greek Letters

α	Inclination angle, °
α_G	In-situ gas void fraction
β_i	Blade projection angle at position i, °
β_H	Blade angle projection in the horizontal plane, °
Γ	Squeeze film penetration factor
ε	Energy needed to move a unit volume of material from body, MT^{-2} , $grfcm/cm^3$, or dimensionless constant for squeeze film effect
θ	Impact angle, °
θ_0	Impact angle at which the horizontal velocity component becomes zero when leaving the body, °
ν	Poisson's ratio of sphere
ρ_A	Average density, ML^{-3} , kg/m^3
ρ_g	Gas density, ML^{-3} , lb/ft^3
ρ_l	Liquid density, ML^{-3} , lb/ft^3
ρ_f	Fluid density, ML^{-3} , kg/m^3
ρ_p	Particle density, ML^{-3} , kg/m^3
σ	Interfacial tension, MT^{-2} , N/m or specific conductivity of the two materials
σ_y	Yield stress of target $ML^{-1}T^{-2}$, N/m^2

Subscripts

ave Average

<i>C</i>	Cutting
<i>D</i>	Deformation
<i>el</i>	Elastic limit
<i>P</i>	Sand particle
<i>S</i>	Component surface
<i>t</i>	Total

BIBLIOGRAPHY

- Ahlert, K. (1994). Effects of Particle Impingement Angle and Surface Wetting on Solid Particle Erosion of AISI 1018 Steel. Ph.D. Dissertation, The University of Tulsa.
- Arabnejad, H., Mansouri, A., Shirazi, S. A., and McLaury, B. S. (2015). Development of Mechanistic Erosion Equation for Solid Particles. *Wear*, 332–333, 1044–1050.
<https://doi.org/10.1016/j.wear.2015.01.031>
- Archard, J. F. (1953). Contact and Rubbing of Flat Surfaces. *Journal of Applied Physics*, 24(8), 981–988. <https://doi.org/10.1063/1.1721448>
- Bai, C., Zheng, D., Hure, R., Saleh, R., Carvajal, N., and Morrison, G. (2019). The Impact of Journal Bearing Wear on an Electric Submersible Pump in Two-Phase and Three-Phase Flow. *Journal of Tribology*, 141(5), 051702.
<https://doi.org/10.1115/1.4042773>
- Basaran, B. (2017). CFD Simulation for the Erosion on Electrical Submersible Pump due to Viscosity and Air Presence. Ph.D. Dissertation, Texas AandM University.
- Bertoneri, M., Wilcox, M., Toni, L., and Beck, G. (2014). Development of Test Stand for measuring Aerodynamix, Erosion, and Rotordynamic Performance of a Centrifugal Compressor under Wet Gas Conditions. *Proceedings of the ASME Turbo Txpo 2014: Turbine Technical Conference and Exposition*. Düsseldorf, Germany, June 16-20, 2014: Paper No. GT2014-25349.
- Bitter, J. G. A. (1963a). A Study of Erosion Phenomena Part I. *Wear*, 6, 5–21.
[https://doi.org/10.1016/0043-1648\(63\)90003-6](https://doi.org/10.1016/0043-1648(63)90003-6)

- Bitter, J. G. A. (1963b). A Study of Erosion Phenomena Part II. *Wear*, 6, 169–190.
[https://doi.org/10.1016/0043-1648\(63\)90073-5](https://doi.org/10.1016/0043-1648(63)90073-5)
- Chen, X., McLaury, B. S., and Shirazi, S. A. (2004). Application and Experimental Validation of a Computational Fluid Dynamics (CFD)-Based Erosion Prediction Model in Elbows and Plugged Tees. *Computers and Fluids*, 33(10), 1251–1272.
<https://doi.org/10.1016/j.compfluid.2004.02.003>
- Childs, D. W. (1983). Dynamic Analysis of Turbulent Annular Seals based on Hirs' Lubrication Equation. *Journal of Tribology*, 105(3), 429–436.
<https://doi.org/10.1115/1.3254633>
- Coutier-Delgosha, O., Fortes-Patella, R., Reboud, J. L., Hofmann, M., and Stoffel, B. (2003). Experimental and numerical studies in a centrifugal pump with two-dimensional curved blades in cavitating condition. *Journal of Fluids Engineering, Transactions of the ASME*, 125(6), 970–978. <https://doi.org/10.1115/1.1596238>
- Chen, P., Meng, M., Ren, R., Miska, S., Yu, M., Ozbayoglu, E., and Takach, N. (2019). Modeling of PDC Single Cutter – Poroelastic Effects in Rock Cutting Process. *Journal of Petroleum Science and Engineering*, 183, 106389.
<https://doi.org/10.1016/j.petrol.2019.106389>
- Chen, P., Miska, S. Z., Ren, R., Yu, M., Ozbayoglu, E., and Takach, N. (2018). Poroelastic Modeling of Cutting Rock in Pressurized Condition. *Journal of Petroleum Science and Engineering*, 169, 623–635.
<https://doi.org/10.1016/j.petrol.2018.06.009>
- Chi, Y., Sarica, C., and Daraboina, N. (2019). Experimental Investigation of Two-phase Gas-oil Stratified Flow Wax Deposition in Pipeline. *Fuel*, 247, 113–125.

<https://doi.org/10.1016/j.fuel.2019.03.032>

Chi, Y., Zhou, S., Daraboina, N., and Sarica, C. (2018). Experimental Study of Wax Deposition under Two-phase Gas-oil Stratified Flow. *Proceedings of the 11th North American Conference on Multiphase Technology*, 153–167. Banff, Canada, June 8-16, 2016: Paper No. BHR-2018-153.

Daraboina, N., Chi, Y., Sarica, C., Pereyra, E., and Scott, S. L. (2018). Effects of High Pressure on the Performance of Existing Two-Phase Flow models in Wellbores. *Proceedings of the SPE Annual Technical Conference and Exhibition*.

<https://doi.org/10.2118/191597-ms>

Darihaki, F., Zhang, J., and Shirazi, S. A. (2019). Solid Particle Erosion in Gradual Contraction Geometry for a Gas-Solid System. *Wear*, 426–427, 643–651.

<https://doi.org/10.1016/j.wear.2019.01.106>

Davis, R. S. (1992). Equation for the determination of the density of moist air (1981/91). *Metrologia*, 29(1), 67–70. <https://doi.org/10.1088/0026-1394/29/1/008>

Dubey, A., Chi, Y., and Daraboina, N. (2017). Investigating the Performance of Paraffin Inhibitors under Different Operating Conditions. *Proceedings of the SPE Annual Technical Conference and Exhibition*. <https://doi.org/10.2118/187252-ms>

Edwards, J. K. (2000). Development, validation, and application of a three-dimensional , CFD-based erosion prediction procedure. Ph.D. Dissertation, The University of Tulsa.

Falomi, S., Bertoneri, M., Scarbolo, L., and Ferrara, V. (2016). Performance Test of a Liquid Tolerant Impeller and Validation of Wet Compression Predictive Model. *Proceedings of the 45th Turbomachinery and 32nd Pump Symposia*. Houston,

Texas, USA, September 12-15, 2016.

Finnie, I. (1960). Erosion of Surfaces by Solid Particles. *Wear*, 3, 87–103.

[https://doi.org/10.1016/0043-1648\(60\)90055-7](https://doi.org/10.1016/0043-1648(60)90055-7)

Forder, A., Thew, M., and Harrison, D. (1998). A numerical investigation of solid particle erosion experienced within oilfield control valves. *Wear*, 216(2), 184–193.

[https://doi.org/10.1016/S0043-1648\(97\)00217-2](https://doi.org/10.1016/S0043-1648(97)00217-2)

Gahr, K. H. Z. (1998). Wear by hard particles. *Tribology International*, 31(10), 587–596.

[https://doi.org/10.1016/S0301-679X\(98\)00079-6](https://doi.org/10.1016/S0301-679X(98)00079-6)

Grant, G., and Tabakoff, W. (1975). Erosion Prediction in Turbomachinery Resulting from Environmental Solid Particles. *Journal of Aircraft*, 12(5), 471–478.

<https://doi.org/10.2514/3.59826>

Gülich, J. F. (2008). Centrifugal Pumps. *Springer-Verlag*, Berlin Heidelberg,

<https://doi.org/10.1017/CBO9781107415324.004>

Haider, G., Arabnejad, H., Shirazi, S. A., and Mclaury, B. S. (2017a). A Mechanistic Model for Stochastic Rebound of Solid Particles with Application to Erosion Predictions. *Wear*, 376–377, 615–624. <https://doi.org/10.1016/j.wear.2017.02.015>

Haider, G., Asgharpour, A., Zhang, J., and Shirazi, S. A., (2019). A Statistical Approach for Modeling Stochastic Rebound Characteristics of Solid Particles. *Proceedings of the ASME 2019 ASME-JSME-KSME Joint Fluids Engineering Conference*. San Francisco, CA, USA, July 28-Aug 1: Paper No. AJKFLUIDS2019-4655.

<https://doi.org/10.1115/AJKFluids2019-4655>

Haider, Ghulam. (2017b). Mechanistic Modelling for Rebound of Solid Particles with Applications to Erosion Predictions. Master Thesis. The University of Tulsa. Tulsa,

OK.

Hashish, M. (1988). Visualization of the Abrasive-Waterjet Cutting Process.

Experimental Mechanics, 28(2), 159–169. <https://doi.org/10.1007/BF02317567>

Haugen, K., Kvernfold, O., Ronold, A., and Sandberg, R. (1995). Sand erosion of wear-resistant materials: Erosion in choke valves. *Wear*, 186–187, 179–188.

[https://doi.org/10.1016/0043-1648\(95\)07158-X](https://doi.org/10.1016/0043-1648(95)07158-X)

Holm, R. (1967). Electric Contacts Theory and Application. *Springer-Verlag*, Berlin Heidelberg, [https://doi.org/10.1016/0043-1648\(58\)90392-2](https://doi.org/10.1016/0043-1648(58)90392-2)

Jiang, J., Younis, R. M., Thompson, L., and Liu, Z. (2015). Rate Transient Effects of Various Complex Fracture Network Topologies in Unconventional Gas Reservoirs: A Numerical Simulation Study. *Proceedings of the SPE Unconventional Resources Technology Conference, URTeC 2015*. <https://doi.org/10.2118/178701-ms>

King, D. G., Traylor, F. T., and Stewart, R. E. (1983). Abrasion Technology for Electric Submersible Pumps. *Proceedings of the SPE Annual Technical Conference and Exhibition*. <https://doi.org/10.2118/12199-MS>

Krüger, S., Martin, N., and Dupont, P. (2010). Assessment of Wear Erosion in Pump Impellers. *Proceedings of the Twenty-Sixth International Pump Users Symposium*. <https://doi.org/10.1093/nq/s1-III.71.193>

Liu, Y., Chen, S., Guan, B., and Xu, P. (2019a). Layout Optimization of Large-Scale Oil–Gas Gathering System based on Combined Optimization Strategy. *Neurocomputing*, 332, 159–183. <https://doi.org/10.1016/j.neucom.2018.12.021>

Liu, Z., and Forouzanfar, F. (2018). Ensemble Clustering for Efficient Robust Optimization of Naturally Fractured Reservoirs. *Computational Geosciences*, 22(1),

283–296. <https://doi.org/10.1007/s10596-017-9689-1>

Liu, Z., Forouzanfar, F., and Zhao, Y. (2018). Comparison of SQP and AL algorithms for deterministic constrained production optimization of hydrocarbon reservoirs.

Journal of Petroleum Science and Engineering, 171, 542–557.

<https://doi.org/10.1016/j.petrol.2018.06.063>

Liu, Z., and Reynolds, A. C. (2019b). An SQP-filter Algorithm with an Improved Stochastic Gradient for Robust Life-cycle Optimization Problems with Nonlinear Constraints. *Proceedings of the SPE Reservoir Simulation Conference 2019, RSC 2019*, (1988). <https://doi.org/10.2118/193925-ms>

Liu, Z., and Reynolds, A. C. (2019). History Matching an Unconventional Reservoir with a Complex Fracture Network. *Proceedings of the SPE Reservoir Simulation Conference 2019, RSC 2019*. <https://doi.org/10.2118/193921-ms>

Mansouri, A., Arabnejad, H., Shirazi, S. A., and McLaury, B. S. (2014). A Combined CFD/Experimental Methodology for Erosion Prediction. *Wear*, 332–333, 1090–1097. <https://doi.org/10.1016/j.wear.2014.11.025>

Marsis, E., and Russell, R. (2013). A State-of-the-Art Computational Fluid Dynamics Simulation for Erosion Rates Prediction in a Bottom Hole Electrical Submersible Pump. *Proceedings of the SPE Heavy Oil Conference*, 2, 802–815. Calgary, Alberta, Canada, June 11-13, 2013: Paper No. SPE-165452-MS.

Meng, M., Chen, P., and Ren, R. (2019a). Statistic Evaluation of Failure Criteria in Wellbore Stability with Temperature Effects. *Fuel*, 252(April), 730–752.

<https://doi.org/10.1016/j.fuel.2019.04.110>

Meng, M., Chen, P., and Ren, R. (2019b). Statistic Evaluation of Failure Criteria in

Wellbore Stability with Temperature Effects. *Fuel*, 252, 730–752.

<https://doi.org/10.1016/j.fuel.2019.04.110>

Meng, M., Qiu, Z., Zhong, R., Liu, Z., Liu, Y., and Chen, P. (2019). Adsorption Characteristics of Supercritical CO₂/CH₄ on Different Types of Coal and a Machine Learning Approach. *Chemical Engineering Journal*, 368, 847–864.
<https://doi.org/10.1016/j.cej.2019.03.008>

Minemura, K., Zhong, Y., and Uchiyama, T. (1995). Numerical Prediction of Erosion Wear on Pump Casing under Solid-Water Two-Phase Flow Conditions. *Advances in Multiphase Flow*, 61(587), 2571–2578. <https://doi.org/10.1299/kikaib.61.2571>

Morrison, G., Chen, Y., Steck, D., Chen, Y., Bai, C., and Patil, A. (2017). Effect of Gas Presence on Erosive Wear of Split-Vane Electrical Submersible Pump. *Proceedings of the 46th Turbomachinery and 33rd Pump Symposia*. Houston, Texas, USA, December 11-14, 2017.

Morrison, G. L., Carvajal, N., Saleh, R., and Bai, C. (2015). The Measured Impact of Erosion on the Rotodynamic and Performance Characteristics of a Mixed Flow ESP. *Turbomachinery and Pump Symposia*. Houston, Texas, September 14-17, 2015.

Moses, D., Haider, G., and Henshaw, J. (2019). An Investigation of the Failure of a 1/4” Ball Valve. *Engineering Failure Analysis*, 100, 393–405.
<https://doi.org/10.1016/j.engfailanal.2019.02.047>

Muhlbauer, M., Thamsen, P. U., Liersch, J., Michael, J., and Wagner, M. (2018). Construction of a Rain Erosion Test Rig for Wind Energy Blade Coatings. *Proceedings of the ASME 2018 5th Joint US-European Fluids Engineering Division Summer Meeting*. <https://doi.org/10.1088/0268-1242/11/3/009>

- Oka, Y. I., Okamura, K., and Yoshida, T. (2005). Practical Estimation of Erosion Damage Caused by Solid Particle Impact: Part 1: Effects of Impact Parameters on a Predictive Equation. *Wear*, 259(1–6), 95–101.
<https://doi.org/10.1016/j.wear.2005.01.039>
- Oka, Y. I., and Yoshida, T. (2005). Practical Estimation of Erosion Damage Caused by Solid Particle Impact: Part 2: Mechanical Properties of Materials Directly Associated with Erosion Damage. *Wear*, 259(1–6), 102–109.
<https://doi.org/10.1016/j.wear.2005.01.040>
- Parsi, M., Kara, M., Sharma, P., McLaury, B. S., and Shirazi, S. A. (2016). Comparative study of different erosion model predictions for single-phase and multiphase flow conditions. *Proceedings of the Annual Offshore Technology Conference*, 5, 3926–3945.
- Parsi, M., Najmi, K., Najafifard, F., Hassani, S., McLaury, B. S., and Shirazi, S. A. (2014). A Comprehensive Review of Solid Particle Erosion Modeling for Oil and Gas Wells and Pipelines Applications. *Journal of Natural Gas Science and Engineering*, 21, 850–873. <https://doi.org/10.1016/j.jngse.2014.10.001>
- Pirouzpanah, S. (2014). *Experimental Measurement of Multiphase Flow and CFD Erosion Modeling in Electrical Submersible Pumps*. Texas AandM University.
- Pirouzpanah, S., and Morrison, G. L. (2014). Predictive Erosion Modeling in an ESP Pump. *Proceedings of the ASME 2014 4th Joint US-European Fluids Engineering Division Summer Meeting*. Chicago, Illinois, USA, August 3-7, 2014: Paper No. FEDSM2014-21101.
- Recommended Practice RP-O501: Managing Sand Production and Erosion*. (2015).

Hovik, Norway: DNV GL.

Russell, R., Shirazi, S., and Macrae, J. (2004). A New Computational Fluid Dynamics Model to Predict Flow Profiles and Erosion Rates in Downhole Completion Equipment. *Proceedings of the SPE Annual Technical Conference and Exhibition*. Houston, Texas, USA, September 26-29, 2004: Paper No. SPE-90734-MS.

Rabinowicz, E. (1965). Friction and Wear of Materials, *John Wiley and Sons*, New York, 168-169

Salama, M. M. (2000). An alternative to api 14e erosional velocity limits for sand-laden fluids. *Journal of Energy Resources Technology*, 122(2), 71–77.
<https://doi.org/10.1115/1.483167>

Sedrez, T. A., Rajkumar, Y. R., Shirazi, S. A., Khanouki, H. A., and McLaury, B. S. (2018). CFD Predictions and Experiments of Erosion of Elbows in Series in Liquid Dominated Flows. *Proceedings of the ASME 2018 5th Joint US-European Fluids Engineering Division Summer Meeting*, <https://doi.org/10.1115/FEDSM2018-83116>

Shi, Y., Zhu, H., Zhang, J., Yin, B., Xu, R., and Zhao, J. (2017). Investigation of Condition Parameters in Each Stage of a Three-Stage Helico-Axial Multiphase Pump via Numerical Simulation. *Proceedings of the International Offshore and Polar Engineering Conference*, 156–162.

Shi, Y., Zhu, H., Zhang, J., Zhang, J., and Zhao, J. (2018). Experiment and Numerical Study of a New Generation Three-Stage Multiphase Pump. *Journal of Petroleum Science and Engineering*, 169, 471–484.
<https://doi.org/10.1016/j.petrol.2018.06.011>

Tang, H., Zhang, S., Zhang, F., and Venugopal, S. (2019). Time Series Data Analysis for

- Automatic Flow Influx Detection during Drilling. *Journal of Petroleum Science and Engineering*, 172, 1103–1111. <https://doi.org/10.1016/j.petrol.2018.09.018>
- Tilly, G. P. (1973). A Two Stage Mechanism of Ductile Erosion. *Wear*, 23(1), 87–96. [https://doi.org/10.1016/0043-1648\(73\)90044-6](https://doi.org/10.1016/0043-1648(73)90044-6)
- Wakeman, T., and Tabakoff, W. (1982). Measured Particle Rebound Characteristics Useful for Erosion Prediction. *Proceedings of the ASME Turbo Expo*, <https://doi.org/10.1115/82-GT-170>
- Wang, Z., Zhang, J., Shirazi, S. A., and Dou, Y. (2019a). Experimental and Numerical Study of Erosion in a Non-Newtonian Hydraulic Fracturing Fluid. *Wear*, 422–423, 1–8. <https://doi.org/10.1016/j.wear.2018.12.080>
- Wang, Z., Zhang, J., Shirazi, S. A., and Dou, Y. (2019b). Predicting Erosion in a Non-Newtonian Shear-thinning Jet Flow with Validated CFD Models from PIV and PTV Measurements. *Wear*, 426–427, 501–506. <https://doi.org/10.1016/j.wear.2018.12.027>
- Wang, Z., Bai, Y., Zhang, H., and Liu, Y. (2019c). Investigation on Gelation Nucleation Kinetics of Waxy Crude Oil Emulsions by Their Thermal Behavior. *Journal of Petroleum Science and Engineering*, Vol. 181. <https://doi.org/10.1016/j.petrol.2019.106230>
- Wilson, B. L. (1990). The Effects of Abrasives on Electrical Submersible Pumps. *SPE Drilling Engineering*, 5(2), 171–175. <https://doi.org/10.2118/17583-PA>
- Zahedi, P., Asgharpour, A., Khanouki, H. A., McLaury, B. S., and Shirazi, S. A. (2018). Experimental Investigation of Flow Behavior in a Bend and Sand Erosion Pattern under Single-Phase and Multiphase Flow Conditions. *Proceedings of the ASME*

2018 5th Joint US-European Fluids Engineering Division Summer Meeting,

<https://doi.org/10.1115/FEDSM2018-83238>

Zhang, J. (2018). *Improvements to a Semi-Mechanistic erosion Prediction Procedure*.

The University of Tulsa.

Zhang, J., Darihaki, F., Rajkumar, Y., Karimi, S., and Shirazi, S. A. (2019a). Erosion in

Sudden Contractions and Expansions. *Proceedings of the NACE - International*

Corrosion Conference. Nashville, Tennessee, USA, March 24-28, 2019: Paper No.

NACE-2019-13469.

Zhang, J., Darihaki, F., and Shirazi, S. A. (2019b). A Comprehensive CFD-Based

Erosion Prediction for Sharp Bend Geometry with Examination of Grid Effect.

Wear, 430–431, 191–201. <https://doi.org/10.1016/j.wear.2019.04.029>

Zhang, J., McLaury, B. S., and Shirazi, S. A. (2018a). Modeling Sand Fines Erosion in

Elbows Mounted in Series. *Wear*, 402–403, 196–206.

<https://doi.org/10.1016/j.wear.2018.02.009>

Zhang, J., McLaury, B. S., and Shirazi, S. A. (2018b). Modeling Sand Fines Erosion in

Elbows Mounted in Series. *Wear*, 402–403, 196–206.

<https://doi.org/10.1016/j.wear.2018.02.009>

Zhang, P., Zhang, S., Hu, N., Zhang, F., Makhmoor, F., and Sandoval, J. C. (2017).

Effect of pressure depletion on stress field and casing load alteration in mature

fields: A case study. *SPProceedings of the SPE Latin America and Caribbean Mature*

Fields Symposium. <https://doi.org/10.2118/184902-ms>

Zhang, S., Zhong, R., and Liu, Y. (2016). Numerical Modeling of Land Subsidence

Resulting from Oil Production. *50th US Rock Mechanics / Geomechanics*

Symposium 2016, 1, 499–508.

Zhang, Y., Reuterfors, E. P., McLaury, B. S., Shirazi, S. A., and Rybicki, E. F. (2007).

Comparison of Computed and Measured Particle Velocities and Erosion in Water and Air Flows. *Wear*, 263, 330–338. <https://doi.org/10.1016/j.wear.2006.12.048>

Zheng, D. (2013). Three-Phase Erosion Testing and Vibration Analysis of an Electrical Submersible Puypump. Master Thesis, Texas AandM University.

Zhou, S., Yan, H., Su, D., Navaneethakannan, S., and Chi, Y. (2018). Investigation on the Kinetics of Carbon Dioxide Hydrate Formation using Flow Loop Testing. *Journal of Natural Gas Science and Engineering*, 49, 385–392.

<https://doi.org/10.1016/j.jngse.2017.10.022>

Zhu, H., Jianjun, Z., Rutter, R., Jiecheng, Z., and Zhang, H.-Q. (2018a). Sand Erosion Model Prediction, Selection and Comparison for Electrical Submersible Pump (ESP) using CFD Method. *Proceedings of the ASME 2018 5th Joint US-European Fluids Engineering Division Summer Meeting*. <https://doi.org/10.1115/FEDSM2018-83179>

Zhu, H., Zhang, J., Zhu, J., Rutter, R., and Zhang, H.-Q. (2019a). A Numerical Study of Turbulence Model and Rebound Model Effect on Erosion Simulations in an Electrical Submersible Pump (ESP). *Proceedings of the ASME 2019 ASME-JSME-KSME Joint Fluids Engineering Conference*. San Francisco, CA, USA, July 28-Aug 1: Paper No. AJKFLUIDS2019-5538. <https://doi.org/10.1115/AJKFluids2019-5538>

Zhu, H., Zhu, J., Rutter, R., and Zhang, H.-Q. (2019b). A Numerical Study on Erosion Model Selection and Effect of Pump Type and Sand Characters in Electrical Submersible Pumps (ESPs) by Sandy Flow. *Journal of Energy Resources Technology*, 141(12), 122004. <https://doi.org/10.1115/1.4044941>

- Zhu, H., Zhu, J., Zhang, J., and Zhang, H. Q. (2017a). Efficiency and Critical Velocity Analysis of Gravitational Separator through CFD Simulation. *Proceedings of the ASME International Mechanical Engineering Congress and Exposition*, <https://doi.org/10.1115/IMECE2017-71230>
- Zhu, H., Zhu, J., Zhou, Z., Rutter, R., Forsberg, M., Gunter, S., and Zhang, H. Q. (2019c). Experimental Study of Sand Erosion in Multistage Electrical Submersible Pump ESP: Performance Degradation, Wear and Vibration. *Proceedings of the SPE International Petroleum Technology Conference*. <https://doi.org/10.2523/IPTC-19264-MS>
- Zhu, H., Zhu, J., Zhou, Z., Rutter, R., and Zhang, H. Q. (2019d). Wear and Its Effect on Electrical Submersible Pump ESP Performance Degradation by Sandy Flow: Experiments and Modeling. *Proceedings of the Offshore Technology Conference*. <https://doi.org/10.4043/29480-MS>
- Zhu, J., Banjar, H., Xia, Z., and Zhang, H. Q. (2016). CFD Simulation and Experimental Study of Oil Viscosity Effect on Multi-Stage Electrical Submersible Pump (ESP) Performance. *Journal of Petroleum Science and Engineering*, 146, 735–745. <https://doi.org/10.1016/j.petrol.2016.07.033>
- Zhu, J., Farfan, J. A. M., Zhang, J., Cuamatzi-Melendez, R., Zhu, H., and Zhang, H. Q. (2018b). Flow Pattern Prediction in Electrical Submersible Pump (ESP) under Gassy Flow Conditions using Transient Multiphase CFD Methods with Visualization Experimental Validation. *Proceedings of the ASME 2018 5th Joint US-European Fluids Engineering Division Summer Meeting*, <https://doi.org/10.1115/FEDSM2018-83081>

- Zhu, J., Wang, Z., Zhu, H., Cuamatzi-Melendez, R., Martinez-Farfan, J. A., Jiecheng, Z., and Zhang, H. Q. (2018c). Mechanistic Modeling of Electrical Submersible Pump ESP Boosting Pressure under Gassy Flow Conditions and Experimental Validation. *Proceedings of the SPE Annual Technical Conference and Exhibition*.
- Zhu, J., and Zhang, H. Q. (2014). CFD Simulation of ESP Performance and Bubble Size Estimation under Gassy Conditions. *Proceedings of the SPE Annual Technical Conference and Exhibition, 2039–2053*.
<https://doi.org/https://doi.org/10.2118/170727-MS>
- Zhu, J., and Zhang, H. Q. (2016). Mechanistic modeling and numerical simulation of in-situ gas void fraction inside ESP impeller. *Journal of Natural Gas Science and Engineering, 36*, 144–154. <https://doi.org/10.1016/j.jngse.2016.10.020>
- Zhu, J., Zhang, J., Cao, G., Zhao, Q., Peng, J., Zhu, H., and Zhang, H. Q. (2019e). Modeling Flow Pattern Transitions in Electrical Submersible Pump under Gassy Flow Conditions. *Journal of Petroleum Science and Engineering, 180*, 471–484.
<https://doi.org/10.1016/j.petrol.2019.05.059>
- Zhu, J., Zhang, J., Zhu, H., and Zhang, H. Q. (2018d). A Mechanistic Model to Predict Flow Pattern Transitions in Electrical Submersible Pump under Gassy Flow Condition. *Proceedings of the SPE Artificial Lift Conference and Exhibition*.
<https://doi.org/10.2118/190927-MS>
- Zhu, J., Cao, G., Tian, W., Zhao, Q., Zhu, H., Song, J., ... Lin, Z. (2019f). Improved Data Mining for Production Diagnosis of Gas Wells with Plunger Lift through Dynamic Simulations. *Proceedings of SPE Annual Technical Conference and Exhibition*.
<https://doi.org/10.2118/196201-MS>

- Zhu, J., Zhu, H., Cao, G., Banjar, H., Peng, J., Zhao, Q., and Zhang, H.-Q. (2019g). A New Mechanistic Model for Oil-Water Emulsion Rheology and Boosting Pressure Prediction in Electrical Submersible Pumps ESP. *Proceedings of the SPE Annual Technical Conference and Exhibition*. <https://doi.org/10.2118/196155-MS>
- Zhu, J., Zhu, H., Zhao, Q., Fu, W., Shi, Y., and Zhang, H. Q. (2019h). A Transient Plunger Lift Model for Liquid Unloading from Gas Wells. *Proceedings of SPE International Petroleum Technology Conference*. <https://doi.org/10.2523/19211-MS>
- Zhu, J., Zhu, H., Cao, G., Zhang, J., Peng, J., Banjar, H., and Zhang, H. Q. (2019i). A New Mechanistic Model to Predict Boosting Pressure of Electrical Submersible Pumps ESPs under High-Viscosity Fluid Flow with Validations by Experimental Data. *Proceedings of the SPE Gulf Coast Section Electric Submersible Pumps Symposium*. <https://doi.org/10.2118/194384-MS>
- Zhu, J., Zhu, H., Wang, Z., Zhang, J., Cuamatzi-Melendez, R., Farfan, J. A. M., and Zhang, H. Q. (2018e). Surfactant Effect on Air/Water Flow in a Multistage Electrical Submersible Pump (ESP). *Experimental Thermal and Fluid Science*, 98, 95–111. <https://doi.org/10.1016/j.expthermflusci.2018.05.013>
- Zhu, J., Zhu, H., Zhang, J., and Zhang, H. Q. (2017b). An Experimental Study of Surfactant Effect on Gas Tolerance in Electrical Submersible Pump (ESP). *Proceedings of the ASME International Mechanical Engineering Congress and Exposition*, <https://doi.org/10.1115/IMECE2017-70165>
- Zhu, J., Zhu, H., Zhang, J., and Zhang, H. Q. (2019j). A Numerical Study on Flow Patterns inside an Electrical Submersible Pump (ESP) and Comparison with

Visualization Experiments. *Journal of Petroleum Science and Engineering*, 173,
339–350. <https://doi.org/10.1016/j.petrol.2018.10.038>

APPENDIX A

CALCULATION EQUATIONS FOR SINGLE-PHASE FLUID FLOW IN ESPS

The mechanistic model of ESP boosting pressure under single-phase liquid flow developed by Zhu et al. (2019g) is presented in this section.

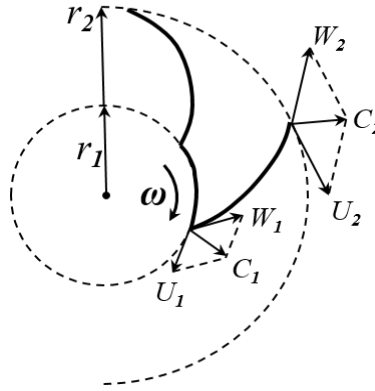


Figure A.1 Schematic of the impeller flow channel

Based on velocity triangles in Figure A.1, the theoretical head for a centrifugal pump can be expressed as below without inlet rotation:

$$H_E = \frac{U_2^2}{g} - \frac{U_2 C_{2m}}{g \tan \beta_2}, \quad (\text{A.1})$$

where U_2 is the outlet tangential velocity, β_2 is the blade angle from the tangential direction at impeller outlet, and

$$C_{2M} = \frac{Q + Q_{LK}}{(2\pi R_2 - Z_I T_B) y_{I2}}, \quad (\text{A.2})$$

is the meridional velocity at the impeller outlet, where Q is the liquid flow rate, Q_{LK} is the leakage flow rate, R_2 is the impeller outlet radius, Z_I is the impeller blade number, T_B is the blade thickness projected to the radial direction, and y_{II} is the impeller inlet height.

Assuming at the best match point (BMP), the direction of the fluid absolute velocity at the impeller outlet matches the designed flow direction from the impeller to the diffuser. Mismatches in both the flow direction and amplitude occur at the flow rates below and above the BMP. Therefore, an effective velocity should be used to replace C_2 at flow rates lower or higher than the flow rate corresponding to the BMP.

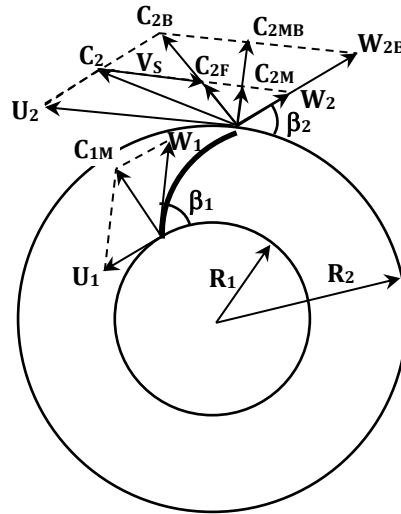


Figure A.2 Velocity triangles at impeller outlet for $Q < Q_{BMP}$

As shown in Figure A.2, when $Q < Q_{BMP}$, the fluid flow velocity outside the impeller is

$$C_{2F} = C_{2B} \frac{Q}{Q_{BMP}}, \quad (\text{A.3})$$

where C_{2B} is the absolute fluid velocity at the impeller outlet corresponding to the BMP.

The theoretical fluid velocity at the blade tip C_2 is higher than C_{2F} . This velocity difference causes a shear. The shear velocity can be calculated as

$$V_s = U_2 \frac{Q_{BEP} - Q}{Q_{BEP}} \quad (A.4)$$

The projected velocity, C_{2P} , is the projection of C_2 in the direction of C_{2B} which is the designed flow direction corresponding to the BMP that can be derived from the equation below:

$$C_2^2 - C_{2P}^2 = V_s^2 - (C_{2P} - C_{2F})^2 \quad (A.5)$$

By solving Equation (A.5)

$$C_{2P} = \frac{C_2^2 + C_{2F}^2 - V_s^2}{2C_{2F}} \quad (A.6)$$

As shown in Figure A.2, a recirculation occurs due to the shear. As a result, the theoretical kinetic energy will be reduced and only partially converted to static pressure. The recirculation is dependent on the shear velocity, the channel size, and the fluid viscosity. A Reynolds number can be used to estimate the recirculation effect:

$$Re_C = \frac{\rho V_s D_C}{\mu} \quad (A.7)$$

where D_C is the representative impeller channel width at the outlet in the flow direction:

$$D_C = \frac{2\pi R_2 \sin \beta_2 - T_B}{Z_1} \quad (A.8)$$

The shear effect is also dependent on fluid viscosity. Therefore, the following correlation is proposed to estimate the effective velocity based on comparisons with experimental results

$$C_{2E} = C_{2F} + \sigma (C_{2P} - C_{2F}) \quad (A.9)$$

and

$$\sigma = \frac{\left(\frac{\mu_w}{\mu}\right)^{0.5}}{1 + 0.02 Re_c^{0.2}}, \quad (A.10)$$

where μ_w is water viscosity. Then, the original Euler equation becomes

$$H_{EE} = H_E + \frac{C_{2E}^2 - C_2^2}{2g}. \quad (A.11)$$

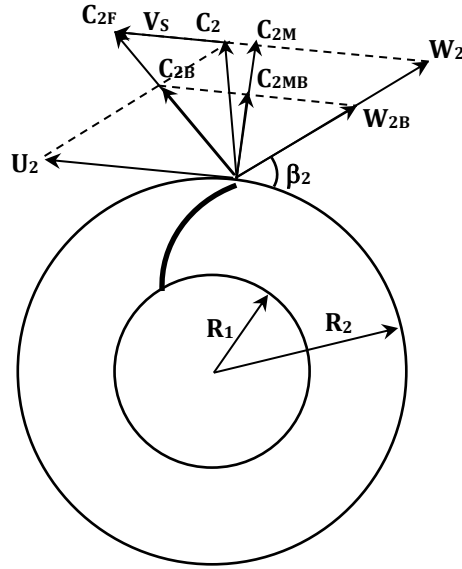


Figure A.3 Velocity triangles at impeller outlet for $Q > Q_{BMP}$

As shown in Figure A.3, when $Q > Q_{BMP}$, the fluid flow velocity outside of the impeller is:

$$C_{2F} = C_{2B} \frac{Q}{Q_{BEP}}, \quad (A.12)$$

and the shear velocity is:

$$V_s = U_2 \frac{Q - Q_{BEP}}{Q_{BEP}}. \quad (A.13)$$

The effective velocity, C_{2E} , is the projection of C_2 in the direction of C_{2B} which can be derived by:

$$C_2^2 - C_{2E}^2 = V_S^2 - (C_{2F} - C_{2E})^2 \quad (A.14)$$

By solving Equation (A.14) we can get:

$$C_{2E} = \frac{C_2^2 + C_{2F}^2 - V_S^2}{2C_{2F}} \quad (A.15)$$

Therefore, the effective Euler equation can be written as:

$$H_{EE} = H_E + \frac{C_{2E}^2 - C_2^2}{2g} \quad (A.16)$$

Flows in the impeller and diffuser are treated as channel flows. Similar as in a pipe flow, the friction loss in the impeller can be expressed as:

$$H_{FI} = f_{FI} \frac{V_I^2 L_I}{2gD_I} \quad (A.17)$$

where f_{FI} is the friction factor, V_I is the representative fluid velocity, L_I is the channel length, and D_I is the representative (hydraulic) diameter of the channel. Similarly, the friction loss in the diffuser can be estimated as:

$$H_{FD} = f_{FD} \frac{V_D^2 L_D}{2gD_D} \quad (A.18)$$

where f_{FD} is the friction factor, V_D is the representative fluid velocity, L_D is the channel length, and D_D is the representative (hydraulic) diameter of the channel. The Moody friction factors are functions of Reynolds number and the relative roughness of the walls. Churchill's equations are used to calculate the friction factors across the transition from

laminar flow to turbulent flow. The representative Reynolds numbers in the impeller and diffuser are:

$$Re_I = \frac{\rho V_I D_I}{\mu} \quad (\text{A.19})$$

and

$$Re_D = \frac{\rho V_D D_D}{\mu} \quad (\text{A.20})$$

where ρ is the fluid density and μ is the fluid viscosity. Then, the representative diameter of the impeller channel is defined as:

$$D_I = \frac{4Vol_I}{A_{SI}} \quad (\text{A.21})$$

where Vol_I is the volume of an impeller channel, and A_{SI} is the total wall area of an impeller channel. Similarly, the representative diameter of the diffuser channel is:

$$D_D = \frac{4Vol_D}{A_{SD}} \quad (\text{A.22})$$

where Vol_D is the volume of an impeller channel, and A_{SD} is the total wall area of an impeller channel. The representative fluid velocity in the impeller channel is:

$$V_I = \frac{Q + Q_{LK}}{A_I Z_I} \quad (\text{A.23})$$

where Q_{LK} is the leakage flow rate, A_I is the representative impeller channel cross-sectional area, and Z_I is the impeller blade number. The representative fluid velocity in the diffuser channel is:

$$V_D = \frac{Q}{A_D Z_D}, \quad (\text{A.24})$$

where A_D is the representative diffuser channel cross-sectional area, and Z_D is the diffuser vane number.

$$A_I = \frac{Vol_I}{L_I} \quad (\text{A.25})$$

and

$$A_D = \frac{Vol_D}{L_D}. \quad (\text{A.26})$$

When fluid flows from impeller to diffuser and from diffuser to the inlet of the next impeller, pressure head losses are caused due to the changes of flow directions. The head loss for the turn from the impeller to the diffuser can be estimated as:

$$H_{TI} = f_{TI} \frac{V_I^2}{2g}. \quad (\text{A.27})$$

The head loss for the turn from the diffuser to the next impeller can be estimated as:

$$H_{TD} = f_{TD} \frac{V_D^2}{2g}, \quad (\text{A.28})$$

where f_{TI} and f_{TD} are the local head loss coefficients, and a value of 1.0 is used.

To calculate the leakage flow rate, the pressure head difference across the leakage can be estimated as:

$$H_{LK} = H_{IO} - \frac{U_2^2 - U_{LK}^2}{8g}, \quad (\text{A.29})$$

where H_{IO} is the head increase across the impeller, and U_{LK} is the tangential velocity due to the impeller rotation at the leakage:

$$U_{LK} = R_{LK}\Omega, \quad (\text{A.30})$$

where R_{LK} is the radius corresponding to the leakage. The centrifugal force field on the front or back surface of the impeller acts against the pressure between the impeller and diffuser. Since the fluid rotation is caused by only one side, half of the tangential velocity of the impeller rotation may be counted. The head increase by the impeller can be estimated as:

$$H_{IO} = H_{EE} - H_{FI} - H_{TI}. \quad (\text{A.31})$$

The head loss across the leakage consists of contraction, expansion and friction components:

$$H_{LK} = 0.5 \frac{V_L^2}{2g} + 1.0 \frac{V_L^2}{2g} + f_{LK} \frac{V_L^2 L_G}{2g S_L}, \quad (\text{A.32})$$

where L_G is the leakage channel length, S_L is the width of the leakage. Solving Equations (A.29) to (A.32), the fluid velocity through the leakage can be calculated as:

$$V_L = \sqrt{\frac{2gH_{LK}}{f_{LK} \frac{L_G}{S_L} + 1.5}}. \quad (\text{A.33})$$

Assuming smooth leakage channel, the friction factor f_{LK} can be estimated based on Reynolds number:

$$Re_L = \frac{\rho V_L S_L}{\mu}. \quad (\text{A.34})$$

Then, the leakage flow rate can be calculated:

$$Q_{LK} = 2\pi R_{LK} S_L V_L \quad (A.35)$$

Finally, the total stage head increment is:

$$H_P = H_{EE} - H_{FI} - H_{FD} - H_{TI} - H_{TD} \quad (A.36)$$

Figure A.4 shows the ESP single-phase liquid pressure increment calculation procedure. It should be noted, Equations (A.32) to (A.36) are replaced in this study in Section 4.2.1.

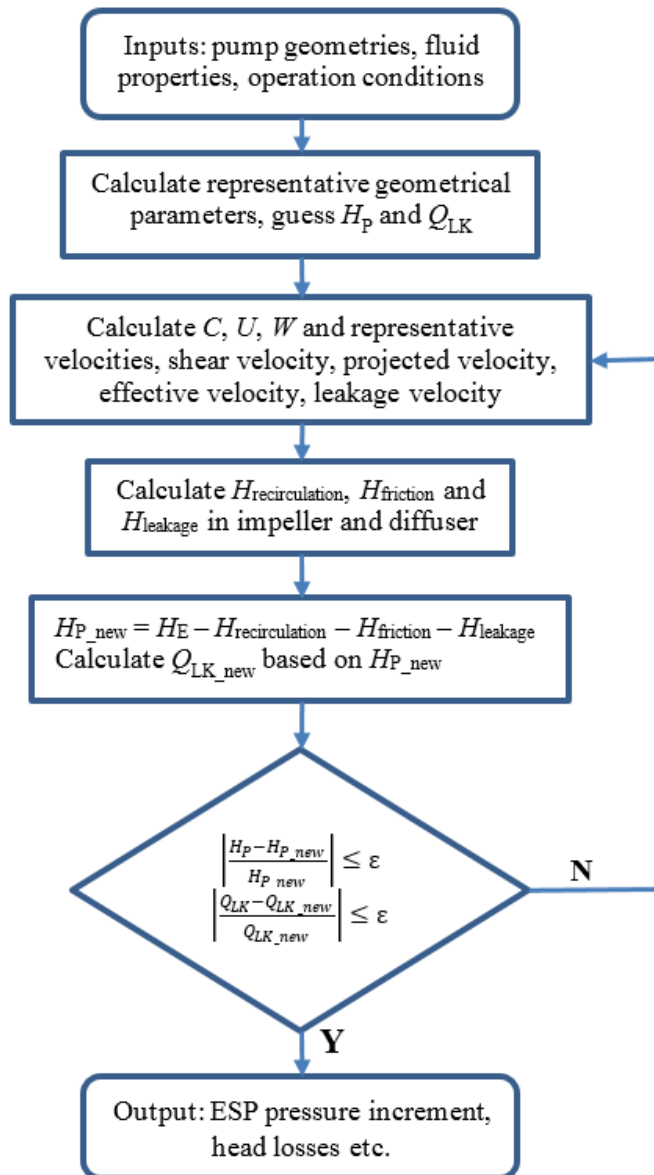


Figure A.4 Flow chart for calculating ESP single-phase pressure increment

APPENDIX B

PUMP GEOMETRY AND WEIGHT MEASUREMENT

In this section, all the pump geometry and weight measurement is recorded and shown in the following tables

B.1 Case-1 Water-Sand at $N = 3600$ rpm, $Q_L = 3100$ bpd

Table B.1 Case 1: Diffuser position 1: diffuser skirt ring ID (in)

Stage/Time	0	2	8	16	32	64
1	2.07590	2.07645	2.07680	2.08060	2.08335	2.08430
2	2.07590	2.07690	2.07835	2.08090	2.08415	2.08455
3	2.07720	2.07665	2.07690	2.08010	2.08315	2.08470
4	2.07490	2.07665	2.07770	2.08120	2.08485	2.08580
5	2.07520	2.07670	2.07775	2.07960	2.08355	2.08395
6	2.07550	2.07665	2.07680	2.07990	2.08410	2.08580
7	2.07680	2.07690	2.07725	2.08020	2.08375	2.08445
8	2.07600	2.07680	2.07830	2.08040	2.08285	2.08360
9	2.07680	2.07580	2.07730	2.08010	2.08485	2.08525
10	2.07555	2.07730	2.07925	2.08050	2.08325	2.08415
11	2.07570	2.07610	2.07730	2.07940	2.08255	2.08355
12	2.07740	2.07645	2.07700	2.07680	2.07690	2.07700

Table B.2 Case 1: Diffuser position 2: diffuser hub ID (SCS diffuser bore of steel) (in)

Stage/Time	0	2	8	16	32	64
1	0.88520	0.88840	0.88870	0.88980	0.89050	0.89740
2	0.88415	0.88480	0.88590	0.88780	0.89035	0.89475
3	0.88410	0.88470	0.88635	0.88870	0.89050	0.89360
4	0.88370	0.88380	0.88525	0.88710	0.89100	0.89745
5	0.88400	0.88450	0.88650	0.88775	0.89100	0.89310
6	0.88400	0.88450	0.88640	0.88750	0.89190	0.89745
7	0.88510	0.88420	0.88630	0.88790	0.89075	0.89350
8	0.88440	0.88510	0.88520	0.88600	0.89255	0.89320
9	0.88470	0.88550	0.88850	0.89030	0.89415	0.89840
10	0.88400	0.88555	0.88600	0.88710	0.88995	0.89685

11	0.88390	0.88550	0.88765	0.89040	0.89495	0.89855
12	0.88370	0.88555	0.88890	0.88980	0.89220	0.89575

Table B.3 Case 1: Diffuser position 3: diffuser balance ring ID (in)

Stage/Time	0	2	8	16	32	64
1	2.47750	2.48050	2.48453	2.48467	2.48563	2.48560
2	2.48133	2.48150	2.48433	2.48750	2.48960	2.49083
3	2.47867	2.48017	2.48433	2.48667	2.48693	2.48883
4	2.48000	2.48167	2.48467	2.49033	2.49150	2.49433
5	2.47850	2.48117	2.48417	2.48467	2.48627	2.48750
6	2.47983	2.48167	2.48733	2.48967	2.49083	2.49483
7	2.48133	2.48150	2.48450	2.48633	2.48650	2.48817
8	2.47900	2.48133	2.48573	2.48767	2.48917	2.49017
9	2.48100	2.48167	2.48670	2.48750	2.48967	2.49300
10	2.48500	2.48167	2.48567	2.48667	2.48890	2.49083
11	2.48267	2.48217	2.48617	2.48733	2.49083	2.49317
12	2.48083	2.48150	2.48650	2.48567	2.48950	2.49050

Table B.4 Case 1: Diffuser position 4: diffuser inside shroud ID (in)

Stage/Time	0	2	8	16	32	64
1	/	/	/	/	/	/
2	3.14390	3.14385	3.14345	3.14150	3.14220	3.14670
3	3.14510	3.14315	3.14350	3.14490	3.14575	3.14570
4	3.14450	3.14488	3.14395	3.14330	3.14530	3.14805
5	3.14440	3.14508	3.14585	3.14530	3.14470	3.14675
6	3.14315	3.14380	3.14355	3.14380	3.14385	3.14550
7	3.14240	3.14380	3.14355	3.14400	3.14470	3.14560
8	3.14380	3.14395	3.14405	3.14420	3.14460	3.14550
9	3.14430	3.14410	3.14400	3.14320	3.14375	3.14610
10	3.14330	3.14350	3.14330	3.14300	3.14450	3.14510
11	3.14310	3.14440	3.14285	3.14540	3.14680	3.14830
12	3.14345	3.14355	3.14510	3.14340	3.14415	3.14505

Table B.5 Case 1: Diffuser position 5: diffuser skirt ring depth (in)

Stage/Time	0	2	8	16	32	64
1	0.49100	0.49100	0.49163	0.49177	0.49177	0.49143
2	0.49200	0.49200	0.49257	0.49297	0.49340	0.49320
3	0.49050	0.48950	0.49140	0.49123	0.49110	0.49077
4	0.49030	0.49050	0.49147	0.49153	0.49153	0.49087
5	0.49030	0.49150	0.49147	0.49150	0.49143	0.49217
6	0.49000	0.49100	0.49183	0.49127	0.49070	0.49057
7	0.48900	0.49000	0.49077	0.49067	0.49050	0.49117
8	0.48960	0.49100	0.49207	0.49222	0.49240	0.49233

9	0.48980	0.49100	0.49133	0.49170	0.49217	0.49197
10	0.48900	0.49150	0.49287	0.49307	0.49323	0.49333
11	0.48950	0.49100	0.49253	0.49243	0.49253	0.49200
12	0.49000	0.49050	0.49087	/	0.49047	0.48910

Table B.6 Case 1: Diffuser position 6: diffuser hub ID (SCS diffuser bore by carbide) (in)

Stage/Time	0	2	8	16	32	64
1	0.94517	0.94515	0.94525	0.94520	0.94530	0.94570
2	0.94517	0.94525	0.94530	0.94500	0.94530	0.94620
3	0.88450	0.88640	0.88640	0.88810	0.88990	0.89360
4	0.94533	0.94545	0.94550	0.94540	0.94540	0.94600
5	0.88300	0.88745	0.88745	0.88900	0.88990	0.89310
6	0.94500	0.94485	0.94485	0.94500	0.94515	0.94570
7	0.88233	0.88680	0.88680	0.88820	0.88890	0.89350
8	0.94500	0.94505	0.94500	0.94500	0.94520	0.94580
9	0.88533	0.87900	0.87900	0.89140	0.89425	0.89840
10	0.94517	0.94535	0.94535	0.94550	0.94570	0.94630
11	0.88450	0.88780	0.88780	0.88900	0.89150	0.89855
12	0.94533	0.94557	0.94590	0.94630	0.94715	0.94875

Table B.7 Case 1: Impeller position 1: impeller hub ID (in)

Stage/Time	0	2	8	16	32	64
1	0.68850	0.68800	0.68862	0.69105	0.68970	0.68970
2	0.68850	0.68883	0.68877	0.69010	0.68995	0.68995
3	0.68900	0.68883	0.68917	0.69040	0.69020	0.69020
4	0.68933	0.68800	0.68795	0.68920	0.68915	0.68915
5	0.68950	0.68933	0.68917	0.69070	0.69060	0.69060
6	0.68817	0.68867	0.68890	0.68985	0.68975	0.68975
7	0.68783	0.68883	0.68842	0.68910	0.68910	0.68910
8	0.68817	0.68933	0.68888	0.69060	0.69060	0.69060
9	0.68817	0.68817	0.68927	0.69020	0.69015	0.69015
10	0.68850	0.69150	0.68993	0.69005	0.69000	0.69000
11	0.68867	0.69200	0.68823	0.69000	0.69015	0.69015
12	0.68817	0.69200	0.68748	0.69010	0.69010	0.69010

Table B.8 Case 1: Impeller position 2: impeller hub OD (in)

Stage/Time	0	2	8	16	32	64
1	0.87450	0.87400	0.87317	0.87083	0.86833	0.86517
2	0.87433	0.87367	0.87350	0.87200	0.87183	0.87117
3	0.87500	0.87383	0.87317	0.87100	0.87000	0.86800
4	0.87450	0.87350	0.87383	0.87250	0.87250	0.87267
5	0.87450	0.87367	0.87283	0.87083	0.86900	0.86517
6	0.87450	0.87400	0.87317	0.87117	0.87083	0.86917

7	0.87450	0.87367	0.87283	0.87133	0.86950	0.86667
8	0.87450	0.87400	0.87350	0.87183	0.87067	0.86900
9	0.87300	0.87333	0.87117	0.86933	0.86767	0.86350
10	0.87450	0.87383	0.87333	0.87167	0.87100	0.86967
11	0.87450	0.87383	0.87333	0.87133	0.86967	0.86733
12	0.87500	0.87333	0.87250	0.86967	0.86600	0.85867

Table B.9 Case 1: Impeller position 3: impeller balance ring OD (in)

Stage/Time	0	2	8	16	32	64
1	2.46950	2.46433	2.46425	2.46290	2.46172	2.46203
2	2.46950	2.46633	2.46685	2.46342	2.46162	2.45747
3	2.47050	2.46600	2.46437	2.45957	2.45762	2.45343
4	2.47100	2.46650	2.46647	2.46275	2.46148	2.45858
5	2.47100	2.46650	2.46530	2.46098	2.45798	2.45595
6	2.47050	2.46733	2.46715	2.46448	2.46205	2.46002
7	2.47050	2.46650	2.46228	2.46197	2.45855	2.45535
8	2.47000	2.46700	2.46617	2.46340	2.46080	2.45837
9	2.46650	2.46600	2.46655	2.46387	2.46070	2.45948
10	2.46650	2.46650	2.46578	2.46302	2.45943	2.45712
11	2.46650	2.46650	2.46583	2.46465	2.46215	2.45980
12	2.46700	2.46650	2.46455	2.46152	2.45910	2.45430

Table B.10 Case 1: Impeller position 4: impeller skirt ring OD (in)

Stage/Time	0	2	8	16	32	64
1	2.06083	2.05817	2.05747	2.05487	2.05353	2.05215
2	2.06083	2.05833	2.05730	2.05400	2.05123	2.04738
3	2.06200	2.05800	2.05665	2.05313	2.05072	2.04818
4	2.06233	2.05850	2.05715	2.05340	2.05105	2.04768
5	2.06300	2.05867	2.05577	2.05382	2.05147	2.04807
6	2.06200	2.05817	2.05727	2.05422	2.05188	2.04843
7	2.06233	2.05800	2.05610	2.05383	2.05147	2.04873
8	2.06050	2.05783	2.05560	2.05263	2.05103	2.04800
9	2.06033	2.05800	2.05612	2.05443	2.05267	2.04928
10	2.06350	2.05950	2.05553	2.05362	2.05115	2.04835
11	2.06100	2.05867	2.05738	2.05562	2.05328	2.05007
12	2.06283	2.05900	2.05942	2.05640	2.05373	2.04953

Table B.11 Case 1: Impeller position 5: impeller outside shroud OD (in)

Stage/Time	0	2	8	16	32	64
1	3.10250	3.10100	3.10250	3.10302	3.10138	3.09928
2	3.10050	3.09850	3.10220	3.10207	3.10132	3.10107
3	3.10200	3.09950	3.10143	3.10140	3.10075	3.09882
4	3.10350	3.10150	3.10458	3.10432	3.10292	3.10182

5	3.10300	3.10100	3.10383	3.10430	3.10373	3.10372
6	3.10300	3.10100	3.10528	3.10528	3.10497	3.10472
7	3.10250	3.09900	3.10162	3.10063	3.10112	3.10013
8	3.10000	3.10050	3.10592	3.10420	3.10447	3.10180
9	3.10050	3.10050	3.10273	3.10203	3.10177	3.10122
10	3.10100	3.10150	3.10453	3.10432	3.10430	3.10402
11	3.10200	3.09850	3.10220	3.10195	3.10018	3.09962
12	3.09500	3.09850	3.10187	3.10160	3.10145	3.10073

Table B.12 Case 1: Inter-stage clearance (SCS inter-stage of steel) (in)

Stage/Time	0	2	8	16	32	64
1	0.01200	0.01440	0.01553	0.01897	0.02217	0.03023
2	0.01167	0.01113	0.01240	0.01580	0.01852	0.02358
3	0.00950	0.01087	0.01318	0.01770	0.02050	0.02560
4	0.01083	0.01030	0.01142	0.01460	0.01850	0.02278
5	0.00850	0.01083	0.01367	0.01692	0.02200	0.02793
6	0.00833	0.01050	0.01323	0.01633	0.02107	0.02628
7	0.00783	0.01053	0.01347	0.01657	0.02125	0.02683
8	0.00800	0.01110	0.01170	0.01417	0.02188	0.02420
9	0.01233	0.01217	0.01733	0.02097	0.02648	0.03490
10	0.01083	0.01172	0.01267	0.01543	0.01895	0.02468
11	0.01000	0.01167	0.01432	0.01907	0.02528	0.03122
12	0.01050	0.01222	0.01640	0.02013	0.02620	0.03708

Table B.13 Case 1: Inter-stage clearance (SCS inter-stage of carbide) (in)

Stage/Time	0	8	32	64
1	0	8	32	64
2	0.00840	0.00863	0.00850	0.00910
3	0.00825	0.00877	0.00887	0.00963
4	0.00840	0.01578	0.02367	0.03087
5	0.00850	0.00888	0.00887	0.00950
6	0.00687	0.01325	0.02310	0.02940
7	0.00818	0.00843	0.00862	0.00898
8	0.00628	0.01420	0.02218	0.03013
9	0.00798	0.00812	0.00832	0.00902
10	0.00823	0.00673	0.02538	0.03152
11	0.00812	0.00895	0.00888	0.00943
12	0.00728	0.01537	0.02423	0.03330

Table B.14 Case 1: Balance ring clearance (in)

Stage/Time	0	2	8	16	32	64
1	0.01000	0.01617	0.02028	0.02177	0.02392	0.02357
2	0.01383	0.01517	0.01748	0.02408	0.02798	0.03337

3	0.01017	0.01417	0.01997	0.02710	0.02932	0.03540
4	0.01100	0.01517	0.01820	0.02758	0.03002	0.03575
5	0.00950	0.01467	0.01887	0.02368	0.02828	0.03155
6	0.01133	0.01433	0.02018	0.02518	0.02878	0.03482
7	0.01283	0.01500	0.02222	0.02437	0.02795	0.03282
8	0.01100	0.01433	0.01957	0.02427	0.02837	0.03180
9	0.01650	0.01567	0.02015	0.02363	0.02897	0.03352
10	0.02050	0.01517	0.01988	0.02365	0.02947	0.03372
11	0.01817	0.01567	0.02033	0.02268	0.02868	0.03337
12	0.01583	0.01500	0.02195	0.02415	0.03040	0.03620

Table B.15 Case 1: Skirt ring clearance (in)

Stage/Time	0	2	8	16	32	64
1						
2	0.01837	0.01812	0.01950	0.02660	0.03212	0.03692
3	0.01810	0.01890	0.02170	0.02777	0.03343	0.03637
4	0.01707	0.01815	0.01975	0.02670	0.03210	0.03702
5	0.01630	0.01798	0.02193	0.02738	0.03338	0.03773
6	0.01750	0.01853	0.02048	0.02538	0.03167	0.03552
7	0.01672	0.01865	0.02070	0.02607	0.03263	0.03707
8	0.01890	0.01907	0.02165	0.02757	0.03272	0.03645
9	0.01927	0.01880	0.02218	0.02597	0.03018	0.03432
10	0.01530	0.01630	0.02177	0.02648	0.03370	0.03690
11	0.01880	0.01863	0.02187	0.02488	0.02997	0.03408
12	0.01707	0.01710	0.01788	0.02300	0.02882	0.03402

Table B.16 Case 1: Sleeve/bushing OD (in)

Stage/Time	0	8	32	64
Bottom bearing	0.93710	0.93677	0.93583	0.93497
1	0.93710	0.93677	0.93583	0.93497
2	0.93677	0.93662	0.93680	0.93660
3	0.93692	0.93653	0.93643	0.93657
4	0.87610	0.87062	0.86623	0.86273
5	0.93683	0.93662	0.93653	0.93650
6	0.87613	0.87420	0.86680	0.86370
7	0.93682	0.93642	0.93653	0.93672
8	0.87605	0.87260	0.86672	0.86337
9	0.93702	0.93688	0.93688	0.93678
10	0.87710	0.87227	0.86887	0.86688
11	0.93705	0.93640	0.93682	0.93687
12	0.87722	0.87243	0.86727	0.86525
Top bearing	0.93647	0.93603	0.93467	0.93395

Table B.17 Case 1: Impeller weight loss (g)

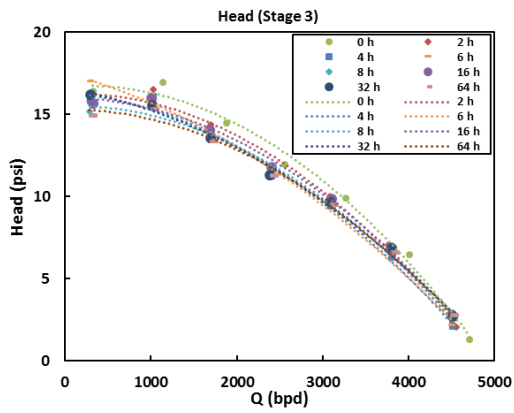
Stage/Time	0	8	16	32	64
1	314.40000	313.14770	300.23480	296.50000	293.14780
2	316.70000	313.81287	310.74550	309.72000	307.27350
3	319.04000	315.45643	313.50090	312.36000	309.21610
4	315.53000	313.74067	312.21677	315.35000	308.98220
5	322.64000	318.56067	316.64337	311.84000	312.64130
6	321.05000	317.35303	316.85667	315.54000	312.06740
7	311.10000	316.50750	315.19680	314.07000	311.53250
8	314.96000	310.77823	310.72667	309.28000	306.08830
9	311.94000	307.83083	306.35723	305.40000	303.27970
10	322.21000	318.60973	317.26953	315.49000	312.79550
11	316.14000	312.21863	312.07877	309.79000	306.96360
12	316.35000	312.65447	310.42227	309.09000	306.01073

Table B.18 Case 1: Diffuser weight loss (g)

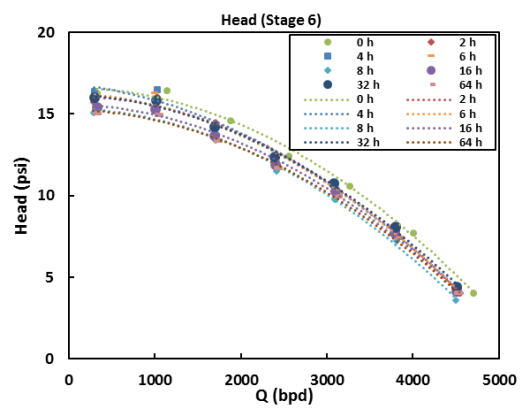
Stage/Time	0	8	16	32	64
1	1136.37000	1134.17000	1132.89000	1130.56000	1126.05000
2	1109.50000	1107.84000	1106.62000	1103.91000	1099.81000
3	1152.09000	1147.45000	1147.84000	1144.47000	1139.60000
4	1076.72000	1074.94000	1073.55000	1071.05000	1066.10000
5	1146.20000	1143.90000	1142.26000	1137.04000	1135.45000
6	1083.41000	1081.68000	1080.29000	1077.47000	1072.60000
7	1145.93000	1144.16000	1142.55000	1140.10000	1135.50000
8	1120.27000	1118.49000	1117.27000	1112.51000	1111.69000
9	1077.59000	1075.53000	1073.71000	1070.58000	1065.64000
10	1112.84000	1111.11000	1109.77000	1104.48000	1102.03000
11	1088.78000	1086.86000	1085.19000	1082.28000	1076.98000
12	1148.54000	1147.66000	1146.59000	1143.56000	1140.15000

Table B.19 Case 1: Sleeve weight loss (g)

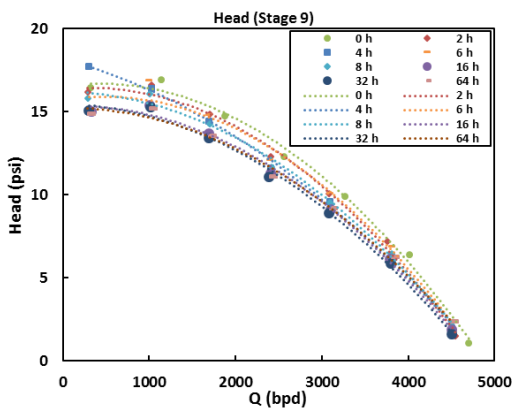
Stage/Time	0	8	16	32	64
1	52.60800	52.35150	52.33830	52.30970	52.60800
2	52.37050	52.35890	52.32126	52.25360	52.37050
3	40.84290	40.34170	39.77155	39.26270	40.84290
4	52.37330	52.35580	52.32135	52.25740	52.37330
5	41.11180	40.64580	40.17850	39.61010	41.11180
6	52.49290	52.47307	52.44735	52.39960	52.49290
7	41.30530	40.80583	40.36870	39.74440	41.30530
8	52.28830	52.27853	52.25120	52.22220	52.28830
9	41.47550	41.09097	40.69920	40.33470	41.47550
10	52.50370	52.49497	52.47210	52.44080	52.50370
11	40.75780	40.61078	40.18600	39.69270	40.75780
12	/	/	/	/	/



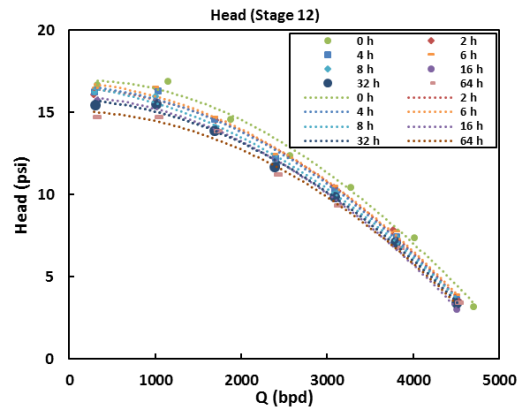
(a)



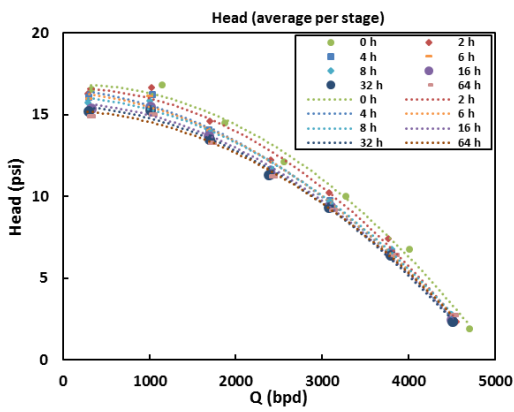
(b)



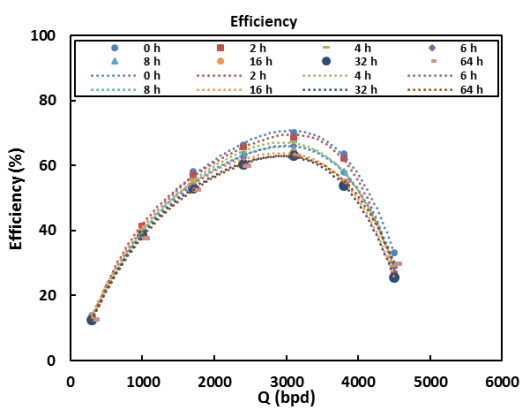
(c)



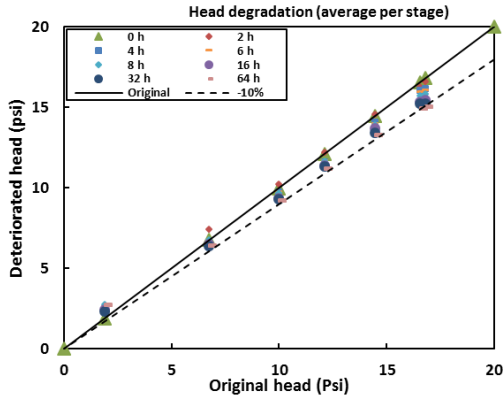
(d)



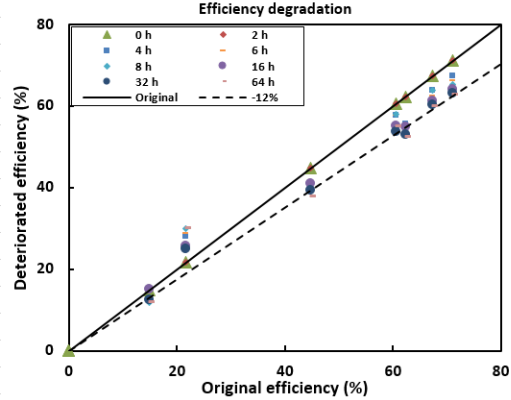
(e)



(f)



(g)



(h)

Figure B.1 Case 1 performance degradation (a) head of stage 3, (b) head of stage 6, (c) head of stage 9, (d) head of stage 12, (e) average head, (f) pump efficiency, (g) average head degradation, (h), efficiency degradation

B.2 Case-2 Water-Sand at $N = 2400$ rpm, $Q_L = 3100$ bpd

Table B.20 Case 2: Diffuser position 1: diffuser skirt ring ID (in)

Stage/Time	0	2	4	8	16	32	64
1	2.07585	2.07775	2.07895	2.0795	2.08055	2.0815	2.0829
2	2.0757	2.0786	2.0808	2.0809	2.08145	2.0819	2.0834
3	2.0765	2.078	2.07905	2.0786	2.0796	2.08075	2.0813
4	2.0767	2.0782	2.07975	2.08	2.08145	2.0825	2.0835
5	2.0746	2.079	2.0798	2.08	2.0824	2.082	2.0842
6	2.0754	2.07765	2.0793	2.0799	2.08115	2.0816	2.0822
7	2.0754	2.0782	2.0795	2.08055	2.0809	2.0823	2.0828
8	2.0759	2.0777	2.07905	2.0799	2.0804	2.0811	2.0825
9	2.0758	2.0784	2.0794	2.0807	2.08115	2.0817	2.0827
10	2.07535	2.07725	2.0795	2.0803	2.08045	2.0818	2.0825
11	2.07555	2.0785	2.07965	2.0798	2.0804	2.0819	2.0831
12	2.07585	2.0758	2.07535	2.0748	2.0755	2.0748	2.07715

Table B.21 Case 2: Diffuser position 2: diffuser hub ID (SCS diffuser bore of steel) (in)

Stage/Time	0	2	4	8	16	32	64
1	0.8842	0.88485	0.8859	0.88625	0.8877	0.8886	0.89145
2	0.8842	0.8868	0.8876	0.8884	0.8902	0.8913	0.893
3	0.88455	0.88615	0.8876	0.88855	0.8906	0.8916	0.8924
4	0.884	0.8853	0.8854	0.88645	0.8875	0.8891	0.8925
5	0.8842	0.8865	0.8885	0.8899	0.8925	0.8939	0.8938
6	0.8843	0.8849	0.8855	0.8867	0.8893	0.8917	0.894
7	0.88435	0.8868	0.8878	0.88945	0.8912	0.8936	0.89545

8	0.88405	0.8847	0.88525	0.8864	0.8878	0.8896	0.8929
9	0.8846	0.8871	0.88835	0.8894	0.8913	0.8928	0.8952
10	0.8839	0.88545	0.886	0.8867	0.8883	0.8907	0.8936
11	0.8841	0.8862	0.88795	0.889	0.8905	0.892	0.8937
12	0.8844	0.88625	0.88865	0.8893	0.8905	0.8916	0.8968

Table B.22 Case 2: Diffuser position 3: diffuser balance ring ID (in)

Stage/Time	0	2	4	8	16	32	64
1	2.4815	2.4855	2.48717	2.48883	2.488	2.49012	2.49282
2	2.4815	2.48467	2.48767	2.48967	2.49	2.49178	2.49348
3	2.481	2.484	2.48567	2.48877	2.49	2.48812	2.49098
4	2.482	2.48517	2.4875	2.49037	2.49	2.49195	2.49515
5	2.48267	2.4855	2.48767	2.48967	2.49	2.49228	2.49515
6	2.48167	2.4845	2.487	2.48917	2.49	2.49095	2.49482
7	2.482	2.48467	2.487	2.49	2.49	2.49112	2.49382
8	2.48167	2.48483	2.48767	2.4895	2.49	2.49095	2.49298
9	2.48383	2.48583	2.4875	2.49033	2.49	2.49062	2.49415
10	2.48167	2.4845	2.48667	2.48967	2.49	2.49112	2.49282
11	2.48167	2.48483	2.4875	2.48967	2.49	2.49112	2.49365
12	2.48167	2.484	2.48583	2.488	2.49	2.49028	2.49365

Table B.23 Case 2: Diffuser position 4: diffuser inside shroud ID (in)

Stage/Time	0	2	4	8	16	32	64
1	3.14245	3.1428	3.1425	3.14235	3.14195	3.14215	3.143
2	3.1443	3.1447	3.145	3.1446	3.1448	3.1452	3.1453
3	3.1432	3.1437	3.1439	3.1439	3.1438	3.1439	3.14475
4	3.1439	3.144	3.14425	3.14445	3.14425	3.1446	3.1473
5	3.1444	3.14525	3.14575	3.14535	3.1457	3.14595	3.1461
6	3.1436	3.14455	3.1452	3.1455	3.14565	3.1459	3.1461
7	3.1435	3.1441	3.1448	3.14505	3.14555	3.1456	3.1463
8	3.1437	3.14475	3.1454	3.1462	3.14615	3.14665	3.147
9	3.1456	3.14645	3.14635	3.14715	3.1471	3.1473	3.148
10	3.1435	3.14525	3.14535	3.1461	3.1463	3.1468	3.14735
11	3.1442	3.1444	3.1453	3.14565	3.14535	3.1461	3.1463
12	3.1435	3.1453	3.14555	3.1451	3.14	3.1406	3.1462

Table B.24 Case 2: Diffuser position 5: diffuser skirt ring depth (in)

Stage/Time	0	2	4	8	16	32	64
1	0.486	0.4865	0.4888	0.48877	0.4892	0.48873	0.48923
2	0.487	0.4895	0.49033	0.48987	0.48947	0.48993	0.4901
3	0.485	0.4895	0.4905	0.4904	0.4906	0.49123	0.49067
4	0.487	0.49	0.4914	0.49067	0.49107	0.4909	0.4913
5	0.485	0.4866	0.48917	0.48887	0.48907	0.4895	0.48973

6	0.4862	0.4886	0.49017	0.49	0.49007	0.49077	0.4897
7	0.486	0.4885	0.48983	0.489	0.4894	0.4904	0.48973
8	0.4862	0.4884	0.4905	0.48927	0.48967	0.4905	0.48967
9	0.488	0.489	0.491	0.4906	0.4901	0.49	0.49093
10	0.4862	0.4895	0.491	0.49083	0.49067	0.4905	0.49057
11	0.487	0.489	0.4905	0.49	0.49017	0.49067	0.49013
12	0.4862	0.4866	0.4882	0.48707	0.48687	0.48967	0.4905

Table B.25 Case 2: Diffuser position 6: diffuser hub ID (SCS diffuser bore of carbide)
(in)

Stage/Time	0	2	16	32	64
1	0.94505	0.94475	0.9451	0.945	0.9451
2	0.9456	0.94545	0.9457	0.9455	0.9459
3	0.8845	0.8873	0.88978	0.8902	0.89155
4	0.9455	0.9475	0.9456	0.9455	0.9461
5	0.8844	0.88775	0.89112	0.8922	0.89305
6	0.9454	0.94525	0.9457	0.9458	0.9459
7	0.8844	0.8881	0.89212	0.8918	0.8941
8	0.94555	0.9454	0.9453	0.9453	0.9456
9	0.8851	0.8882	0.89162	0.893	0.8944
10	0.94555	0.94535	0.94525	0.9454	0.9452
11	0.8846	0.88805	0.89278	0.8931	0.8948
12	0.9455	0.9453	0.946	0.9464	0.9506

Table B.26 Case 2: Impeller position 1: impeller hub ID (in)

Stage/Time	0	2	4	8	16	32	64
1	0.6892	0.6899	0.6897	0.6897	0.6902	0.6907	0.6907
2	0.68935	0.6904	0.68995	0.6903	0.69045	0.6908	0.6908
3	0.6892	0.6906	0.6901	0.6906	0.6907	0.6906	0.6906
4	0.6901	0.68935	0.6891	0.68885	0.68965	0.6895	0.6895
5	0.6897	0.69	0.68955	0.6896	0.6898	0.6903	0.6903
6	0.6894	0.6907	0.6904	0.6906	0.6911	0.6912	0.6912
7	0.69035	0.68975	0.68925	0.68965	0.69	0.6899	0.6899
8	0.6898	0.6898	0.68965	0.68985	0.69015	0.6903	0.6903
9	0.6891	0.6907	0.69035	0.69045	0.6908	0.6906	0.6906
10	0.69025	0.6894	0.6893	0.68935	0.6896	0.6897	0.6897
11	0.6901	0.68955	0.6894	0.6895	0.68965	0.6899	0.6899
12	0.68975	0.6895	0.6891	0.68945	0.68975	0.6897	0.6897

Table B.27 Case 2: Impeller position 2: impeller hub OD (in)

Stage/Time	0	2	4	8	16	32	64
1	0.87485	0.87487	0.87472	0.87432	0.87347	0.87297	0.87113
2	0.87488	0.87508	0.87518	0.8747	0.8735	0.87293	0.8718

3	0.87545	0.8728	0.87173	0.87035	0.86785	0.86655	0.8653
4	0.87562	0.87497	0.87518	0.87538	0.87542	0.8757	0.87617
5	0.87533	0.8725	0.8718	0.87078	0.86855	0.86803	0.86717
6	0.87525	0.8743	0.87428	0.87393	0.87272	0.87203	0.87065
7	0.87458	0.87323	0.87252	0.87178	0.86982	0.86862	0.86773
8	0.87428	0.87528	0.87507	0.8747	0.87338	0.87332	0.8722
9	0.87457	0.87383	0.8731	0.87257	0.871	0.87023	0.8695
10	0.87493	0.87447	0.8744	0.8742	0.87323	0.87253	0.87153
11	0.87498	0.87305	0.87217	0.87182	0.87063	0.8704	0.86933
12	0.87508	0.87245	0.87087	0.87082	0.87002	0.86967	0.86888

Table B.28 Case 2: Impeller position 3: impeller balance ring OD (in)

Stage/Time	0	2	4	8	16	32	64
1	2.46892	2.4652	2.46315	2.46207	2.46098	2.4603	2.4591
2	2.46872	2.46718	2.46513	2.46282	2.46082	2.45968	2.46025
3	2.46827	2.46603	2.46235	2.46002	2.4579	2.45702	2.4561
4	2.46888	2.46557	2.46462	2.46193	2.46102	2.46	2.46003
5	2.4689	2.4668	2.46515	2.46325	2.46105	2.46048	2.45948
6	2.46877	2.4662	2.46508	2.46257	2.4613	2.46032	2.45895
7	2.46915	2.46627	2.46477	2.4621	2.46067	2.45975	2.45895
8	2.46945	2.46587	2.4641	2.4616	2.46042	2.45859	2.45898
9	2.47032	2.46688	2.46522	2.46228	2.46147	2.46057	2.46017
10	2.46872	2.4661	2.46438	2.4619	2.46103	2.46023	2.45988
11	2.4692	2.46592	2.46428	2.4625	2.46135	2.45975	2.45802
12	2.46885	2.46578	2.46347	2.46173	2.46072	2.45963	2.4578

Table B.29 Case 2: Impeller position 4: impeller skirt ring OD (in)

Stage/Time	0	2	4	8	16	32	64
1	2.06172	2.06152	2.0607	2.0603	2.05567	2.05408	2.0512
2	2.06185	2.05945	2.05663	2.05602	2.0539	2.05348	2.05213
3	2.0624	2.05847	2.05577	2.05497	2.05355	2.05192	2.05105
4	2.06025	2.0583	2.05542	2.0547	2.05282	2.05188	2.05062
5	2.06223	2.06035	2.05825	2.05692	2.0545	2.05365	2.05245
6	2.06257	2.05867	2.05685	2.05567	2.05285	2.05242	2.05118
7	2.062	2.05907	2.05705	2.05543	2.05368	2.05238	2.05132
8	2.06098	2.05773	2.05572	2.0534	2.0523	2.05132	2.0501
9	2.06143	2.05917	2.0563	2.05472	2.05378	2.05237	2.05133
10	2.06155	2.05832	2.05622	2.05417	2.05335	2.05262	2.05145
11	2.06187	2.06002	2.05653	2.0554	2.05447	2.05298	2.0524
12	2.06197	2.05853	2.05578	2.05493	2.05422	2.05303	2.05092

Table B.30 Case 2: Impeller position 5: impeller outside shroud OD (in)

Stage/Time	0	2	4	8	16	32	64
------------	---	---	---	---	----	----	----

1	3.10245	3.1032	3.10365	3.10323	3.10335	3.10298	3.103
2	3.1037	3.10385	3.10418	3.10362	3.10365	3.10392	3.1036
3	3.10475	3.10465	3.10483	3.10512	3.10427	3.105	3.1051
4	3.10295	3.1032	3.10368	3.1032	3.10332	3.1035	3.10358
5	3.105	3.105	3.10522	3.10522	3.10475	3.10505	3.1049
6	3.10215	3.1022	3.1023	3.10222	3.1016	3.10207	3.1021
7	3.105	3.1051	3.10498	3.10492	3.10467	3.1053	3.10488
8	3.1038	3.1041	3.1042	3.10442	3.10385	3.10388	3.10402
9	3.1033	3.10435	3.10443	3.10425	3.10352	3.10382	3.10403
10	3.1039	3.10385	3.10405	3.10412	3.10347	3.10377	3.10378
11	3.1001	3.0999	3.1006	3.10058	3.10038	3.09998	3.10038
12	3.1034	3.10355	3.10478	3.10442	3.10398	3.10467	3.1045

Table B.31 Case 2: Inter-stage clearance (SCS inter-stage of steel) (in)

Stage/Time	0	2	4	8	16	32	64
1	0.0093	0.0100	0.0112	0.0119	0.0142	0.0156	0.0203
2	0.0093	0.0117	0.0124	0.0137	0.0167	0.0184	0.0212
3	0.0091	0.0133	0.0159	0.0182	0.0227	0.0250	0.0271
4	0.0084	0.0103	0.0102	0.0111	0.0121	0.0134	0.0163
5	0.0089	0.0140	0.0167	0.0191	0.0240	0.0259	0.0266
6	0.0091	0.0106	0.0112	0.0128	0.0166	0.0197	0.0233
7	0.0098	0.0136	0.0153	0.0177	0.0214	0.0250	0.0277
8	0.0098	0.0094	0.0102	0.0117	0.0144	0.0163	0.0207
9	0.0100	0.0133	0.0153	0.0168	0.0203	0.0226	0.0257
10	0.0090	0.0110	0.0116	0.0125	0.0151	0.0182	0.0221
11	0.0091	0.0132	0.0158	0.0172	0.0199	0.0216	0.0244
12	0.0093	0.0138	0.0178	0.0185	0.0205	0.0219	0.0279

Table B.32 Case 2: Inter-stage clearance (SCS inter-stage of carbide) (in)

Stage/Time	0	2	16	32	64
1	0.0080	0.0077	0.0084	0.0081	0.0082
2	0.0087	0.0085	0.0091	0.0088	0.0091
3	0.0080	0.0134	0.0213	0.0237	0.0267
4	0.0085	0.0107	0.0089	0.0086	0.0093
5	0.0082	0.0146	0.0240	0.0260	0.0276
6	0.0084	0.0084	0.0092	0.0091	0.0093
7	0.0071	0.0139	0.0220	0.0233	0.0267
8	0.0086	0.0086	0.0087	0.0085	0.0089
9	0.0084	0.0143	0.0224	0.0252	0.0277
10	0.0089	0.0088	0.0086	0.0088	0.0086
11	0.0084	0.0149	0.0234	0.0250	0.0282
12	0.0085	0.0084	0.0098	0.0103	0.0150

Table B.33 Case 2: Balance ring clearance (in)

Stage/Time	0	2	4	8	16	32	64
1	0.0126	0.0203	0.0240	0.0268	0.02702	0.0298	0.0337
2	0.0128	0.0175	0.0225	0.0268	0.02918	0.0321	0.0332
3	0.0127	0.0180	0.0233	0.0287	0.0321	0.0311	0.0349
4	0.0131	0.0196	0.0229	0.0284	0.02898	0.0319	0.0351
5	0.0138	0.0187	0.0225	0.0264	0.02895	0.0318	0.0357
6	0.0129	0.0183	0.0219	0.0266	0.0287	0.0306	0.0359
7	0.0128	0.0184	0.0222	0.0279	0.02933	0.0314	0.0349
8	0.0122	0.0190	0.0236	0.0279	0.02958	0.0324	0.0340
9	0.0135	0.0190	0.0223	0.0281	0.02853	0.0300	0.0340
10	0.0129	0.0184	0.0223	0.0278	0.02897	0.0309	0.0329
11	0.0125	0.0189	0.0232	0.0272	0.02865	0.0314	0.0356
12	0.0128	0.0182	0.0224	0.0263	0.02928	0.0307	0.0358

Table B.34 Case 2: Skirt ring clearance (in)

Stage/Time	0	2	4	8	16	32	64
1	/	/	/	/	/	/	/
2	0.0140	0.0183	0.0223	0.02348	0.02665	0.02802	0.03077
3	0.0133	0.0201	0.0250	0.02593	0.0279	0.02998	0.03235
4	0.0163	0.0197	0.0236	0.0239	0.02678	0.02887	0.03068
5	0.0145	0.0178	0.0215	0.02308	0.02695	0.02885	0.03105
6	0.0120	0.0203	0.0229	0.02433	0.02955	0.02958	0.03302
7	0.0134	0.0186	0.0222	0.02447	0.02747	0.02922	0.03088
8	0.0144	0.0205	0.0238	0.02715	0.0286	0.03098	0.0327
9	0.0145	0.0185	0.0228	0.02518	0.02662	0.02873	0.03117
10	0.0143	0.0201	0.0232	0.02653	0.0278	0.02908	0.03125
11	0.0135	0.0172	0.0230	0.0249	0.02598	0.02882	0.0301
12	0.0136	0.0200	0.0239	0.02487	0.02618	0.02887	0.03218

Table B.35 Case 2: Sleeve/bushing OD (in)

Stage/Time	0	2	4	8	16	32	64
Bottom bearing	0.937	0.93695	0.93687	0.93673	0.93648	0.93588	0.93548
1	0.93705	0.93708	0.93712	0.93715	0.93673	0.93685	0.93687
2	0.93688	0.93697	0.937	0.93698	0.93663	0.93675	0.93677
3	0.87655	0.87392	0.8723	0.87083	0.86845	0.86648	0.86488
4	0.93702	0.93682	0.937	0.937	0.93673	0.93692	0.93683
5	0.8762	0.87315	0.8717	0.87053	0.86708	0.86623	0.86547
6	0.937	0.93687	0.93708	0.93702	0.93653	0.9367	0.9366
7	0.87733	0.87423	0.87317	0.8722	0.87013	0.86845	0.86738
8	0.93692	0.93685	0.93702	0.93705	0.93662	0.93682	0.93675
9	0.87668	0.87393	0.87278	0.87175	0.86922	0.86783	0.86667
10	0.9367	0.9366	0.93677	0.93695	0.93667	0.93665	0.93663

11	0.87618	0.87313	0.87188	0.87092	0.86937	0.86805	0.86665
12	0.937	0.93688	0.9368	0.93655	0.93622	0.93605	0.93563
Top bearing	0.937	0.9365	0.936	0.935	0.93408	0.93422	0.93382

Table B.36 Case 2: Impeller weight loss (g)

Stage/Time	0.00	2.00	4.00	8.00	16.00	32.00	64.00
1	319.21	316.15	315.81	314.47	313.21	311.68	306.98
2	315.02	314.83	313.75	312.89	312.36	311.73	310.62
3	322.16	323.26	323.00	321.69	320.94	319.67	317.52
4	321.72	320.94	320.75	320.31	319.56	318.85	317.49
5	323.36	318.77	318.16	321.29	320.58	319.66	317.87
6	314.65	313.78	313.64	316.26	315.55	314.44	312.21
7	318.60	317.72	317.73	317.72	317.04	316.17	314.85
8	313.37	312.54	312.18	311.36	310.92	310.23	308.91
9	312.45	311.59	309.65	309.01	308.60	308.08	306.93
10	313.94	313.11	312.85	312.12	311.80	311.16	309.95
11	312.05	310.83	309.17	308.49	308.17	307.66	306.51
12	318.81	317.18	316.38	315.69	315.31	314.70	312.66

Table B.37 Case 2: Diffuser weight loss (g)

Stage/Time	0	2	4	8	16	32	64
1	1096	1095.52	1094.13	1094.03	1093.68	1091.9	1089.29
2	1082.3	1081.66	1079.63	1080.38	1080.17	1078.09	1075.71
3	1154.07	1152.49	1151.11	1150.49	1149.42	1146.92	1143.59
4	1075.44	1074.18	1072.54	1075.28	1074.82	1072.92	1070.25
5	1083.55	1081.83	1080.55	1083.18	1081.72	1079.37	1075.68
6	1090.13	1089.46	1088.26	1088.64	1087.93	1085.88	1082.78
7	1087.23	1085.55	1084.43	1087.87	1087.12	1084.41	1081.24
8	1069.81	1069.11	1067.88	1069.52	1069.29	1067.14	1064.41
9	1079.16	1077.59	1075.92	1076.02	1075.46	1073.49	1070.76
10	1071.45	1070.56	1069.39	1069.11	1068.94	1066.84	1064.21
11	1075.48	1073.64	1072.36	1073.71	1073.47	1071.38	1068.39
12	1087.15	1086.11	1085.23	1086.66	1086.47	1084.32	

Table B.38 Case 2: Sleeve weight loss (g)

Stage/Time	0.000	2.000	4.000	8.000	16.000	32.000	64.000
1	52.570	52.565	52.560	52.535	52.520	52.520	52.480
2	52.694	52.693	52.686	52.660	52.680	52.650	52.630
3	41.722	41.193	40.922	40.709	40.420	40.160	39.820
4	52.514	52.503	52.497	52.474	52.470	52.450	52.430
5	41.686	41.069	40.850	40.685	40.290	40.120	39.790
6	52.618	48.932	52.589	52.670	52.670	52.660	52.570
7	41.755	41.161	40.978	40.785	40.620	40.410	40.110

8	52.587	52.582	52.573	52.535	52.520	52.510	52.490
9	41.727	41.167	40.951	40.712	40.480	40.310	39.950
10	52.703	52.694	52.688	52.668	52.660	52.660	52.610
11	41.621	41.027	40.806	40.593	40.450	40.880	39.870
12	/	/	/	/	/	/	/

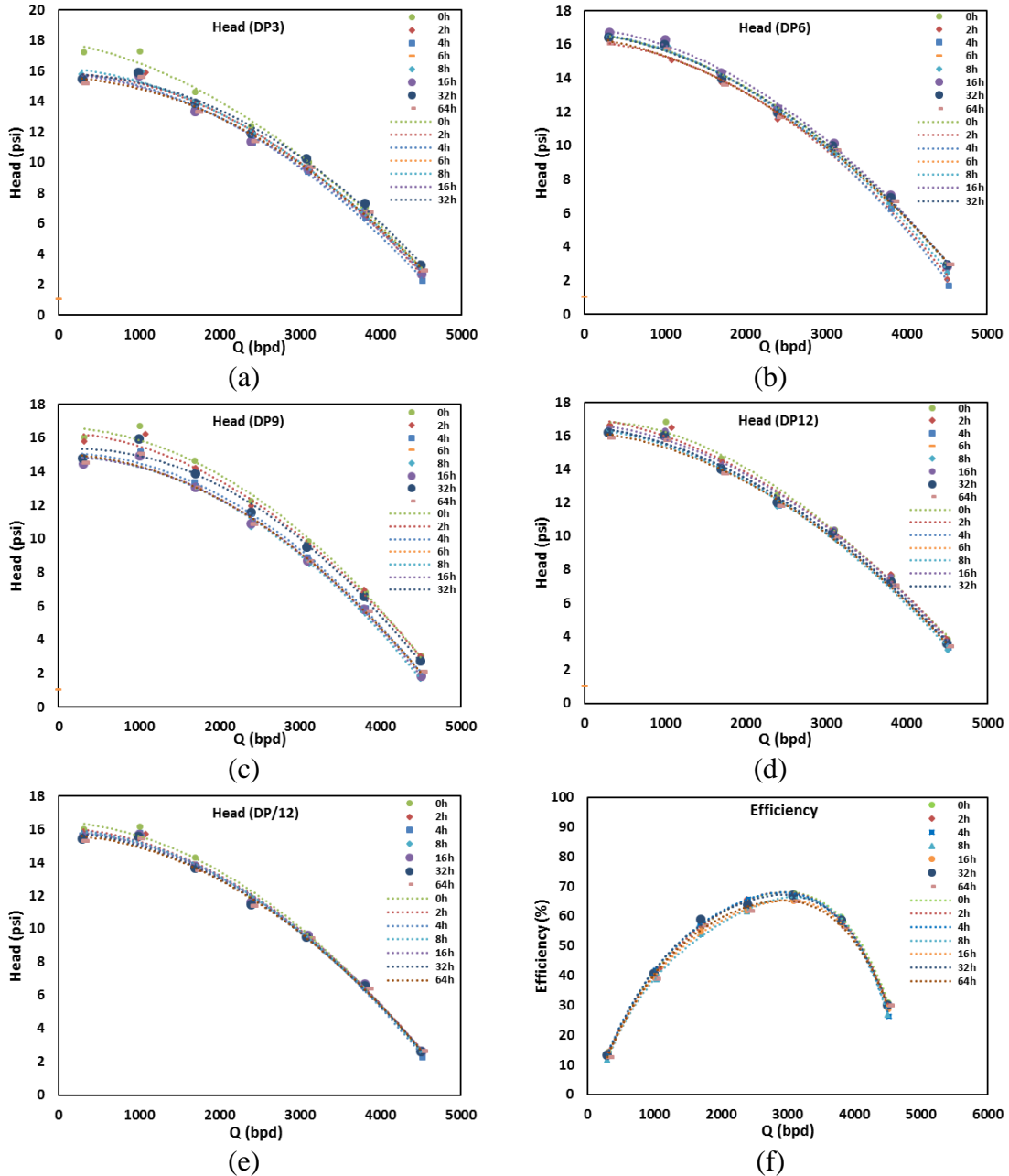


Figure B.2 Case 2 performance degradation (a) head of stage 3, (b) head of stage 6, (c) head of stage 9, (d) head of stage 12, (e) average head, (f) pump efficiency

B.3 Case-3 Air-Water-Sand at $N = 3600$ rpm, $Q_L = 3100$ bpd, $GVF = 15\%$

Table B.39 Case 3: Diffuser position 1: diffuser skirt ring ID (in)

Stage/Time	0	8	16	32	64
1	2.0759	2.08045	2.0807	2.082	2.08325
2	2.0759	2.08	2.0807	2.0816	2.0828
3	2.0772	2.08125	2.0816	2.08265	2.084
4	2.0749	2.0799	2.0808	2.0823	2.08345
5	2.0752	2.07975	2.08065	2.08135	2.08235
6	2.0755	2.0796	2.0806	2.08165	2.0825
7	2.0768	2.0798	2.0802	2.0814	2.08265
8	2.076	2.08045	2.0807	2.08225	2.0833
9	2.0768	2.0808	2.0819	2.08315	2.0839
10	2.07555	2.0808	2.08125	2.0825	2.0832
11	2.0757	2.08015	2.0805	2.0821	2.08275
12	2.0774	2.0757	2.0757	2.0758	2.0758

Table B.40 Case 3: Diffuser position 2: diffuser hub ID (SCS diffuser bore of steel) (in)

Stage/Time	0	8	16	32	64
1	0.8852	0.8903	0.89155	0.8939	0.8975
2	0.88415	0.887	0.8881	0.8898	0.8919
3	0.8841	0.8882	0.8898	0.89155	0.8946
4	0.8837	0.88755	0.8894	0.8905	0.893
5	0.884	0.888	0.8899	0.89135	0.894
6	0.884	0.88655	0.8898	0.8913	0.8931
7	0.8851	0.8886	0.89095	0.8928	0.8966
8	0.8844	0.88775	0.88905	0.8925	0.8941
9	0.8847	0.8891	0.8914	0.892	0.8938
10	0.884	0.8874	0.89	0.8901	0.8911
11	0.8839	0.8885	0.8913	0.893	0.89515
12	0.8837	0.888	0.8904	0.893	0.8944

Table B.41 Case 3: Diffuser position 3: diffuser balance ring ID (in)

Stage/Time	0	8	16	32	64
1	2.48182	2.48832	2.49015	2.49212	2.49528
2	2.48132	2.48615	2.48848	2.48995	2.49095
3	2.47932	2.48465	2.48682	2.48728	2.48828
4	2.48148	2.48698	2.49098	2.49212	2.49378
5	2.48065	2.48682	2.48815	2.49028	2.49178
6	2.48065	2.48465	2.48932	2.49045	2.49178
7	2.48065	2.48582	2.48882	2.49012	2.49162
8	2.48115	2.48798	2.48898	2.49045	2.49245
9	2.47982	2.48448	2.48665	2.48678	2.48778

10	2.48	2.48765	2.49048	2.49128	2.49262
11	2.48132	2.48732	2.48882	2.48995	2.49195
12	2.48132	2.48865	2.48815	2.49145	2.49162

Table B.42 Case 3: Diffuser position 4: diffuser inside shroud ID (in)

Stage/Time	0	8	16	32	64
1	3.14415	3.14335	3.1432	3.1431	3.1435
2	3.1439	3.14435	3.1443	3.14425	3.1453
3	3.1451	3.1452	3.1456	3.1457	3.1457
4	3.1445	3.1447	3.14515	3.14547	3.14545
5	3.1444	3.1448	3.1453	3.1454	3.146
6	3.14315	3.1439	3.1436	3.14425	3.1445
7	3.1424	3.1433	3.14365	3.14375	3.1442
8	3.1438	3.1437	3.14345	3.1435	3.14425
9	3.1443	3.14465	3.1451	3.1452	3.1455
10	3.1433	3.14435	3.1445	3.1448	3.1454
11	3.1431	3.14435	3.1444	3.1448	3.1453
12	3.14345	3.1437	3.1438	3.1439	3.1445

Table B.43 Case 3: Diffuser position 5: diffuser skirt ring depth (in)

Stage/Time	0	8	16	32	64
1	0.491	0.49133	0.49167	0.4915	0.49167
2	0.492	0.4928	0.49267	0.49263	0.4924
3	0.4905	0.49167	0.49147	0.4918	0.49187
4	0.4903	0.49257	0.4926	0.4924	0.4926
5	0.4903	0.49147	0.49143	0.4917	0.4914
6	0.49	0.4922	0.4922	0.49223	0.49173
7	0.489	0.4897	0.49007	0.49	0.49
8	0.4896	0.49223	0.49167	0.49163	0.4914
9	0.4898	0.49087	0.49217	0.491	0.491
10	0.489	0.493	0.49313	0.49317	0.49317
11	0.4895	0.49157	0.49127	0.4911	0.49173
12	0.49	0.49007	0.49	0.49	0.49

Table B.44 Case 3: Diffuser position 6: diffuser hub ID (SCS diffuser bore of carbide) (in)

Stage/Time	0	8	16	32	64
1	0.9454	0.9452	0.94625	0.9465	0.9474
2	0.945	0.945	0.9452	0.9456	0.94625
3	0.8838	0.8839	0.8899	0.891	0.8929
4	0.945	0.945	0.9458	0.94645	0.9468
5	0.8842	0.8842	0.89225	0.8926	0.894
6	0.945	0.945	0.9456	0.9457	0.9462

7	0.8844	0.8845	0.892	0.8923	0.8952
8	0.945	0.945	0.94555	0.9456	0.9457
9	0.8846	0.8845	0.8904	0.8915	0.8929
10	0.945	0.945	0.94565	0.9454	0.94525
11	0.8842	0.8842	0.8928	0.894	0.8948
12	0.945	0.9452	0.94665	0.9471	0.94925

Table B.45 Case 3: Impeller position 1: impeller hub ID (in)

Stage/Time	0	8	16	32	64
1	0.6902	0.69023	0.69025	0.6904	0.6904
2	0.6897	0.69018	0.6905	0.69045	0.69045
3	0.6899	0.68996	0.69	0.6899	0.6899
4	0.6902	0.69014	0.6901	0.6903	0.6903
5	0.6902	0.69029	0.69035	0.6901	0.6901
6	0.6901	0.69034	0.6905	0.6901	0.6901
7	0.6903	0.69048	0.6906	0.69035	0.69035
8	0.6908	0.69098	0.6911	0.691	0.691
9	0.69105	0.69138	0.6916	0.69135	0.69135
10	0.6908	0.6908	0.6908	0.69035	0.69035
11	0.6907	0.69106	0.6913	0.691	0.691
12	0.6905	0.69068	0.6908	0.69065	0.69065

Table B.46 Case 3: Impeller position 2: impeller hub OD (in)

Stage/Time	0	8	16	32	64
1	0.8745	0.87117	0.87067	0.86783	0.86633
2	0.8745	0.8715	0.86928	0.87033	0.87033
3	0.8745	0.87	0.86667	0.86483	0.86183
4	0.8745	0.87017	0.86983	0.86933	0.869
5	0.8745	0.87	0.86983	0.8685	0.86767
6	0.8745	0.86917	0.87067	0.87167	0.87133
7	0.8745	0.87033	0.86867	0.869	0.8665
8	0.8745	0.8685	0.8705	0.87033	0.87033
9	0.873	0.86933	0.86767	0.867	0.86517
10	0.8745	0.87083	0.87033	0.87167	0.8715
11	0.8745	0.87067	0.86933	0.8685	0.86817
12	0.875	0.8695	0.86867	0.867	0.86633

Table B.47 Case 3: Impeller position 3: impeller balance ring OD (in)

Stage/Time	0	8	16	32	64
1	2.46997	2.46403	2.46295	2.46073	2.45825
2	2.4688	2.46275	2.46147	2.46017	2.45845
3	2.46935	2.46022	2.45885	2.45553	2.45213
4	2.46868	2.46313	2.46225	2.461	2.45888

5	2.47065	2.4635	2.46248	2.46115	2.45932
6	2.46955	2.46282	2.46123	2.45947	2.45798
7	2.468	2.4621	2.46103	2.45955	2.45642
8	2.46917	2.46282	2.46182	2.46033	2.45928
9	2.46955	2.46228	2.46032	2.45758	2.45542
10	2.46992	2.46345	2.46247	2.4608	2.4601
11	2.46827	2.46398	2.46287	2.46078	2.46028
12	2.46997	2.46297	2.46163	2.45933	2.45843

Table B.48 Case 3: Impeller position 4: impeller skirt ring OD (in)

Stage/Time	0	8	16	32	64
1	2.0625	2.05698	2.05445	2.05112	2.0493
2	2.062	2.057	2.05515	2.05352	2.05055
3	2.06215	2.05713	2.0557	2.05415	2.0523
4	2.06082	2.05625	2.05565	2.05365	2.05107
5	2.06243	2.05652	2.05502	2.05277	2.0505
6	2.06098	2.05638	2.055	2.05352	2.05178
7	2.06178	2.05502	2.05322	2.05122	2.0494
8	2.06162	2.05602	2.05503	2.05353	2.05047
9	2.06228	2.0563	2.05505	2.05355	2.05178
10	2.0621	2.05675	2.05495	2.05338	2.05158
11	2.0615	2.05555	2.05462	2.0529	2.05155
12	2.06143	2.05705	2.05625	2.05457	2.05303

Table B.49 Case 3: Impeller position 5: impeller outside shroud OD (in)

Stage/Time	0	8	16	32	64
1	3.1025	3.10438	3.10563	3.10512	3.10528
2	3.102	3.1031	3.10383	3.10345	3.10363
3	3.102	3.10261	3.10302	3.10285	3.10277
4	3.1035	3.10442	3.10503	3.10477	3.10467
5	3.103	3.104	3.10467	3.10375	3.10452
6	3.103	3.10256	3.10227	3.10168	3.10223
7	3.1025	3.10306	3.10343	3.10275	3.10273
8	3.1	3.10283	3.10472	3.10475	3.10472
9	3.1005	3.10302	3.10492	3.10453	3.10412
10	3.101	3.10272	3.10387	3.10405	3.10385
11	3.102	3.10369	3.10548	3.10482	3.1051
12	3.1	3.10234	3.10502	3.1047	3.10482

Table B.50 Case 3: Inter-stage clearance (SCS inter-stage of steel) (in)

Stage/Time	0	8	16	32	64
1	0.0107	0.0191	0.0209	0.0261	0.0312
2	0.0097	0.0155	0.0188	0.0195	0.0216

3	0.0096	0.0182	0.0231	0.0267	0.0328
4	0.0092	0.0174	0.0196	0.0212	0.0240
5	0.0095	0.0180	0.0201	0.0228	0.0263
6	0.0095	0.0174	0.0191	0.0196	0.0218
7	0.0102	0.0183	0.0223	0.0238	0.0301
8	0.0099	0.0193	0.0185	0.0222	0.0238
9	0.0117	0.0198	0.0237	0.0250	0.0286
10	0.0095	0.0166	0.0197	0.0184	0.0196
11	0.0094	0.0178	0.0220	0.0245	0.0270
12	0.0087	0.0185	0.0217	0.0260	0.0281

Table B.51 Case 3: Inter-stage clearance (SCS inter-stage of carbide) (in)

Stage/Time	0	8	16	32	64
1	0.0084	0.0096	0.0102	0.0103	0.0112
2	0.0082	0.0085	0.0088	0.0093	0.0100
3	0.0072	0.0166	0.0192	0.0272	0.0291
4	0.0083	0.0091	0.0094	0.0101	0.0104
5	0.0073	0.0176	0.0218	0.0240	0.0254
6	0.0083	0.0087	0.0090	0.0094	0.0099
7	0.0074	0.0187	0.0224	0.0267	0.0296
8	0.0081	0.0086	0.0088	0.0092	0.0093
9	0.0074	0.0188	0.0214	0.0270	0.0285
10	0.0084	0.0093	0.0091	0.0090	0.0088
11	0.0074	0.0193	0.0228	0.0260	0.0268
12	0.0084	0.0116	0.0133	0.0131	0.0152

Table B.52 Case 3: Balance ring clearance (in)

Stage/Time	0	8	16	32	64
1	0.0118	0.0243	0.0272	0.0314	0.0370
2	0.0125	0.0234	0.02702	0.0298	0.0325
3	0.0100	0.0244	0.02797	0.0318	0.0362
4	0.0128	0.0238	0.02873	0.0311	0.0349
5	0.0100	0.0233	0.02567	0.0291	0.0325
6	0.0111	0.0218	0.02808	0.0310	0.0338
7	0.0118	0.0237	0.02778	0.0306	0.0352
8	0.0120	0.0252	0.02717	0.0301	0.0332
9	0.0103	0.0222	0.02633	0.0292	0.0324
10	0.0101	0.0242	0.02802	0.0305	0.0325
11	0.0130	0.0233	0.02595	0.0292	0.0317
12	0.0113	0.0257	0.02652	0.0321	0.0332

Table B.53 Case 3: Skirt ring clearance (in)

Stage/Time	0	8	16	32	64
------------	---	---	----	----	----

1					
2	0.0139	0.02345	0.02555	0.02848	0.0327
3	0.0137	0.02287	0.025	0.02745	0.0305
4	0.0164	0.025	0.02595	0.029	0.03293
5	0.0125	0.02338	0.02578	0.02953	0.03295
6	0.0142	0.02337	0.02565	0.02783	0.03057
7	0.0137	0.02458	0.02738	0.03043	0.0331
8	0.0152	0.02378	0.02517	0.02787	0.03218
9	0.0137	0.02415	0.02565	0.0287	0.03152
10	0.0147	0.02405	0.02695	0.02977	0.03232
11	0.0140	0.02525	0.02663	0.0296	0.03165
12	0.0143	0.0231	0.02425	0.02753	0.02972

Table B.54 Case 3: Sleeve/bushing OD (in)

Stage/Time	0	8	16	32	64
Bottom bearing	0.93718	0.93675	0.93667	0.93612	0.935
1	0.93677	0.93608	0.93607	0.93625	0.93617
2	0.93682	0.93647	0.93642	0.93655	0.9363
3	0.87667	0.8721	0.87072	0.86725	0.86382
4	0.93668	0.93635	0.93645	0.93652	0.93637
5	0.87685	0.87252	0.87042	0.87002	0.86863
6	0.9367	0.93633	0.93658	0.93648	0.93628
7	0.87707	0.87222	0.8696	0.86908	0.86562
8	0.93687	0.93648	0.93673	0.93678	0.93642
9	0.87715	0.8709	0.869	0.86688	0.86445
10	0.93663	0.93637	0.9366	0.93668	0.93645
11	0.8768	0.8721	0.87005	0.8688	0.86803
12	0.93677	0.9345	0.93333	0.93588	0.93402
Top bearing 1	0.937	0.93672	0.93692	0.9359	0.93337
Top bearing 2	0.937	0.9368	0.9364	0.93658	0.93528

Table B.55 Case 3: Impeller weight loss (g)

Stage/Time	0	8	16	32	64
1	320.78	318.92	315.93	314.5	312.56
2	316.21	313.02	312.51	311.69	310.56
3	316.99	312.03	311.08	309.65	308.03
4	312.35	308.5	307.97	306.92	305.29
5	323.57	318.01	317.25	316.2	314.66
6	313.08	309.48	308.89	307.88	306.52
7	311.91	308.47	307.95	307.08	305.62
8	313.43	309.71	309.24	308.21	306.66
9	320.46	315.78	314.62	313.11	311.51
10	317.74	314.17	313.58	312.5	311.01
11	317.07	314.14	313.33	312.37	311.38

12	319.57	316.15	315.61	314.57	313.35
----	--------	--------	--------	--------	--------

Table B.56 Case 3: Diffuser weight loss (g)

Stage/Time	0	8	16	32	64
1	1079.81	1076.92	1075.51	1072.71	1068.8
2	1077.6	1075.68	1074.45	1072.15	1068.79
3	1156.12	1152.25	1150.62	1147.59	1143.25
4	1089.36	1086.92	1085.53	1082.77	1078.5
5	1078.47	1074.81	1073.28	1070.73	1066.78
6	1085.13	1082.95	1081.67	1079.13	1075.26
7	1094.08	1090.6	1089.35	1086.65	1082.16
8	1086.22	1084.01	1082.71	1080.21	1076.48
9	1156.61	1152.76	1151.16	1148.61	1145.05
10	1090.99	1086.63	1085.15	1082.19	1078.06
11	1072.49	1069.6	1067.99	1065.52	1061.9
12	1097.24	1095.37	1093.81	1091.35	1087.23

Table B.57 Case 3: Sleeve weight loss (g)

Stage/Time	0	8	16	32	64
Bottom bearing 1	56.99	56.75	56.61	56.2	55.42
Bottom bearing 2	57.09	57.02	56.98	56.83	56.56
1	52.73	52.64	52.55	52.32	51.96
2	52.53	52.48	52.43	52.33	52.2
3	41.83	41.05	40.72	40.16	39.47
4	52.46	52.44	52.4	52.27	52.12
5	41.75	40.95	40.67	40.42	39.99
6	52.69	52.62	52.61	52.5	52.3
7	41.46	40.53	40.24	40	39.38
8	52.64	52.56	52.54	52.41	52.21
9	41.19	40.18	39.85	39.42	38.85
10	52.52	52.48	52.46	52.38	52.28
11	41.55	40.68	40.38	40.06	39.82
12	57.1	57	56.92	56.78	56.44
Top bearing 1	57.14	57.1	57.04	56.89	56.55
Top bearing 2	57.14	0	57.05	0	56.66

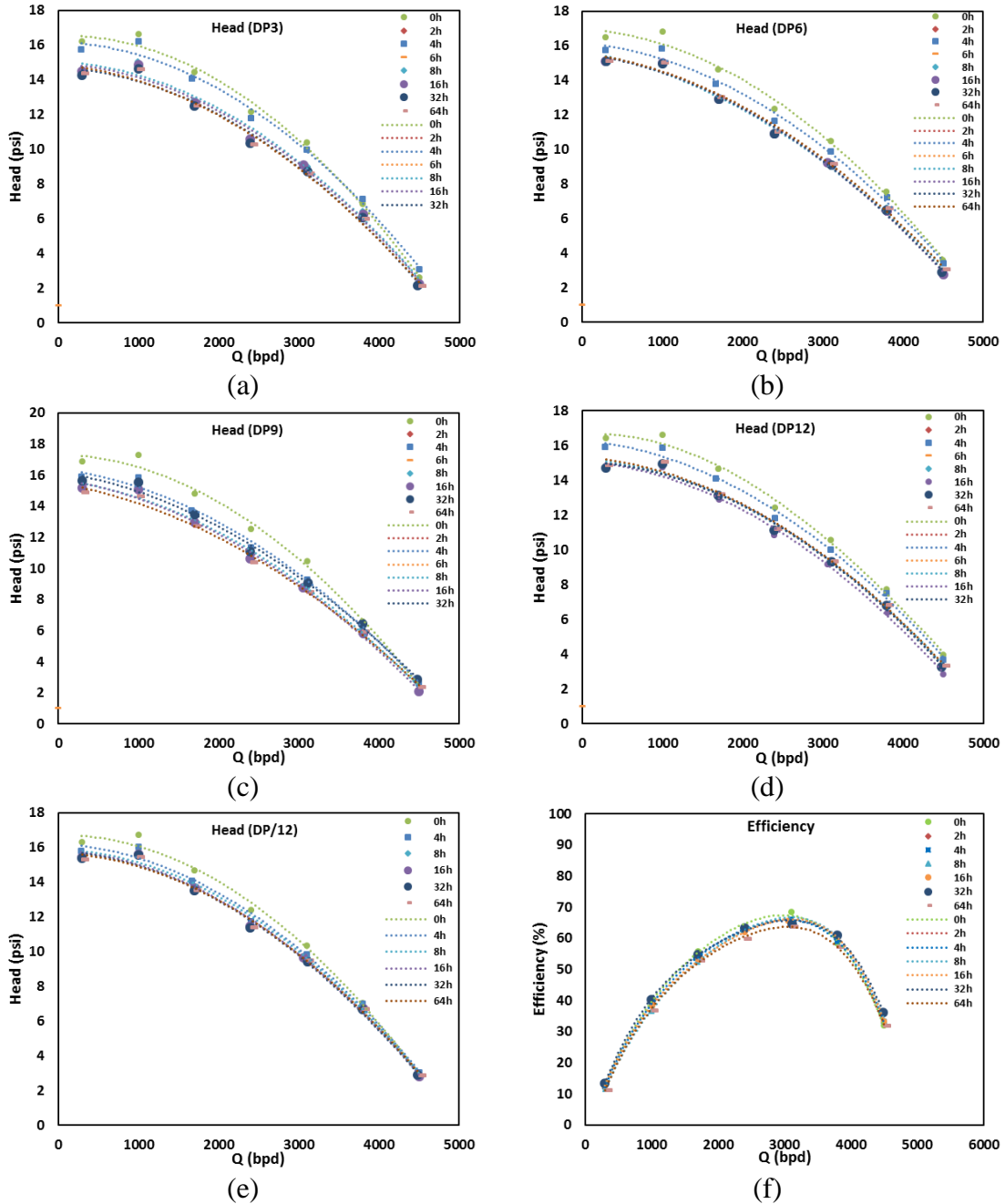


Figure B.3 Case 3 performance degradation (a) head of stage 3, (b) head of stage 6, (c) head of stage 9, (d) head of stage 12, (e) average head, (f) Pump efficiency

B.4 Case-4 Air-Water-Sand at $N = 3600$ rpm, $Q_L = 3100$ bpd, $GVF = 7.5\%$

Table B.58 Case 4: Diffuser position 1: diffuser skirt ring ID (in)

Stage/Time	0	8	16	32	64
------------	---	---	----	----	----

1	2.0756	2.07915	2.0808	2.0821	2.0838
2	2.07635	2.08025	2.08095	2.0821	2.0823
3	2.07645	2.0796	2.0803	2.0815	2.083
4	2.07575	2.0806	2.08145	2.0827	2.0843
5	2.0754	2.0799	2.0807	2.0821	2.0832
6	2.0761	2.08035	2.0811	2.084	2.0848
7	2.0757	2.0797	2.0806	2.0825	2.08385
8	2.0757	2.0799	2.0808	2.0823	2.0847
9	2.0753	2.0795	2.08025	2.0824	2.08275
10	2.07545	2.08	2.08055	2.0828	2.0848
11	2.07675	2.0792	2.0797	2.0804	2.0806
12	2.0766	2.0766	2.0767	2.0767	2.0765

Table B.59 Case 4: Diffuser position 2: diffuser hub ID (SCS diffuser bore of steel) (in)

Stage/Time	0	8	16	32	64
1	0.8841	0.8863	0.887	0.8917	0.8956
2	0.8837	0.8851	0.8869	0.8888	0.89175
3	0.8847	0.88825	0.8886	0.8901	0.8911
4	0.8842	0.8865	0.8889	0.8925	0.89535
5	0.8842	0.8898	0.8915	0.894	0.89605
6	0.8836	0.886	0.88635	0.8895	0.89175
7	0.8839	0.8901	0.8921	0.8937	0.8964
8	0.8842	0.8861	0.8868	0.8884	0.8927
9	0.8842	0.8899	0.8922	0.89365	0.8957
10	0.884	0.8867	0.8877	0.8903	0.8925
11	0.8845	0.8884	0.8892	0.8904	0.89235
12	0.8841	0.8898	0.8915	0.8949	0.8976

Table B.60 Case 4: Diffuser position 3: diffuser balance ring ID (in)

Stage/Time	0	8	16	32	64
1	2.480483	2.48815	2.489483	2.491617	2.493117
2	2.480483	2.484817	2.487983	2.490283	2.492283
3	2.479483	2.48315	2.486817	2.488117	2.490617
4	2.48015	2.485483	2.490433	2.48995	2.493283
5	2.480317	2.486983	2.490483	2.490283	2.493617
6	2.47965	2.485983	2.489317	2.491283	2.494783
7	2.47965	2.486317	2.49015	2.48995	2.492617
8	2.479983	2.485983	2.489483	2.489117	2.49295
9	2.48065	2.487817	2.490317	2.490783	2.494283
10	2.48	2.486817	2.487983	2.489783	2.494283
11	2.47915	2.48165	2.48415	2.484783	2.488283
12	2.480983	2.483317	2.48715	2.490283	2.494623

Table B.61 Case 4: Diffuser position 4: diffuser inside shroud ID (in)

Stage/Time	0	8	16	32	64
1	3.14485	3.1431	3.1436	3.1442	3.145
2	3.1436	3.1439	3.14405	3.14505	3.1449
3	3.1439	3.1441	3.14425	3.1448	3.1455
4	3.1435	3.1428	3.14315	3.1442	3.1451
5	3.14625	3.14695	3.1467	3.1478	3.1477
6	3.1441	3.1455	3.1444	3.1453	3.145
7	3.144	3.14505	3.144	3.145	3.1451
8	3.1436	3.14525	3.1445	3.1456	3.1459
9	3.1426	3.14525	3.1442	3.145	3.1449
10	3.14385	3.14585	3.1455	3.1465	3.1464
11	3.14395	3.14545	3.1443	3.1453	3.1456
12	3.144	3.14565	3.1446	3.1449	3.1454

Table B.62 Case 4: Diffuser position 5: diffuser skirt ring depth (in)

Stage/Time	0	8	16	32	64
1	0.491	0.493	0.492	0.4927333	0.491867
2	0.491	0.492067	0.4915	0.4912333	0.491167
3	0.4896	0.491333	0.49183333	0.4916	0.492067
4	0.4905	0.492233	0.49246667	0.4922333	0.4924
5	0.4915	0.4927	0.49266667	0.4924	0.4926
6	0.491	0.491767	0.49166667	0.4914	0.491367
7	0.4915	0.492667	0.4925	0.4925667	0.492667
8	0.49	0.493167	0.49316667	0.4929	0.493333
9	0.49	0.4923	0.493	0.4920667	0.4923
10	0.4905	0.492867	0.493	0.4928	0.492933
11	0.49	0.491	0.49113333	0.4909333	0.491133
12	0.4918	0.491167	0.49143333	0.4912333	0.4914

Table B.63 Case 4: Diffuser position 6: diffuser hub ID (SCS diffuser bore of carbide) (in)

Stage/Time	0	8	16	32	64
1	0.9455	0.9459	0.94585	0.9457	0.9457
2	0.9455	0.9458	0.9459	0.9457	0.9458
3	0.8843	0.8902	0.8912	0.8911	0.8925
4	0.9456	0.9458	0.946	0.94645	0.947
5	0.8845	0.8913	0.89275	0.89435	0.896
6	0.9454	0.94525	0.9456	0.9462	0.9467
7	0.8842	0.8915	0.89355	0.8944	0.896
8	0.945	0.9451	0.9451	0.9452	0.9459
9	0.8838	0.89025	0.89255	0.8935	0.8948
10	0.9452	0.9452	0.94545	0.9454	0.9458
11	0.8838	0.88845	0.889	0.8903	0.8914

12	0.9447	0.94525	0.9462	0.9468	0.9489
----	--------	---------	--------	--------	--------

Table Case 4: B.64 Impeller position 1: impeller hub ID (in)

Stage/Time	0	8	16	32	64
1	0.691	0.6918	0.69175	0.69175	0.69175
2	0.6907	0.6899	0.6898	0.6898	0.6898
3	0.6897	0.6905	0.69015	0.69015	0.69015
4	0.6902	0.69	0.6902	0.6902	0.6902
5	0.6898	0.6897	0.6902	0.6902	0.6902
6	0.6919	0.6922	0.6919	0.6919	0.6919
7	0.6903	0.6901	0.69	0.69	0.69
8	0.6893	0.68925	0.68935	0.68935	0.68935
9	0.6898	0.6901	0.69	0.69	0.69
10	0.689	0.6906	0.69075	0.69075	0.69075
11	0.6907	0.691	0.6909	0.6909	0.6909
12	0.6891	0.6906	0.6894	0.6894	0.6894

Table B.65 Case 4: Impeller position 2: impeller hub OD (in)

Stage/Time	0	8	16	32	64
1	0.8755	0.87475	0.873433	0.872317	0.87
2	0.875617	0.87555	0.873633	0.8727	0.87095
3	0.87585	0.869433	0.867667	0.8663	0.863067
4	0.8757	0.87595	0.8758	0.8757	0.875867
5	0.875967	0.872383	0.87065	0.8697	0.86885
6	0.8759	0.875233	0.8752	0.875433	0.875567
7	0.875333	0.8718	0.870067	0.86965	0.8677
8	0.875667	0.87565	0.87535	0.875767	0.875767
9	0.875367	0.871317	0.868917	0.868617	0.866933
10	0.875783	0.874483	0.873383	0.871767	0.869367
11	0.87525	0.870917	0.869033	0.866767	0.86425
12	0.875367	0.871367	0.869967	0.86825	0.864783

Table B.66 Case 4: Impeller position 3: impeller balance ring OD (in)

Stage/Time	0	8	16	32	64
1	2.469967	2.463833	2.462117	2.461717	2.46115
2	2.4688	2.4642	2.4624	2.461033	2.4583
3	2.46935	2.4599	2.4585	2.4563	2.451883
4	2.468683	2.463043	2.461883	2.460467	2.4594
5	2.47065	2.465067	2.463717	2.461683	2.459967
6	2.46955	2.463917	2.463267	2.46005	2.458483
7	2.468	2.46255	2.461967	2.460617	2.458067
8	2.469167	2.464383	2.463267	2.46195	2.459933
9	2.46955	2.464517	2.462667	2.461583	2.458733

10	2.469917	2.464167	2.463333	2.4612	2.45755
11	2.468267	2.462317	2.460867	2.4568	2.452967
12	2.469967	2.464517	2.46345	2.460817	2.459467

Table B.67 Case 4: Impeller position 4: impeller skirt ring OD (in)

Stage/Time	0	8	16	32	64
1	2.0625	2.056633	2.05445	2.053733	2.04925
2	2.062	2.055383	2.054283	2.0527	2.04975
3	2.06215	2.0565	2.05525	2.053467	2.051783
4	2.060817	2.05425	2.052867	2.051317	2.048233
5	2.062433	2.0551	2.05395	2.0529	2.05065
6	2.060983	2.056583	2.05465	2.05285	2.05065
7	2.061783	2.056783	2.055417	2.052067	2.0505
8	2.061617	2.0548	2.053283	2.051817	2.049767
9	2.062283	2.055933	2.054567	2.052467	2.050533
10	2.0621	2.05555	2.053333	2.051533	2.049067
11	2.0615	2.055667	2.054833	2.052417	2.04955
12	2.061433	2.05665	2.055867	2.0526	2.049017

Table B.68 Case 4: Impeller position 5: impeller outside shroud OD (in)

Stage/Time	0	8	16	32	64
1	3.10555	3.1054	3.10485	3.1045833	3.101567
2	3.10475	3.10425	3.10683333	3.1063333	3.106633
3	3.10475	3.104033	3.10401667	3.1036833	3.104183
4	3.10495	3.10455	3.10475	3.1046667	3.1043
5	3.10195	3.102733	3.10291667	3.1025833	3.101267
6	3.10465	3.106467	3.10405	3.1032833	3.103783
7	3.10285	3.102683	3.10275	3.1023167	3.102483
8	3.1043	3.104817	3.10476667	3.10425	3.104417
9	3.1037	3.103733	3.10381667	3.10345	3.103467
10	3.10705	3.1056	3.1043	3.1047333	3.1046
11	3.1034	3.104267	3.10336667	3.1032667	3.103317
12	3.1055	3.105783	3.10511667	3.1043667	3.105383

Table B.69 Case 4: Inter-stage clearance (SCS inter-stage of steel) (in)

Stage/Time	0	8	16	32	64
1	0.0086	0.0115	0.0136	0.0194	0.0256
2	0.0081	0.0095	0.0133	0.0161	0.0208
3	0.0088	0.0188	0.0209	0.0238	0.0280
4	0.0084	0.0105	0.0133	0.0168	0.0195
5	0.0082	0.0174	0.0208	0.0243	0.0272
6	0.0077	0.0108	0.0112	0.0141	0.0162
7	0.0086	0.0183	0.0220	0.0240	0.0287

8	0.0085	0.0105	0.0115	0.0126	0.0169
9	0.0088	0.0186	0.0233	0.0250	0.0288
10	0.0082	0.0122	0.0143	0.0185	0.0231
11	0.0093	0.0175	0.0202	0.0236	0.0281
12	0.0087	0.0184	0.0215	0.0267	0.0328

Table B.70 Case 4: Inter-stage clearance (SCS inter-stage of carbide) (in)

Stage/Time	0	8	16	32	64
1	0.0088	0.0094	0.0095	0.0093	0.0095
2	0.0085	0.0091	0.0091	0.0086	0.0089
3	0.0074	0.0200	0.0226	0.0237	0.0278
4	0.0087	0.0092	0.0094	0.0096	0.0103
5	0.0073	0.0195	0.0220	0.0254	0.0279
6	0.0087	0.0088	0.0092	0.0096	0.0101
7	0.0069	0.0203	0.0235	0.0251	0.0287
8	0.0081	0.0086	0.0087	0.0085	0.0094
9	0.0068	0.0196	0.0242	0.0263	0.0291
10	0.0082	0.0083	0.0087	0.0084	0.0088
11	0.0069	0.0182	0.0205	0.0246	0.0292
12	0.0081	0.0089	0.0109	0.0122	0.0168

Table B.71 Case 4: Balance ring clearance (in)

Stage/Time	0	8	16	32	64
1	0.0105	0.0243	0.027367	0.0299	0.0320
2	0.0117	0.0206	0.025583	0.0293	0.0340
3	0.0101	0.0233	0.028317	0.0318	0.0387
4	0.0115	0.0224	0.02855	0.0295	0.0339
5	0.0097	0.0219	0.026767	0.0286	0.0336
6	0.0101	0.0221	0.02605	0.0312	0.0363
7	0.0116	0.0238	0.028183	0.0293	0.0345
8	0.0108	0.0216	0.026217	0.0272	0.0330
9	0.0111	0.0233	0.02765	0.0292	0.0356
10	0.0101	0.0226	0.02465	0.0286	0.0367
11	0.0109	0.0193	0.023283	0.0280	0.0353
12	0.0110	0.0188	0.0237	0.0295	0.0352

Table B.72 Case 4: Skirt ring clearance (in)

Stage/Time	0	8	16	32	64
1					
2	0.0088	0.0094	0.0095	0.0093	0.0095
3	0.0085	0.0091	0.0091	0.0086	0.0089
4	0.0074	0.0200	0.0226	0.0237	0.0278
5	0.0087	0.0092	0.0094	0.0096	0.0103

6	0.0073	0.0195	0.0220	0.0204	0.0279
7	0.0087	0.0088	-0.4408	0.0096	0.0101
8	0.0069	0.0203	0.0235	0.0201	0.0287
9	0.0081	0.0086	0.0087	0.0085	0.0094
10	0.0068	0.0196	0.0242	0.0213	0.0291
11	0.0082	0.0083	0.0087	0.0084	0.0088
12	0.0069	0.0182	0.0205	0.0246	0.0292

Table B.73 Case 4: Sleeve/bushing OD (in)

Stage/Time	0	8	16	32	64
Bottom bearing	0.936883	0.93705	0.93645	0.935383	0.93185
1	0.93675	0.936517	0.936383	0.936383	0.93625
2	0.937017	0.93665	0.936817	0.937067	0.93695
3	0.87685	0.870167	0.86865	0.8674	0.86475
4	0.936917	0.936633	0.936567	0.936867	0.9367
5	0.87715	0.871783	0.870783	0.868967	0.868118
6	0.936717	0.936417	0.9364	0.93665	0.936567
7	0.8773	0.871183	0.870067	0.86925	0.86725
8	0.936883	0.936533	0.936433	0.93675	0.9365
9	0.876983	0.870683	0.868333	0.867217	0.865733
10	0.937	0.936867	0.936733	0.937	0.936983
11	0.876933	0.8703	0.868517	0.8657	0.8622
12	0.93655	0.936333	0.935283	0.934633	0.932083
Top bearing 1	0.93735	0.937133	0.936717	0.936267	0.935117
Top bearing 2	0.9373	0.937	0.936367	0.935883	0.934217

Table B.74 Case 4: Impeller weight loss (g)

Stage/Time	0	8	16	32	64
1	326.17	322.72	320.61	318.04	316.54
2	325.05	322.4	319.48	318.37	316.65
3	322.62	317.18	316.48	315.34	313.29
4	313.4	309.96	309.37	308.29	306.55
5	305.55	302.13	301.66	300.79	299.37
6	314.45	312.41	311.66	310.34	308.78
7	321.12	316.38	315.8	314.63	312.98
8	312.14	308.82	308.33	307.41	305.82
9	321.79	318.76	317.77	316.84	315.34
10	314.71	312.46	311.61	310.26	308.46
11	313.27	309	308.13	306.62	304.51
12	311.66	307.4	306.94	305.83	304.1

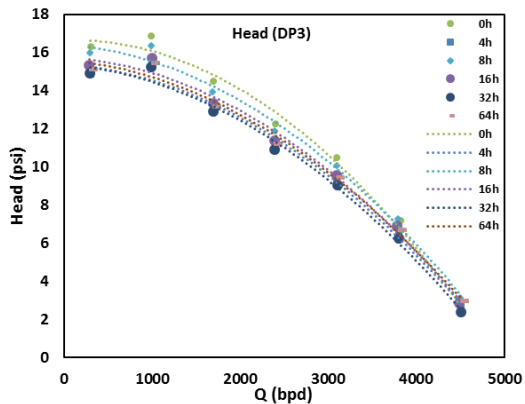
Table B.75 Case 4: Diffuser weight loss (g)

Stage/Time	0	8	16	32	64
------------	---	---	----	----	----

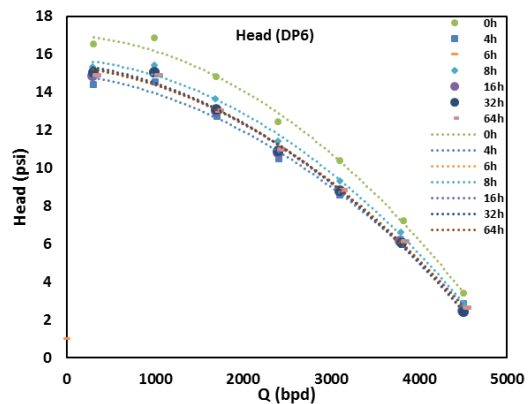
1	1087.2675	1085.23	1084.03	1081.69	1077.7
2	1086.2375	1085.2	1083.66	1081.66	1077.5
3	1147.6875	1143.5	1141.68	1139.27	1134.3
4	1064.6775	1062.55	1061.41	1059.39	1054.77
5	1077.6775	1074.12	1072.65	1070.24	1066.06
6	1083.6875	1082.27	1080.85	1078.6	1075.04
7	1083.9175	1079.3	1077.84	1070.5	1071.18
8	1077.2175	1075.01	1073.81	1071.65	1067.15
9	1088.6075	1085.14	1083.13	1080.53	1075.96
10	1080.0975	1076.79	1075.52	1073.32	1069.15
11	1138.8275	1135.4	1133.87	1131.48	1127.33
12	1072.5775	1070.79	1069.52	1067.61	1063.5

Table B.76 Case 4: Sleeve weight loss (g)

Stage/Time	0	8	16	32	64
Bottom bearing 1	57.2	56.98	56.88	56.62	56.22
Bottom bearing 2	57.18	57.21	57.11	56.82	56.18
1	52.55	52.51	52.46	52.4	52.3
2	52.39	52.34	52.22	52.15	52
3	42.03	40.92	40.58	40.33	39.86
4	52.67	52.64	52.57	52.49	52.36
5	41.48	40.91	40.72	40.39	40.17
6	52.59	52.52	52.47	52.37	52.26
7	41.85	40.89	40.63	40.4	40.01
8	52.6	52.55	52.49	52.41	52.27
9	41.6	40.59	40.19	39.95	39.58
10	52.61	52.55	52.49	52.41	52.15
11	41.38	40.29	40.02	39.5	38.91
12	56.94	56.84	56.72	56.47	56.04
Top bearing 1	57.31	57.18	57.15	57.07	56.92
Top bearing 2	57.3	57.21	57.13	56.92	56.46



(a)



(b)

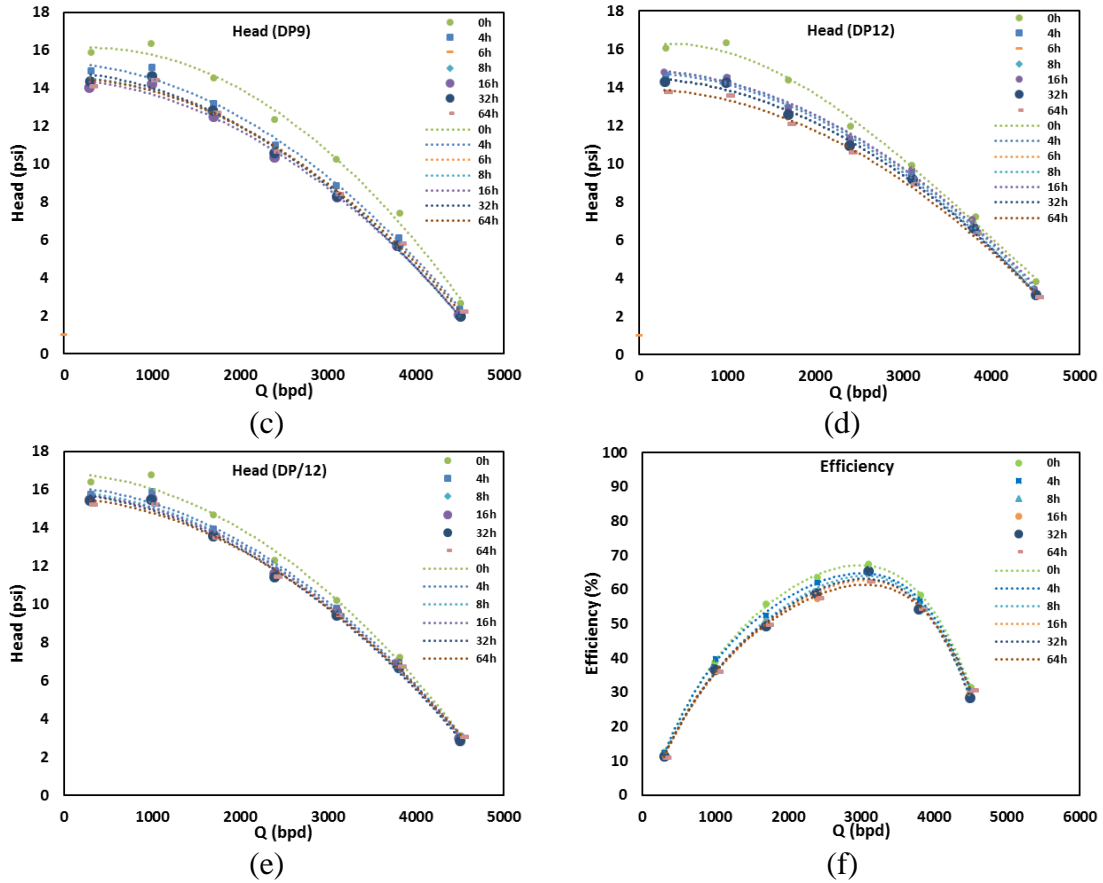
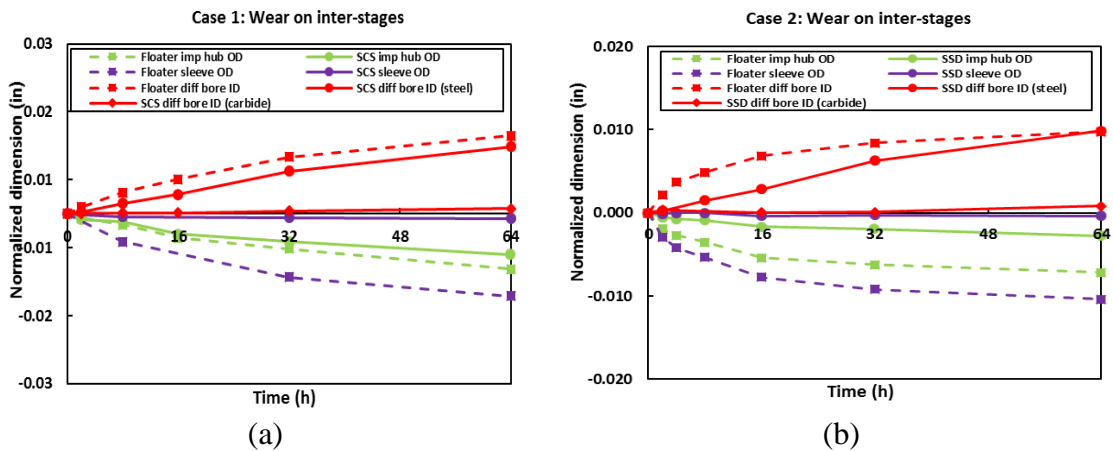
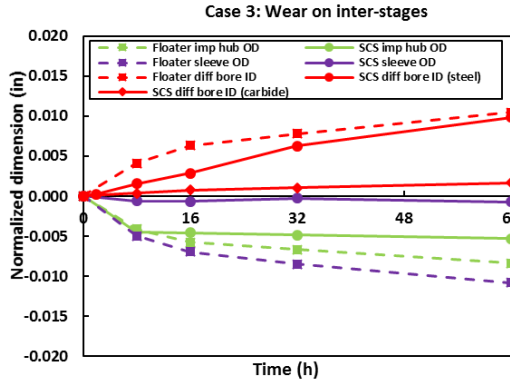


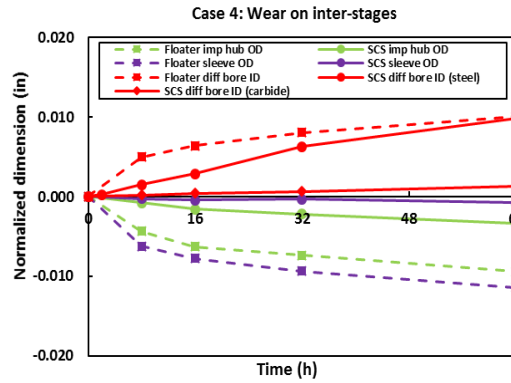
Figure B.4 Case 4 performance degradation (a) head of stage 3, (b) head of stage 6, (c) head of stage 9, (d) head of stage 12, (e) average head, (f) pump efficiency

B.5 Pump geometry comparison plots



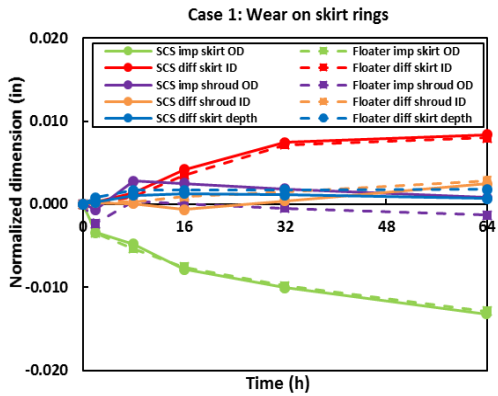


(c)

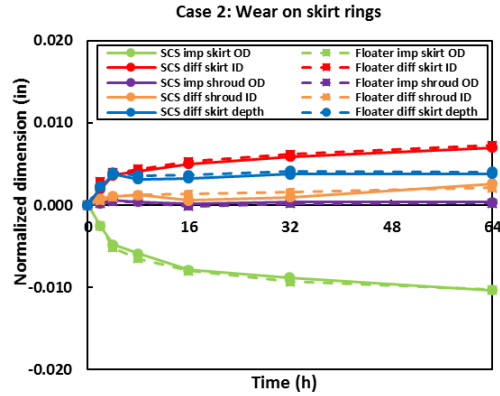


(d)

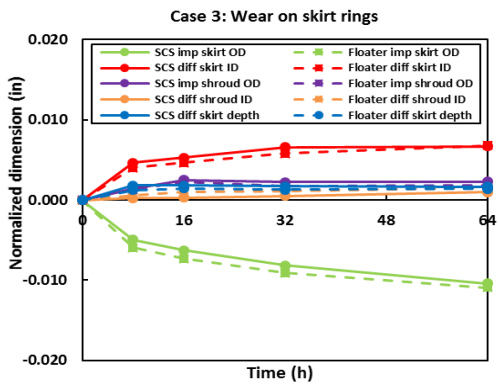
Figure B.5 Geometry changes in the inter-stage clearance, (a) Case 1: water-sand, $Q_L = 3100$ bpd, $N = 3600$ rpm, (b) Case 2: water-sand, $Q_L = 3100$ bpd, $N = 2400$ rpm, (c) Case 3: water-air-sand, $Q_L = 3100$ bpd, $N = 3600$ rpm, $GVF = 15\%$ (d) Case 4: water-air-sand, $Q_L = 3100$ bpd, $N = 3600$ rpm, $GVF = 7.5\%$



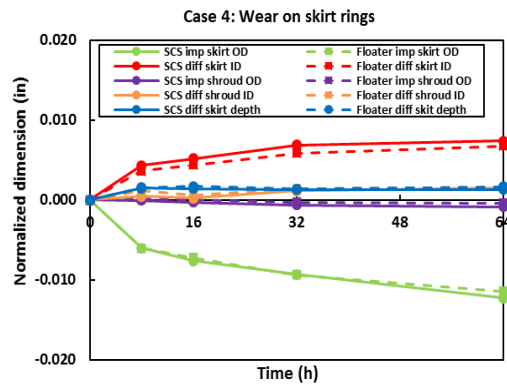
(a)



(b)

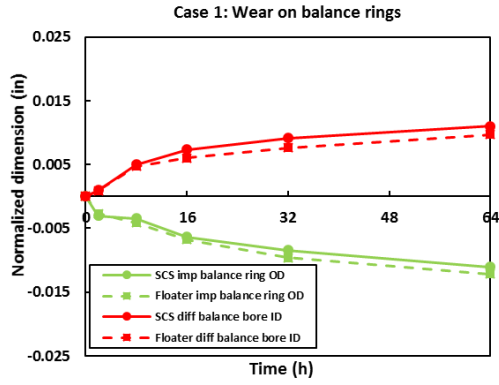


(c)

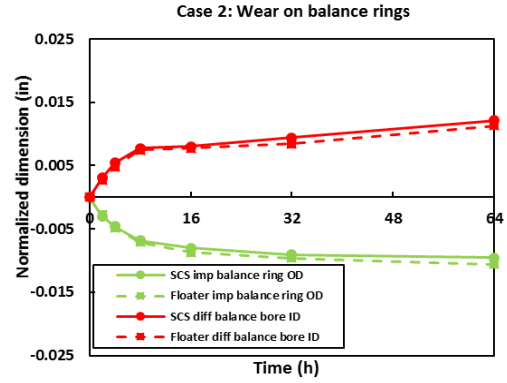


(d)

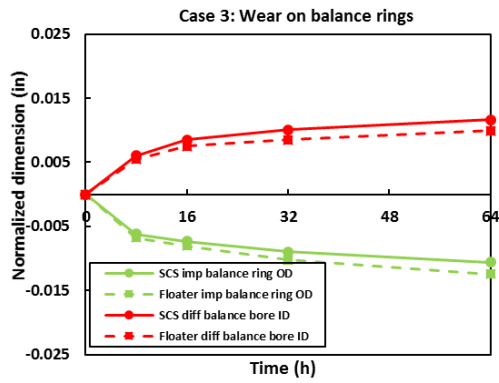
Figure B.6 Geometry changes in the skirt-ring clearance, (a) Case 1: water-sand, $Q_L = 3100$ bpd, $N = 3600$ rpm, (b) Case 2: water-sand, $Q_L = 3100$ bpd, $N = 2400$ rpm, (c) Case 3: water-air-sand, $Q_L = 3100$ bpd, $N = 3600$ rpm, $GVF = 15\%$ (d) Case 4: water-air-sand, $Q_L = 3100$ bpd, $N = 3600$ rpm, $GVF = 7.5\%$



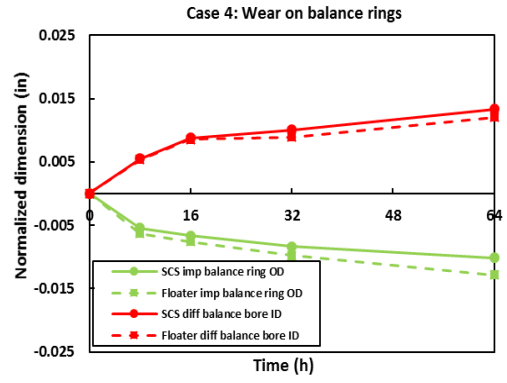
(a)



(b)



(c)



(d)

Figure B.7 Geometry changes in the balance ring clearance, (a) Case 1: water-sand, $Q_L = 3100$ bpd, $N = 3600$ rpm, (b) Case 2: water-sand, $Q_L = 3100$ bpd, $N = 2400$ rpm, (c) Case 3: water-air-sand, $Q_L = 3100$ bpd, $N = 3600$ rpm, $GVF = 15\%$ (d) Case 4: water-air-sand, $Q_L = 3100$ bpd, $N = 3600$ rpm, $GVF = 7.5\%$

APPENDIX C

ERROR ANALYSIS

For geometry and weight loss measurements, the experimental error originates directly from measuring instruments, the uncertainty is shown in Table C.1. Then, the relative uncertainty for length (or diameter) and weight can be easily calculated by the following equations:

$$\varepsilon_L = \frac{\delta L}{L} \quad (\text{C.1})$$

and

$$\varepsilon_m = \frac{\delta m}{m} . \quad (\text{C.2})$$

The clearance uncertainty should consider the measurement error from both inner and outer diameter readings. Therefore, the uncertainty can be calculated as:

$$\delta W_c = \sqrt{\delta d_{OD}^2 + \delta d_{ID}^2} \quad (\text{C.3})$$

and

$$\varepsilon_c = \frac{\delta W_c}{W_c} . \quad (\text{C.4})$$

By using equation (C.3), the clearance uncertainty is dominated by the tool that has a higher uncertainty. For example, if caliper and micrometer are used together, the uncertainty is mainly affected by the caliper as shown in Appendix C. It should be noted that the geometry of Pump 1 is measured by a caliper with a much lower accuracy before 16 hours test. The uncertainty is shown as “clearance by caliper” in Table C.2. Later on,

new electronic micrometers were ordered to improve the accuracy. That can be the reason for the geometry derivation between Pump 1 and others. The uncertainty and relative uncertainty are shown in Table C.2.

As mentioned in Section 2.1. The average surface erosion rate can be roughly calculated by subtracting the abrasion weight losses from the total weight loss shown in Equations (C.5) and (C.6). The uncertainty of abrasion weight loss of each position of impeller (or diffuser) is estimated with Equation (C.7). Finally, the uncertainty of total abrasion weight loss for impeller or diffuser can be obtained by Equation (C.8).

$$m_{erosion} = m_{erosion} - \sum_1^5 m_{position,i} , \quad (C.5)$$

$$m_{position,i} = \rho_{pump} |d_{0h,i} - d_{64h,i}| \times \frac{\pi}{2} (d_{0h,i} + d_{64h,i}) \times L_{c,i} , \quad (C.6)$$

$$\delta m_{position,i} = \pi \rho_{pump} \sqrt{(d_{0h,i} L_{c,i} \delta d_{0h,i})^2 + (d_{64h,i} L_{c,i} \delta d_{64h,i})^2 + (|d_{0h,i}^2 - d_{64h,i}^2| \delta L_{c,i})^2} \quad (C.7)$$

and

$$\delta m_{erosion} = \sqrt{\delta m_{total}^2 + \sum_1^5 (m_{abrasion,i})^2} . \quad (C.8)$$

The surface average erosion rate (ER_{ave}) can be calculated through equation (C.9), where A is the flow channel surface area of the impeller (or diffuser) obtained through ANSYS Fluent, and T is recorded erosion time. Assuming the uncertainty of A from ANSYS can be neglected, then the uncertainty δER_{ave} and relative uncertainty ε_{ER} can be obtained by Equations (C.11) and (C.12), respectively. Assuming δT is 4 hours of a 64-hour test, δER_{ave} and ε_{ER} are obtained and shown in Table C.2.

$$ER = \frac{m_{erosion}}{AT} , \quad (C.9)$$

$$\delta ER_{ave} = \sqrt{\left(\frac{\partial ER_{ave}}{\partial m_{erosion}} \delta m_{erosion}\right)^2 + \left(\frac{\partial ER_{ave}}{\partial T} \delta T\right)^2}, \quad (C.10)$$

$$\delta ER_{ave} = \sqrt{\left(\frac{\delta m_{erosion}}{AT}\right)^2 + \left(\frac{\delta T m_{erosion}}{AT^2}\right)^2}, \quad (C.11)$$

and

$$\varepsilon_{er} = \frac{\delta ER_{ave}}{ER_{ave}} = \frac{\sqrt{\delta m_{erosion}^2 + \left(\frac{\delta T m_{erosion}}{T}\right)^2}}{m_{erosion}}. \quad (C.12)$$

Table C.1 Instrument specification

Tool	Model	Range	Uncertainty
Outside micrometer	Anytime Tools	0-6"	±0.00005"
Inside micrometer	Mitutoyo	0.6-0.65"	±0.0002"
Inside micrometer	Mitutoyo	0.8-1.0"	±0.0002"
Inside micrometer	Mitutoyo	2.0-2.5"	±0.0002"
Inside micrometer	Mitutoyo	3.0-3.5"	±0.0002"
Depth meter	445BZ-6RL	0-6"	±0.001"
Digital caliper	500-754-20CERT	0-12"	±0.0005"
Precision balance	OHAUS Balance	0-1500g	±0.01g
Coriolis liquid flow meter	E-Hauser Promass 80F	0 ~ 18 kg/s	±0.05%
Coriolis gas flow meter	Micro Motion CMF025	0 ~ 0.3 kg/s	±0.05%
Temperature transmitter	Endress Hauser TMT82	-20-200 ⁰ C	±0.25%
Pressure transmitter	Endress Hauser PMC71	6 ~ 600 psig	±0.1%
Difference pressure sensor	Endress Hauser PMD75	0.45-45 psig	±0.1%
Torque sensor	Himmelstein 28004T	0-5000 lbf-in	±7.5 lbf-in

The head, temperature, flow rate, torque, and density uncertainty are also generated by measuring sensors, whose uncertainties are shown in Table C.1. The gas void fracture (GVF, λ) at pump intake is calculated by pressure, temperature, mass flow rate as shown in the following equations (Zhu, et al., 2018c).

$$\delta \lambda = \sqrt{\left(\frac{\partial \lambda}{\partial T} \delta T\right)^2 + \left(\frac{\partial \lambda}{\partial P} \delta P\right)^2 + \left(\frac{\partial \lambda}{\partial \dot{m}_G} \delta \dot{m}_G\right)^2 + \left(\frac{\partial \lambda}{\partial \dot{m}_L} \delta \dot{m}_L\right)^2}, \quad (C.13)$$

$$\frac{\partial \lambda}{\partial T} = \rho_L \dot{m}_G \dot{m}_L (\rho_L \dot{m}_G + \rho_G \dot{m}_L)^{-2} \frac{p M_a}{ZRT} \left[1 - x_v \left(1 - \frac{M_v}{M_a} \right) \right], \quad (\text{C.14})$$

$$\frac{\partial \lambda}{\partial P} = -\rho_L \dot{m}_G \dot{m}_L (\rho_L \dot{m}_G + \rho_G \dot{m}_L)^{-2} \frac{p M_a}{ZRT} \left[1 - x_v \left(1 - \frac{M_v}{M_a} \right) \right], \quad (\text{C.15})$$

$$\frac{\partial \lambda}{\partial \dot{m}_G} = \frac{1}{\rho_G} \left(\frac{\dot{m}_G}{\rho_G} + \frac{\dot{m}_L}{\rho_L} \right)^{-1} - \frac{\dot{m}_G}{\rho_G^2} \left(\frac{\dot{m}_G}{\rho_G} + \frac{\dot{m}_L}{\rho_L} \right)^{-2}, \quad (\text{C.16})$$

and

$$\frac{\partial \lambda}{\partial \dot{m}_L} = -\frac{\dot{m}_G}{\rho_G \rho_L} \left(\frac{\dot{m}_G}{\rho_G} + \frac{\dot{m}_L}{\rho_L} \right)^{-2}, \quad (\text{C.17})$$

where \dot{m}_G and \dot{m}_L are gas and liquid mass flowrates, respectively; x_v , M_v , M_a are gas properties, which can be found in appendix D. Then, the relative uncertainty of *GVF* is below 5% as shown in Table C.2.

Table C.2 Uncertainty and relative uncertainty

Tool	Range	Uncertainty	Relative uncertainty
Diffuser skirt ring ID (in)	2.075-2.085	±0.0002"	0.010%
Diffuser hub ID-steel (in)	0.885-0.900	±0.0002"	0.235%
Diffuser balance ring ID (in)	2.475-2.495	±0.0002"	0.008%
Diffuser inside shroud ID (in)	3.142-3.149	±0.0002"	0.006%
Diffuser skirt ring depth (in)	0.489-0.494	±0.001"	0.204%
Diffuser hub ID-carbide (in)	0.945-0.947	±0.0002"	0.021%
Impeller hub ID (in)	0.688-0.691	±0.0002"	0.029%
Impeller hub OD (in)	0.875-0.858	±0.00005"	0.006%
Impeller balance ring OD (in)	2.472-2.452	±0.00005"	0.002%
Impeller skirt ring OD (in)	2.060-2.048	±0.00005"	0.002%
Impeller inside shroud OD (in)	3.102-3.095	±0.00005"	0.002%
Inter-stage clearance-carbide (in)	0.008-0.028	±0.00021"	2.625%-0.750%
Inter-stage clearance-steel (in)	0.007-0.010	±0.00021"	3.000%-2.100%
Balance ring clearance (in)	0.012-0.036	±0.001"	8.333%-2.778%
Skirt ring clearance (in)	0.012-0.034	±0.00021"	1.750%-0.618%

Clearance by caliper (in)	0.010-0.020	±0.00141”	14.10%-7.050%
Steel sleeve OD (in)	0.880-0.860	±0.00005”	0.006%
Carbide sleeve OD (in)	0.940-0.935	±0.00005”	0.005%
Impeller weight (g)	325.00-305.00	±0.01g	0.003%
Diffuser weight (g)	1200.0-1050.0	±0.01g	0.001%
Impeller weight loss (g)	5.00-9.00	±0.014g	0.280%-0.156%
Diffuser weight loss (g)	7.00-12.00	±0.014g	0.200%-0.117%
Impeller abrasion weight loss (g)	2.00-3.00	±0.109g	5.450%-3.633%
Diffuser abrasion weight loss (g)	2.00-3.00	±0.159g	7.950%-5.300%
Impeller erosion weight loss (g)	3.00-5.00	±0.109g	3.633%-2.180%
Diffuser erosion weight loss (g)	5.00-8.00	±0.160g	3.200%-2.000%
Impeller ave erosion rate (kg/m ² s)	~1E-6	/	5.175%-5.945%
Diffuser ave erosion rate (kg/m ² s)	~1E-6	/	5.091%-5.665%
Torque	100-220 lbf-in	±7.5 lbf-in	7.500%-3.41%
Gas void fracture (%)	0-15	/	~5.000%

APPENDIX D

GAS PROPERTY CALCULATION

By using equations in this section, gas properties and pump intake *GVF* can be obtained. The moist air density can be calculated based on CIPM-81 correlations (Davis, 1992):

$$\rho = \frac{pM_a}{ZRT} \left[1 - x_v \left(1 - \frac{M_v}{M_a} \right) \right], \quad (\text{D.1})$$

where p is pressure, T is temperature, x_v is the mole fraction of water vapor, M_a is the molar mass of dry air, M_v is the molar mass of water, R is the molar gas constant, and Z is the compressibility factor. M_a is calculated by an auxiliary equation:

$$M_a = 28.9635 + 12.011(x_{CO_2} - 0.0004), \quad (\text{D.2})$$

where x_{CO_2} is the mole fraction of carbon dioxide. x_v is calculated by the following equations:

$$x_v = f(p, T_R) \frac{p_{SV}(T_R)}{p}, \quad (\text{D.3})$$

$$p_{SV} = \exp \left(AT^2 + BT + C + \frac{D}{T} \right), \quad (\text{D.4})$$

and

$$f = \alpha + \beta p + \gamma T^2, \quad (\text{D.5})$$

where p_{SV} is the saturation vapor pressure and f is the enhancement factor. The coefficients $A, B, C, D, \alpha, \beta,$ and γ can be found in Table D.1. Finally, the compressibility factor Z can be calculated as:

$$Z = 1 - \frac{P}{T} \left[a_0 + a_1 T + a_2 T^2 + (b_0 + b_1 T) x_v + (c_0 + c_1) x_v^2 \right] + \frac{P^2}{T^2} (a + e x_v^2), \quad (\text{D.6})$$

where the coefficients are also included in Table D.1.

Table D.1 Coefficients for gas property calculation

Parameters	Coefficients		Values
Saturation vapor pressure p_{SV}	A	$10^{-5} K^{-2}$	1.2811805
	B	$10^{-2} K^{-1}$	-1.9509874
	C		34.04926034
	D	$10^3 K$	-6.3536311
Enhancement factor f	α		1.00062
	β	$10^{-8} Pa^{-1}$	3.14
	γ	$10^{-7} K^{-2}$	5.6
Compressibility factor Z	a_0	$10^{-6} KPa^{-1}$	1.62419
	a_1	$10^{-8} Pa^{-1}$	-2.8969
	a_2	$10^{-10} K^{-1} Pa^{-1}$	1.0880
	b_0	$10^{-6} KPa^{-1}$	5.757
	b_1	$10^{-8} Pa^{-1}$	-2.589
	c_0	$10^{-4} KPa^{-1}$	1.9297
	c_1	$10^6 Pa^{-1}$	-2.285
	d	$10^{-11} K^2 Pa^{-2}$	1.73
e	$10^{-8} K^2 Pa^{-2}$	-1.034	
Gas constant R	R	$Jmol^{-1} K^{-1}$	8.31441
$M_a(x_{CO_2}=0.0004)/R$	$M_a R^{-1}$	$10^{-3} kg KJ^{-1}$	3.48353